

The Physics of Spallation Processes

Theory, Experiments and Applications

von
Frank Goldenbaum

Von der Bergischen Universität Wuppertal
Fachbereich C - Mathematik und Naturwissenschaften
genehmigte Habilitationsschrift zur Erlangung der *venia legendi*

- December 2003 -

Die Atomik ist ein sehr verzwicktes Theorem, und man kann ihr mit Hilfe der Algebra beikommen, man muss dabei aber graduell vorgehen, denn sonst kann es passieren, dass man die ganze Nacht damit verbringt, einen kleinen Teil davon mit Rechenschiebern und Kosinen und anderen ähnlichen Instrumenten zu beweisen, ohne zum Schluss an das zu glauben, was man bewiesen hat.

(Flann O'Brien)

Abstract

A recent renaissance of interest for energetic proton induced production of neutrons originates largely from the inception of projects for target stations of intense spallation neutron sources (like the planned European Spallation Source ESS, the SNS in the US and J-PARC in Japan), accelerator-driven nuclear reactors, nuclear waste transmutation, and also from the application for radioactive beams. The ultimate objective is that the essential high- and intermediate energy nuclear data, required in the framework of such applications will be available in an energy range where currently almost no data exist. Although in this work the issue has been quite successfully addressed experimentally by varying the incident proton energy for various target materials and by covering a huge collection of different target geometries—providing an exhaustive matrix of benchmark data—the overriding challenge is to increase the predictive power of transport codes employed for various applications in particle physics. To scrutinize several of such codes, reaction cross sections, hadronic interaction lengths, average neutron multiplicities, neutron multiplicity and energy distributions, and the development of hadronic showers are here investigated. The problem of radiation-induced damage of window- and target-materials employed in spallation neutron sources due to embrittlement and blistering caused by helium gas production is expatiated in the current work. As for example production cross section measurements for light charged particles on thin targets point out that appreciable distinctions exist not only for different experiments, but also within the models applied here. The performance and flexibility of program packages like HERMES, LCS or MCNPX and their validation by using experiments is demonstrated.

Besides this application driven motivation for investigating GeV proton-induced spallation reactions, a more fundamental or nuclear physics aspect related to the excitation of heavy nuclei and the investigation of their subsequent de-excitation and fragmentation modes will be presented. The exploration of hot excited nuclear matter implies the understanding of their formation under extreme conditions (temperature, pressure). To this the transition of an ensemble of nucleons to thermal equilibrium has to be analyzed. As experimental observables the energy spectra of high-energetic charged particles like p, d, t, ^3He , ^4He , IMF(intermediate mass fragments), FF(fission fragments) are studied in coincidence with neutrons for light particle induced reactions on various targets. These observables allow for a quantitative determination of the energy relaxation process. The thermal excitation energy E^* transferred to the nucleus is found to be less than 30% of the total available energy (kinetic energy of projectiles + eventually annihilation energy in case of \bar{p}), irrespective of the projectile type. Therefore exotic decay modes like multifragmentation are unlikely and the experimental abundance of IMFs can be fully explained by statistical models, i.e. no evidence for multifragmentation up to $E^* \approx 1$ GeV is found and nuclei decay predominantly statistically, i.e. by evaporation. If multifragmentation is defined as a process that has 3 or more IMFs in the exit channel, an onset is found at about 4 MeV/nucleon. Even at highest excitation energies as for example for the 1.2 GeV $\bar{p}+\text{Cu}$ and $\bar{p}+\text{Ag}$ reactions the average IMF multiplicities restrain to values of 1 and 2, respectively. In accordance to this phenomenon up to the highest E^* the excited heavy nuclei are shown to survive as self bound objects as high fission probabilities clearly indicate. For the 1.2 GeV $\bar{p}+\text{Cu}$ reaction the onset of vaporization is observed at about 7.5 MeV/nucleon, with a total vaporization cross section of 3 mb.

Kurzfassung der Ergebnisse

Die Entwicklung neuartiger technologischer Großprojekte hat zu einer Renaissance des Interesses an der protoninduzierten Produktion von Neutronen geführt. Zu diesen zählen hochintensive Spallationsneutronenquellen (wie z.B. die European Spallation Source ESS, die SNS in den USA oder die J-PARC in Japan), beschleunigergetriebene unterkritische Reaktorsysteme, Anlagen zur Beseitigung radioaktiven Abfalls und Experimente mit radioaktiven Strahlen. Im Rahmen solcher Anwendungen ist die effektivste Art, die Primärstrahlenergie der Protonen in nutzbare Neutronen zu konvertieren, von höchster Wichtigkeit. Dieser Thematik ist in der vorliegenden Arbeit experimentell nachgegangen worden, indem bei Variation der Protoneneinschußenergie unterschiedlichste Target-Materialien und -Geometrien untersucht wurden. Die sehr umfangreiche Datenbasis stellt die Grundlage für extensive Vergleichsmöglichkeiten mit Modellrechnungen gängiger Computer Codes dar, die vielfältige Anwendung in der Teilchenphysik finden. Um diese Transportcodes (HERMES, LCS oder MCNPX) in ihrer Prognosequalität beurteilen zu können, werden Reaktionsquerschnitte, hadronische Wechselwirkungslängen, mittlere Neutronenmultiplizitäten, Neutronenmultiplizitäts- und Energieverteilungen und die Entwicklung hadronischer Schauer studiert. Das Problem strahlungsinduzierter Schädigung durch He-Produktion (Materialversprödung, atomare Versetzungen,...) des Fensters und der Target-Materialien, die in den Spallationsneutronenquellen eingesetzt werden sollen, ist in der aktuellen Arbeit ausgeführt. Beispielsweise zeigen protoneninduzierte Produktionswirkungsquerschnitte leichter geladener Teilchen aus dünnen Targets beträchtliche Abweichungen nicht nur für unterschiedliche Experimente, sondern auch innerhalb der Modelle.

Neben diesem anwendungsorientierten Aspekt liegt der Schwerpunkt dieser Arbeit in dem Studium der Spallationsphysik selbst. Es wurde erstmalig die Anregung schwerer Kerne unter Ausschluß dynamischer Effekte und die anschließenden Zerfallsmodi der heißen Kernmaterie studiert. Die Untersuchung heißer, angeregter Kernmaterie setzt das Verständnis der Erzeugung unter extremen Bedingungen (Druck, Temperatur) voraus. Hierzu muß der Übergang eines Ensembles aus Nukleonen zum thermischen Gleichgewicht analysiert werden. Als experimentelle Observable dienen die Energiespektren geladener Teilchen wie p, d, t, ^3He , ^4He , IMF, FF (fission fragments), die in Koinzidenz mit Neutronen nach Beschuß verschiedenster Targets mit leichten Teilchen gemessen wurden. Diese Observablen ermöglichen die quantitative Bestimmung der Energierelaxation in den untersuchten Reaktionen. Unabhängig von dem Projektteilchen beträgt der Anteil der thermischen Anregungsenergie E^* , die in dem Kern deponiert werden kann nur maximal 30% der totalen zur Verfügung stehenden Energie. Damit sind erwartete exotische Zerfallsprozesse wie z.B. Multifragmentation (MF) unwahrscheinlich und der experimentelle Produktionsquerschnitt für IMFs läßt sich vollständig mit statistischen Modellen erschöpfen, i.e. es liegen—zumindest für Anregungsenergien bis rund 1 GeV—keine Hinweise für MF-Phänomene vor. Definiert man MF als einen Prozeß, bei dem 3 oder mehr IMFs im Ausgangskanal gefunden werden, findet man die Schwelle bei 4 MeV/Nukleon. Selbst für höchste hier erreichbare E^* betragen die IMF Multiplizitäten beispielsweise für die 1.2 GeV $\bar{p}+\text{Cu}$ und $\bar{p}+\text{Ag}$ Reaktionen im Mittel nur $\langle M_{\text{IMF}} \rangle = 1$ bzw. 2. In Einklang mit dieser Beobachtung demonstrieren hohe Spaltwahrscheinlichkeiten schwerer Kerne, daß angeregte heiße Materie als gebundenes Objekt hohe Temperaturen überleben kann. Vaporisation wird für die 1.2 GeV $\bar{p}+\text{Cu}$ Reaktion ab etwa 7.5 MeV/Nukleon beobachtet, wobei dessen Wirkungsquerschnitt bei knapp 3 mb liegt.

Contents

1	Introduction	1
2	Research with Neutrons	5
2.1	The science case	6
2.1.1	Solid state physics	7
2.1.2	Materials science and Engineering	7
2.1.3	Chemical structure, kinetics and dynamics	7
2.1.4	Soft condensed matter	8
2.1.5	Biology and biotechnology	8
2.1.6	Earth and environmental science	8
2.1.7	Fundamental neutron physics	9
2.1.8	Muons as probes for condensed matter	9
2.2	Research reactors or pulsed spallation sources?	10
2.3	The European Spallation Neutron Source ESS	13
2.3.1	Short history of ESS	14
2.3.2	Technical design of ESS	15
	The Ion-source and the linear accelerator	16
	The compressor-rings	17
	The target stations	17
	The instruments and modes of operations	22
	Costs, time schedule and location	23
2.4	Concepts of transmutation	25
2.5	The “Energy-Amplifier”	27
2.6	Conclusion “Research with Neutrons”	29
3	Neutron production	30
3.1	The Spallation Process	31
3.2	Calculations of hadronic showers	33
4	Theory/Models	35
4.1	Transport equation	35
4.2	Nuclear physics models	37
4.3	Modeling of transport processes	38
4.4	Parameter discussion	44
4.4.1	Level density description	45

4.4.2	Coulomb Barriers for charged particle emission and feedback on neutrons	46
4.4.3	Equilibration time	48
4.5	Particular decay modes of hot nuclei	49
4.5.1	Fission	49
4.5.2	Vaporization and multifragmentation	53
5	Why nuclear physics experiments?	57
5.1	Application driven motivation	57
5.2	Astrophysics driven motivation	58
5.3	Nuclear physics driven motivation	59
6	Experiments	63
6.1	The COoler SYnchrotron COSY	63
6.2	The NESSI experiment	65
6.2.1	Objective	65
	Experiments at LEAR, PS (CERN) and COSY (FZJ)	66
6.2.2	Experimental setup	67
	The 4π sr neutron-detector	68
	Efficiency of the BNB-Detector	70
	Additional neutrons produced in the scintillator liquid	71
	The 4π sr Silicon-Detector	74
	Efficiency of the Si-Detectors	75
6.2.3	Corrections on the data	75
6.2.4	Trigger conditions	75
	The Targets	76
6.2.5	Plan of anticipated research	77
6.3	The PISA experiment	77
6.3.1	Objective	77
6.3.2	Experimental setup	78
	The channelplate detectors	79
	The Bragg curve detector	80
	The phoswich detectors	82
6.4	The JESSICA experiment	82
6.4.1	Objective	82
6.4.2	Advanced moderators at JESSICA	83
6.4.3	Experimental setup and method	86
7	Results and comparison with theory	89
7.1	Results NESSI Experiment/Theory	89
7.1.1	Thick targets	90
	The light signal of the BNB	90
	Reaction cross section and hadronic interaction length	90
	Neutron multiplicities	92
	Mean neutron multiplicities	92

	Neutron multiplicity distributions	93
	The economy of neutron production	99
	Neutron production by π, K, \bar{p}, p, d projectiles	100
	The GCCI level density and the MPM	103
	Coulomb barriers in thick targets	104
7.1.2	Thin targets	106
	Thermal excitation energy E^*	106
	Neutron multiplicity M_n -distributions for thin targets	115
	Particle production cross sections σ_n, σ_H and σ_{He} for thin targets	116
	Composite Particle Emission	119
	Fission	123
	Vaporization and Multifragmentation	127
7.1.3	Conclusion NESSI	130
7.2	Results PISA Experiment/Theory	132
7.3	Data Library of H- and He in p-induced reactions	137
7.4	Results JESSICA Experiment/Theory	137
8	Conclusion	142
	References	146

Chapter 1

Introduction

Neutron production in spallation reactions induced by energetic particles in heavy targets has been observed already in the late 40's. As a result of a continuous progress in accelerator technology, the construction of powerful intense spallation sources became possible, providing new opportunities for solid state physics, life and material science. In fact, a variety of projects have been initiated recently, including the construction at the Paul Scherer Institute (SINQ) [Bau96] of an accelerator-based, continuous neutron source and including several pulsed, high-intensity neutron sources, planned or under construction. Among the latter projects are the ambitious 10 MW European Spallation Neutron Source ESS [ess02-III, Gol02]¹, the 2 MW Spallation Neutron Source SNS [App95, sns02] in the US, and the Japanese facility J-PARC at KEK/JAERI [Nag99]. As genesis or originator of all spallation sources the Intense Pulsed Neutron System (IPNS) [Car78] as a national facility for condensed matter research realized at the Argonne National Laboratory may be considered. Studies for intense neutron generators (ING) based on Pb-Bi targets and a tremendous beam power of 65 MW (1 GeV proton beam) have been reported already 1966 by G.A. Bartholomew and P.R. Tunnicliffe [Bar66] - however the project was terminated in 1968. A very good review of early work before 1978 can be found in ref. [Bar78].

Intense, short-pulse neutron beams from accelerator-based sources make it possible to study a wide range of scientific problems via neutron scattering, exploiting time-of-flight techniques and allowing kinetic studies of various processes. In addition, powerful neutron sources, such as the sub-critical spallation/fission hybrid reactors [Nif99, Rub95, Rub97], provide a basis for various, potentially important applications often entitled as ADS—“Accelerator Driven Systems”. For example, such facilities may be used to effectively produce tritium [Bro96] or to achieve the incineration or transmutation of radioactive nuclear waste [Bow92, AIP94, Bow96b, Ven96, Fil97, ENEA01]. It is also important that the accelerator-based neutron sources are much more acceptable from the environmental point of view than nuclear reactors and that they show greater promise for future improvements in peak neutron intensities. However the notion to operate the planned high intense European neutron facility ESS also as a “multi-purpose-facility” like the Japanese project has meanwhile been disapproved due to consolidated findings of the CONCERT study [Con01].

¹In the original ESS feasibility study of 1996 [ess96-III] the spallation source was planned to have two short pulse target stations and 5 MW power. The new concept favors both a so called long pulse and a short pulse target station with 5 MW *each*.

The emphasis of the current work is focused on matters related to the design of the target station of the spallation source from a nuclear physics point of view, rather than on the accelerator relevant questions or on instrumentation of such facilities. The two latter aspects are—in the framework of the ESS—the tasks of the leading research centers RAL (ISIS [Isi99] at Rutherford-Appleton Laboratory located near Oxford) and HMI (Hahn-Meitner Institut Berlin GmbH).

Most of the occurring questions can be examined nowadays by simulations. The simulation is frequently even the only way to understand particularly complex systems. Therefore in the present work not only the nuclear physics experimental approaches at the COoler SYnchrotron COSY in Jülich will be described, but also some essential and basic aspects on the theoretical understanding. Today with the development of models, methods and data from the reactor physics, fusion technology, nuclear physics and high-energy physics information is accessible, which enables the application of particle transport computer simulations to certain specific queries. The particular challenge requested to the models is due to the description of hadronic and electromagnetic phenomena over 10 orders of magnitude ranging from the incident proton energies (GeV) down to the energy of the moderated sub-thermal neutron (meV). The complex features of neutron cross sections in the low energy region cannot be calculated from first principles using properties of the nucleus. Hence data must be determined empirically as a function of energy for each nuclide and for each reaction. In general these data cannot be interpolated over large energy intervals, because of the irregular resonance structure, although Breit-Wigner or other semi-empirical relations often allow a characterization of the cross sections in terms of few empirical parameters per resonance. Therefore cross sections as well as energy and angular distributions of the resulting secondary particles for hundreds of isotopes over an energy range from 10^{-5} eV to 150 MeV have been evaluated and culminated in nuclear data files (e.g. ENDF [End79, End01], JENDL [Jen95, Jen02], JEFF [Jef94, Jef02], CENDL-2 [Cen91, Cen92], BROND-2 [Bro94] et al.).

The motivation for investigating GeV proton-nucleus spallation reactions has two aspects:

- an applied one related to the current development of “large scale projects” or more specifically of intense spallation neutron sources, like in particular the ESS-project.
- and a more fundamental or nuclear physics aspect related to the excitation of heavy nuclei and the investigation of their de-excitation and fragmentation modes.

Both aspects justify a renewed effort in the investigation of spallation reactions, either because of the much more detailed experimental data needed for a thorough validation of the modern high energy transport codes, which are used for the design of spallation neutron sources, or, as an essential complement to recent heavy-ion studies of the disintegration modes of very highly excited nuclei. Moreover, the progress made in the experimental techniques since the early spallation investigations allows a much closer insight into the spallation reaction itself as well as into the dynamics and the time scales of the subsequent nuclear fragmentation.

Here in particular the nuclear physics experiments NESSI (NEutron Scintillator and Silicon Detector), PISA (Proton Induced SpAllation) and JESSICA (Jülich Experimental SpAllation target Setup In Cosy Area) carried out at COSY for the energy range up to

2.5 GeV incident proton energy will be subject. As for example the systematics of neutron production cross sections and neutron energy spectra as a function of incident proton energy, target material, and target geometry are not well known or documented in the literature.

The NESSI and the former PS208 collaboration at CERN have—in order to fill these gaps systematically—performed a series of proton- and antiproton induced experiments [Egi00, Enke99, Fil01, Fil01b, Fil99, Gol01, Gol00, Gol00b, Gol99b, Gol99d, Gol99e, Gol99f, Gol98b, Gol96, Gol96b, Her01, Hil01, Hil98, Hil96b, Hil95b, Hil95c, Jah01, Jah99, Jah96, Jah95, Jah95b, Let00, Lot01, Lot99, Lot98, Lot97, Pie00, Pie99, Pie97, Sch97] using a highly efficient 4π sr gadolinium loaded scintillator neutron detector [Gal94, Gal01] partly in combination with a 4π sr silicon detector [Boh92, Fig95, Pau92] for charged particles. These measurements covered a large range of incident hadron (p, \bar{p}, π^\pm, K and d) energies, as well as a variety of target materials and geometries. In contrast to the older measurements of typically only average neutron multiplicities [Fra65, Rus80, Arm84, Vas90, Nik90, Tak97, Ara99], the NESSI experiments have provided also event-by-event information on these multiplicities.

PISA effectively considered as successor of or supplement to NESSI is an experiment currently under construction at the internal ring COSY. Recent test-measurements provided first data currently being analyzed and briefly presented here.

JESSICA is a 1:1 ESS Hg target-reflector-moderator mockup which aims at studying sub-thermal neutrons using advanced moderators. Time-dependent neutron spectra are investigated by Bragg reflection and 'time-of-flight' (TOF)-methods.

The extensive set of benchmark data obtained in the NESSI, PISA and JESSICA experiments imposes strong constraints on the theoretical modeling of the occurring interactions [Enke99, Gol01, Gol00, Gol00b, Gol99b, Gol99e, Her01, Hil01], and allows one to calibrate and improve widely-used high-energy transport codes [Fil00, Fil96, Ste98]. The accuracy of such codes is critical for the design of high-power target stations, since the optimization of geometrically expanded high power target stations will finally rely on general Monte-Carlo particle transport codes having maximum predictive power.

In particular above 1 GeV so far only limited data [Fil97, Hsi97, Shu97] were available for light charged particles, intermediate mass and fission fragments. Calculated data deviate as much as a factor of 5-10. With NESSI, H and He production cross sections which are of particular interest for studying radiation damage in target and structure materials have been measured. Kinetic energy and angular distributions of H- and He-isotopes as a function of thermal excitation energy E^* have been deduced [Enke99, Gol96b, Her00, Pie00]—following a procedure described in detail in ref. [Gol96b, Pie00].

Unfortunately the experimental setup of NESSI [Enke99, Gol96, Gol96b, Let00] is not suited for measuring the kinetic energy or angular distribution of neutrons as for example reported for 800 MeV proton-induced reactions on heavy thick targets in ref. [Rus80] or thick tungsten targets [Tak97]. These spectra would be of particular interest for shielding requirements of spallation neutron sources. Published data for 800 MeV p+Pb vary, for instance, by a factor of two at neutron energies above 50 MeV [Rus80, Ami92, Sta93, Mar97]. Energy spectra and angular distributions of neutrons have recently been measured at various incident projectile energies [Ler01, Egi00, Led99, Tit00, Ish97, Mei99]. Isotopic distributions and kinetic energies of residual nuclides have recently been studied by exploiting

inverse kinematics of relativistic heavy ions (at 0.8 GeV/A) on a hydrogen target at GSI Darmstadt [Wla00, Rej01, Enq01, Ben01] and Hannover University [Glo96, Glo01]. A systematics of proton induced fission cross section data has recently been compiled at Uppsala and Jyväskylä Universities [Pro01, Rub01]. These additional observables certainly are of large interest for assessing the radioactivity and radio-toxicity of target materials and for representing further constraints to the models [Glo01, Kor01, Ler01].

This work is partitioned into 8 chapters. Chapter 2 and 3 represent as science case an overview on present and anticipated research with neutrons and the current methods to produce them. The projects and aspects in the framework of ADS will be addressed in chapter 2 in particular in the context of high intensity spallation neutron sources as for example the European Spallation Neutron Source ESS [ess96-III, ess02-III].

Chapter 3 presents the different means to produce neutrons in general with special emphasis on the spallation process and a phenomenological description of the spallation process itself including the propagation and development of hadronic and electromagnetic showers in thick target materials as a function of incident proton energy.

Chapter 4 will be devoted to the characterization and evaluation of theoretical models being used in the present work. First the basic ideas and validity ranges of the physics models are discussed before presenting the realization and implementation within the code-packages, such as HERMES [Ste98, Clo88, Fil00c], LCS [Pra89], or MCNPX [Hug97]. In addition to the “standard” intra-nuclear cascade (INC) codes, derivatives of the code Bertini [Ber63, Ber69, Ber70, Ber72], the present study comprises also the time-dependent Liege INCL2.0 code [Cug81, Cug84, Cug87, Cug97a, Cug97b] coupled with the evaporation code GEMINI [Cha88]. Relevant key parameters selectable in these codes are introduced. The theoretical description of particular decay modes of hot nuclei as for example vaporization, multifragmentation and fission are discussed.

Both the application driven as well as the more fundamental nuclear physics or astrophysics provoked motivation justifying the investigation of (anti-)proton-induced spallation reactions in the GeV range is discussed in detail in chapter 5.

After a brief description in chapter 6 of the objectives and the respective experimental methods and setups of the three different experiments NESSI, PISA, and JESSICA currently installed at the Cooler Synchrotron COSY (Jülich), chapter 7 is dedicated to comparing the results of simulation calculations to the experimental data. Such a comparison has revealed serious limitations of the mainstream models. Striking deficiencies of the theoretical models are discussed.

The overall objective of this work is to obtain a comprehensive understanding and modeling of nuclear reactions in the 20-2500MeV region, which are specific to spallation physics aspects. The essential goal can only be accomplished by means of a well-balanced combination of basic cross section measurements, nuclear model simulations and data evaluations as summarized in chapter 8.

Chapter 2

Research with Neutrons

A neutron is an uncharged (electrically neutral) subatomic particle with mass 1,839 times that of the electron. Neutrons are stable when bound in an atomic nucleus, whilst having a mean lifetime of approximately 900 seconds as a free particle, decaying through the weak interaction into a proton, an electron, and an antineutrino. The neutron (like the proton) is the ground state of a three-quark system and consists of one “up” and two “down” quarks with spin 1/2 and baryon number 1. QCD allows the calculation of particle masses and magnetic moments; predictions, 939 MeV and -1.86 nuclear magneton, compare well with measured values, 939.6 MeV and -1.913 nuclear magneton. The neutron and the proton form nearly the entire mass of atomic nuclei, so they are both called nucleons. They interact through the nuclear, weak, electromagnetic and gravitational forces.

At the end of the second World War researchers in the USA gained access to the large neutron fluxes that even relatively modest nuclear reactors were capable of delivering. For more than a decade (Nobel Prize in physics to Sir James Chadwick in 1935 for the neutron discovery in 1932) neutrons had then been known as building blocks in the atomic nucleus. Enrico Fermi showed in 1942 that neutrons from fission of the uranium nucleus could support a controlled chain reaction. He had earlier made the important discovery that slowed-down or thermal neutrons show a much greater inclination to react than fast ones do (Nobel Prize for this discovery, among others, to Fermi in 1938). The special properties of these slow neutrons make them suitable for detecting the positions and movements of atoms. Even before the entry of the nuclear reactors into the research arena, results of using simple neutron sources had indicated that neutron beams could be used for studying solid bodies and liquids (condensed matter). However, there were many difficulties to overcome before these possibilities could be realized. The 1994 Nobel Prize in Physics was awarded to Bertram Brockhouse and Clifford Shull for their pioneering contributions to the development of neutron scattering techniques (neutron diffraction and neutron spectroscopy) for studies of condensed matter. In simple terms, they helped answer the questions of where atoms “are” and of what atoms “do”.

Neutrons are an ideal probe for investigation of the structural and dynamical properties of matter. Their electrical neutrality enables them to penetrate deep into matter and due to the low energy the matter can be studied without being destroyed. The magnetic moment enables neutrons to explore microscopic magnetic structures and study magnetic fluctuations. The energies of thermal neutrons are similar to the energies of elementary excitations in solids and consequently molecular vibrations, lattice modes and the dynamics of atomic motions can be probed. Very much the same is true for the wavelengths of

thermal neutrons being similar to the atomic spacings and therefore a means to determine structural information from 10^{-13} to 10^{-4} cm or crystal structures and atomic spacings. Applying a method called “contrast variation” complex molecular structures can be differentiated since the scattering amplitude of neutrons depends strongly on individual isotopes. Due to the unique sensitivity of neutrons to hydrogen atoms, the best way to see a part of a biomolecule, nucleic acid or a protein in a chromosome is through isotope substitution-replacing hydrogen by heavy hydrogen (deuterium) atoms. In particular for light atoms this physical property makes neutron scattering out-classing compared to investigations using x-rays, because neutrons scatter from materials by interacting with the nucleus rather than the electron cloud of an atom. This means that the neutron scattering power (cross-section) of an atom is not strongly related to its atomic number (the number of positive protons in the atom, and therefore number of negative electrons, since the atom must remain neutral), unlike X-rays and electrons where the scattering power increases in proportion to the number of electrons in the atom. Therefore neutron scattering has three significant advantages:

- it is easier to sense light atoms, such as hydrogen, in the presence of heavier ones
- neighboring elements in the periodic table generally have substantially different scattering cross sections and can be distinguished
- the nuclear dependence of scattering allows isotopes of the same element to have substantially different scattering lengths for neutrons. Isotopic substitution can be used to label different parts of the molecules making up a material.

Moreover the absolute value of the x-ray scattering cross sections is particularly small for light atoms compared to neutron scattering cross sections. The capability of neutrons localizing other light atoms among heavy atoms allows scientists to determine the critical positions of light oxygen atoms in yttrium-barium-copper oxide (YBCO)—a promising high temperature superconducting ceramic. The span of applications is ranging from the basic research of materials science (structure of new alloys or modern plastics and ceramics) up to the enlightenment of the structure and function of proteins, enzymes and other bio molecules. Engineering scientists use neutrons for the investigation of highly loaded components (e.g. turbine blades) and measuring of the inner forces of workpieces, geo scientists for the research of rock samples or chemists for the acknowledgement of catalytical processes or the structure of re-developed molecules. Neutrons scattered from hydrogen in water can locate bits of moisture in jet wings indicating microscopic cracking and early corrosion.

2.1 The science case

The science case is such many fold and voluminous that in the following only a small representative selection can be shown up in order to motivate the need for a new generation of high intensity neutron sources. A more detailed compilation can be found in Volume(s) II “The Scientific Case” [ess96-II, ess02-II] and the Engelberg Progress Report [Eng01]. To anticipate, many questions in almost all research disciplines desire for higher intensities and better monochromatization than currently available with existing sources.

2.1.1 Solid state physics

Neutrons are the key to our understandings of solids. Nowadays advances in solid state physics provide the backbone of many technologies. One example is molecular and organic magnets i.e. solids built from structurally well defined clusters of magnetic ions in a complex environment. Such systems are of fundamental importance and could also serve as atomic scale information storage systems. Research on the electron-electron interactions underpinning such phenomena as high-temperature superconductivity and “colossal” magneto-resistance are at the cutting edge of solid state physics. The high neutron flux anticipated at next generation facilities will enable experiments on excitation continua of metallic systems, among others, that will yield a wealth of new information. Alternatively NMR techniques yield valuable local data on the magnetic susceptibility of solids, but interpretation of these data requires knowledge of the material-specific hyperfine interactions. The interaction parameters are difficult to calculate and to measure independently, especially for complex materials. Even if they could be calculated accurately, NMR would remain constrained to energies several orders of magnitude below those of electronic correlation effects. Synchrotron radiation is another valuable characterization tool for solid state magnetism. However, the cross section for charge scattering is several orders of magnitude larger than that for magnetic scattering of photons. Thus, even magnetic structure determinations of simple single-crystalline solids by magnetic x-ray scattering are exceedingly difficult. A quantitative determination of the magnetic collective modes and excitation continua of complex electronic materials by inelastic x-ray scattering will not be feasible in the foreseeable future.

2.1.2 Materials science and Engineering

The interaction of a neutron with the nucleus of an atom is weak, (but not negligible) making the neutron a highly penetrating probe. This allows the investigation of the interior of materials, rather than the surface layers probed by techniques such as X-ray scattering, electron microscopy or optical methods. This feature also makes the use of complex sample environments such as cryostats, furnaces and pressure cells quite routine, and enables the measurement of bulk processes under realistic conditions. High intensity spallation neutron sources will allow for the first time to investigate materials in *real time* with *realistic dimensions* and under *real conditions*. One example is the deformation of materials and the understanding of the mechanisms involved. New solid state joining techniques require more accurate information about the generation of residual stresses that will add to in-service stresses and shorten component life. Finite element modeling has become the main method for the design and assessment of engineering structures. Such models cannot be developed reliably without accurate information to validate them. Neutron diffraction is the only technique that can do this, providing measurements deep inside most engineering materials.

2.1.3 Chemical structure, kinetics and dynamics

Neutrons are spin-1/2 particles and therefore have a magnetic moment that can couple directly to spatial and temporal variations of the magnetization of materials on an atomic

scale. Unlike other forms of radiation, neutrons are ideally suited to the study of microscopic magnetism, magnetic structures and short wavelength magnetic fluctuations. The cross-sections for magnetic scattering and scattering from the chemical structure are fortunately of the same magnitude, permitting the simultaneous measurement of the magnetic and chemical behavior of materials. Chemists ask for higher performance materials, cleaner environments and improved efficiency in the use of chemicals. The aim is to develop molecular materials with useful and tune-able physical properties such as magnetism, superconductivity, nonlinear optical activity, polymorphism, etc. The understanding of intermolecular interactions that hold 3-D arrays of molecules together as e.g. weak hydrogen bonding interactions is mandatory. Neutron research will allow for more rational crystal engineering, enabling chemists to tailor properties by designing structures, e.g. of pharmaceuticals.

2.1.4 Soft condensed matter

High penetrability, space time resolution at proper scales and variation of contrast qualify neutrons as a unique tool for studying the structural and dynamical properties of soft matter at a molecular level. One challenge of basic soft condensed matter science is the development of a molecular rheology, i.e. an understanding of mechanical and rheological properties on the basis of molecular motion. This aim requires space time resolution on widely differing length and time scales and the selective observation of key components. Neutrons are uniquely suited to meet these goals, however advances in instrumental techniques and neutron flux are required, far beyond the present state of the art.

2.1.5 Biology and biotechnology

Neutrons are non-destructive probes, even to complex and delicate biological or polymeric samples. Neutrons are of major importance, when information on hydrogen atoms - their positions, hydrogen bonds, the role of water, hydrogen motions - as well as contrast variation on larger scales and dynamical features in general are of interest. Unfortunately, present neutron intensities are too low to expect progress in a broad sense. Present neutron sources require large sample sizes, which are often not available. Their limited intensity renders multidimensional contrast variation schemes impossible and constrains time resolution severely. Next generation sources will enable the miniaturization of neutron-scattering techniques and facilitate multiparameter studies. The future intention is to provide tools for finding molecular markers for early stage detection of illnesses. Neutron data on such complex systems become a prerequisite for the design of more advanced combinations of biological matter with solid surfaces for biochips, including bio-sensors.

2.1.6 Earth and environmental science

Thanks to the latest generation of diffractometers and spectrometers at the most modern neutron sources, neutron scattering has recently been added to the methods applied in earth science. However as for example one of the most significant issues in earth science related to the prediction of earth quakes and vulcanic eruptions remains out of the reach

of present day neutron instrumentation. The reliability of models crucially depends on the knowledge of the physical and chemical properties of the materials involved (oceanic crust, upper mantle, continental crust). Mineral structures and material behaviors under extreme temperature and pressure conditions simulating the real conditions deep in earth would be in the field of in-situ studies when more intense neutron sources would be available.

2.1.7 Fundamental neutron physics

The features of neutrons appearing as both composite particles and quantum waves have been investigated with thermal, cold and ultra cold neutrons at many sources. Accurate measurements of the neutron β -decay confirmed the number of particle families predicted in the Standard Model at three. Neutron experiments have made substantial contributions to our understanding of strong, electroweak and gravitational interactions. A significantly higher intensity and pulse structure of future generation neutron sources would provide new possibilities for fundamental neutron physics experiments. One of several questions concerns the handedness of the universe. The grand unified theory assumes a left-right symmetric universe and explains the evident left handedness of nature through a spontaneous symmetry breaking caused by a phase transition of the vacuum, a scenario which would entail a small right handed component for the neutrinos. Looking at the decay of a neutron into a hydrogen atom could provide a definite answer, since one of the four hydrogen hyperfine states cannot be populated at all if neutrinos are completely left handed. The best way to check whether deviations in the singlet scattering lengths signal a breakdown of isospin invariance, is a direct scattering measurement of the neutron-neutron scattering at very low energy as available at the ESS. Ultra cold neutrons could be used to study elastic and inelastic surface reflections and quantum gravitational states.

2.1.8 Muons as probes for condensed matter

Spallation neutron sources as discussed in the following chapter represent at the same time an intense resource of muons. Muons provide an alternative to the neutron as a probe of condensed matter and are frequently used in complementary experiments. The muon can be implanted into virtually any material and its spin polarization monitored to determine its site in crystal lattices or molecules, giving information about the local atomic structure and dynamics. Resulting from the decay of positive or negative pions into a muon and a neutrino, muons have spin $1/2$, carry one elementary electric charge, and have a mass about 207 times the rest mass of the electron or $1/9$ th of the proton rest mass. Thus, from a particle-physics point of view they are "heavy electrons", whereas from a solid-state-physics or chemistry point of view they are "light protons". In the rest frame of the pion, the muon magnetic moment is antiparallel to the muon momentum, allowing muon beams with a very high degree of spin polarization (nearly 100% when the muons are collected from pions decaying at rest) to be produced. Free muons have a mean lifetime of $2.2 \mu\text{s}$, decaying into a positron and two neutrinos, with the positron emitted preferentially in the direction of the muon spin, allowing the time evolution of

the muon polarization to be measured by detecting the position of the decay positrons. Why using muons for condensed matter studies?

- The muon is essentially a sensitive microscopic magnetometer with a magnetic moment three times that of the proton. In condensed matter, muons are repelled by the nuclei, and thus muons probe magnetic fields in the interstitial regions between the atoms. The frequencies of muon resonance or precession signals give a direct measurement of local magnetic or hyperfine fields. Measurements of the relaxation of the muon polarization characterize the distribution of these fields.
- In contrast to the neutron, the muon is usually a perturbative probe since it represents a defect carrying a unit positive charge. The defect interactions are essentially identical to those of the proton, allowing, for example, studies of the isolated hydrogen defect centers in semiconductors via their muonium analogues.
- In insulators, semiconductors, and in organic materials positive muons may capture an electron, to form hydrogen-like quasi-atoms known as muonium (Mu). Due to the hyperfine interaction between muon and electron spin, muonium is an even more sensitive magnetic probe than the bare muon. Muonium can be used as a substitute for hydrogen in organic molecules or radicals, giving information on the structure, dynamics and reactions of these species.
- Muons have approximately one-ninth of the proton mass, resulting in large isotope effects. This favors the observation of quantum effects, notably the influence of zero point energy in chemical bonds and quantum tunneling.

2.2 Research reactors or pulsed spallation sources?

Presently, Germany runs three medium flux reactors, the BER-II at Berlin, the FRJ-II at Jülich and the FRG-1 at Geesthacht. Except of the first one which was refurbished around 1990, the reactors were built between 1950 and 1960. The FRJ-II and the FRG-1 are expected to be shut down within the next five years while BER-II is envisaged to be operational for another 20 years or more. The new reactor FRM-II in Munich, having about a factor of two less neutron flux than the High Flux Reactor (HFR) at the ILL in Grenoble, was scheduled to become operational in 2002; however, due to a continuing retardation of the final operation license by federal authorities its timely availability for scientific usage remains undecided. The present European research base of neutron sources consists of several reactors and two spallation sources of different neutron fluxes as listed in Tab. 2.1.

Neutron scattering is still very much an intensity limited technique. Future user communities will be interested in increasingly more complex materials and more complex questions about them: The emphasis will be on higher precision and better resolution.

Neutron fluxes from traditional reactors have nearly reached their limits because of heat dissipation in the core. Precision and resolution depends on increasingly better neutron monochromatization. Better monochromatization in turn entails less intensity or lower precision. Consequently pulsed spallation neutron sources with orders of magnitude

Table 2.1: Compilation of of European and Russian reactors and spallation sources.

Country	facility	power	n-flux [$\text{n cm}^{-2} \text{s}^{-1}$]
Czech Republic	^a LVR-15 Prague	10 MW	1×10^{14}
France	^a ILL Grenoble	52 MW	1.2×10^{15}
	^a LLB-Orphee Saclay	14 MW	3×10^{14}
Germany	^a FRJ-II Jülich	23 MW	2×10^{14}
	^a BER-II Berlin	10 MW	2×10^{14}
	^a FRG-1 Geesthacht	5 MW	8×10^{13}
	^{a,b} FRM-II Munich	20 MW	7×10^{14}
Hungary	^a BRR	10 MW	1.6×10^{14}
Netherlands	^a HCR Delft	2 MW	2×10^{13}
Norway	^a JEEP2	2 MW	2.2×10^{13}
Russia	^c IBR-2	2 MW	1×10^{16}
Sweden	^a NFL R2	50 MW	1×10^{14}
Switzerland	^d SINQ Villingen	1 MW	2×10^{14}
UK	^e ISIS Abington	156 kW	$2 - 10 \times 10^{15}$

^aresearch reactor

^bunder construction

^cpulsed reactor

^dcontinuous spallation source

^epulsed spallation source, neutron flux given as peak value, second target station is planned.

higher peak fluxes shall be built. As for example the ESS will have a thermal neutron peak flux of up to $2 \times 10^{17} \text{n cm}^{-2} \text{s}^{-1}$. Since the early 50ties the intensity of neutron sources has increased just by a factor of four. In contrast the ESS will yield in a tremendous progress. Its intensity increase by two orders of magnitude will revolutionize the neutron science. To convey an impression of the potential power of the ESS, today's most powerful pulsed neutron spallation source, ISIS (UK) [Isi99], produces short pulses of an even higher peak flux than those provided by the world's strongest research reactor at the Institut Laue-Langevin. But ISIS' peak-intensity is only 1/30 of that projected for ESS.

The need for both reactor based (normally steady-state or continuous) and accelerator based (pulsed) neutron sources has long been realized by the neutron science community. Due to the dramatic improvements in accelerator technology in recent years, generally neutron pulses can be produced with much higher intensity than that available from continuous sources. Furthermore, unlike the situation at a continuous neutron source, pulsed sources allow the determination of the kinetic energy of individual neutrons using "time-of-flight" methods and making "movies" of molecules in motion. Like a flashing strobe light providing high speed illumination of an object the ESS as for example will produce pulses of neutrons every 20 ms with 30 times more neutrons than are produced at the most powerful pulsed neutron sources currently available.

Urgent need for new generation intense neutron sources is also clearly demonstrated when comparing the number of active researchers in the neutron scattering community

with the drastically decreasing sources being available in the near future. About 4000 scientists in Europe – more than 800 in Germany – use neutrons in their field of research. The European Neutron Scattering Association (ENSA) found not only physicists interested in neutron scattering research, but also a broad spectrum of other disciplines as demonstrated in the upper panel of Fig. 2.1. Chemists, materials scientists and members of the life, earth and engineering science communities view neutron scattering as an essential tool in their exploration and exploitation of the structure and dynamics of condensed matter. New science and industrial applications increased the demand for more intense sources. This demand is completely contrary to the worldwide decline of existing sources in the near future—a tendency predicted by the Organization of Economic and Cooperative Development (OECD). The latter effect shown in the lower panel of Fig. 2.1 is mainly due to the shutdown of aging research reactors.

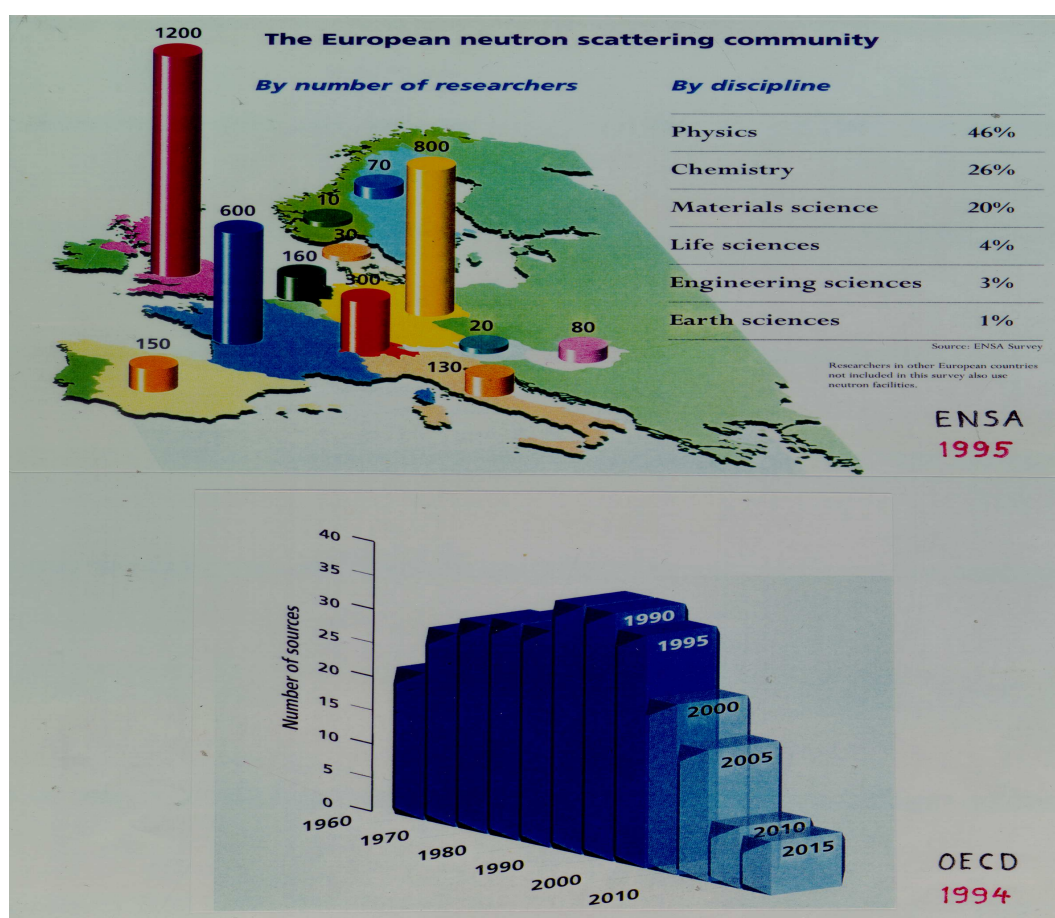


Figure 2.1: *Opposing the number of researchers in the neutron scattering community with the decreasing number of sources available.*

Accelerator based spallation neutron sources present an inherently safe way to produce neutrons, because the neutron production stops when the proton beam is turned off. It also produces few hazardous materials.

All these factors underscore the need for next generation neutron sources.

2.3 The European Spallation Neutron Source ESS

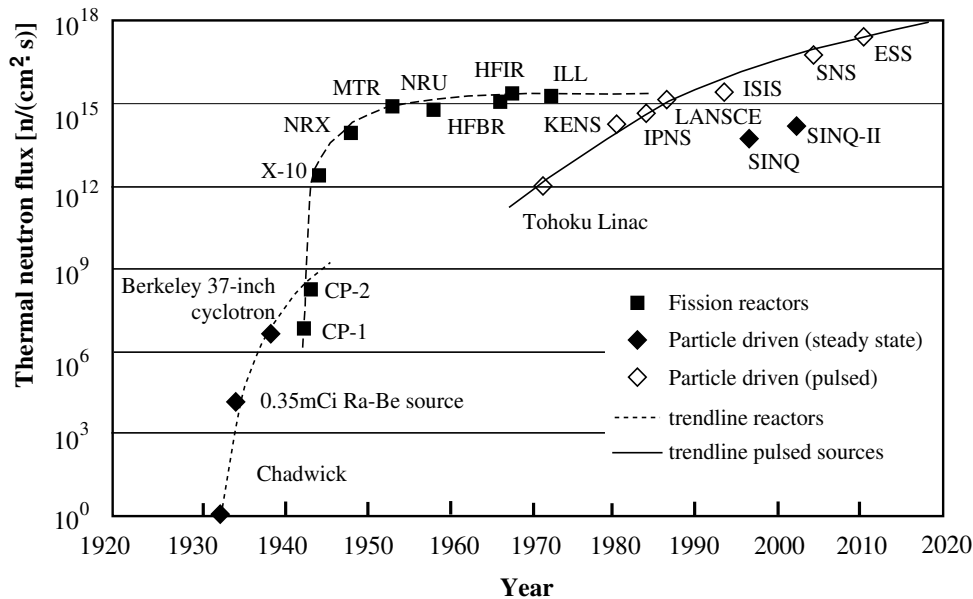


Figure 2.2: *Evolution of the performance of reactors and pulsed spallation sources.*

Fig. 2.2 provides insight to trends in the developments in neutron reactor and accelerator facilities over time, starting with the discovery of the neutron by Sir James Chadwick in 1932. The figure compares the peak thermal neutron flux versus the year the facility began or is scheduled for operation. Note that the figure compares peak fluxes for both steady-state and pulsed sources, and even though the pulsed sources have high peak fluxes, they lack the integrated neutrons of steady-state sources; and while peak flux is an important parameter for neutron scattering, total flux is needed for such objectives as transmutation or isotope production. While reactor sources have leveled off, accelerator-based sources show considerable promise for even higher intensities in the future.

Advances in accelerator design and technology, new approaches to instrumentation design and measurement techniques, and increasing difficulties in gaining environmental acceptance for nuclear research reactors (especially in Germany) have all contributed to the trend toward using accelerators for the new sources being planned. As for example with a beam power more than 30 times that of ISIS and improved instrumentation for pulsed sources, effective intensity gains up to three orders of magnitude over ISIS can be anticipated in some cases through combination of source brightness and instrument development. The European Spallation Source ESS [ess02-III, Gol02] being discussed in more detail in the following is found to be the most ambitious project besides the SNS is the US. However a high power spallation source like the ESS, injecting a 1.334 GeV / 62.5 A peak current pulsed proton beam into liquid Hg at a 50 Hz repetition rate has never before been realized. Therefore technical boundaries need to be pushed beyond present limits. Furthermore only a limited amount of both theoretical and experimental data on the nuclear spallation process, cross sections and reaction products are available for such target stations. One of the goals of this work is to provide such nuclear data for spallation sources.

2.3.1 Short history of ESS

The accelerator-based pulsed high intensity neutron source running at ISIS (RAL) [Isi99] and the Intense Pulsed Neutron System (IPNS) [Car78] as a national facility for condensed matter research realized at the ANL may be considered as the genesis of the ESS. In the following a brief historical survey is given:

1977-84 Study, design and construction of the national spallation source ISIS in the UK

1984 British spallation source ISIS operational

1979-85 Feasibility study for a National German Spallation Source SNQ; the project was finally not approved

1990 Recommendation from a CEC Panel on Large Scale Facilities: Carry out studies for next generation neutron sources

1991-92 Joint initiative from Forschungszentrum Jülich and Rutherford Appleton Laboratory (UK): Series of workshops held identifying the concept of a future European spallation source; proposal for a pulsed neutron source:

- 5MW beam power, $1\mu\text{s}$ proton pulse length
- 2 target stations: 5 MW at 50 Hz, 1 MW at 10 Hz

1993 Start of the multi-national study (8 European countries & CEC), establishment of the ESS scientific council

1996 Publication of the ESS “Final” report

- Volume I - The European Spallation Source
- Volume II - The Scientific Case [ess96-II]
- Volume III - The Technical Study [ess96-III]
- Identification of further high priority R&D work

1997 Establishment of ESS R&D Council

1997-2001 ESS R&D phase

2001 Workshop in Engelberg [Eng01]; proposal for both:

- short pulse target station (SPTS, 50 Hz, $1.4\mu\text{s}$, 5 MW)
- long pulse target station (LPTS, $16\frac{2}{3}$ Hz, 2 ms, 5MW)

2002 Publication of the ESS revised report as presented on the “Bonn-event”

- Volume I - European Source of Science [ess02-I]
- Volume II - New Science and Technology for the 21st Century [ess02-II]
- Volume III - Technical Report [ess02-III]
- Volume IV - Instruments and user support [ess02-IV]

The final approval of the European Spallation Source presumes a teamwork not only on a national level, but also on a broad European or even worldwide cooperation.

2.3.2 Technical design of ESS

A spallation neutron source is an accelerator driven facility. The process involving the scientific community that has settled on the functional requirements for ESS has been long deliberate and evolutionary. There were rapid advances in neutron science not long after the first neutron sources were built and utilized. As improved cold neutron sources, neutron guides and advanced instrumentation were developed, the applicability of neutron scattering to a much broader range of science became apparent. New research reactors and accelerator based sources have been built during the last 20 years. The unanimous demand for a short-pulse spallation source (proton pulses of $1.4 \mu\text{s}$ or shorter) resulted in subdividing the task into three major fields of study:

1. the injector and the linear accelerator (linac)
2. one or more ring(s) for compressing the (long) linac pulses
3. the target station(s).

Since the 1996 ESS-feasibility study [ess96-III] the reference concept remained largely unchanged, because only little engineering work has been done in the meantime. Therefore in the following only a brief description is given and the most important changes are summarized. A schematical sketch of the currently anticipated facility comprising the linear-accelerator/compressor-ring/SP- and LP target-station is given in Fig. 2.3 [ess02-III].

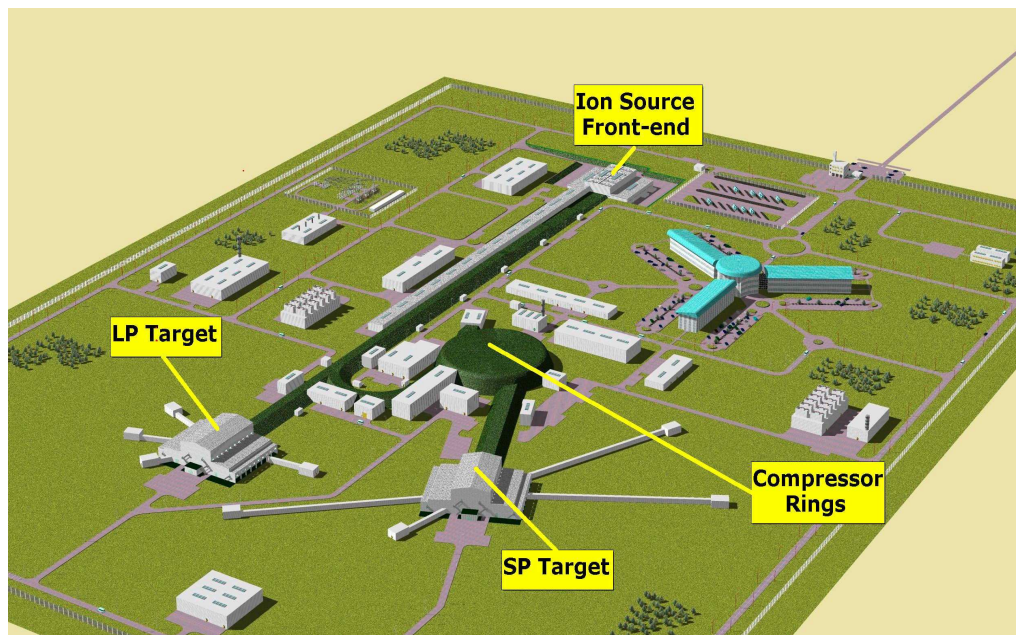


Figure 2.3: *ESS - a possible layout: Artist's view of the ESS facility showing the ion source, the linac tunnel leading to the accumulator and compressor rings from where the beam is distributed to the short pulse target station. The long pulse target station with instruments is directly connected to the linac.*

The Ion-source and the linear accelerator

Negatively charged hydrogen (H^-) ions are produced by an ion source. As shown as a basic scheme in Fig. 2.4 the ion beams accelerated in a sequence of radio-frequency quadrupoles (RFQ) and a drift-tube linac (DTL) will be combined in a funneling section at an energy of about 20 MeV for further acceleration in a second DTL up to 90 MeV. From there on a linac system of cell-coupled structures (CCL) takes the beam up to its final energy of 1334 MeV. The design is optimized for very low beam losses (≤ 1 nA/m) in order to allow hands-on-maintenance and repair even at the high energy part. For a high current pulsed accelerator the choice between normal or superconducting (sc) high energy part of the linac is by no means trivial. As a consequence the ESS project has on purpose followed two different ways: The first is to revise the 96' [ess96-III] accelerator proposal in view of the R&D efforts and the second is to look at a SC version based on the ESS-CEA CONCERT study [Con01]. It appears that both designs are capable of delivering the required performance. Currently ESS is assessing in more details risks, costs and engineering fine-tuning. As compared to the earlier design [Pab99] the normal conducting linac layout has recently evolved to a coupled cavity linac (NCCCL) operating at 560 Hz [Gar99]. The recently decided modification in operating frequencies from 175,

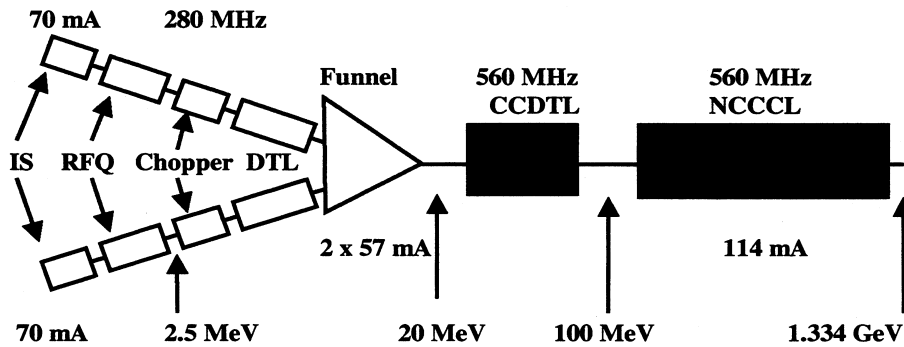
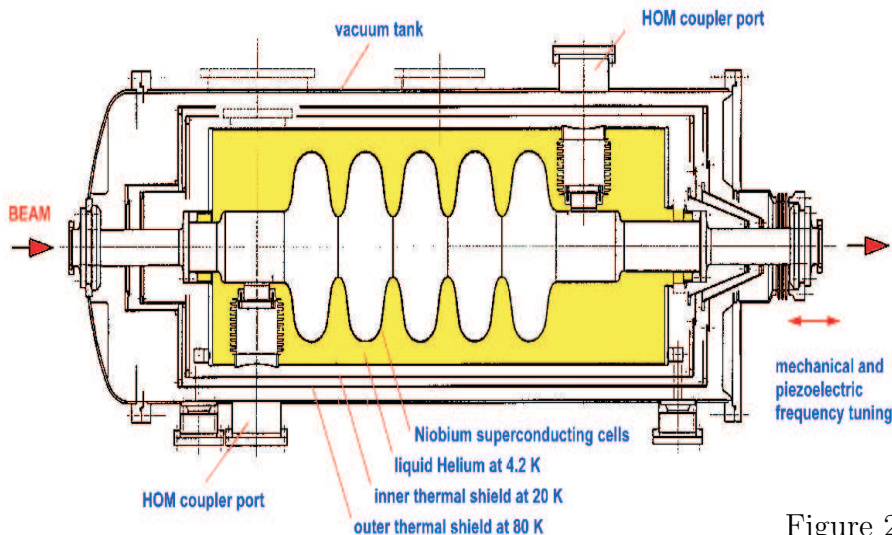


Figure 2.4: Revision of the 1996 ESS accelerator design

350, 700 to 280, 560 MHz is a good compromise for various linac stages. The peak bunch current in the main part of the accelerator is reduced by a factor of two compared with the original reference design as each rf cycle now contains beam. Complete beam tracking with space charge effects has now been carried out from the RFQ to the exit of the CCL. Beam chopping as required to generate the clean micro-pulses necessary for injection into the ring will be done at an energy of 2.5 MeV in the two front ends. The majority of length of the linac will be taken up by the CCL structure, for which a superconducting version is being developed to shorten its overall length and reduce operating costs. These savings should overcompensate for the additional costs of refrigeration and the more expensive superconducting cavities. The final beam emittances are a factor of two and three lower in the transversal planes and in the longitudinal plane, respectively in comparison to the original design [Pab99]. A high frequency supra-conducting cavity is shown in Fig. 2.5. Details on R&D results for the accelerator are given in refs. [ess96-III, ess02-III, Fil01d, Gol02] and references therein.

Figure 2.5: *ACCEL-Modul*

The compressor-rings

The negatively charged hydrogen (H^-) ions are passed through a foil, which strips off each ion's two electrons, converting it into a proton. The protons likewise pass into two rings where they accumulate in bunches. Space charge problems and low injection losses require the use of two compressor storage rings, one on top of the other. Approximately 1000 turns are accumulated and all 2×10^{14} protons are kicked out at once, producing a pulse less than $1 \mu\text{s}$ in duration. Powers in the 5 megawatt range (time average) are beyond the current technology limits for a single ring. Of several possible options for the linac/ring combination, a solution was favored with a supra-conducting linac delivering the full energy of 1.334 GeV and two compressor rings working in parallel rather than a lower-energy linac and a rapid cycling synchrotron.

The target stations

The science advisory group has reassessed the ESS proposal from 1996 and at the workshop in Engelberg [Eng01] the need was clearly demonstrated to have both a short pulse target station (SPTS, 50 Hz, $1.4 \mu\text{s}$, 5 MW) and a long pulse target station (LPTS, $16 \frac{2}{3}$ Hz, 2 ms, 5MW). Thus the ESS linac is required to deliver additionally 2 ms long 1.334 GeV beams of about 110 mA peak current interleaved between the 50 Hz pulses drawn directly into the target station. Compared to the short pulses, in this case the number of neutrons per pulse increases by a factor of 3. It is conceivable that following an optimization the neutron flux available from the moderators could increase by factors of 2-3 for the LPTS.

The two target stations could be of essentially identical design, as far as the targets and their handling systems are concerned. Differences may result in the moderator layout and in the beam lines. Good cryogenic moderators are, therefore, at a premium, and an initiative has been started, to develop an advanced system based on solid pellets of high slowing down power which are annealed periodically to limit radiation damage and to release stored energy at regular intervals.

The horizontal beam injection for both systems (SPTS and LPTS) and the liquid state of Mercury at room temperature (melting point -38°C , boiling point at ambient pressure

350°C) also favor a design concept, where the closed mercury loops are mounted on a movable support which can roll back from its operating position into a service hot cell for maintenance. The support trolley also contains a shielded drain tank into which the whole mercury loop can be emptied when breaking the container becomes necessary in order to exchange any component, in particular the snout that is exposed to the high radiation field during operation. This snout is surrounded by a separately cooled, double walled shroud which is connected to the drain tank and would allow to catch any mercury and return it to the drain tank safely, in case there would be a leak in the target container snout. The main problems whose significance and possible remedies are presently being assessed are: the generation of pressure waves due to the pulsed power input in the liquid and the effect of irradiation under stress of the solid container.

A cut away view of the target container of the SPTS and its surroundings (reflector/moderator units) is shown in Fig. 2.6. An extended horizontally (flat) target geometry was chosen for better neutronic coupling to the moderators. The small H_2O or supercritical H_2 moderators are located above and below the target and are viewed by horizontal neutron beam tubes in a way that avoids direct sight on the target. The surrounding reflector material is D_2O cooled lead. The layout of the LPTS is currently under evaluation.

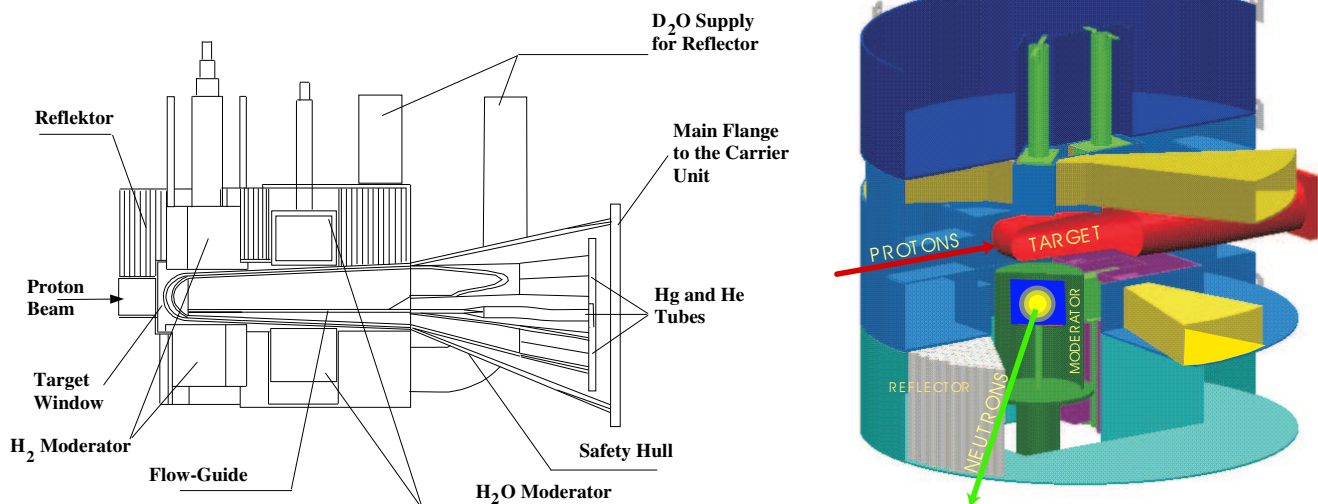


Figure 2.6: Schematic drawing and 3-d view of the target/reflector/moderator unit as proposed in the 96' ESS feasibility study [ess96-III].

The neutrons emerging from the target are slowed down by moderators, which are located below and above the target, because neutrons produced in the spallation process have high energies and are useless for condensed matter studies unless thermalized. Those which escape from the moderators in the direction of the open neutron port are “useful” neutrons, i.e. they have defined energies and a pulse with a well defined time structure. Finally the moderators will be surrounded by a Pb-reflector cooled with heavy water allowing neutrons emerging in other directions of being scattered (reflected) back into the moderators. De-ionized water will cool the mercury, the shielding, vessels, reflectors, and other assemblies inside the shielding stack.

Because of the enormous amount (100kJ)¹ of energy that the short powerful pulses of the incoming 1.3 GeV proton beam will deposit in the spallation target, it was decided to use a liquid mercury target rather than a solid target such as tantalum or tungsten. The proposition has already been made in the feasibility study of ESS in 1996 [ess96-III] and the proposal has been adopted by the SNS spallation source project [sns02] now being under construction in Oak-Ridge. Summarized, the choice in favor of liquid mercury for the target was motivated by several aspects: it is not damaged by radiation, as are solids; it shows a relatively low specific activation; it has a high atomic number and density, making it a source of numerous neutrons; and, because it is liquid at room temperature², it is better able than a solid to dissipate the large, rapid rise in temperature and withstand the shock effects from the rapid high-energy pulses.

With its two target stations and high neutron flux, ESS will be an extremely powerful facility, well suited to meet the user's demands to the next generation neutron sources. Its design and construction will, however, pose several technological challenges both on the accelerator as well as on the target side, and will generate a wealth of information relevant to possible future accelerator driven devices in nuclear technology.

Table 2.2: Peak current neutron density in [$1/(\text{cm}^2 \text{ s sr } \text{\AA})$] for different neutron wavelengths from a cold coupled H_2 -moderator. For the short pulse station the FWHM of the peak is given in parenthesis in [μs].

wavelength	2 \AA	4 \AA	6 \AA	10 \AA
long	2.05×10^{14}	9.12×10^{13}	3.12×10^{13}	2.95×10^{12}
short	$1.486 \times 10^{15}(43)$	$3.708 \times 10^{14}(120)$	$1.035 \times 10^{14}(150)$	$7.532 \times 10^{12}(232)$
ratio sh/lg	7	4	3	2.5
ILL	H12*: 3.5×10^{13}	H1: 4×10^{12}	H15: 6×10^{11}	H17: 10^{11}
ratio long/ILL	6	23	52	30

*thermal beam hole.

For both target stations various moderator-reflector concepts have been considered as for example different geometries and material compositions. These choices show substantial influence on the neutron flux- and neutron current densities. Pb, Be, C and Hg reflectors as well as composite systems made from these materials have been studied. Also the effect of coupling and poisoning of moderator systems on the pulse shape and intensity of neutron spectra has been investigated. As far as the geometry is concerned the calculations of the neutronic performance of the long pulse target station have up to now been based on configurations typical for short pulse stations except that for the long pulse target station only two moderators an ambient water and a liquid para H_2 at 20 K moderator instead of four are currently foreseen. The thickness of the moderator is 5 cm. In case of the cold H_2 moderator an extended water pre-moderator with a thickness of 2.5 cm is applied. Based on MCNPX [Hug97] MC-simulations, the available peak neutron current densities as a function of wavelength for the long and short pulse target stations

¹for comparison the SNS and the JNS project operate with 30-40 kJ/pulse

²No auxiliary heating is required and no risk of damaging the container by volume changes in the solid state is posed.

are compared in Tab. 2.2 for a cold coupled H_2 -moderator [Fil01c]. Values in parenthesis note the FWHM of the peak for the short pulse target station. In addition the ILL average fluxes are given [Ill01]. Furthermore the ratio of the short and long pulse peak fluxes as well as the ratio between the long pulse peak flux and the ILL flux are given. Please note, that the long pulse target station is not at all optimized.

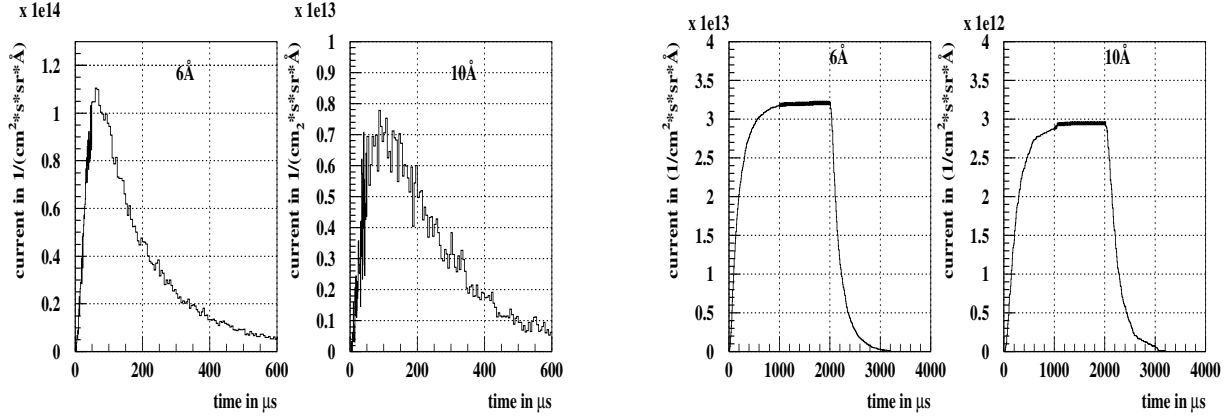


Figure 2.7: Time spectra of the neutron current density for a coupled H_2 -moderator at the short (left panels) and long pulse (right panels) target station.

Fig.2.7 presents for a neutron wavelength of 6 and 10 Å the simulated neutron current density distributions of a cold coupled H_2 -moderator for both target stations. In the case of the short pulse target for long wave lengths pulses with half width in the order of $200\mu\text{s}$ evolve, while for the long pulse saturation is observed and neutron pulses with a broad plateau length of 2 ms emerge. The peak flux for cold neutrons differs by factors between 2.5 and 4 for the two target stations.

In contrast to the values quoted in the ESS feasibility study [ess96-III] assuming an idealized case of a simplified geometry, Tab. 2.3 and Tab. 2.4 summarize for the short and long pulse target station the peak and average neutron flux- ($\hat{\Phi}$, $\bar{\Phi}$) and current (\hat{J} , \bar{J}) densities for a perturbed more realistic system, e.g. including beam holes etc.

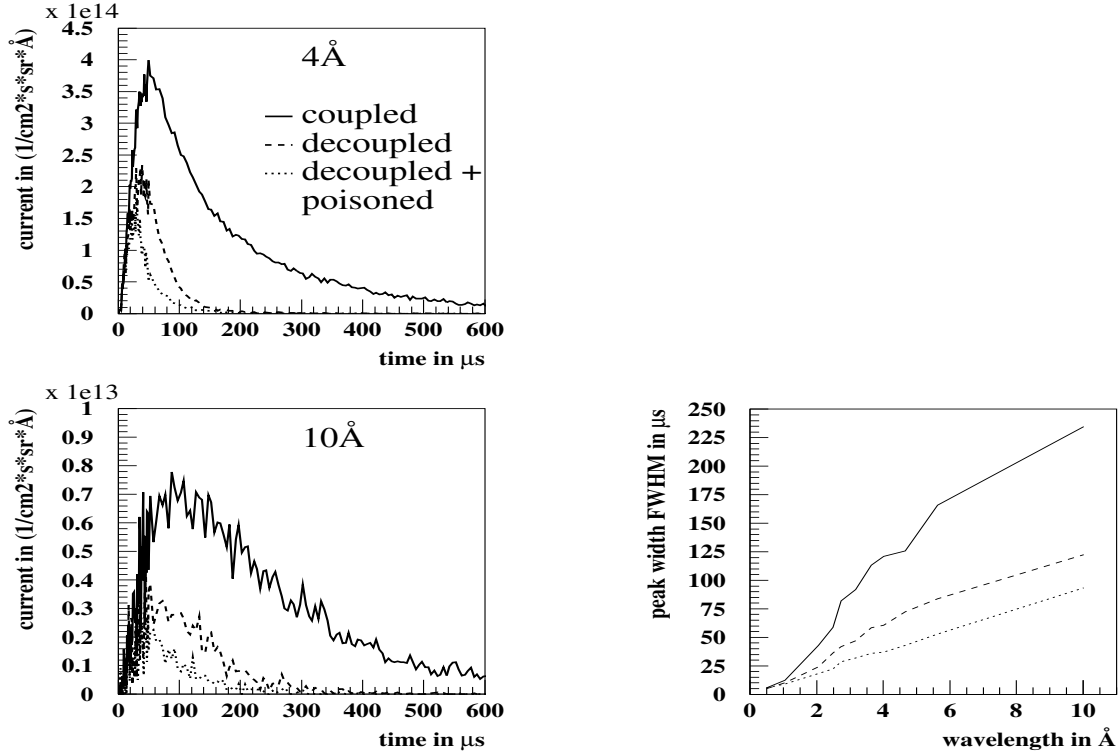
Table 2.3: Expected peak and average thermal ($E \leq 431$ meV) neutron flux densities for a premoderated cold (20 K) coupled para- H_2 and an ambient coupled H_2O moderator.

moderator type	SPTS		LPTS	
	$\hat{\Phi}$	$\bar{\Phi}$	$\hat{\Phi}$	$\bar{\Phi}$
para H_2 [n/(cm ² s)]	9.0×10^{16}	3.2×10^{14}	7.0×10^{15}	2.3×10^{14}
amb. water [n/(cm ² s)]	1.3×10^{17}	3.1×10^{14}	9.0×10^{15}	3.0×10^{14}

The simulations were performed for a cold (20 K) coupled H_2 and an ambient coupled H_2O moderator and a Pb reflector of 180 cm diameter and height. In case of short pulse spallation sources, in order to prevent already moderated neutrons from entering or returning to the moderator and deteriorating the pulse shape a decoupling Cd-layer can be placed between reflector and moderator. Additionally poisoning with a 0.5 mm thick Gd-layer in the midplane of the moderator decreases further the width of the pulse shape.

Table 2.4: same as Tab. 2.3, but for current densities; norm. to solid angle of 4° opening.

moderator type	SPTS		LPTS	
	\hat{J}	\bar{J}	\hat{J}	\bar{J}
para H_2 [n/(cm ² s sr)]	6.8×10^{15}	2.5×10^{13}	6.3×10^{14}	2.1×10^{13}
amb. water [n/(cm ² s sr)]	9.8×10^{15}	1.8×10^{13}	5.0×10^{14}	1.7×10^{13}

Figure 2.8: Neutron current density spectra (left panels) and neutron pulse widths (FWHM, right panel) as a function of wavelength for coupled (solid line), decoupled (dashed line) and decoupled+poisoned (dotted line) para- H_2 moderators.

The influence of decoupling and poisoning³ on the neutron pulse width for a 20 K liquid para- H_2 moderator is shown in Fig. 2.8. When analysing the neutron current density spectra (left panels of Fig. 2.8) for different wavelengths, an increase of the peak width is observed with increasing wavelength (right panel), simply because for larger wavelengths or smaller energies the thermalization of neutrons lasts longer. Irrespective of the selected wavelength the pulse width can be reduced to less than 40% when decoupling and poisoning the para- H_2 moderator. Unfortunately at the same time the neutron current density is also decreasing by up to a factor of three as shown in the left panel of Fig. 2.8.

The burn-up of the poisoning layer inside the moderator due to nuclear reactions has a strong impact on its expected life time. Assuming e.g. a thermal neutron flux of $\Phi_{th} = 5 \times 10^{13}$ n/cm²s at the poisoning surface a life time of 106 days results for a 0.5 mm thick Gd layer. The neutron absorbing isotopes with cross sections of several 10^5 barn

³The purpose and realization of decoupling and poisoning is also illustrated in sec. 6.4.2 on page 86.

are ^{155}Gd and ^{157}Gd . The areal density for the 0.5 mm layer is 4.6×10^{20} atoms per cm^2 . For the estimation it was assumed that all neutrons are absorbed in one of these isotopes. Also including breeding of ^{155}Gd and ^{157}Gd does not significantly increase the expected life time. On this issue certainly further studies are necessary and the demands and requests of the instrument community have carefully to be accounted for.

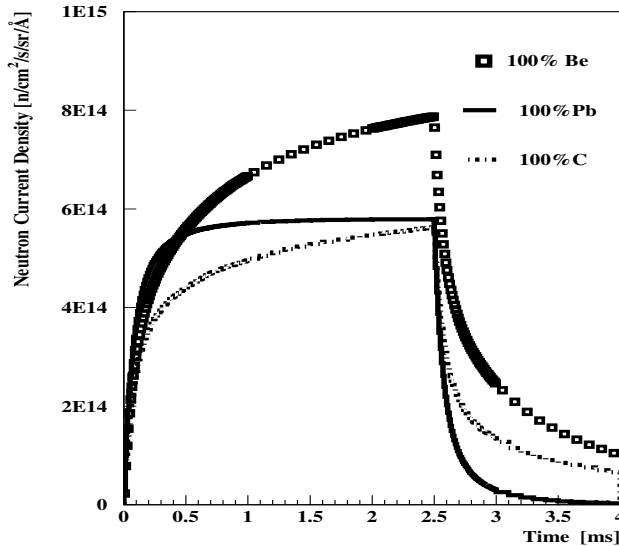


Figure 2.9: *Time distribution of thermal neutron current densities for different reflector materials. Here a liquid H_2 -moderator at 20 K has been used.*

For the LPTS Fig. 2.9 demonstrates the influence of different reflector compositions on the neutron current densities. Up to 35% higher current is obtained for a Be than for a Pb reflector. However the decay time is longer as compared to Pb. The decay constants for Pb, C and Be are 95, 153 and 198 μs , respectively. Besides the shortest decay time, the Pb option shows a long period of constant neutron current during the pulse.

The instruments and modes of operations

Neutron channels—openings in the shielding of the target—enable the neutrons to travel to the instruments where the experiments are being carried out. The instruments, typically 24 for each target, some of them as far away as 200 m, are arranged radially around each target station. On a pulsed source, neutrons with different energy (velocity) arrive at the sample and typically only a part of the neutron spectrum can be used even if the pulse repetition rate is well matched to the experiment considered. Faster (hot and thermal) neutrons can take advantage of pulses closer to each other (5-20 ms) than slower cold neutrons, for which at least 50 ms is optimally needed between subsequent pulses. The combination of a 50 Hz short pulse and a $16\frac{2}{3}$ Hz long pulse target station allows ESS to cover the whole range of neutron energies for condensed matter research with an efficiency 2-5 times superior to the single target short pulse approach followed by existing pulsed spallation sources or facilities currently under construction. The long pulse source as well as the high power short pulse source require new developments in experimental techniques, such as phased chopper systems, new neutron optical components based on the recently developed super-mirror technology. Active pulse shaping techniques by shoppers and neutron guides are seen as important innovation in the instrumentation concept.

Costs, time schedule and location

ESS cost planning includes a new and updated cost assessment by the end of 2003, taking into account the revised facility concept and bottom up estimates based on considerably better design details than those available in 1996, when the cost was estimated on the basis of the feasibility study. The split of the total cost for development and construction is roughly as follows: 37% for accelerator facilities, 18% for target systems, 28% for buildings and infrastructure and 17% for scientific utilization.

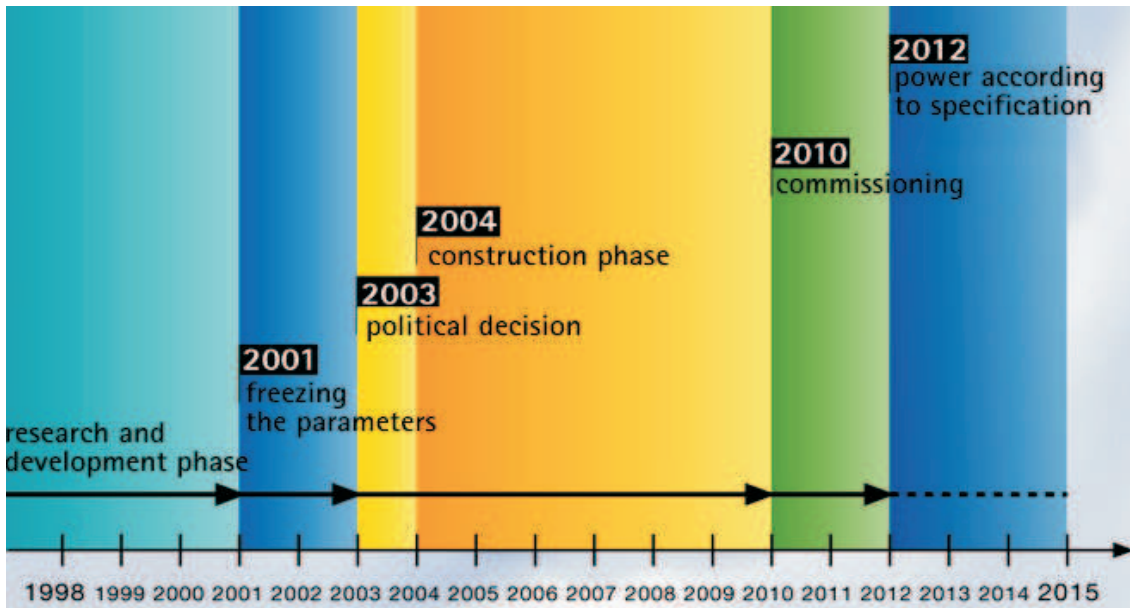


Figure 2.10: *Anticipated time schedule of the ESS-project*

The overall costs for development plus construction including all staff costs amounts to 1400 MEuro while the operational costs per year (incl. staff) are estimated to be of the order of 150 MEuro.

For the present phase (-2003) participating laboratories and organizations have signed a Memorandum of understanding (MoU) which formalizes the commitments of parties to strengthen central management and streamline Council decision making. An acceleration of the project time scale as shown in Fig. 2.10 is requested which should culminate in a comprehensive progress report of the ESS in December 2003. In parallel R&D is done in order to freeze the parameter. The more politically driven decision concerning the host will be taken hopefully in 2004 after which the construction phase will immediately follow. The full operation after commissioning is expected not earlier than 2012.

On a European scale there are several locations that have expressed interest in hosting the facility: Daresbury (UK), a consortium supporting a location in Southern Scandinavia, two sites in France, (FZJ) Jülich in the Euregio of Nordrhein Westfalen and the MicroTechPark Thalheim-Sandersdorf in the Halle/Saale region.

The main parameters of ESS are summarized in Tab. 2.5.

Table 2.5: ESS mercury target stations performance parameters.

ESS beam parameters	
particles	protons
kinetic energy	1.334 GeV
beam cross section	elliptical 6×20 cm ² , parabolic beam intensity dist.
average current SPTS/LPTS	3.75 mA / 3.75 mA
average beam power SPTS/LPTS	5 MW / 5 MW
peak current SPTS/LPTS	62.5 A / 112.5 mA
pulse frequency SPTS/LPTS	50 Hz / $16\frac{2}{3}$ Hz
pulse width SPTS/LPTS	$1.4 \mu\text{s}$ ($2 \times 600\text{ns} + 200\text{ns}$ gap) / 2 ms
ESS mercury target station performance parameters	
beam power on targets	5 MW at 50 Hz (SPTS) 5 MW at $16\frac{2}{3}$ Hz (LPTS)
target material	mercury
target type	liquid flow target
target container	martensitic steel
moderators	H_2O at ambient temperature, coupled/decoupled liquid H_2 at 20 K, coupled/decoupled
reflector	lead, D_2O cooled
heat deposition in target	2.8 MW at each of the two targets
local peak power deposition in target	2.5 kW/cm ³ (average)
induced specific radioactivity for a 15 tons Hg-system	8 GBq/g at shutdown; 0.8 GBq/g after 1 week
spec. after heat of target material	0.67 mW/g at shutdown; 0.12 mW/g after 1 day
Neutronic performance of coupled H_2O -moderators at 5 MW SPTS	
average thermal neutron flux density for 5 MW target	3.1×10^{14} neutrons/(cm ² s), $E \leq 431$ meV
peak thermal neutron flux density	1.3×10^{17} neutrons/(cm ² s), $E \leq 431$ meV
decay time of flux density	150 μs (wavelength dependent)
Neutronic performance of a coupled H_2 -mod. with H_2O -pre-mod. at 5 MW LPTS	
average neutron flux density for 5 MW target	2.3×10^{14} neutrons/(cm ² s), $E \leq 431$ meV
peak neutron flux density	7.0×10^{15} neutrons/(cm ² s), $E \leq 431$ meV
decay time of flux density	150 μs (dominant mode)
Details are given in refs. [ess96-III, ess02-III, Con01, Eng01, Gar99, Pab99, Fil01d].	

2.4 Concepts of transmutation

In the last years on several international conferences the physics, technologies and economic aspects of energy generation and transmutation of nuclear waste by Accelerator Driven Systems (ADS) were discussed and published in great detail [Bow92, AIP94, Bow96b, Ven96, Rub96b, Rub95, Rub97, Fil97, Pab97, ENEA01]. As for example the International Atomic Energy Agency IAEA [IAEA97] reviews explicitly the existing projects and international activities as e.g. the JAERI OMEGA project in Japan, the Los Alamos and Brookhaven National Laboratory ADS projects, the CERN-group conceptional design of a high power energy amplifier, the ADS program in Russia and France as well as the European community projects. The physics design of ADS and the design of the so-called Energy Amplifier (EA, cf. sect. 2.5) is expatiated in detail also in several comprehensive compilations of the AIP (American Institute of Physics) conference contributions 346 [AIP94] and the Proc. of the 2nd Int. Conf. on Accelerator Driven Transmutation (ADT) held in Kalmar, Sweden [Ven96, Rub96b].

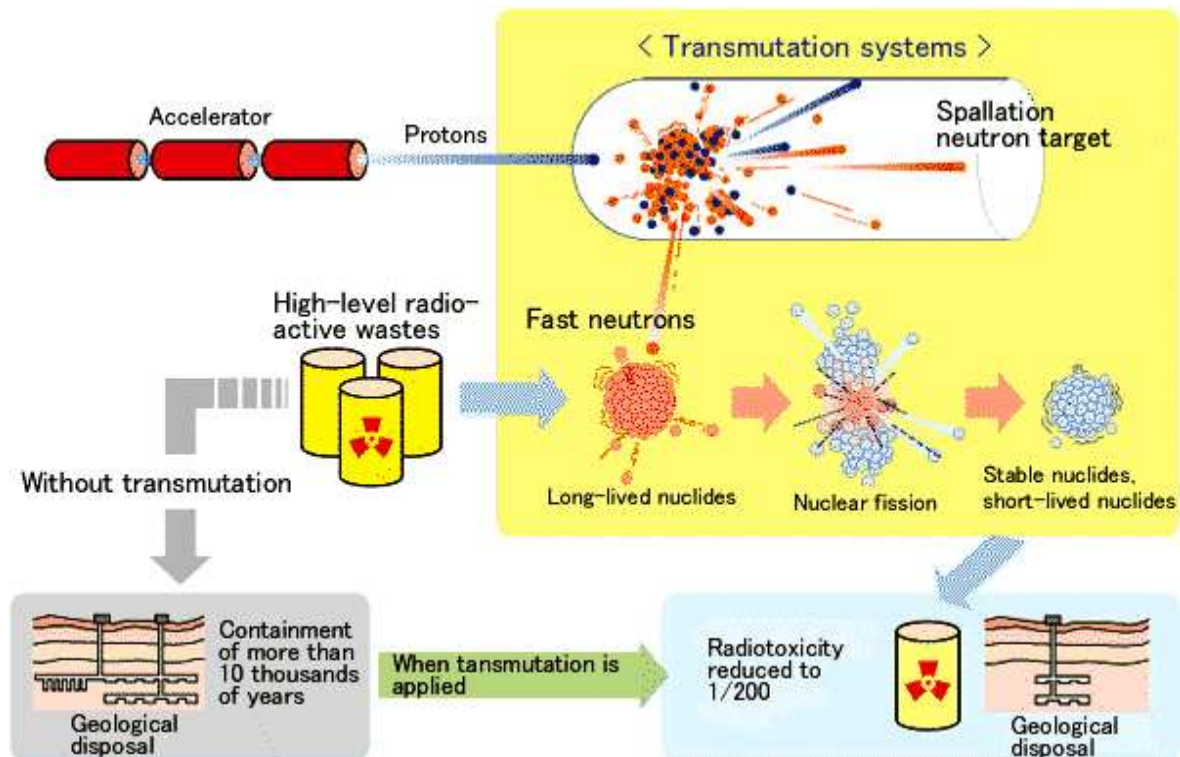


Figure 2.11: Accelerator driven transmutation of radioactive waste.

Scientists are divided on the choice of geological repositories for long lived waste disposal. It is in fact impossible to guarantee the integrity of this kind of storage for future generations. A definitive solution to the problem would be the complete elimination of the most offending isotopes with the help of nuclear reactions which would allow long-lived elements to "transmute" into stable ones. The application of high intense proton Accelerator driven systems for the Transmutation of long lived radioactive Waste (ATW)

is discussed as an alternative to the controversial storage and could strongly influence the debatable fuel cycle and future energy production.

ATW as schematically shown in Fig. 2.11 is a technological approach to a possible reduction of the hazards of permanent spent nuclear fuel disposal. It utilizes three "building blocks", (1) a linear accelerator capable of delivering a proton beam with mega-Watts of beam power, (2) a subcritical nuclear assembly where the proton beam is converted by spallation reactions into an intense neutron flux, with which fissile isotopes and long-lived fission products are transmuted into short-lived radio-isotopes or stable nuclei, and (3) a chemical process for treating nuclear waste to isolate long-lived radio-isotopes and transuranics for initial or recycle irradiation.

The research on transmutation is not only aimed at the destruction of transuranics elements, which represent the most toxic part of nuclear waste, but it is also devoted to the elimination of the most dangerous fission fragments. Most of these elements have a lifetime that rarely lasts more than decades or centuries. This means that, by eliminating the few most offending long-lived fission fragments, one could dispose the rest in controlled secular repositories for a few centuries to eliminate all danger completely. The biggest achievement would be the elimination of the need for geological repositories.

Table 2.6: Most dangerous fission fragments produced annually by one GWe power reactor. The volume of inert material is indicated on the right in which the elements should be diluted, to be considered as dangerous as industrial or medical radioactive waste, and to be stored in uncontrolled surface repositories, according to American regulations. The elimination of iodine and technetium, the most dangerous isotopes, would allow a consistent reduction in the volume of storage waste.

Radio Isotope	Half life	Weight (kg)	Radio-toxicity (Sv)	Class A dilution (m^3)
^{99}Tc	211.000 years	16,61	27670	947,65
^{129}I	15,7 million years	8,09	19580	178,47
^{135}Cs	2,3 million years	34,12	9870	39,32
^{93}Zr	1,53 million years	26,11	2380	18,75
^{125}Sn	100.000 years	1,19	3200	9,65
^{79}Se	650.000 years	0,3	745	0,59

By examining the radio-toxicity of long-lived fission fragments, it is clear that the most offending are few in number. In particular, ^{129}I and ^{99}Tc are by far the most dangerous for their solubility and mobility in the biosphere. These light elements cannot fission like the transuranics, so a different technique has to be adopted to eliminate them. The technique consists of artificially accelerating their natural decay by using neutrons again. The goal is to let the dangerous elements capture a neutron, in order to increase their energy and become unstable, as they will rapidly decay in stable elements. This process also occurs in reactors, but it is not efficient enough and the eliminated quantities are smaller than the produced ones.

The solution to this problem has been suggested by Physics Nobel prize laureate Carlo Rubbia and his research on so-called ADS (Accelerator Driven System). The secret is to

spoil particular neutron energies that massively increase the capture probability: the so-called resonances. If the energy of the neutrons emitted in nuclear reactions is decreased very slowly, it is sure that sooner or later the neutron will be captured by the resonance of the radioactive element that has to be destroyed. To do so, neutrons interact with a heavy element so that they are able to transfer only a small fraction of their energy: they will then lose energy in small steps. The element which is used is lead, which has the added advantage of having a small tendency to capture neutrons itself. This element, which is already ideal for transuranics transmutation, seems to be the key element for the elimination of any dangerous waste. The principle has again been demonstrated at CERN, with the TARC experiment (Transmutation by Adiabatic Resonance Crossing) [Aba01, Aba02, Rev99]. The process is so efficient that it can be applied not only to fission fragments transmutation, but also to activate stable elements and produce radioactive isotopes to be used in medicine as tracers in radiological analysis or in cancer therapy. Computer simulation of the interaction of a single proton into a 334 ton lead block used in the TARC experiment at CERN show that on the average 147 neutrons are produced that, before being absorbed, will interact with the Pb atoms about 55,000 times. In such a cloud it is very easy for a radioactive element to capture a neutron and become stable.

The spallation reaction is not the only mechanism involved in the destruction of the transuranics elements. In fact, the probability of breaking up a heavy nucleus like plutonium, instead of being captured by it, increases with the energy of the striking neutron. Therefore, it is necessary to maintain the neutrons produced in the cascade to a very high energy. This is particularly favorable if liquid Pb is used as coolant, a solution that has already been adopted in the alfa class Russian submarines in the fifties, but that has to be reproduced today using current standards observed by the industry in the west. The use of particle accelerators therefore seems to be the perfect solution to the problem of radioactive waste, but like all technologies connected with the nuclei of elements, it has to be studied in great depth and tested before being used on a large scale.

The results of the research on the transmutation of radioactive waste allow us to foresee a different strategy of energy production and nuclear waste disposal for the future, which is much more suitable for future generations, because it allows the elimination of contamination risks associated with a possible failure of geological repositories. Transmutation techniques can be applied to both military and civil waste: military plutonium is in fact an excellent fuel for ADS. The demonstration of the transmutation technique could bring about the elimination of all plutonium in the next 50 years!

2.5 The “Energy-Amplifier”

On the basis of former ideas formulated starting from the fifties, in 1993 Carlo Rubbia took up once again the challenge to operate particle accelerators not only for the transmutation concept as discussed in the previous section, but also for energy production [Car93, And95]. The principle of the spallation is similar to that of fission: accelerated protons are sent to a target made of a heavy element like Pb, Hg or W whose nuclei can be broken up or charged with energy. The interaction always results in the release of a large quantity of neutrons (up to a few tens for each proton sent) that can then be used to

induce fission reactions, like in a reactor. The difference is that the fissions are not enough to startup a (so-called critical) chain reaction, but only a cascade of fissions that is called "sub-critical" since it can be stopped in about a millisecond if the accelerator is turned off. This is an enormous advantage in terms of safety. The nuclear cascade, like in the case of a reactor, produces a large quantity of heat, generally much more than that used to operate the accelerator, which can be used to produce energy. For this reason Carlo Rubbia called his machine: The Energy Amplifier (schematically shown in Fig. 2.12). In

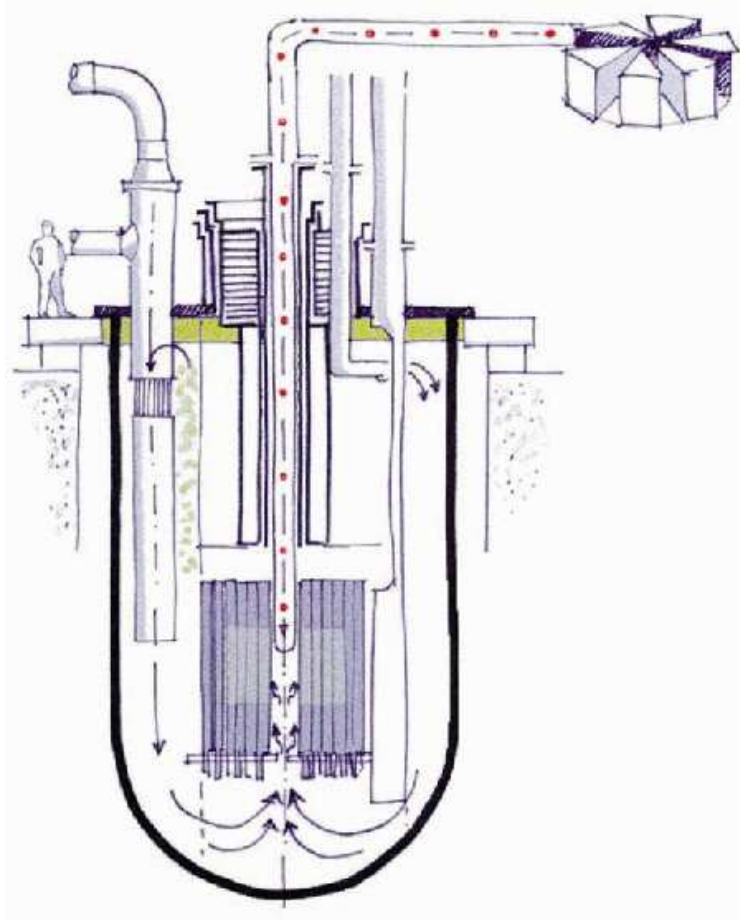


Figure 2.12: *Energy Amplifier scheme: a particle beam produced by an accelerator enters a sub-critical system, similar to a traditional reactor, producing a cascade of nuclear reactions that can be used to destroy radioactive nuclear waste and to produce energy.*

1994 Professor Rubbia's team demonstrated the working principle of an Energy Amplifier [Rub93, Rub94]. A detailed description of the Pb-cooled sub-critical system ($k_{eff} = 0.98$) designed for a thermal power of 1500 MW_{th} is given in ref. [Rub95, Rub96b]. A small subcritical system made of water and natural uranium was irradiated by a particle beam at CERN, obtaining an energy gain of about a factor 30, as calculations had predicted. From the heat released in the nuclear cascade about a Watt of energy was produced: too little to destroy nuclear waste, but enough to demonstrate the principle and to verify the precision of the calculations.

An European effort at building such a machine in one of the EU countries could give a definitive answer in a few years to one of the most critical problems of the end of last century, opening up the way at last to a clean and potentially powerful source of energy.

The possibility of having a neutron source external to a nuclear system, will allow the use of thorium in the future: a fuel much cleaner than uranium. This element is not fissionable, but by capturing a neutron it can be transformed into ^{233}U , an isotope having favorable properties quite similar to the ones of ^{235}U , as for example being equally fissionable and having resembling capture cross sections. The advantage is that thorium needs to capture 7 neutrons to transform itself into plutonium 239, which is almost impossible given the fact that many other nuclear reactions are competing with capture in a subcritical core. Practically, over a thorium fast reactor lifetime only a few grams of plutonium can be produced and an even lower quantity of the other transuranics, which constitute the most toxic part of a traditional uranium reactor’s waste. The huge amount of thorium available in the earth’s crust opens the way to a source of energy which is exploitable for thousands of years. For the Energy Amplifier, different strategies for the transmutation of long-lived fission fragments are indicated. After 500 years the toxicity of the radioactive waste is below that produced by Coal burning to produce an equivalent amount of energy.

For a detailed concept of the Energy Amplifier refer to refs. [AIP94, Rub96b, Rub95, Rub97, Pab97, IAEA97, ENEA01] and references therein.

2.6 Conclusion “Research with Neutrons”

Summarized the high intense spallation neutron source project is pioneering the most advanced fields for the science and technology of the 21st century. It is expected that the collaboration of many European and international institutions with different experience and knowledge will bring significant progress. From the scientific point of view the highest power neutron source will be one of the most significant facilities in the world which can be utilized by pharmaceuticals, agriculture, materials science, physics, chemistry and general industries. The aspect of transmutation processing has important socio-economic significance in determining the spent fuel policy of the next generation and is an urgent subject that should be researched and developed systematically under worldwide cooperation. R&D is expected to be further promoted by enhancing cooperation of researchers worldwide. Already the feasibility studies [ess96-III, ess02-III] have approved that the ESS-project has been well examined and elaborated. Technically the project could be realized within the planned costs. Scientific demands and requirements by the user community could well be met. As far as international positioning is concerned the project certainly would attract worldwide researchers as one of a small number of world-scale research facilities.

Chapter 3

Neutron production

Neutrons are strongly bound in the nucleus of the atoms and it takes a large amount of energy to release them. Up to now the primary source of neutrons are research reactors built for nuclear industry. Neutrons can be produced or released from bound states within the nucleus to the free state by

- charged particle reactions: e.g. ${}^9\text{Be} + \text{p} \rightarrow {}^9\text{B} + \text{n}$, ${}^2\text{H} + {}^3\text{H} \rightarrow {}^4\text{He} + \text{n}$
The interaction involves only a single reaction channel, formation of a compound nucleus that decays rapidly, the products carrying off the net binding energy of the reactants and the kinetic energy of the incoming particles.
- fission: e.g. ${}^{235}\text{U} + \text{n} \rightarrow \text{A}^* + \text{B}^* + xn; \langle x \rangle \approx 2.5$
Fission as schematically shown in the lower panel of Fig. 3.2 is currently the most common way of producing neutrons for scattering research. In fissile targets it is induced by the capture of a neutron. Typically for ${}^{235}\text{U}$, 2 or 3 neutrons are released on the average of which only one is available for use, since the other are needed for initiating further fission reactions or are lost in non-fission reaction channels or absorbed for control mechanisms. About 180 MeV total kinetic energy of the fission fragments (FF) has to be removed from the reactor per fission in order to gain one neutron. The average kinetic energy of the neutrons is about 2 MeV distributed in an “evaporation”-like spectrum, $N(E) \sim E^{1/2} \exp(-E/T)$ with $T \approx 1.29$ MeV.
- photoproduction: e.g. ${}^{181}\text{Ta} + \gamma \rightarrow {}^{180}\text{Ta} + \text{n}$, ${}^2\text{H} + \gamma \rightarrow {}^1\text{H} + \text{n}$
Nuclei absorb γ 's and the resulting excited nucleus de-excites by emitting a neutron. Photoproduction is most efficient in heavy targets for about 20 MeV γ 's. Neutrons appear with energies equal to the excess of γ energy over the binding energy.
- excited-state decay: e.g. ${}^{13}\text{C}^{**} \rightarrow {}^{12}\text{C}^* + \text{n}$, ${}^{130}\text{Sn}^{**} \rightarrow {}^{129}\text{Sn} + \text{n}$
Products of fission and other reactions and their β -decay siblings include nuclei that can decay by emitting a neutron.
- (n,xn)-reactions: e.g. ${}^9\text{Be} + \text{n} \rightarrow {}^8\text{Be}^* + 2\text{n}$
An energetic neutron can impact sufficient energy in a collision on ${}^2\text{H}$ or ${}^9\text{Be}$ to liberate the loosely bound neutron. Thresholds are 4 and 2 MeV, respectively. Cross sections above the threshold rise to several 100 mb.
- spallation reactions: e.g. $\text{p} + {}^{201}\text{Hg} \rightarrow \text{A}^* + \text{B}^* + xn; \langle x \rangle \approx 20$
this process is described in more detail in the following section.

3.1 The Spallation Process

The definition found in Nuclear Physics Academic press: "Spallation—a type of nuclear reaction in which the high-energy level of incident particles causes the nucleus to eject more than three particles, thus changing both its mass number and its atomic number. Also, nuclear spallation" has to be slightly specified in the context of accelerator driven systems or high intense neutron sources. Here spallation is the disintegration of a nucleus by means of high energetic proton induced reactions. Typically approximately 20 neutrons are created per incident GeV proton. This is 20 times as much as for a fission reaction in a conventional nuclear power plant with energy spectra of the neutrons similar up to the evaporation regime, but extending to higher kinetic energies up to the incident proton energy in case of spallation reactions as shown in Fig. 3.1.

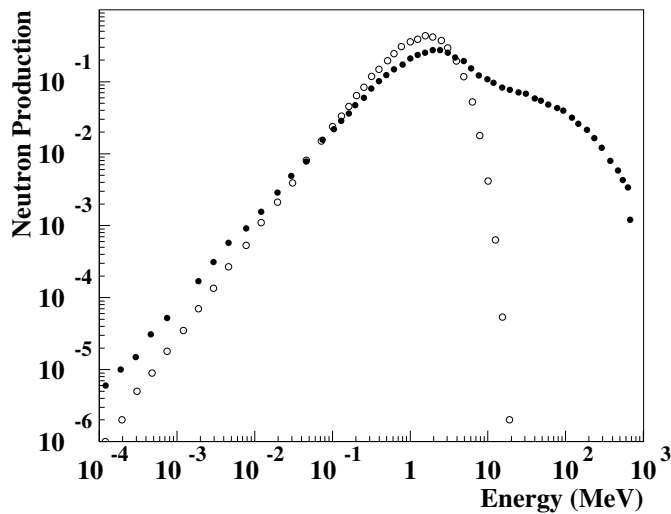


Figure 3.1: Neutron kinetic energy spectra from a fission reactor and from spallation (800 MeV p, Los Alamos Neutron Scattering Center-LANSCE). In order to facilitate the comparison the integrals of the spectra have been normalized to unity. Data adapted from [Lan91].

When a high energy hadron (or lepton) interacts with a nucleus of the target material causing an **intra-nuclear** cascade (INC) inside the nucleus within a time scale of the order of 10^{-22} s, many secondary particles (n,p, π -mesons) are emitted which could themselves have a high enough energy to produce further secondaries when they interact, thus creating an **inter-nuclear** cascade, placing many individual nuclei into highly excited states as schematically shown in the upper panel of Fig. 3.2. The nuclei then release energy by evaporating nucleons (mainly neutrons), d, t, α 's and γ 's, some of which will leave the target. The process of evaporation taking place within a much longer time scale¹ of 10^{-18} to 10^{-16} s may be characterized by a nuclear temperature $T = 2 \dots 8$ MeV, so that for the spectrum of emitted neutrons Maxwellian distributions

$$d\phi(E_n) = \frac{E_n}{T^2} \exp\left(\frac{-E_n}{T}\right) dE_n \quad (3.1)$$

emerge, with E_n being the kinetic energy of the emitted neutrons. Also unstable secondary particles can be created which may have a sufficiently long lifetime that a part of them will have time to interact before they decay or, if they do decay, form particles which themselves have to be taken into account. Leptons however only rarely interact with nuclei but, if they are charged they will contribute to the radiation field by ionization

¹depending strongly on the thermal excitation energy E^* of the hot nucleus

they produce in the material through which they pass. For charged particles the rate of energy loss (the stopping power $S[\text{MeV g}^{-1}\text{cm}^{-2}]$) depends on the particle charge, its velocity and the electron density of the material. The range of a charged particle is obtained by summing the energy loss rate up to the point where the energy loss equals the particle energy. The inelastic interaction of a high energy hadron striking a nucleus of the material through which it passes approaches the geometric cross section of the nucleus. A systematic review on interaction cross sections σ suggests for hadron energies larger than 120 MeV the empirical dependence $\sigma = 42A^{0.7} \times 10^{-27}[\text{cm}^2]$ with A the atomic mass of the target nucleus. The mean free path length λ is related to σ by $\lambda = A/(N\sigma)$, where N is the Avogadro number. Combining the two equations results in $\lambda = 40A^{0.3} \text{ g cm}^{-2}$.

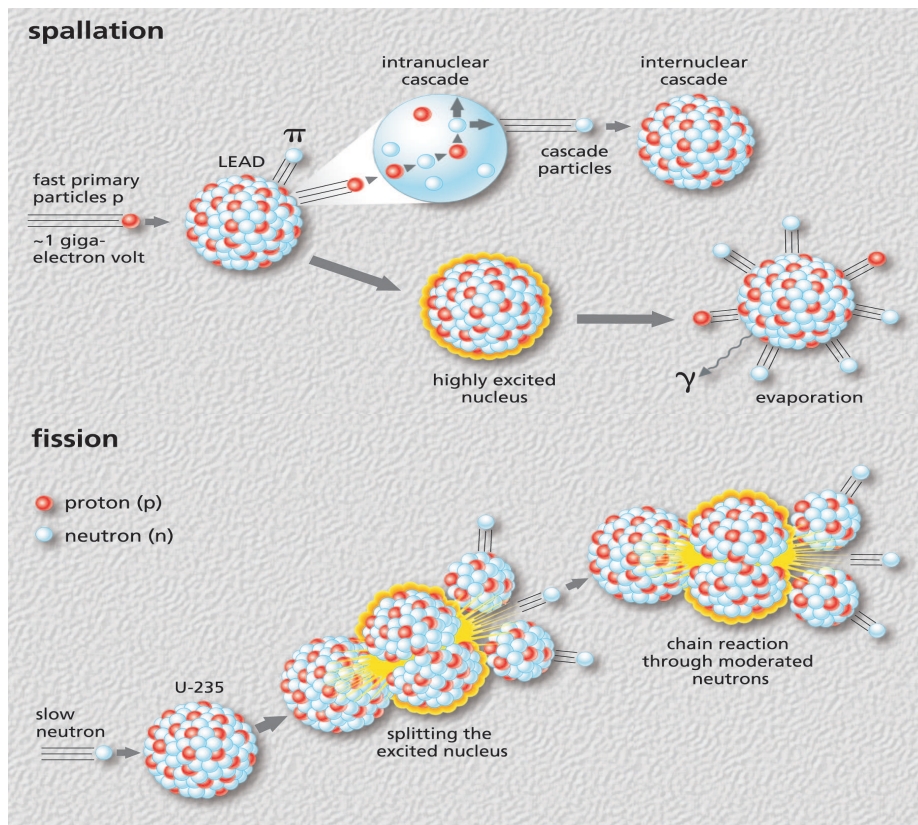


Figure 3.2: Schematical sketch of the spallation and the fission process.

Except for fission, all spallation processes are endothermic; a notable fraction of the incoming charged particle energy is taken up as neutron separating energy (about 8 MeV per neutron) and kinetic energy (about 2-3 MeV/neutron). However spallation produces large numbers of neutrons per incident proton and up to about 1 GeV some linear relation between the total neutron production yield and the proton energy exists [Fra65, Lan91]. However at higher proton beam energies the neutron production rate falls away from the linear rule due to the increase of π^0 production and the subsequent 2γ -decay into the electromagnetic channel—the so called “electromagnetic drain” on the hadron cascade. The rapid decay (half-life 10^{-16} s) does not allow the π^0 to take part in the inter-nuclear cascade although the π^\pm do. The π^\pm decay time (26 ns) is sufficiently long to allow for

further hadronic interactions once the π^\pm are created. At still higher energies, well above 10 GeV, other meson production channels open up which in addition deplete the cascade of energy². Using Monte-Carlo methods, the spatial distribution of such hadronic showers inside a massive cylindrical Pb-target will be discussed in the following.

3.2 Calculations of hadronic showers

In the case of thick targets, the reaction scenario includes secondary and higher-order reactions induced by the reaction products themselves and, therefore, the calculations must include a 3-dimensional simulation of inter-nuclear cascades. Such a 3-dimensional description of the propagation of the inter-nuclear cascade and the transport of particles in thick targets is a rather complex problem that involves various boundary conditions. This issue is addressed in the following, where the propagation of various species of particle types (p, n) is considered separately in longitudinal and radial directions. The energy losses of high-energy particles (≥ 1 GeV) traveling through matter are mainly determined by the production of secondary particles and not due to electronic stopping which is dominating at lower bombarding energies. Thus, the main feature of the cascade is an initial increase of the particle intensity with depth and time. As already mentioned, if the energy of the produced secondary particles is high enough, they in turn knock out additional particles. There exists however a physical limit for the development of further cascades, because the initial energy of the primary particle is distributed among the produced particles. Therefore, the multiplicities tend to decrease again during the cascade process and fade away because the average energy of the cascade particles decreases and a greater fraction of the individual particle energy is now dissipated by ionization losses. At the end of the inter-nuclear cascade process, subsequent emission of many low energy particles, mainly neutrons, takes place, known as evaporation process [Wei40].

The development of *electromagnetic* showers with their principal production processes - bremsstrahlung for electrons and positrons, pair production for photons, becoming energy dependent above 1 GeV - are well described by quantum electro dynamics (QED-theory) over a wide energy range. In HERMES this is taken into account by the EGS4 code as will be discussed in section 4.3. The complexity and entanglement of all intra- and inter-nuclear cascade processes finally causing the production of neutrons requires a complex record keeping of all particles actually participating in terms of energy, direction and location. The simulated propagation of the three-dimensional hadronic showers following the bombardment of cylindrical lead targets of 35 cm x 15 cm (for the length and diameter, respectively) by 0.4, 1.2 and 2.5 GeV protons is illustrated in the contour plots of Fig. 3.3.

In the HETC+MORSE (cf.sect. 4.3) Monte-Carlo calculations to produce the data for Fig. 3.3 the cylindrical target is divided into cylindrical zones of 0.5 cm in radial (r) and 1 cm (z) in longitudinal direction and the *tracklength flux*³ [Clo88] is represented. The symmetry axis of the cylinder is oriented in z direction and pointing downstream the proton beam. The tracklength flux of neutrons (left) and protons (right) reflects the radial and longitudinal propagation of particles involved in the intra- and internuclear cascades

²an effect being responsible for the decrease of the number of neutrons plotted in Fig. 7.9 of sect. 7.1.1

³tracklength flux as defined in equation 4.2 of sect. 4.1

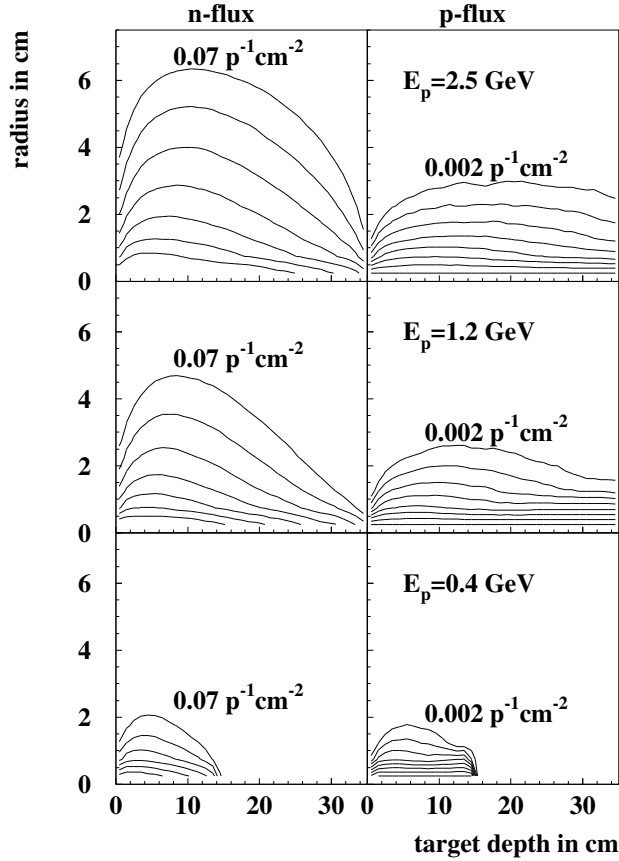


Figure 3.3: Neutron- (left panels) and proton (right panels) flux (per square centimeter and source proton, $\text{cm}^{-2}\text{p}^{-1}$) of a hadronic shower in a cylindrical target of 35 cm x 15 cm lead as a function of incident energy of the protons (2.5, 1.2 and 0.4 GeV, top to bottom). Sequent lines are separated by factors of 1.5. Calculation have been performed using the HERMES package (see text)

inside the target volume. The tracklength flux comprises both—cascade and evaporation particles. Primary beam protons are *not* included for the proton tracklength flux in Fig. 3.3. Multiplying the proton beam current [protons per second] by the tracklength flux specified in Fig.3.3, the flux generally used in units of $[1/\text{cm}^2\text{s}]$ is obtained.

As a general tendency one observes a deeper and deeper penetration into the target the higher the kinetic energy of the incident proton is. The maximum of the evolution in radial direction is found after the hadronic cascade has already propagated 5 to 10 cm in longitudinal direction. Neutrons tend to spread out radially much more than protons do, because especially low energy protons experience high electronic stopping power and consequently short range. That's also why protons develop along their trajectory in a more narrow cone. Note the different absolute tracklength flux of more than one order of magnitude between neutrons and protons.

For low incident proton energies (0.4 GeV) it is well shown that the cascade rapidly becomes extinct, since the leading particles are stopped before being able to convert their energy effectively into the production of neutrons or protons, while for large kinetic energies ($\approx \text{GeV}$) the range due to the stopping power of protons in the lead target is larger than the dimension of the cylinder in z . Although the presentation of hadronic cascades in the $r - z$ -plane is illustrative to explain phenomenologically the interplay of intra- and internuclear cascade descriptions and the well known consequences of stopping powers applied to charged particles, a more quantitative analysis would include the study of kinetic energy and multiplicity spectra or angular distributions of particles released. The next chapter is devoted to the theoretical background of the models applied.

Chapter 4

Theory/Models

4.1 Transport equation

Phenomena in radiation physics and particle transport of leptons, baryons, mesons and energetic photons can be described by the Boltzmann integro-differential equation settled in 1872. The equation will be briefly described here, because Monte-Carlo and deterministic approaches employ solutions of the equation for neutron and gamma-transport. It is a continuity equation in phase space consisting of three space coordinates, the kinetic energy and the direction of motion. Solutions of the Boltzmann equation which here are just briefly presented in order to introduce some nomenclature are evaluated in more detail in the literature for reactor physics [Eme69] and for fusion technology [Dol82]. The non-relativistic Boltzmann equation can be written as

$$\begin{aligned}
 \frac{1}{v_i} \left(\frac{\partial \dot{\Phi}_i}{\partial t} \right) &= \overbrace{-\vec{\Omega} \nabla \dot{\Phi}_i}^I \\
 &+ \overbrace{\sum_j \left[\int \int \sigma_{ij}(\vec{x}, E^B \rightarrow E, \vec{\Omega}^B \rightarrow \vec{\Omega}) \dot{\Phi}_j(\vec{x}, E^B, \vec{\Omega}^B, t) dE^B d\vec{\Omega}^B \right] - \sigma_i(\vec{x}, E) \dot{\Phi}_i}^{II} \\
 &+ \overbrace{S \left[\frac{\partial \dot{\Phi}_i}{\partial E} - \frac{\dot{\Phi}_i}{2E} \right]}^{III} - \overbrace{\frac{\ln 2}{v E_{1/2,i}} \dot{\Phi}_i + \sum_j b_{ij} \frac{\ln 2}{v E_{1/2,i}}}_{IV} + \overbrace{Y_i(\vec{x}, E, \vec{\Omega}, t)}^V
 \end{aligned} \tag{4.1}$$

where $\dot{\Phi}_i(\vec{x}, E, \vec{\Omega}, t)$ is the angular dependent unknown flux, i.e. the number of particles of type i in the volume element $dx dy dz$ at \vec{x} at time t , in the energy element dE at E with a direction of motion within $d\Omega$ at $\vec{\Omega}$, multiplied by the speed v_i of the particle. It gives the number of particles per cm^2 , per MeV, per steradian and per second at a given location at a given time.

(I) the first term in Eq. 4.1 reflects the translation/reduction of the phase space $-\text{div} [\vec{\Omega} \dot{\Phi}_i(\vec{x}, E, \vec{\Omega}, t)] = -\vec{\Omega} \nabla \dot{\Phi}_i$.

(II) considers the particle nucleus interaction (energy, angle and particle type are changed). $\sigma_{ij}(\vec{x}, E^B \rightarrow E, \vec{\Omega}^B \rightarrow \vec{\Omega})$ is the macroscopic cross section for the production of i -

type particles with space coordinates $(\vec{x}, E, \vec{\Omega})$ as a result of a collision of a j -type particle with phase space coordinates $(\vec{x}, E^B, \vec{\Omega}^B)$. $\sigma_i(\vec{x}, E)$ is the macroscopic total collision cross section.

- (III) S is the “stopping power” which describes how particles lose energy continuously at rate S per unit path length. The density distribution of particles with energy E^B is $\dot{\Phi}_i(\vec{x}, E^B, \vec{\Omega}^B, t)S(\vec{x}, E^B)$ and after slowing down to energy E : $\dot{\Phi}_i(\vec{x}, E, \vec{\Omega}^B, t)S(\vec{x}, E)$.
- (IV) represents particle decay: $E_{1/2,i}$ is the half life of particle i . b_{ij} is the branching ratio of the decay channel leading to particle i from particle j .
- (V) Y_i is the external source term (e.g. a particle beam, neutrons from an $\alpha - n$ source or photons from radioactive material).

Equation 4.1 is a system of coupled transport equations, which is, in general difficult to solve. Solving the equation for hadronic cascades is more difficult than, for instance, for neutrons in the core of a nuclear reactor because of secondary particle production. Thus the solution involves solving the fluxes for many different particle types. In the following, some of the most useful quantities characterizing the radiation field are listed:

- The integral quantity (actually used to define the *angular flux* $\dot{\Phi}_i(\vec{x}, E, \vec{\Omega}, t)$ in units of $[\text{cm}^{-2}\text{s}^{-1}\text{sr}^{-1}\text{eV}^{-1}]$ is the *fluence* $\dot{\Phi}_i(\vec{x})$

$$\dot{\Phi}_i(\vec{x}) = \int_E dE \int_{4\pi} d\vec{\Omega} \int_t \dot{\Phi}_i(\vec{x}, E, \vec{\Omega}, t) \quad (4.2)$$

The official definition of fluence by the International Commission on Radiation Units and Measurements (ICRU, 1993) [icru93] is based on crossing of a surface and defines the fluence as the quotient of dN by $d\alpha$, where dN is the number of particles incident on a sphere of cross sectional area $d\alpha$, $\dot{\Phi}_i(\vec{x}) = dN/d\alpha$. This definition is the source of frequent mistakes. It is not to be interpreted as “flow” or “flux” of particles through a surface, but to be understood as a density of particle path-length in an infinitesimal volume: $\dot{\Phi}_i(\vec{x}) = \lim_{\Delta V \rightarrow 0} \sum_i s_i / \Delta V$ [$\text{cm} \times \text{cm}^{-3} = \text{cm}^{-2}$], where $\sum_i s_i$ is the sum of path-length segments. The fluence is therefore a measure of the concentration of the particle path in an infinitesimal volume element around a space point. If the particle’s path-length is measured in units of mean free path $\lambda = 1/\sigma$, the expression of fluence is equivalent to the density of collisions $\sigma \dot{\Phi}_i(\vec{x})$. The most important fluence estimator (which was also applied in sect. 3.2, is the track-length estimator which represents the average fluence in a space region when the sum of track-lengths is divided by the volume). Frequently the fluence is calculated because it is proportional to the effect of interest, since many effects can be expressed as volume concentrations of some quantity proportional to the “number of collisions”.

- The *fluence rate* or *flux density* also referred to as *scalar flux* is expressed in terms of the sum of path segments transversed within a given volume per time unit

$$\dot{\Phi}_i(\vec{x}, t) = \int_{4\pi} d\vec{\Omega} \int_E dE \dot{\Phi}_i(\vec{x}, E, \vec{\Omega}, t) \quad (4.3)$$

In Monte-Carlo calculations with a source given in units of particles per unit time the scalar flux represents a fluence quality.

- The boundary crossing estimator is the *current* J .

$$\vec{J}_i(\vec{x}, t) = 2\pi \int_0^\pi \sin \theta d\theta \int_E dE \cos \theta \dot{\Phi}_i(\vec{x}, E, \vec{\Omega}, t) \quad (4.4)$$

To estimate the average fluence on a boundary, the factor $1/\cos \theta$ for each particle has to be added, where θ is the angle between the particle's direction and the normal to the surface at the crossing point. Therefore the current is equal to the fluence only if all particles pass perpendicular to the surface.

- The *density* of particles or number of particles per volume element $dx dy dz$ is

$$n(\vec{x}, t) = \int_{4\pi} d\vec{\Omega} \int_E dE \dot{\Phi}_i(\vec{x}, E, \vec{\Omega}, t) / v \quad (4.5)$$

- The *energy* spectrum of particles can be expressed by

$$\dot{\Phi}_i(\vec{x}, E, t) = \int_{4\pi} d\vec{\Omega} \dot{\Phi}_i(\vec{x}, E, \vec{\Omega}, t) \quad (4.6)$$

Essentially two classes of numerical procedures and special techniques have emerged for solving the transport equation and finding expedient solutions to particular problems. On the one hand there are deterministic methods; the transport equation is discretized using a variety of methods and then solved directly or iteratively. As there are the “straight ahead” approximation [Pas62, Als65], the “spherical harmonics” BL-approximation [Ben67, Joa63] and the methods of “discrete ordinates” (S_N method) [Car64, Car68]. Secondly Monte-Carlo methods [Car75, Kah54] are found. They construct a stochastic model in which the expected value of a certain random variable is equivalent to the value of the physical quantity to be determined. The expected value is estimated by the average of many independent samples representing the random variable. Particle tracks or histories¹ are generated by simulating the real physical situation. There is not even the need to invoke the transport equation for more elementary operations. Only the complete mathematical description of probability relationships is needed that govern the track length of individual particles between interaction points, the choice of interaction type, the new energies and directions and the possible production of secondary particles. Especially for 3-dimensional problems S_N methods and Monte-Carlo techniques as used in the current work turned out to be most advantageous.

4.2 Nuclear physics models

The predictive power of the models discussed in the following can be judged and ranked only in comparison to high quality experiments. These experiments likewise serve the comprehension of the physics implemented in the codes.

The main objective is the development of powerful and accurate models for the description of nucleon-nucleus spallation reactions, based on microscopic many-body theory.

¹The experience a particle undergoes from the time it leaves its source until it is absorbed or until it leaves the system is called the *particle's history*

For incident energies between 150 MeV and 2 GeV to a good approximation collisions can be treated as quasi-free scattering processes and as a starting point the intra-nuclear cascade (INC) followed by the evaporation model are used to predict cross sections. After thermalization has been achieved on a timescale longer than 10^{-20} s the hot excited remnant nuclei—characterized by its mass, charge, angular momentum and thermal excitation energy—decay by the emission of low energy particles or by fissioning. This second step is generally described by evaporation-fission models. On the low energy side (below 150 MeV), the INC may not longer be adequate and the reaction is preferably described by optical models for elastic scattering, coupled channel models for reactions [Ray88] to discrete states and quasi-particle methods to account for structure functions. More recently, also the quantum molecular model (QMD) [Aic91] was applied for the initial excitation in proton-induced spallation reactions [Nii95, Chi96].

As a final objective, the improved event generators with refined implementation of various features like Pauli principle, in-medium effects, stopping time, etc. will be included in high-energy macroscopic transport-codes for thick target scenarios.

4.3 Modeling of transport processes

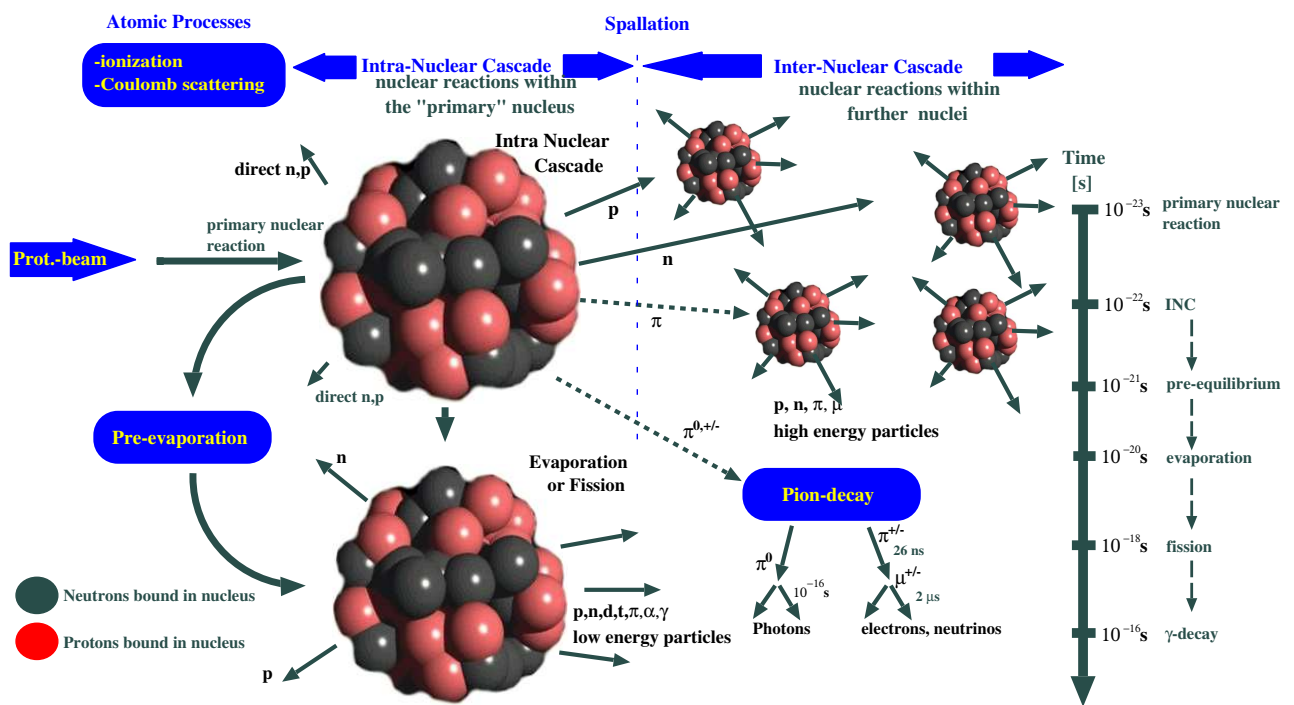


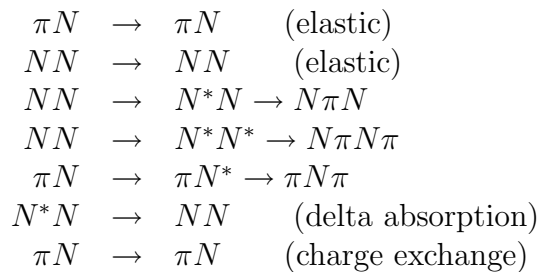
Figure 4.1: Illustration of particle interactions on the intra-, inter- and evaporation level.

An energetic particle entering a massive target gives rise to a complex chain of interactions resulting in the emission of various particles, some of which are able to escape the target volume. The latter particles can be detected in the experiment and provide information on the transport processes involved. As mentioned, these processes as illustrated

in Fig. 4.1 can be viewed as a convolution of two types of cascades, such that particles released in a primary intra-nuclear cascade (INC) [Ser47] give rise to an inter-nuclear cascade of secondary and higher-order reactions in the surrounding target material.

INC versions currently on the market model the multi-body problem numerically [Ber63, Cug87, Cug97a, Cug97b, Gol88, Yar81, Pra88b, Pra89, Pra97] using Monte-Carlo techniques. They all use the following simplifying assumptions:

- The hadron-nucleus interaction is a sequence of independent collisions of primary and secondary particles with the nucleons of the nucleus.
- Cascade particles follow classical trajectories and do not interact with each other.
- The interaction is based on free elementary cross sections. In-medium effects are generally not taken into account. These cross sections have been derived from empirical approximations of



data; Pauli blocking¹, the Fermi motion of the target and projectile nuclei², pion production, and the effects of the target mean field are included.

- The nucleus is viewed as degenerate Fermi gas of neutrons and protons.

The assumptions for which the fundamental presumptions (within the INC) are valid are:

1. the De-Broglie-wavelength λ of cascade particles is smaller than the average distance of nucleons in the nucleus ($\delta \approx 1.3fm$) and the mean free path length L in nuclear matter: $\lambda \ll \delta, \lambda \ll L$. For high energies this presumption is certainly valid and the interacting nucleons do not “see” the nucleus as whole but as an assembly of individual nucleons bound together by their mean field.

¹In Bertini and ISABEL models, the nucleus is a continuous medium in which the incident particle collides according to its mean free path with a nucleon. This nucleon is then set into motion and can undergo further collisions. In the INCL2.0 code, all the nucleons are moving according to an initial Fermi distribution and collide as soon as they reach their minimum distance of approach or are reflected on the wall of the nuclear potential. The cascade propagation is followed as a function of time in the INCL2.0 and ISABEL, but not in the Bertini model, as will be discussed in sect. 4.4.3.

²In the Bertini model, all collisions leading to a particle momentum below the Fermi level are forbidden, irrespective of the progressive depletion of the Fermi sea during the process. In the INCL2.0 and ISABEL models, attempt is made to take into account the real occupation rate. In the INCL2.0 model, for instance, this is done statistically by allowing the collisions of two nucleons with a probability equal to the occupation rate in a small phase space volume around the nucleons.

2. the duration of the elementary impact $\tau_{\text{int}} \sim r_{\text{int}}/v$ is smaller than the time between two collisions, i.e. the radius of strong interaction is smaller than the mean free path length: $r_{\text{int}} \ll L$
3. the number of participating cascade particles N_c should be considerably smaller than the number of target nucleons A_t : $N_c \ll A_t$

As for example for the $\bar{p}p$ -interaction in Fig. 4.2 the total, annihilation, elastic scattering and charge exchange cross sections ($\sigma_{\text{tot}}, \sigma_{\text{ann}}, \sigma_{\text{el}}, \sigma_{\text{ex}}$) applied in the INC models are shown as a function of \bar{p} momentum. The annihilation cross section σ_{ann} dominates at low momenta, but decreases for $p_{\bar{p}} \sim 2$ GeV/c down to approximately 50 mb. Data on $\bar{p}p$ - and $\bar{p}n$ cross sections published by Rafelski et al. [Raf80] agree with the ones shown here. For small \bar{p} momenta, σ_{ann} for $\bar{p}p$ annihilation is twice as large as for the \bar{p} -annihilation on a neutron $\bar{p}n$ [Egi87]. At higher momenta $\bar{p}p$ and $\bar{p}n$ are almost identical [Raf80].

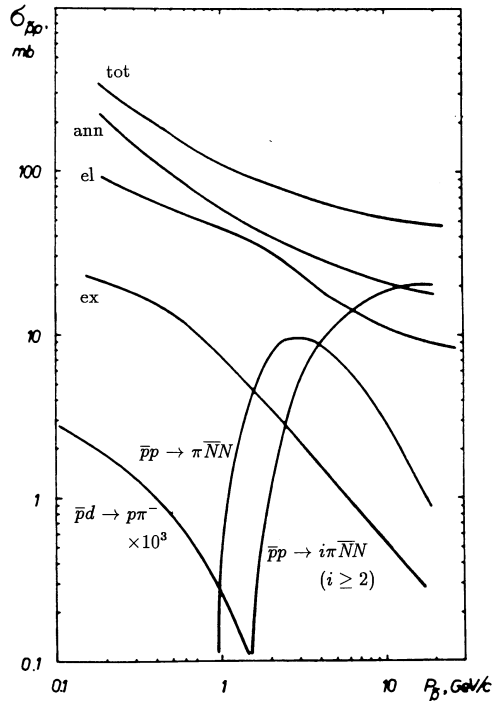


Figure 4.2: Total and partial cross sections of $\bar{p}p$ -interaction as function of \bar{p} -momentum (adapted from [Gol88]).

In the present study, two sets of computer programs are considered for particle transport in thick targets, which generate predictions that can be compared to the experimental observations. These sets are the **H**igh **E**nergy **R**adiation **M**onte **C**arlo **E**laborate **S**ystem (HERMES) [Ste98, Clo88, Fil00c] package and the Los Alamos High-Energy Transport (LAHET) Code System (LCS) (version2.7d) [Pra89]. HERMES [Ste98, Clo88, Fil00c] is a collection of Monte Carlo codes simulating the transport of particles through and the interaction with matter. The process diagram of the HERMES package is presented in Fig. 4.3.

As shown in Fig. 4.2, for momenta $p_{\bar{p}} \leq 1$ GeV/c the dominant channels of $\bar{p}p$ -interaction are:

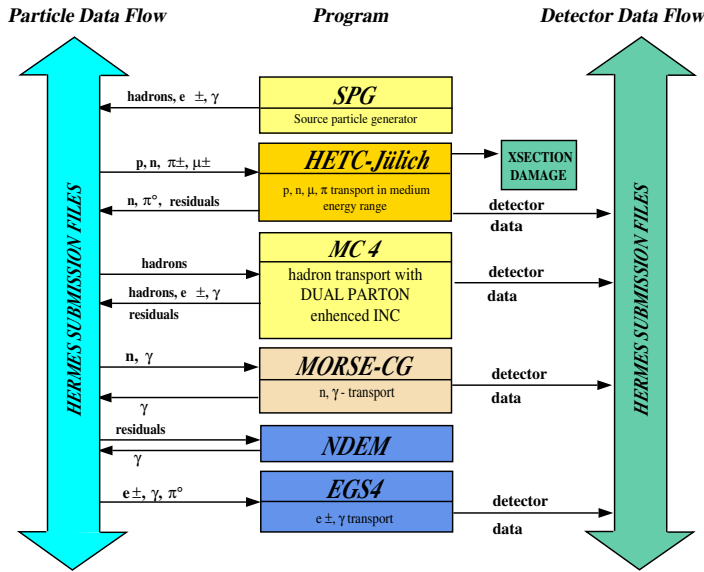
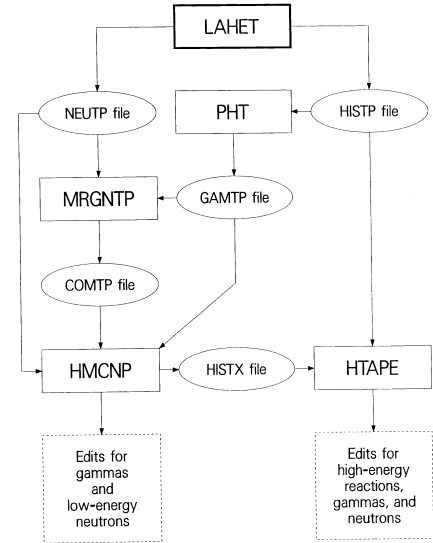
$$\begin{aligned} \bar{p}p \rightarrow i\pi \quad (i \geq 2) &\implies \text{annihilation} \\ \bar{p}p \rightarrow \bar{p}p &\implies \text{elast. scattering} \\ \bar{p}p \rightarrow \bar{n}n &\implies \text{charge exchange} \end{aligned}$$

For $p_{\bar{p}} > 1$ GeV/c pion production and multi-pion production without annihilation accrue:

$$\begin{aligned} \bar{p}p &\rightarrow \pi \bar{N}N \\ \bar{p}p &\rightarrow i\pi \bar{N}N \quad (i \geq 2) \end{aligned} \quad (4.7)$$

Most INC-models also consider the absorption on two nucleons [Cug84]:

$$\bar{N} + NN \rightarrow N + \pi \quad (4.8)$$

Figure 4.3: *HERMES* processing diagram.Figure 4.4: *LCS* and data files [Pra89]

There are six constituent computer codes in the HERMES package describing the projectile production (SPG), the interactions induced in the target material by various classes of particles in various energy ranges (HETC-Jülich, MC4, MORSE-CG, EGS4), as well as the de-excitation of target residues (NDEM). These constituent computer codes exchange input/output data via standardized HERMES submission files, such that a particle or a γ -ray data found in the output of one program is used as an input for the program that is best suited for its handling. Then this particular program takes on itself to follow the subsequent history of the particle in question.

Within the HERMES package (Fig. 4.3), the hadronic part of the particle shower is modeled by the High-Energy Transport Code HETC-Jülich or alternatively the Monte-Carlo code MC4 [Ste98] both comprising the fission/evaporation process. In brief, MC4 is the successor package of HERMES and will be publicly available in the near future. MC4 is intended to overcome the drawbacks of HETC using a modular structure where up to date models can easily be plugged in, providing the necessary transport algorithms, analysis algorithms and a user interface. In HERMES low-energy neutrons ($E \leq 20$ MeV) are handled by the code MORSE [Clo88, Emm75] utilizing the **E**valuated **N**uclear **D**ata **F**ile/**B** (ENDF/B)-based neutron cross section libraries. The de-excitation of residues by γ -emission is handled by the module **N**ucleus **d**e-**E**xcitation **M**odule NDEM. The history of the γ -rays resulting from the latter decay, as well as of those originating from the π^0 -decay, is then followed by the Electron Gamma Shower Code EGS4 [Nel85]. A suite of additional programs was used to perform simple data management and analysis functions.

The HERMES package allows one to model the history of secondary particles produced in primary collisions at energies ranging from thermal to relativistic. It considers explicitly protons, neutrons, π^\pm , π^0 , μ^\pm , e^\pm , and light ions up to a mass number of $A=10$, and allows one to treat complex geometries and material configurations.

Spallation induced material damage and matters relevant to radioactivity are covered by the packages SID and ORIHET [Bel73], respectively. Final analysis and graphical representation of the correlated data can be performed by using STATIST.

The structure of the Los Alamos High-Energy Transport Code System (LCS) [Pra89] is illustrated in Fig. 4.4. In this case, the hadronic part of the particle shower is modeled by the Los Alamos High-Energy Transport code LAHET, while particle tracking is handled by the LANL Monte Carlo N-Particle (MCNP) code [Bri97]. The major capabilities of LAHET and MCNP have been combined into the merged code MCNPX [Hug97]. The code PHT is used to generate from the LAHET output file a photon source file, which is then used as input for the code HMCNP. The latter is a derivative of the MCNP code, now accepting external neutron and photon data files created by LAHET or PHT. The file generated by PHT includes data on pions and de-excitation γ -rays. Information on neutrons of energies below 20 MeV is written to a source file for further processing with HMCNP. HTAPE is a general-purpose sorting routine for LAHET history files. Simulation observables include surface current and flux, neutron tracklength flux, particle yields and energy spectra, energy deposits and balance, distribution of residual nuclei and their excitation energies.

The code LAHET offers two options for handling intra-nuclear cascades. As an alternative to the Bertini [Ber63, Ber69, Ber70, Ber72] intra-nuclear cascade code used in HERMES, it includes the ISABEL [Yar79, Yar81] INC routines, which allow one to treat also nucleus-nucleus interactions. In the ISABEL INC routines, the nuclear density is approximated by up to 16 discrete bins, rather than by three bins as in the Bertini INC code and a sharp surface as in INCL2.0. ISABEL also models antiproton annihilation with emission of kaons and pions.

In modeling the de-excitation of the produced excited nuclei due to fission/evaporation, the HERMES package relies on the RAL [Atc89, Atc94] code. LAHET includes additionally the ORNL [Bar81] description. Both statistical evaporation models are implemented in the Dresner evaporation code [Dre62, Wei40] based on the Weisskopf-Ewing approach and are restricted to fission for elements $Z \geq 91$. The disintegration of light nuclei ($A \leq 17$) can be modeled optionally by the Fermi breakup model [Bre81]. In this model the de-excitation process is treated as a sequence of simultaneous breakups of the hot nucleus into two or more products, each of which may be a stable or unstable nucleus or a nucleon. Baryon number, charge, energy and momentum are conserved in all codes.

The LCS provides an option of including, as an intermediate step between the fast INC and the slow evaporation process, pre-equilibrium processes. It is invoked at the completion of the INC with an initial particle-hole configuration and an excitation energy determined by the outcome of the cascade. The processes are modeled by the multistage, multi-step exciton model (MPM) [Pra88b] and allow one to handle the formation of composite particles like deuterons, tritons, ${}^3\text{He}$ and α -particles (beyond the emission of neutrons and protons) *before* statistical equilibrium is reached.

Particles are transported until a lower energy threshold of E_{\min} is reached. Values of this threshold are set to 1 MeV, 0.149 MeV, and 0.113 MeV, for protons, pions, and muons, respectively.

Another modification to the Bertini-type INC implemented in LAHET is applied to (p,n) and (n,p) INC reactions: The outgoing particle energy is corrected by the binding

energy difference in the entrance and exit channels. As a result the high energy emission spectrum is much better described and the overall energy balance in the INC is significantly improved.

Many of the calculations performed in the current work for thin targets (interactions without secondary particle production) have been performed with the Liege INCL2.0 model [Cug84, Cug87, Cug89, Cug89a, Cug92, Cug97a, Cug97b] combined to the statistical evaporation code GEMINI [Cha88] (version 5/97).

Unless stated otherwise in specific cases, in most simulation calculations discussed in the following sections, the set of standard parameters listed in Tab. 4.1 was used. The various code packages differ essentially by the choice of the parameters (cf. sect. 4.4), improvements implemented in the original models or because they include alternative specifications or prescriptions.

A list of INCE Event generators, latest state-of-the-art radiation transport code systems for spallation source design and applications, recent new models together with the authors and references is given in Tab. 4.2.

Table 4.1: Set of standard parameters for HERMES, LCS and MCNPX.

basic assumptions	
Intranuclear Cascade	Bertini INC [Ber63, Ber69, Ber70, Ber72]
Monte Carlo technique	“space-like”
nuclear density distribution	$\rho(r) = \rho_0(\exp((r - c)/a) + 1)^{-1}$ $c = 1.07A^{1/3}$ fm, $a = 0.545$ fm, $\rho_0 = 0.17Ze/A$ fm ⁻³ $\rho(r) = \alpha_i\rho_0$; $\alpha_1 = 0.9$, $\alpha_2 = 0.2$, $\alpha_3 = 0.01$
nuclear density depletion	not considered
options chosen by the user	
cut off for switching INC/evap.	7 MeV (n), 7 MeV+Coulomb barrier (p)
equilibrium stage	Dresner model [Dre62] for n, p, d, t, ³ He, ⁴ He emission+fission+ γ
fission-evaporation model	RAL[Atc89, Atc94]
level density description	HETC (cf. sect. 4.4.1)
B0 parameter	Pb: a=A/10, W,Hg: a=A/8
Coulomb barriers	according to equation 4.12
elastic scattering	switched on for protons, neutrons
cut off energy for n transport	HETC $E_{\text{kin}}^n > 20$ MeV, MORSE/MCNP $E_{\text{kin}}^n \leq 20$ MeV
cut off energy for p, π , μ transport	1, 0.149 and 0.113 MeV (only HETC)
proton beam	pencil-beam
pre-equilibrium model	off

Details are given in ref. [Clo88, Pra89, Hug97, Atc89, Atc94, Dre62, Fil00c].

Table 4.2: Compilation of INCE event generators.

model/purpose	main author [ref.]	comments ^a
INCE event generators		
^b Bertini INC Model	H.Bertini [Ber63, Ber69, Ber70, Ber72]	impl. in HERMES,MCNPX
^b Dresner Evap Model	L.Dresner (ORNL) [Dre62]	impl. in HERMES,MCNPX
^b ISABEL Model	Y.Yariv [Yar79, Yar81]	Soreq, Israel
^b INCL2.0 Model	J.Cugnon [Cug87, Cug97a, Cug97b]	Univ.Liege
Fluka Event Generators ^c	A.Ferrari [Fer96, Fas00]	Univ.Milano, Cern
^b GEMINI Evap. Model	R.Charity [Cha88] (version 5/97)	Washington Univ.St.Louis
CEM	S.Mashnik [Fil00]	LANL
^b MC4 Generators	G.Sterzenbach [Ste98]	FZ-Jülich
^b Moscow Generator	Ye.Golubeva [Gol88, Gol94, Ilj92]	Troitsk
MICRES	D.Theis [Ack02, The92]	Univ.Bonn
MARS	N.Mokhov [Mok98, Mok00]	FNAL
Code Systems		
CALOR	T. Gabriel et al. [Gab96]	HETC based; ORNL
^b HERMES	P. Cloth et al. [Clo88, Ste98, Fil00c]	HETC based; FZ-Jülich
^b LCS	R. Prael et al. [Pra89, Pra97]	HETC based; LANL
^b MCNPX	H.G. Hughes et al. [Hug97, Hug00]	HETC,CEM,ISABEL; LANL
TIERCE	O. Bersillon [Ber96]	HETC based; CEA
PSI/HETC/O5R	F. Atchison [Atc94]	HETC based; PSI
NMTC/JAM	K. Niita, H. Takada [Nii01, Tak00]	Jaeri/KEK
SHIELD	N.M. Sobolevsky et al. [Sob94]	
^c FLUKA	A. Fasso et al. [Fas00]	CERN, Milano
Cross section calculation and evaluation		
ALICE	M. Blann [Bla75, Bla94]	LLNL
GNASH	P.G. Young, M.B. Chadwick [You92]	LANL,LLNL
NJOY	R.E. MacFarlane [Mac94]	LANL

^aA comprehensive overview is given in ref. [Fil96, Fil00] and the MC-2000 proceedings [Fil00c].

^bused in the current work

^cFluka is capable of simulating particle cascades in matter from TeV (!) energies down to meV applying the dual parton model for highest energies (≥ 4 GeV) and the resonance production and decay model for energies between 2.5 and 4 GeV.

4.4 Parameter discussion

In fact from the simulation point of view there is a great variety of models, parameters and options implemented in all program suites under consideration in the current contribution that can be used to describe the physical behavior of a system.

A multitude of different INC models (Bertini, ISABEL, INCL2.0 and many more) is applicable and many parameters not only within the INC-codes but also within the

statistical evaporation codes appended may influence the resulting abundance or spectra of particles created.

LCS offers a great freedom in the choice of different level density descriptions, e.g the Gilbert Cameron Cook Ignatyuk, the HETC, and the Jülich model. As mentioned optionally the Multistage Pre-equilibrium Model (MPM) [Pra88b] can be switched between INC and the equilibrium phase.

Different descriptions of Coulomb barriers in the RAL [Atc89, Atc94] and Dresner models [Dre62, Wei40] are resulting in rather different production cross sections particular for charged particles (but also for neutrons). The models assume constant or excitation energy dependent Coulomb barriers.

As a new approach the INCL2.0 code is started to be implemented in the MC4 transport model giving rise to further parameters as for example the switching time from INC to evaporation (in INCL2.0 the INC is treated time-step wise) or the very fundamental variable of the nuclear radius r_0 being much smaller in the INCL2.0 model than in the Bertini based codes. Furthermore the aim is to isolate relevant cross sections, the treatment of Pauli-blocking and higher excitations. The efforts on the model implementations are still in progress.

Therefore, a study was performed in order to investigate the predictive power of the combination of these models by inter-comparing theoretical models and confronting the various approaches with experimental results. In the following first a fragmentary assortment of biasing aspects will be given. The author does not raise the claim to exhaust the limitless diversity of parameters offered by all program suites.

4.4.1 Level density description

As the thermal excitation energy E^* of a nucleus increases, excited level stages get closer together in energy. At large E^* , the density of excited levels $1/D$ with D being the average distance between the levels has the form $1/D \propto \exp^{2(aE^*)^2}$, where a is affecting the decay width Γ of particles emitted during the evaporation process and called the level density. One option to describe a , is the energy independent HETC formalism. In this case parameterization is done via the B_0 parameter [Clo88, Pra88b] and the level density is given by:

$$a = \frac{A}{B_0} \cdot \left(1 + \frac{Y\Delta^2}{A^2} \right) \quad (4.9)$$

with A the mass number, $\Delta = A - 2Z$, Z the charge number and Y being a value normally set to 1.5. In this contribution for all incident proton energies the level density parameters B_0 have been chosen conventionally to be 8 MeV^{-1} for W and Hg and 10 MeV^{-1} for Pb due to shell effects for the latter nucleus. However this choice might not be fully justified for the Pb target taking into account that most of the nuclei at the end of the cascades are removed from Pb and moreover, excited enough for the shell effects to be, at least, partially washed out.

Another model provided by LCS includes excitation energy damped shell effects of the level densities by using the Ignatyuk formalism [Ign75] as implemented in the GNASH code [You92]. The level density parameter a is calculated via

$$a(E^*) = \alpha \left[1 + \left(\frac{(1 - e^{-\gamma E^*}) \delta W}{E^*} \right) \right] \quad (4.10)$$

where $\gamma = 0.05 \text{MeV}^{-1}$, α is the asymptotic value of $\lim_{E^* \rightarrow \infty} a(E^*)$ given as a function of mass, and δW is a term concerning shell effects. Another provision is that $\lim_{E^* \rightarrow 0} a(E^*) = a_0$ with a_0 being the Gilbert-Cameron-Cook (GCCCI) level density parameterization [Gil65].

The third possibility of parameterization is the Jülich level density formulation. This model is using energy independent B_0 parameters tabulated as a function of mass [Clo88].

In the calculations performed the HETC and the GCCCI level density descriptions have been applied. Calculations with the Jülich level density model have not been executed, because this model is only valid in the low excitation energy domain where shell effects act.

4.4.2 Coulomb Barriers for charged particle emission and feed-back on neutrons

The excited compound nuclei (mass A), atomic number Z , and thermal excitation energy E^* formed after the INC are de-exciting by the emission of various particles, e.g. neutrons, protons, deuterons, etc.

Within the models there are different descriptions of the effective barriers, to which—in contrast to neutrons—charged particles are subject during their evaporation, although one could assume first naively the fact that only charged particles could be influenced directly by variation of these Coulomb barriers.

The HERMES or LCS/MCNPX program packages have the possibility to select optionally between the ORNL/Dresner description [Dre62] and the RAL [Atc89, Atc94] formalism.

The effective barriers V_D in the Dresner formalism read

$$V_D = 0.846927 \cdot k_x \cdot \frac{Z_{\text{ejec}} \cdot Z}{R_x + R} \quad (4.11)$$

whereby Z_{ejec} and Z are the atomic numbers and R_x and R the atomic radii of the ejectile (tabulated) and destination nucleus $R = (A - A_{\text{ejec}})^{1/3}$, respectively. The tabulated factors $k_x \leq 1$ for different Z_{ejec} of ejectiles make allowance for a potential barrier penetration.

The description in the RAL formalism following the Le Couteur approach [Ber81] is very similar to the ORNL/Dresner description (cf. eq. 4.13), except that the Coulomb barriers are further down-scaled by a factor [Dos58]

$$V_R = V_D \cdot \left(1 + a \cdot \frac{E^*}{Z_{\text{ejec}}} \right)^{-1} \quad \text{with} \quad a = 0.005 [\text{MeV}^{-1}] \quad (4.12)$$

with E^* being the thermal excitation energy of the evaporating nucleus. The original idea of the Coulomb reduction was to take account for an E^* dependent shape deformation

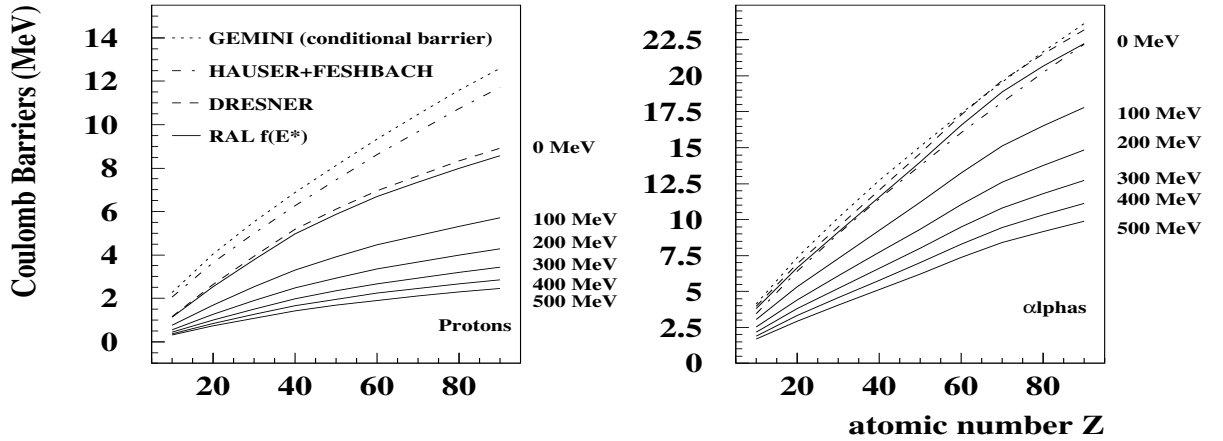


Figure 4.5: Coulomb barriers as a function of Z of the emitting compound nucleus for protons (left) and alpha-particles (right) following various models. For the RAL option (solid lines) the influence of the thermal excitation energy on the Coulomb barrier is indicated on the right hand side of the graphs.

during the emission like the one well established for the fission process. The exact relation between the ORNL/Dresner and the RAL Coulomb barriers for $E^* = 0$ MeV is:

$$V_c(\text{ORNL}) = 1.042 \cdot V_c(\text{RAL}, E^* = 0) \quad (4.13)$$

In the statistical evaporation code GEMINI [Cha88]—optionally chosen for the calculations of production cross sections in sect. 7.1—the Coulomb barrier is given by

$$V_c = \frac{1.44 \cdot Z_{\text{ejec}} \cdot Z}{r_0 \cdot (A_{\text{ejec}}^{1/3} + A^{1/3}) + s} \quad (4.14)$$

with $s=2$ fm and the nuclear radius parameter $r_0=1.12$ fm. As compared to equation 4.14 and as shown in Fig. 4.5 the option “Hauser-Feshbach” alternatively implemented in GEMINI for $Z \leq 2$ emission results in very similar barriers for p or α ’s, respectively.

Fig. 4.5 shows the Coulomb barriers experienced by protons and α -particles emitted from an excited compound nucleus with atomic number Z . In the limit of low excitations the RAL and Dresner descriptions correspond within several per cent and are in case of He also in agreement with the barriers applied in GEMINI. However the barriers reduce drastically, if in the case of the RAL option higher excitation energies are regarded. Since the charged particles are confronted with a lower barrier they could be released much easier and the originally deposited thermal energy is effectively cleared away not only by neutrons but also by charged particles. The calculated energy spectra of charged particles (in particular the spectra of d, t, ^3He and ^4He -particles) are clearly enhanced at low kinetic energy in comparison with measured spectra [Enke99] and because the energy conservation must be fulfilled, the variation of the Coulomb barriers likewise has an influence not only on the kinetic energy spectra, but also on the multiplicities of the observed neutrons as will be discussed in more detail in sect. 7.1. The question raised—but not to be answered here—is whether a decrease of the Coulomb potential with increasing excitation energy is physically justified. On one hand authors determine inverse reaction

cross sections according to formulas which take a decrease of the Coulomb potential with increasing excitation energy into consideration [Dos58]-on the other hand people claim the Le Couteur approach to be responsible for overestimation of the helium production cross sections in structural materials irradiated by protons and neutrons at energies up to 800 MeV [Kon92].

4.4.3 Equilibration time

Fig. 4.6 represents for some selected nuclei the dynamical picture of energy dissipation after the primary reaction (here after $\bar{p}A$ annihilation at rest):

1. the mean excitation energy of the target nucleus first increases during the first πN -collisions and approaches its maximum after $\approx 6 - 8$ fm/c. During this fast phase ($\tau_{cas} \sim \tau_0$) the nucleus de-excites via pre-equilibrium processes and loses more than half of the originally transferred energy. ($\tau_0 \approx 10^{-22}$ s is the time a projectile needs to penetrate the nucleus.)
2. after approximately 30 fm/c ($\tau_{eq} \sim 5-10 \tau_0$) the statistical equilibrium of the Compound nucleus is reached.
3. during the last slow phase ($\tau_{ev} \gg \tau_0$) the highly excited hot thermalized residual nucleus decays and de-excites via evaporation

Of special interest are the equilibration criteria after the prompt INC which define the transition from the fast INC phase to the evaporation step. After each INC a more or less equilibrated excited nucleus is left over. In the INCL2.0 code in which the INC is followed as a function of time the critical criteria for the decision to switch from the INC to the statistical decay is given by the equilibration time τ_{eq} which depends on target (Fig. 4.6), incident energy and impact parameter. Also in proton induced reactions typical mean values are $\langle \tau_{eq} \rangle = 18$ and 25 fm/c for 1.2 GeV p+Fe and U, respectively. The times τ_{eq} correspond to changes in the slope of the time dependent emission rates of cascade particles as calculated within the models.

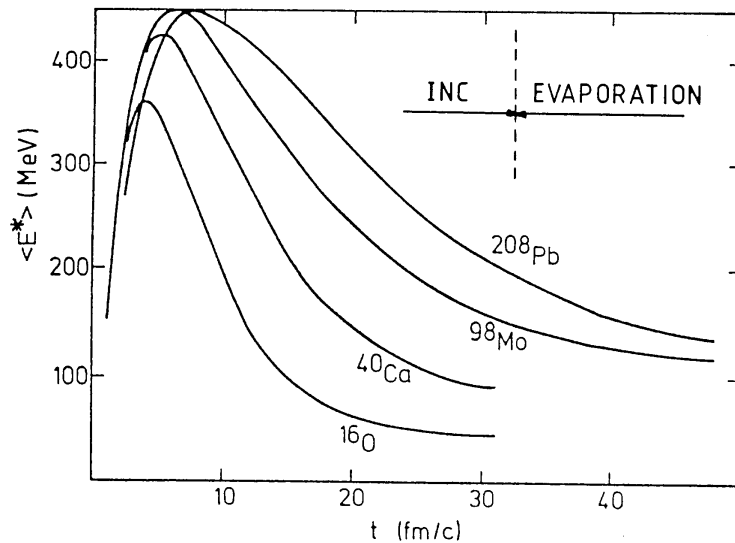


Figure 4.6: *Development of the energy relaxation following \bar{p} -annihilation at rest on different nuclei (adapted from [Cug89a,Cug87]).*

The sensitivity of modifying the equilibration time τ_{eq} in the INCL2.0 code between 14.5 and 37 fm/c for the reaction 1.8 GeV p+Au is discussed in ref. [Enke99]. It was shown that for very long equilibration times the production cross sections of nucleons became insensitive to time, because there is a compensation between nucleons emitted during the INC and those evaporated afterwards. This compensation however does not apply for composite particles since their emission is not considered in the INC-stage.

Within the Bertini type INC models, the switching from a code modeling a fast INC-process to one modeling the subsequent disintegration of the nucleus by statistical evaporation processes is generally controlled by particle energy values. The switch occurs whenever the kinetic energy of the fastest cascade particle inside the target nucleus is not sufficient to overcome the energy necessary to escape from the nucleus. In LCS, the value of the neutron cutoff energy is randomly chosen between zero and twice the mean binding energy. For protons, this code assumes a cutoff energy that is equal to the larger of the two, the Coulomb barrier or the neutron cutoff energy. HERMES, on the other hand, uses for the cutoff energies fixed values of 7 MeV and 7 MeV plus the Coulomb barrier, for neutrons and protons, respectively.

For the calculations in the current work, the standard criteria for the equilibration time τ_{eq} (INCL2.0) and cutoff energy (Bertini type INC models) were applied.

4.5 Particular decay modes of hot nuclei

4.5.1 Fission

The binary splitting of an excited nucleus into two approximately equal parts is still considered as one of the most interesting phenomena of collective motion of nuclear matter and as an excellent example of the nuclear multi-particle problem [Hil89]. A simple model regarding the nucleus as an incompressible liquid is drawn by the Liquid Drop Model, LDM [Nix69]. Analog to a liquid drop, a surface tension is responsible for the inner forces acting on all surface nucleons. As demonstrated in Fig. 4.7 fission is understood as a consequence of the deformation when repelling electrostatic Coulomb forces on the protons overbalance the short ranging attractive nuclear forces. A ground-state-deformed nucleus is situated in the minimum of the potential energy which increases with increasing deformation towards the so-called saddle point deformation. Beyond the saddle point the potential energy declines due to the decreasing Coulomb repulsion until the scission point is reached. Then the nucleus is constricted in such a way that fragmentation into two parts is likely. The fission barrier B_f represents the difference of potential energy at the ground-state and the saddle point deformation. As shown in Fig. 4.8 there is a maximum of B_f at $A \simeq 70$ and a substantial decline for light and heavy nuclei. Also with increasing E^* the fission barrier declines, because due to the expansion of the nucleus at high excitations the surface energy decreases faster than the Coulomb energy. The barrier is also a function of the angular momentum of the nucleus, because additional rotational energies disperse the nucleus. These phenomena are considered in the “rotating LDM” [Coh74] which describes

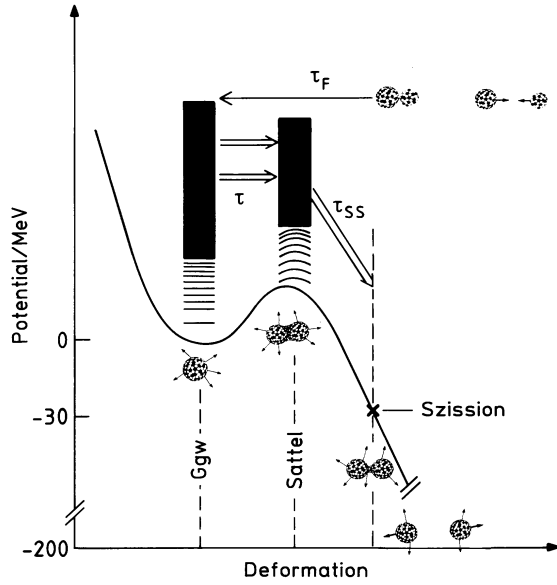


Figure 4.7: Potential energy as a function of deformation. The transition time from equilibrium (Ggw) to the saddle point τ and the one from saddle to scission τ_{ss} is indicated (Fig. adapted from [Hil91]).

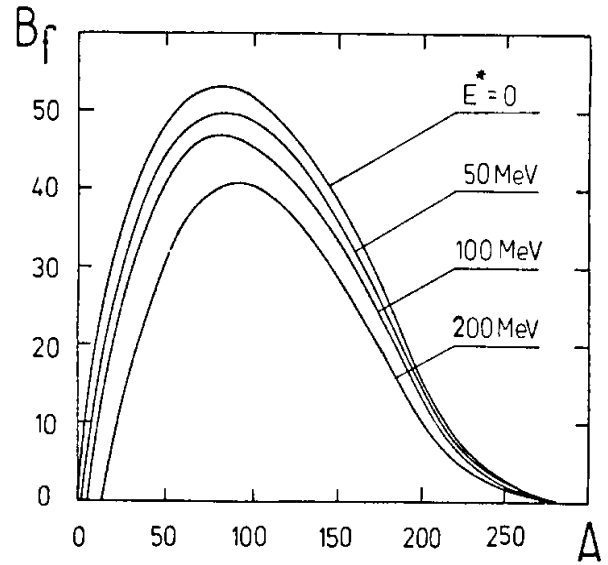


Figure 4.8: Fission barrier B_f as a function of atomic number A and E^* along the β -stability line (Fig. adapted from [Ilj78]). B_f is given in units of MeV.

the fissility by equation 4.15 [New90].

$$\chi = \frac{E_c^0}{2 \cdot E_s^0} = \frac{Z^2/A}{50.883(1 - 1.7826 \cdot I^2)} \quad \text{with} \quad I = (N - Z)/A \quad (4.15)$$

E_c^0 and E_s^0 being the Coulomb and surface energy of the nucleus in the ground state, Z , N and A the atomic-, neutron- and mass numbers.

Asymmetric mass splittings at low E^* cannot be explained by the LDM. Shell effects have to be taken into account, which however disappear for excitations larger than a few 10 MeV [Mor95b, Rub96, Kon99, Gil83]. At high E^* , fission is in competition to the successive neutron emission of the excited nucleus. The competition between fission and particle emission as well as the characteristics of fission products can be described by statistical models. Under the assumption of thermal equilibrium the probability for fission or neutron emission can be described according to equation 4.16 by the ratio of decay widths Γ_n and Γ_f [Van73].

$$\frac{\Gamma_n}{\Gamma_f} = \frac{4A^{2/3}a_f(E^* - B_n)}{C_0a_n[2a_f^{1/2}(E^* - B_f)^{1/2} - 1]} \exp\left(2a_n^{1/2}(E^* - B_n)^{1/2} - 2a_f^{1/2}(E^* - B_f)^{1/2}\right) \quad (4.16)$$

B_f , E^* and B_n represent the height of the fission barrier, the excitation energy and the binding energy of the neutron; the constant C_0 is $C_0 = \hbar^2/2m_n r_0^2$ (m_n =neutron mass) and a_f and a_n are the level density parameter at the saddle point and the ground state deformation after the emission of a neutron.

For small angular momenta and nuclei with fission barriers smaller than their neutron binding energy ($B_f < B_n$ in eq. 4.16), the fission takes place early, since Γ_n/Γ_f increases after the emission of each emitted neutron. For high angular momenta Γ_n/Γ_f decreases with increasing E^* and consequently the nucleus fissions at a later stage.

A phenomenological approach for fission product yield calculations at intermediate incident particle energy has been proposed by A.Yu. Konobeyev et al. [Kon99]. This approach is based on the Fong statistical model and empirical expressions. A good agreement with experimental data was demonstrated.

For a comprehensive description of the dynamics of the fission process the concept of dissipation and the viscosity of nuclear matter refer to review articles [Kra40, Nix69, Boh39, Dav76, Gro75, Weg74, Swi80, Blo78]. Dissipative processes are accompanied by statistical fluctuations which exchange energy between intrinsic and collective degrees of freedom. Latterly collective transport models are discussed which consider these statistical fluctuations [Fro93, Wei87, Gra84, Gra86]. Besides the saddle to scission time τ_{ss} these models require a transient time³ τ . The transient time is a function of dissipation or friction and can be parameterized by the so-called Kramers-factor [Gra80]. The total time scale τ_F of the dynamical fission process is described by the sum of transient time and saddle to scission time $\tau_F = \tau + \tau_{ss}$ (Fig. 4.7). Actually the time shall not be subdivided into pre- and post saddle, because in reality the saddle point could be passed through several times. In collective transport models the dynamical process of the system from the ground state to the scission is continuously traced. While the characteristic time scales for processes described by intrinsic degrees of freedom is of the order of 10^{-23} s [Wei80], the ones for collective motions are two orders of magnitude larger. Therefore a theory is proposed decoupling the Hamiltonian for the total energy of the system into a collective and an intrinsic part. The transport equations are controlled by one or several transport coefficients, as e.g. the reduced dissipation coefficient β , which reflects the coupling strength between the collective and intrinsic degrees of freedom. These coefficients can be used for defining the time scale of the process. The total energy of the system in the collective transport model is given by the temperature dependent function $H(q, p, T)$ [Boh75, Hof83]:

$$H(q, p, T) = E_{kin}(q, p) + F(q, T) \quad (4.17)$$

$E_{kin}(q, p)$ and $F(q, T)$ are the kinetic and free energy of the system and $q \equiv q_1, q_2, \dots, q_N$ denote the N generalized collective coordinates representing the form of the system. $p_i = M_{ij}(q) \dot{q}_j$ are the collective generalized momenta. The dynamics of the system and the equations of motion, which contain the effects of dissipation can be deduced from the Hamiltonian equations [Gol80]:

$$\dot{q}_i = \frac{\partial H}{\partial p_i} = \frac{\partial E_{kin}}{\partial p_i} \quad (4.18)$$

$$\dot{p}_i = \left(\frac{\partial H}{\partial q_i} \right) \Big|_S + Q_i + \delta X_i = \left(\frac{\partial F}{\partial q_i} \right) \Big|_T + \frac{\partial E_{kin}}{\partial q_i} + \frac{\partial \mathcal{F}}{\partial \dot{q}_i} + \delta X_i \quad (4.19)$$

The dissipative force Q is expressed by the "Rayleigh dissipation function" \mathcal{F} and a fluctuation term δX_i . The conservative force $\left(\frac{\partial H}{\partial q_i} \right) \Big|_S$ can be described either by the free

³transient time — time the system needs for passing the saddle point configuration

energy F or the entropy S according to the thermodynamical relation

$$\left(\frac{\partial H}{\partial q_i}\right)\Big|_S = \left(\frac{\partial F}{\partial q_i}\right)\Big|_T = \left(T\frac{\partial S}{\partial q_i}\right)\Big|_E \quad (4.20)$$

The collective kinetic energy $E_{kin}(q, p)$ is given by $E_{kin}(q, p) = 1/2M_{ij}(q)\dot{q}_i\dot{q}_j$ [Gol80, Nix69]. The Rayleigh dissipation function $\mathcal{F} = 1/2\eta_{ij}(q)\dot{q}_i\dot{q}_j$ [Gol80, Nix69] includes a shape dependent dissipation tensor $\eta_{ij}(q)$, which describes the conversion from collective to single particle energy. For the term representing the fluctuations no history, e.g. no temporal correlations exist (Markovian assumption). Employing in equations 4.18 and 4.19 the collective energy E_{kin} and the dissipation function \mathcal{F} the multi dimensional Langevin equation is obtained, which represents in most general form the collective transport model. Due to the fluctuation term δX the Langevin equation is a stochastic equation with stochastic variables p and q . The temporal evolution of the function $\mathcal{F}(q, p, T)$ in the phase space of collective coordinates and their conjugated momenta is presented by the generalized Fokker-Planck-equation [Ris89]. The stochastic description of the Langevin equation is equivalent to the Fokker-Planck-equation provided the Markovian assumption is accepted. Previous investigations which try to describe the fission process using transport equations are based on the Fokker-Planck-equation with one collective degree of freedom [Gra84, Gra86, Wei87].

These studies certainly resulted in some insight into the dynamics of the fission process, but with the addition of latest precise measurements of the fission lifetime as a function of E^* using blocking effects in a single crystal, important consequences for the dynamical description of the collective process have been illustrated. This work essentially carried out at GANIL, France by F. Goldenbaum, M. Morjean et al. [Gol98, Gol99, Gol99c, Mor98] will not be part of the present paper.

As another approach, besides the application of these transport models, the statistical model can be modified in such a way, that pre- and post saddle time scales are evaluated by the measurement of pre- and post scission particle multiplicities and the magnitude of dissipation is estimated. Measurements of pre-scission neutron multiplicities [Hil81, Gav87, Hin92], light charged particles [Pea88, Les91] and giant γ resonances [But91] allowed for accessing the relative time scales of fission and particle emission. A significant relaxation time of collective degrees of freedom pointing to a large dissipation has been demonstrated. The total time scale of fission has been limited to $\tau_F \leq 50 \times 10^{-21}$ s [Hil81]. J.P. Lestone [Les93b] confines applying his measurements τ_F to $\tau_F \leq 30 \times 10^{-21}$ s.

Neutrons are particularly insensitive to deformations of the decaying nucleus and consequently pre-scission neutron multiplicities can't provide insights into the different stages of the collective motion. They are useful only for predicting the total time from ground state deformation to the scission point. The evaporation of light charged particles in contrast depends on the deformation dependent transmission coefficients and binding energies of the Coulomb field (being itself deformation dependent). Therefore pre- and post saddle evaporation can be distinguished.

In order to investigate the decay of hot nuclei D. Hilscher et al. [Hil89] measured for the first time neutrons emitted prior and post scission for nuclei at temperatures up to $T = 5$ MeV. Independent of the initial temperature the temperature at the scission point was shown to be almost constant (≈ 1 MeV). This finding is consistent with a fixed time

for scission. The nucleus firstly cools down until the evaporation time of the last neutron is in the time scale of fission. Consequently the number of neutrons emitted prior to scission is increasing with increasing E^* , while the number of neutrons emitted from the fission fragments saturates - independent of the original primary E^* - at about 5. Analog to the systematics on post scission neutrons also pre- and post scission protons and alpha particles [Ben93] confirm fission being a slow process.

However the experimental studies on pre- and post scission particle emission suffer the systematic problems of delay at the saddle point. Particles might be emitted prior to the saddle point configuration or during the transition from saddle to scission. Deviations from the fission rate predicted by the transition-state model would reflect only the first component. The experimental deficiency not to be able to distinguish between both components makes a clear argumentation equivocal.

An alternative method to gain information on the temperature dependent nuclear dissipation coefficient is the measurement of fission probability $P_f(E^*)$ for a broad range of excitation energies E^* or temperatures as done in section 7.1.2. The fission probability depends on the rapidity of collective motion starting at the saddle point, e.g. on the value of the transient delay. The larger this transient delay, the more particles are emitted prior to the fission decision. In this case the fission width is reduced and the fissility decreases. Because the decision for fission is drawn at the saddle point, the fission probability is governed by the time passed before reaching the saddle point and not by the one necessary forming the scission configuration. The direct measurement of $P_f(E^*)$ (sec. 7.1.2) therefore is an ideal tool for investigating the dynamics of collective motions.

4.5.2 Vaporization and multifragmentation

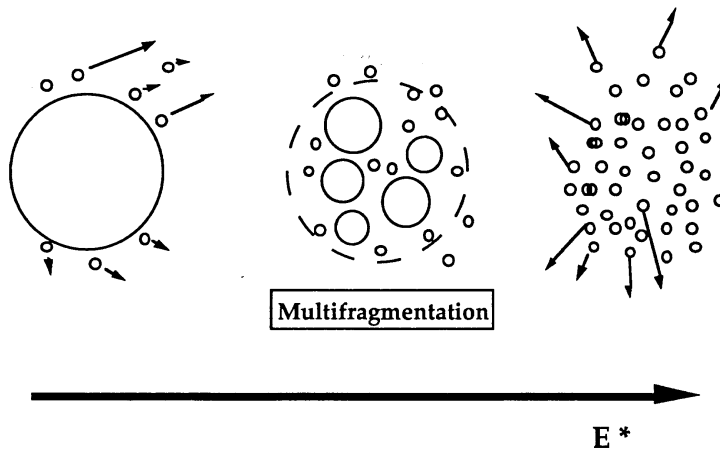


Figure 4.9: Schematic sketch of the three decay modes Spallation-evaporation, multifragmentation and vaporization. The drawn in circle indicates the original size of the target nucleus.

Definition: For the so-called *thermal* multifragmentation (MF) the formation of intermediate mass fragments (IMFs) at higher temperatures is a consequence of increasing thermal motion linked with increasing mean distance of the nucleons. An excited remnant achieves thermal equilibrium state and then expands, eventually reaching the freeze-out volume. At this point it fragments into neutrons, light charged particles and IMFs. Due to the short ranging nuclear forces of nucleons the mean field collapses and IMFs are

formed by condensation. This unique phenomenon can be observed only for nuclei. Dynamical fragmentation in contrast is caused by high angular momenta, compression of the nuclear density, large momentum transfer and the formation of non-compact deformed nuclei. In this case the whole system and its parts (projectile and target remnants) never pass through states of thermal equilibrium. As schematically illustrated in Fig. 4.9 MF is observed in the E^* domain between spallation-evaporation and the “explosive” fragmentation regime. As mentioned in the previous section the global properties of nuclear matter are well described by the LDM for $E^*/A \leq 1$ MeV/nucleon. In this domain the basic decay mechanism is the successive emission of particles via evaporation from the surface of the compound nucleus (left picture in Fig. 4.9) and fission. In case of evaporation a heavy residual remains which is comparable in size to the original target nucleus.

Many models [Bot87, Bot95, Cug89a, Cug93] predict for nuclei $A > 150$ the multi-fragmentation within a range of the excitation energy from 3 to 5 MeV/nucleon. It is open so far whether one may regard the emission of IMFs by the conventional description of the evaporation from an equilibrated source, or whether other simultaneous decay characteristics need to be taken into account [Bot95]. In this intermediate energy region the system fragments into many spallation products, having a size no longer comparable with the target mass (Fig. 4.9, center). There is no accurate definition of the IMFs, however for heavy targets around $A \geq 150$ fragments of mass $5 \leq A \leq 40$ or atomic number $3 \leq Z \leq 20$ are generally considered as IMFs. For E^* in the range of the entire binding energy of the target nucleus (7.5 MeV/nucleon) vaporization (right representation in Fig. 4.9) begins to set in. Vaporization is a specific case of MF and is defined as a decay in which all reaction products have atomic numbers $A \leq 4$.

In particular for MF, the time scale of fragment emission in general and the question of sequential or simultaneous decay of highly excited nuclei is focus of theoretical [Gro90, Mor93b] and experimental [Fox93, Mor93, Bow93] studies. Models have been developed based on the chemical equilibrium [Bon86, Cha88], phase transitions with simultaneous evaporation during the dynamical expansion [Fri90b] or a dynamic of statistical decay [Col92]. Alternatively L.G. Moretto [Mor93, Mor95], K. Tso [Tso95] and A.S. Botvina [Bot95] propose as a signature of statistical nature of MF the linear dependency between the natural logarithm of the decay ratios of an n-body decay as a function of $(E^*)^{-1/2} \propto 1/T$ (Arrhenius-plots). However so-far no clear-cut answer could be given to the question whether the MF is subject to a prompt or sequential decay mechanism [Gol96b]. Also different model approaches try to find an answer whether the multi-fragmentation mechanism is dominated by dynamical or by statistical decay. Some of them describe the multi-fragmentation by instabilities in the gas-liquid phase of the nuclear matter [Cug93, Fri90b]. Analogue to a Van-der-Waals liquid, nuclear matter having a density of ~ 0.17 nucleons/fm³ in the ground state ($T = p = 0$) can be described by phase-diagrams (Fig. 4.10). In the ground state the nucleus resides at $p = T = 0$ and in the liquid phase. After an initial compression induced e.g. by a heavy ion reaction the hot nucleus expands. The hot nuclear matter follows the dashed line (isotherm) of Fig. 4.10 and ends finally as a diluted system in the spinodal region. In this region the compression coefficient κ

$$\kappa = (\partial p / \partial V)_T = -\frac{\rho}{V} \left(\frac{\partial p}{\partial \rho} \right)_T \quad (4.21)$$

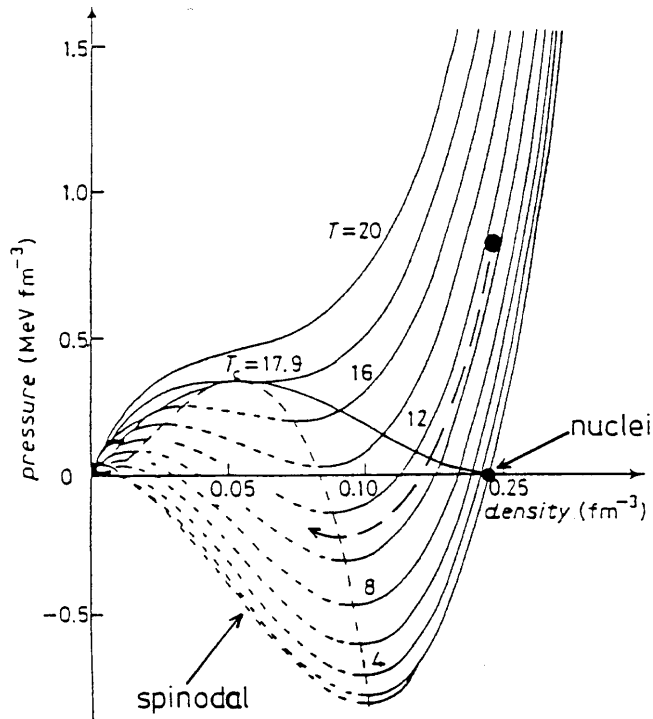


Figure 4.10: Solid lines (isotherm) indicate the pressure of the nuclear matter as function of nuclear density for different fixed temperatures (in MeV). The unstable states of the homogeneous infinitely expanded (and thus idealized) system is represented by the broken area. A nucleus in the ground state resides in the condition $p = T = 0$. The dashed curve shows the expansion of a hot, expanding nuclear system (see text). The line at $T_c = 17.9$ MeV represents pressure and density for which liquid and gas phases co-exist (figure adapted from [Cug93]).

exhibits positive values. Under these conditions ($\rho = 0.2\text{--}0.5 \rho_0$) density fluctuations may easily lead to fragmentation. The phase diagram, as represented in Fig. 4.10, applies only for infinitely expanded homogeneous matter, in which no Coulomb interactions are considered. Therefore the diagram is at most valid for hot neutron stars – but certainly not for real nuclei. This model – so far quantitatively not in detail being established – would reveal MF as a sudden phenomenon.

The formation of cluster in the region of low nuclear density was studied theoretically also by Ph. Chomaz et al. [Cho94]. They showed that – due to the finite range of strong nuclear forces – fluctuations of the system do not have short wavelength components. Consequently the production of fragments of almost same intermediate size are more probable than the formation of small fragments. Theoretically the process of MF can also be described by the percolation theory. Percolation models treat the nucleus as a lattice with nucleons located at nodes of the lattice. It has been found that results of percolation calculations depend significantly upon the details of the lattice structure. For reasons of computational convenience, the simple cubic lattice has most frequently been used in MF-simulations [Bau86], but several studies [Cha91, San93] have found that the face-centered-cubic lattice more accurately reproduces the experimental distributions of fragment masses and their energy spectra. A detailed analysis on fragmentation of excited remnants using the face-centered-cubic lattice model of nuclear structure is given in ref. [Mus02].

Finally also statistical models are used for the description of the fragment emission. They are based either on the sequential binary statistical decay [Cha88] or the simultaneous splitting of the system. The breakup of the system strongly depends on the so-called “freeze out” volume [Bon86, Fri90b, Gro90] and shows a rising probability with increasing excitation energy. Decay models describing the simultaneous breakup take as a basis the accessible phase space, which determines the probabilities of different decay channels. These “phase-space models” describe both – for low excitation energies the evaporation, and for higher energies (on the assumption of an increasing phase space) the breakup into 3, 4, 5 and more fragments of intermediate mass.

Experimentally the subject of different decay modes like fission, evaporation, multi-fragmentation and vaporization will be addressed in section 7.1.2 (NESSI). Also the PISA experiment aims at bringing some insights to the complex decay phenomena of hot excited nuclear matter. However for the PISA experiment currently only preliminary data and will be shown and discussed in section 7.2.

Chapter 5

Why nuclear physics experiments?

5.1 Application driven motivation

Spallation neutron sources (for condensed matter research, nuclear transmutation cf. sec. 2.4 or new concepts for energy production cf. sec. 2.5) consist basically of a high energy and high intensity proton accelerator and, separated by a window, of the target station for the neutron generation as described in Chapter 2.3. The spallation neutron sources exploit the thermal excitation of the heavy target nuclei by GeV protons and their subsequent de-excitation by evaporation of mainly neutrons with energies of a few MeV. Typically only 20% of the incident kinetic energy is dissipated in a first reaction into intrinsic excitation giving rise to the emission of about 15 neutrons (for 2 GeV protons impinging on a Pb target, as for example). The larger fraction of the energy, instead, is carried off during the initial intra nuclear cascade (INC) by a few energetic (hundreds of MeV) particles, mainly nucleons. These cascade and pre-equilibrium particles in turn initiate further nuclear reactions in the extended target, thereby increasing the total number of neutrons created per incident proton to about 40.

The best proton energy for the accelerator is still subject of some consideration. From a materials point of view (e.g. radiation damage) it seems advantageous to use higher energies (some GeV) with the benefit of lower intensity, which could also be reasonable from the physics point of view, if the neutron production were indeed to grow linearly with incident proton energy. The latter assumption is not unconfined true for energies far beyond 1 GeV as discussed later in Fig. 7.9.

It is the one goal of our experiments (cf. sec. 6.2, 6.4, 6.3) to increase the reliability of the models in the GeV energy range where only few and moreover quite diverging data exist. More specifically, it is the aim to measure for various proton energies in the COSY range from 0.4 to 2.5 GeV:

- production cross sections for light particles (p, d, t and He-isotopes) in selected target-, window- and structural materials. He, for instance, is known to destroy the mechanical strength of solids which limits the lifetime of window and target (if solid). The production of tritium as a radioactive gas of considerable toxicity has bearings on radiation safety provisions.
- for the investigation of the spallation reaction or the intra-nuclear cascade (INC): the energy and angular distributions of all light charged particles from pre-equilibrium

and equilibrium stages as well as multiplicities of all particles (n, p, d, t, He) from the nuclear evaporation cascade.

- for the neutron multiplication in thick targets (inter-nuclear cascades): neutron multiplicity distributions and total inelastic cross sections for target-blocks of various thickness, where the incident energy is converted as efficiently as possible into neutron yield. Target-blocks of up to 40cm in length and 15cm in diameter can be housed inside the neutron detector of the NESSI experiment.
- heat deposition in structural materials, the target, moderators and reflectors.
- features and neutronic behavior of ambient water and advanced cold moderators
- efficiency of shielding in particular for high energetic neutrons

Summarized the experimental efforts contribute gaining confidence and fixing parameters in the models currently available. These models are then applied to optimize the layout in terms of material choice, geometry and neutronic performance of accelerator driven systems as e.g. high intensity neutron sources.

5.2 Astrophysics driven motivation

Spallation reactions are also important from an astrophysical point of view. Due to their low binding energies Li, Be and B nuclei are highly unstable especially at temperatures and pressures encountered during stellar nucleosynthesis. The experimental determination of the spallation cross sections for C, N and O targets will provide a valuable data set to improve our understanding of the anomalous abundance of light elements in the cosmic rays and astrophysical questions of nucleosynthesis of the light nuclei in general. As for example the abundance of Li, Be and B in cosmic rays is only several times smaller than the abundance of neighboring nuclei C, N and O, whereas this abundance is 5-6 orders of magnitude smaller when observed in the solar system (the “LiBeB puzzle”). It is believed that Li, Be, and B elements in cosmic rays are mainly produced by spallation of heavier nuclei, e.g. C, N and O via their collisions with light nuclei —mainly protons [Ree94, Sil90]. This scenario was actually already proposed in 1970 by H. Reeves et al. [Ree70] where - contrary to most of the nuclear species, Li, Be and B are formed by the spallative interaction between the energetic Galactic Cosmic Rays and the Interstellar Medium. In opposite to “normal” nucleosynthesis taking place in the stars the spallative origin of elements is sometimes called “non thermal” nucleosynthesis. Similar ratios as mentioned above are also known for the elements with atomic numbers 20-25. However note that this concerns the cosmic rays of energies from 70 to 280 MeV/nucleon. The composition of cosmic rays of energies from outside this range is not known.

Moreover, the knowledge of appropriate cross sections allows to make far reaching conclusions concerning cosmic ray propagation. For example the isotopic composition of Be cosmic rays enables to judge about the propagation time of cosmic rays. The ${}^7\text{Be}$ nuclei which decay only by electron capture (half-life 53 days) are stable in cosmic rays as well as ${}^9\text{Be}$ nuclei which do not decay at all. On the other hand the ${}^{10}\text{Be}$ nuclei are unstable to

beta decay with a half-life 1.6 million years. Due to this relative abundance of Be isotopes changes with time and may be used to determine timescale of cosmic ray propagation. Furthermore, ratios of $^{11}\text{B}/^{10}\text{B}$, $^6\text{Li}/^9\text{Be}$ and B/Be abundances may reflect possible role of large fluxes of low energy cosmic rays as well as may call for some other production mechanism of some of these elements. For example there is a hypothesis of neutrino induced spallation in supernovae which should give contribution to ^{11}B production but does not influence abundance of ^{10}B . However, to account for all details of the relative abundances of all isotopes on the ground of astrophysics models it is required to thoroughly test their predictions. Therefore not only the values of the total production cross sections, relevant in the context of the abundance problem have to be determined experimentally, but also the energy distributions should be known precisely enough to allow checking the applied model. The experiments NESSI and PISA discussed in the current work are an approach to fill this serious lack of such data in the intermediate energy range.

5.3 Nuclear physics driven motivation

Properties of hot nuclear matter can *not* be described by elementary nucleon-nucleon scattering, because even knowing the hadronic interactions the solution of the many-particle system would cause serious problems for heavy nuclei. Instead generally matter is described by macroscopic observables like temperature, density and pressure. For infinite nuclear matter the relation between thermodynamic observables pressure, energy, density ρ and temperature T is given by the equation of state [Sto86]. Except of the saturation density ρ_0 and the energy at this density the form of the equation is not well understood. When expressed in form of a caloric equation of state the energy E_B per Baryon is written:

$$\frac{E_B}{A} = E(\rho, T) = E_T(\rho, T) + E_C(\rho, T = 0) + E_0(\rho = \rho_0, T = T_0) \quad (5.1)$$

with the thermal energy E_T and the compression energy E_C taking the dependency on ρ and T into account and E_0 reflecting the energy in the ground-state. The relation between the equation of state and the mean nuclear potential U is expressed by the kinetic energy density t_v and the density of the total energy h_v : $E_B/A = h_v/\rho$ and $U = \frac{\partial}{\partial \rho}(h_v - t_v)$. The equation of state for nuclear matter gives e.g. insights in phase transitions. At low density ($\rho < \rho_0$) and high T due to the superposition of nuclear and Coulomb forces, nuclei can coexist in liquid and gaseous phase analogous to the Van-der-Waals gas. For extremely high T and ρ a quark-gluon plasma is expected. In this new phase of nuclear matter the quarks are supposed to be (quasi-)free.

With the experiments studied in the current work neither T nor ρ of such high density phases is approached and the nuclear matter in form of an ensemble of A nucleons is neither infinitely expanded nor to be reduced to nucleon-nucleon interactions. However also on the way to this high density phase numerous interesting phenomena exist.

The nuclear physics aspect concerns the decay modes of very highly excited nuclei and has been intensively investigated during the last decade mostly with heavy ion accelerators - with moderate success, however. At high excitation energy one expects more diverse decay modes than evaporation and fission to become accessible to the nucleus: multi-body

fragmentation with the emission of many intermediate-mass fragments (IMF), and, when the excitation exceeds notably the binding energy of the nucleus, also the even more violent vaporization into single nucleons and light nuclei not heavier than alpha particles (complete disintegration of the nuclei into light fragments). In the past heavy-ion collisions in the energy range of up to several 100 MeV/A have often been investigated [Bow91, Tok95, Poc95] and new decay phenomena or novel and relatively scarce modes have indeed been observed. These exotic modes might be due to the unique feature of nuclear matter—namely the superposition of short range nuclear forces and extremely long ranging Coulomb forces. However at the same time these modes represent the superposition of statistically and dynamically driven fragmentations. Also the exact definition of the decaying source from the correct theoretical description point of view is rather ambitious as demonstrated in Fig. 5.1 showing a Landau-Vlasov simulation [Bre93] of the $^{208}\text{Pb}+^{197}\text{Au}$ reaction at 29 MeV/nucleon.

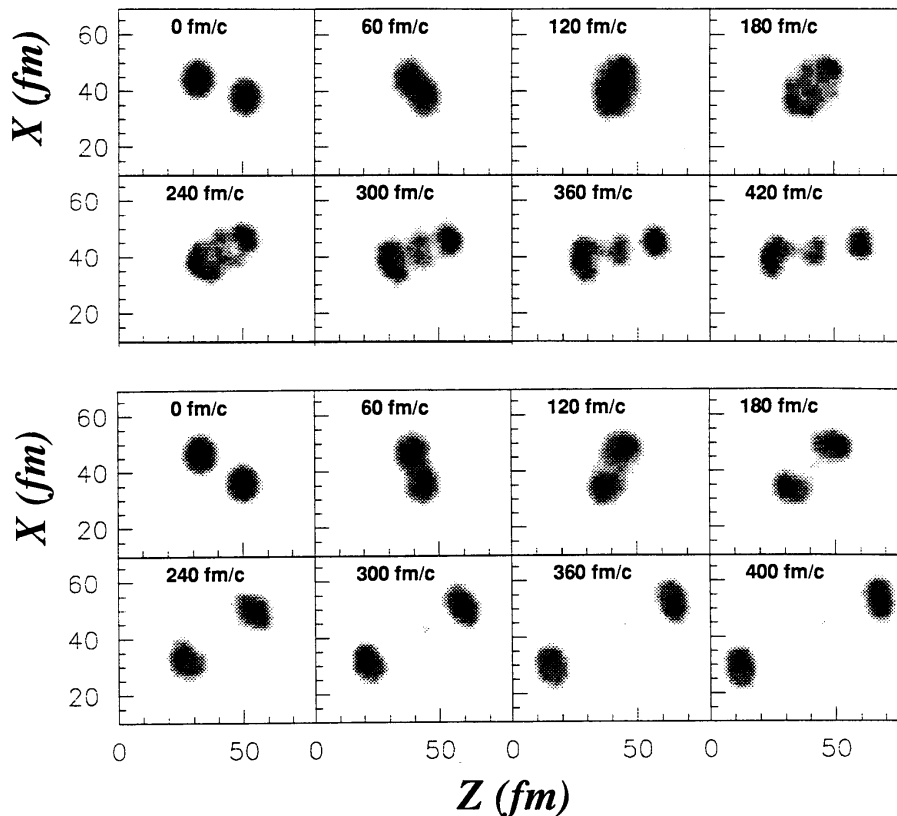


Figure 5.1: Time dependent development of the one-particle-distribution in phase space for the system 29 MeV/u $^{208}\text{Pb}+^{197}\text{Au}$ and an impact parameter $b = 6$ fm (top) and 10 fm (bottom) (adapted from [Bre93]).

The interpretation of these density profiles is all the more difficult the smaller the impact parameter between almost symmetrical masses and the larger the intrinsic spin of the target- and projectile-like fragments is. Still these phenomena rise a variety of open questions: Is the multifragmentation driven by thermal excitation of the nuclei, by repelling Coulomb forces or by deformations and high spins? The interpretation of these sequential or possibly simultaneous decay modes requires a clear distinction of statistical and dynamical fragmentation. The driving forces for these fragmentations still remain obscure, because too many dynamic distortions are inevitably introduced by the heavy-ion reaction together with the thermal excitation, like large angular and linear momenta, density compression or the formation of peculiar unstable non-compact shapes.

Reactions with protons, instead, are much less likely to induce collective excitations in the target nucleus and may thus allow to come closer to what is called statistical fragmentation: the decay of a compound nucleus stocked with purely thermal and equilibrated excitation. The knowledge of these purely statistical decay mechanisms is a prerequisite or key to the understanding of the more complicated effect of collective excitations on the fragmentation. Fundamental properties of hot nuclear matter like heat capacity, specific heat, viscosity and phase transitions are by far not thoroughly explored. Since in this kind of reactions a minimum of compression to the nucleus is induced, the experimental investigation of equation 5.1 is enabled for high T at densities $\rho \approx \rho_0$.

In order to reduce the influence of the entrance channel on the decay modes the nuclear excitation following annihilation of energetic *antiprotons* has been investigated [Egi95, Egi00, Gol96, Gol96b, Gol99d, Hil95c, Jah95b, Jah99, Lot97, Lot99, Lot01, Pie99, Pie00]. Antiprotons annihilate on a single nucleon at the surface of, or even inside the nucleus, thereby producing a pion cloud containing an average of about 5 particles. Due to the high center-of-mass velocity ($\beta_{cm} = 0.63$) of this cloud it is focused forward into the nucleus. Since the pion momenta are comparable to the Fermi momentum of the nucleons in the nucleus, the pions heat the nucleus in a soft radiation-like way [Pol95], even softer and more efficient than in proton- or other light-ion-induced spallation reactions, which have also been exploited recently for this purpose [Enke99, Fil01, Gol99b, Gol99f, Gol00, Gol00b, Gol01, Her01, Lip94, Kwi95, Pie94]. Due to the small radius of interaction volume of 1.8 fm and a coherence length of $c\tau \sim 1.5$ fm in elementary $\bar{N}N$ annihilation reactions extremely high *local* energy densities are obtained. For antiproton induced reactions, INC calculations have been found to provide a reasonable description of the underlying mechanism. They predict that the spin remains low (below maximum $25\hbar$) and that shape distortion and density compression are negligible [Gol88], in contrast to what is expected in heavy-ion reactions. The reaction time for achievement of equilibrium conditions is only about 30 fm/c or 10^{-22} s [Cug87], which is much shorter in general than the dynamical period in heavy-ion reactions [Bau92]. This is all the more important at high temperature ($T \approx 6$ MeV) when the characteristic evaporation time reduces to $t < 10^{-22}$ s, implying little cooling of the compound nucleus during heating.

Summarized light particle induced reactions represent the softest way of producing hot nuclei with the advantage of:

- small compression and shape distortions
- small transfer of linear and angular momenta
- good definition of mass and charge of the decaying compound nucleus
- fast excitation (much faster than non-relativistic heavy ion collisions. Therefore only little cooling during the formation of the hot nuclei)
- existence of reliable reaction models

From previous experiments at Saturne/Saclay [Led98] and at LEAR¹/CERN² [Gol96] (cf. sec. 6.2.1) it is known on the other hand that light projectiles are less effective in

¹LEAR – Low-Energy-Antiproton-Ring

²CERN – Centre Européen pour la Recherche Nucléaire, European Laboratory for Particle Physics, Ch-1211 Geneve 23, Switzerland.

energy dissipation than heavy ions and that therefore even with the maximum energy at COSY, 2.5 GeV, only about 1000 MeV of excitation with reasonable cross section in heavy target nuclei and somewhat less excitation (but higher temperatures) in lighter nuclei (cf. sec. 7.1.2) is reached. Thus fission (cf. sec. 7.1.2) and evaporation in heavy fissile nuclei and the new fragmentation phenomena, or rather their onset, in lighter nuclei can be explored (cf. sec. 7.1.2).

But even the conventional decay modes, evaporation and fission, studied as function of excitation energy become new territory above 200 or 300 MeV of excitation: First of all, the occurrence of fission up to about 1000 MeV of excitation indicates by its slow collective nature, that the nucleus has survived this tremendous excitation as a self-bound system which moreover has reached thermal equilibrium.

Beyond that, from the competition with the faster and well known particle evaporation a time scale can be established for fission (and this separately for the motion from equilibrium deformation to the saddle point and from the saddle to scission). This fission time is related to one of the basic properties of nuclear matter, the nuclear viscosity or dissipation (cf. sec. 7.1.2).

The multi-fragmentation or vaporization phenomena can be observed in lighter nuclei like Cu or Ag (cf. sec. 7.1.2). Here it seems important not only to observe the phenomena and deduce a probability or cross section as a function of E^* for them, as has been mostly done in the past, but also to specify the phenomena more closely. In this respect a particular advantage of the NESSI charged particle detection system described in section 6.2 can be exploited, namely that it registers not only light particles and lighter fragments (IMF's), but also all heavier residues from each reaction. This will allow to built a complete mass- and linear-momentum balance for each reaction and thereby to test the completeness of the multi-fragmentation process. The need for complete measurements if IMF's at these energies is emphasized by the lack of data measured at incident proton energies below 1 GeV.

Drawing conclusions on features of nuclear matter from experimental observations is possible only by an intense comparison between the experiments and the theoretical descriptions. Only using theoretical models assumptions concerning nuclear matter and their influence on observables can be tested. Furthermore models provide to some extend an insight into the dynamics of processes which is generally scarcely or not possible with the "static" observables accessible in the experiments.

Therefore the primary intention of our investigation is to provide exclusive data rather than only to improve the data base of inclusive cross sections. With these exclusive data it is possible for instance not only to reconstruct for each initiated reaction the distribution of the deposited thermal excitation energy (Sec. 7.1.2), but also to investigate pre-equilibrium emission for peripheral and central collisions. This in turn allows to test critical model parameters (Sec. 4.4) which determine the equilibration point after the fast INC-stage and define the transition from the INC-model to an evaporation model for the statistical decay of the equilibrated nucleus (cf. sec.4.3).

Chapter 6

Experiments

In the following first the accelerator used by the three experiments is briefly introduced. The ideas, motivations, experimental methods and respective set ups of NESSI, PISA and JESSICA are presented in the current chapter before in chap. 7 the experimental and theoretical results are shown and compared.

6.1 The COoler SYnchrotron COSY

COSY is the abbreviation for "COoler SYnchrotron", which means as much as accelerator for "cold" particles. However in COSY not only protons can be accelerated up to 96% of the speed of light, but also stored for ultra slow or fast extraction. The COSY ring as shown in Fig. 6.1 consists of a 180 m vacuum tube. Protons in the momentum range between 600 and 3400 MeV/c (corresponding to 175 and 2600 MeV) are accelerated and stored. Protons with the desired energy are available for experiments with the circulating beam ("internal experiments") as well as for experiments with the extracted beam ("external experiments"). Detailed reports on the performance and perspectives of the Cooler Synchrotron COSY are given in refs. [Mai97a, Mai97b, Sto97].

History: As result of the discussion between physicists of the Forschungszentrum Jülich (FZJ) and the surrounding universities in 1980-1986 the COSY working group of North-Rhine/Westphalian universities (= CANU) was established in 1985. This group elaborated a design concept, which was discussed in detail by different expert commissions with the BMFT in 1986. The FZJ internal building decision was endorsed in December 1986 by the main commission of the scientific-technical advisory committee of the FZJ. Laying of the cornerstone took place in summer 1988. In September 1992 for the first time particles were accelerated at COSY. The inauguration took place in April 1993.

Dipoles and quadrupoles: 24 electromagnets deflect the protons rotating in the COSY around 15 degrees each, so that a course closed in 360 degrees results. Quadrupoles exert a force on charged particles, which is attractive in one plane and repulsive in the plane perpendicular. These focusing and defocusing planes ensure the protons being held together to a bundle during acceleration.

Injection: For the injection process the orbit of the particles rotating in the ring is shifted for a short time. The orbit is the position intended of the proton beam for a stable closed course in the ring. The particles are shot in on this disturbed course, and

during the injection the circulating proton beam is reset on the original orbit course. The disturbance of the orbit course is accomplished with the use of so-called bump magnets. The entire injection process takes about 0.01 seconds.

Cooling: By interaction with electron beams (electron-cooling) the proton beam stored in COSY shrinks on the smallest possible expansion. During the "stochastic cooling" the orbit course of the circulating proton jet is measured in pick up's and corrected with the help of the kickers. The position of the jet in COSY is measured by 29 position monitors with an accuracy of approx. 1mm. This position measurement takes place contactlessly, i.e. without direct effect on the jet.

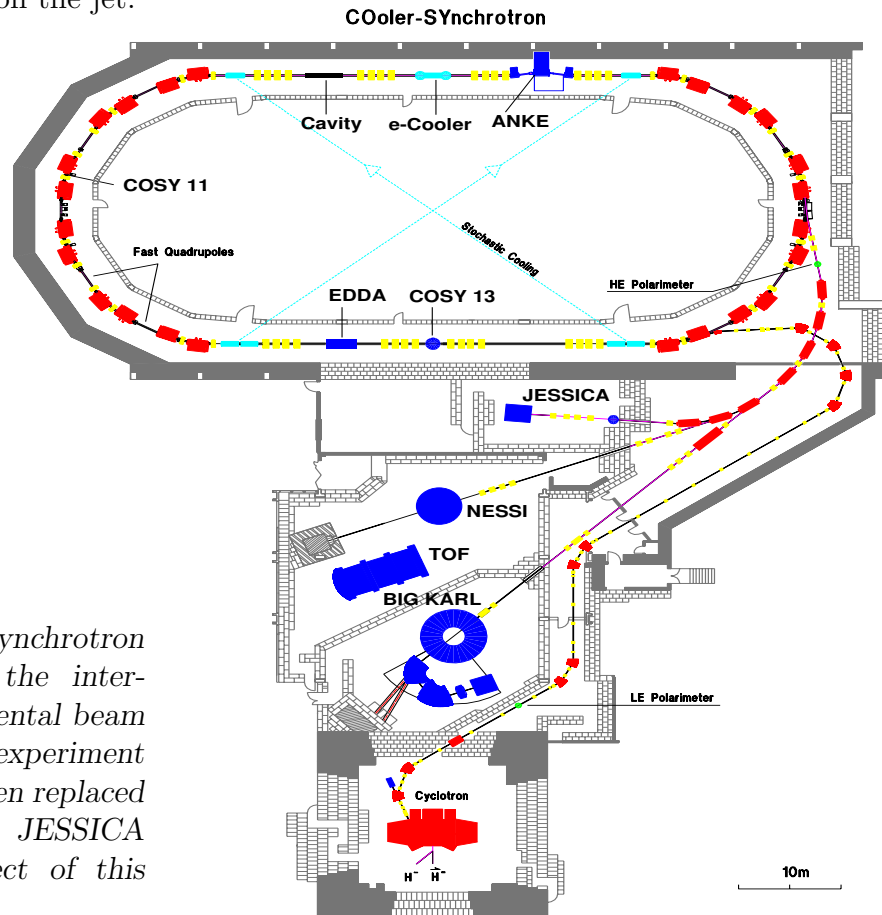


Figure 6.1: Cooler synchrotron COSY in Jülich with the internal and external experimental beam areas. The internal experiment COSY-13 has recently been replaced by the PISA experiment. JESSICA and NESSI being subject of this work are also indicated.

Requirements for JESSICA: In contrast to the slow extraction needed generally for experiments at COSY or the relatively long spills applied for internal experiments, the single turn extraction requested by JESSICA meets some challenge for the COSY crew: Fast beam extraction in the proton energy range of 0.8 to 2.5 GeV is accomplished by the use of a kicker magnet generally employed for beam diagnostic measurements. The cycle starts in the same manner as for resonant beam extraction for external experiments. A closed orbit bump in the horizontal plane is located near the electrostatic septum. The proton beam is bunched with a bunch length in the flat top of about 200-500 ns. The beam intensity peaks at about 10^{10} p in the flat top. By means of the kicker magnet the beam bunch is short time (0.75-2 μ s in width, rise- and fall-time $\leq 1\mu$ s) deflected. The kicker excitation is synchronized with respect to the COSY rf-signal and can be adjusted in time by a programmable delay, so a unique deflection of the total bunch can

be performed (bunch synchronous excitation). Only horizontal beam deflection is possible with the kicker magnet installed at a repetition rate of 1 Hz. The minimal COSY cycle time varied from 5 ms in case of low energy to 2 s in the case of highest energy. In order to extract the whole beam stored in COSY in one single turn, electron cooling is indispensable. The relatively long cooling time needed results in a repetition rate of the extracted proton beam of ≈ 0.03 Hz. The reliability of the kicker magnet has been shown to be rather high. Details are given in ref. [Die98].

6.2 The NESSI experiment

6.2.1 Objective

All previous data on production yields have been obtained by measuring the integral neutron induced activation in a moderator bath surrounding the target, by integrating double differential neutron yields ($d^2\sigma/dEd\Omega$), or by neutron-induced activation in small samples positioned on the target surface. For a summary of such measurements see Ref.[Hil97] where preliminary results of the present work have also been presented. Instead, in the present NESSI study all neutrons produced in each individual shower induced by an incident energetic hadron are counted. In order to demonstrate the inherent capabilities of the new approach the characteristics of the employed detection method will be described briefly in sect. 6.2.2. On one hand emphasis is put on a comparison of model predictions with the data obtained with thick targets, where incident energetic protons in the energy range up to 2.5 GeV at COSY (5 GeV/c hadrons at PS/CERN and up to 1.2 GeV \bar{p} at LEAR/CERN) impinging on massive targets give rise to cascades of nuclear reactions within the bulk target material. In these kinds of setups, charged reaction products are stopped within the target volume and only neutrons are detected. Specifically, of great importance are neutron production cross sections for various incident hadron energies, various target materials, and different target geometries. On the other hand following the motivation of the fundamental physics aspect, results on production cross sections, particle spectra, angular distributions, etc. for neutrons and charged particles taken at thin target measurements have been compared with corresponding simulations in order to decouple the primordial spallation reaction from the subsequent inter-nuclear cascade.

The NESSI and former PS208 collaborations have enriched the available information by the event-wise measurement of the number of neutrons (called hereafter neutron multiplicity M_n) [Fil01, Gol96, Gol96b, Gol99b, Gol01, Hil98, Let00, Lot98, Pie97] using a high efficient 4π sr gadolinium loaded scintillator detector [Gal94, Gal01, Hil98] and provided a heavyset matrix of benchmark data enabling a validation and possibly an improvement of high energy transport codes. As mentioned in contrast to previous measurements the event-wise character of the experiment allowed to gain access even to the distributions dM_n/dN rather than average values only, thus imposing additional constraints for theoretical models [Enke99, Fil01, Gol99d, Gol00, Gol00b, Gol01, Her00]. The first experiment which measured neutron multiplicity distributions for 0.475 and 2 GeV p bombarding thin targets was carried out at Saturne/Saclay by Pienkowski et al. [Pie94].

In the current work both, the so-called “thick-target” scenario where only neutrons can be observed in the NESSI experiment and multiple-nuclear reactions per source particle¹ might take place as well as experiments using thin targets (only one nuclear interaction in the target) will be subject. While the first aspect is triggered by the application driven motivation (sect. 5.1) the second issue reflects the fundamental physics aspect discussed in sect. 5.3. The latter enables a code validation not only for neutrons, but also for charged particles or even for correlations between both [Gol00, Her00, Enke99]. We also demonstrate that insights into the transport process including all cascade particles in thick targets can be gained only by disentangling intra- and inter-nuclear cascades. In addition to the above mentioned neutron measurements recently also light charged particles have been measured with π , p , \bar{p} , ${}^3\text{He}$ and ${}^4\text{He}$ projectiles in the energy region of 1-14 GeV [Gol96, Ahm93, Kwi95, Hsi97, Lip94]. However most of these studies measured energetic cascade and not evaporative light charged particles (p and He) which are needed to reconstruct thermal excitation energies.

Experiments at LEAR, PS (CERN) and COSY (FZJ)

In the framework of the nuclear physics driven motivation described in Sec. 5.3 especially antiproton induced reactions in flight and at rest are capable of exciting nuclear matter without disturbing dynamical effects [Cug84, Cug89] generally induced in heavy ion reactions. Complementary to heavy ion reactions, antiproton induced reactions represent an alternative method for producing highly excited nuclear matter and enable probing the nuclear equation of state at high temperatures. The rather high energy transfer is due to the phase-time-structure of the elementary $N\bar{N}$ -annihilation with a radius of interaction of ≈ 1.8 fm and a coherence length of $c\tau \sim 1.5$ fm. In case of antiproton annihilation at rest, the keV-antiprotons are captured by the nucleus like “heavy electrons”. They cascade down to lower energy levels emitting Auger-electrons and annihilate with a nucleon of the nucleus at the periphery of the nucleus. On the average 5 pions—as well as strange particles K , Λ , Σ —are produced partly heating the nucleus in a radiation like way [Pol94]. Much more thermal excitation energy can be transferred to the nucleus using energetic GeV-antiprotons, because the annihilation takes place much closer to or even inside the nucleus. Increasing the \bar{p} -energy doesn’t a priori implicit high E^* , because at the same time the average kinetic energy of annihilation pions is also increased and the pion absorption via the Δ -resonance becomes less effective. INC model calculations [Gol88, Ilj94] show the spin in \bar{p} reactions to remain small ($\leq 25\hbar$) and the equilibration time (30 fm/c or 10^{-22} s) [Cug87] to be much smaller than the dynamical periods in heavy ion reactions [Bau92]. The latter effect is of extremely high importance when for high temperatures ($T \approx 6$ MeV) the characteristic evaporation times are less than 10^{-22} s. The physical picture of annihilation in flight and at rest for $\bar{p}A$ reactions is drawn in ref. [Gol96b].

For the very first time correlations between neutrons and charged particles following \bar{p} -induced reactions have been measured event-wise and thermal excitation energy distributions have been reconstructed from the experimental observables.

¹Not only the intra-, but also the inter-nuclear cascade contributes to the production of neutrons following interactions induced by secondary particles and therefore resulting in a “multiplication” of neutrons.

The secondary beam facility at the Proton Synchrotron PS at CERN (Geneva) enabled the measurement of M_n simultaneously for p, \bar{p}, d, K and π^\pm at the same incident momentum and charge. Details on this experiment can be found in Ref. [Hil98, Pie94].

The majority of measurements has been performed at COSY Jülich and therefore the essential part of NESSI/PS208 data presented in sect. 7.1 will be on proton-induced reactions. However the two campaigns at LEAR and the PS at CERN complete the systematics and extend the studies to other hadron induced reactions.

Both, thick- and thin-target experiments at LEAR, PS/CERN and at COSY Jülich were carried out within an international collaboration between the FZ-Jülich, the Hahn-Meitner-Institut Berlin, the research center CERN (Geneva), GANIL (Caen), INR (Moscow), Rossendorf (Dresden), INP (Orsay), the universities of Rochester and Warsaw and the TU-Munich comprising currently approximately 20 members. The research program is partly supported by the Helmholtz-Strategy Fond and the TMR-Program of the European Community under contract No.:FMRX-CT98-0244.

6.2.2 Experimental setup

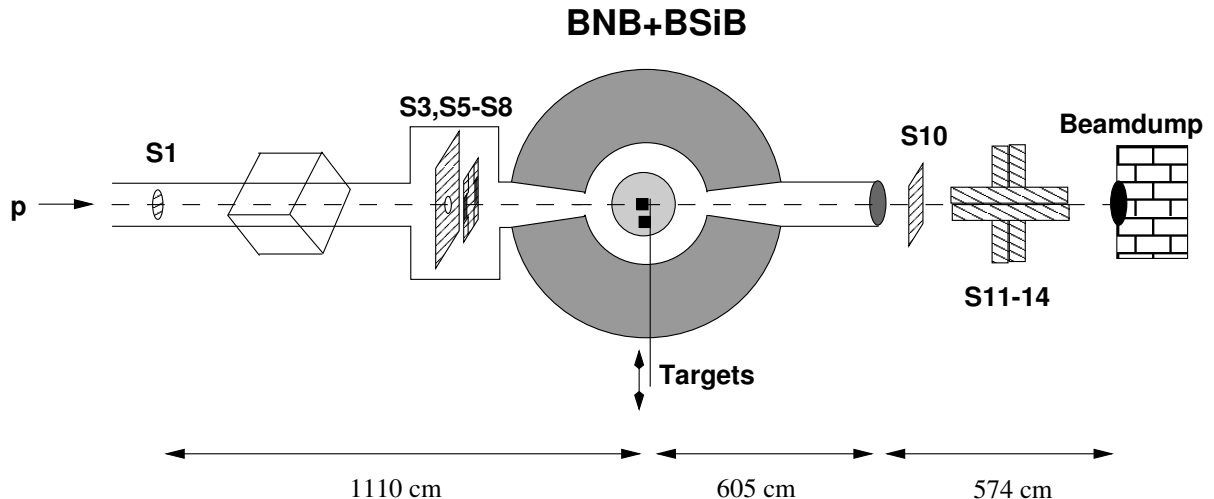


Figure 6.2: Schematical set-up for thin target measurements at COSY.

Except of the exact alignment and some additional Čerenkov detectors needed for incident particle identification² at the PS, the experimental arrangements for the experiments at LEAR, PS and at COSY are basically identical. As illustrated representatively for the COSY experiment in Fig. 6.2 incoming particles were tagged by a thin (0.3 mm)

²Protons of 26 GeV were bombarding a 25 mm-long and 4 mm-diameter Cu production target with a duty cycle of about 2.5%, producing all kinds of particles. Charge and momentum of the incident particles ($p, \bar{p}, d, K, \pi^\pm$) up to 5 GeV/c were selected with a system of dipole and quadrupole magnets. Identification of particle species was performed by measuring time of flight over 16 m in combination with two Čerenkov counters. This TOF was sufficient to separate deuterons and protons from lighter particles (kaons, pions, muons, and positrons) up to 5 GeV/c. In order to separate also the lighter particles we had to exploit two Čerenkov counters \check{C}_1 and \check{C}_2 which triggered, respectively, on pions plus lighter particles and positrons only. Neutron multiplicity distributions could thus be registered simultaneously for reactions induced by p, π^+, K^+, e^+ , and also d^+ on the one hand and by \bar{p} and π^- on the other hand. Muons, however, could not be separated from pions.

plastic scintillator S_1 mounted 11 m upstream from the center of Berlin Neutron Ball (BNB) [Gal94, Gal01, Hil98]. Their rate was adjusted to give a similar reaction rate independent of target thickness, i.e. to some 10^4 pps for thin targets and down to some 200 pps for the 35 cm targets. S_1 served as a beam counter for absolute normalization of measured cross sections and provided the time reference for BNB. The incident protons were also monitored by a set of scintillator detectors $S_3 - S_{14}$ partly serving as veto counters and tagging those protons entering “off-axis”. As mentioned previously, thin-target experiments are aimed essentially at studying the physics of intra-nuclear cascades, with reaction products having negligible chance for secondary interactions with the target matter. Both, neutrons and charged reaction products are detected using two concentric 4π sr detector devices, the BNB and the Berlin Silicon Ball (BSiB) [Enke99, Fig95]. In this set-up, the target is placed in the common operational center of the BNB and BSiB. The latter detector is mounted inside the BNB reaction chamber as schematically indicated in Fig. 6.3. In the following a brief description of the 4π sr detectors, their efficiency and the necessary corrections on the data is presented. For more details confer to references [Let00, Hil98, Pie97, Enke99, Her00, Gol96b, Gol96]. The most recent and comprehensive technical compilations on the two 4π detectors BNB and BSiB are published in refs. [Jah03, Her03]. The electronics and data acquisition is described in [Gol96b].

The 4π sr neutron-detector

The BNB [Hil98, Gal94, Gal01] is a spherical tank (left panel Fig. 6.3) with an outer diameter of 140 cm and an active volume of 1500 liters, filled with gadolinium-loaded organic scintillator NE343 (1,2,4-Trimethylbenzol= C_9H_{12}). It contains a central reaction chamber of 40 cm diameter connected to a high-vacuum beam pipe. The active detector volume is viewed by 24 fast photo-multipliers mounted on the outer shell of the BNB.

The operation of the BNB is based on the detection of gadolinium γ -rays from the capture of neutrons thermalized within the scintillator liquid as shown in the right panel

Table 6.1: Technical data of the 4π sr BNB.

Manufacturer	Hahn-Meitner-Institut Berlin
Volume	1500 Liters
	140 cm
Diameter of reaction chamber	40 cm
Scintillator liquid	NE343 (1,2,4-Trimethylbenzol) C_9H_{12}
Gadolinium Gd	0.4% (weight percent)
Capture cross section ^a for ^{155}Gd and ^{157}Gd	6.1×10^4 and 25.4×10^4 barn
Number of Photo-multipliers	24
Energy resolution	no
Time resolution ^b	≤ 3 ns
lower trigger threshold	2 MeVee (electron equivalent)

^aCapture cross section for thermal neutrons

^brelative to start-detector

of Fig. 6.3. The thermalization of the reaction neutrons is a relatively fast process, occurring on a $0.1 \mu s$ time scale. It is accompanied by a light flash generated mostly by the interaction of the recoiling nuclei (mostly hydrogen, but also carbon and oxygen) with the scintillator. This flash, combined with the light produced in the interaction of reaction γ -rays and charged reaction products with the scintillator, gives rise to a “prompt” signal - one of the observables in NESSI experiments.

A prompt light flash indicates an energy deposit in the detector by any reaction product. As it is detected with virtually unit efficiency, it can be used to measure the total reaction cross section, including reactions without neutron emission. Experimentally, one recognizes prompt signals based on their coincidence with valid “start” signals, which are generated by projectiles traversing the thin scintillation detector $S1$ placed at the entrance to the BNB reaction chamber. The reaction probability P_{Reac} for thin targets is obtained by comparing the number of prompt signals with the number of incident particles.

The fast thermalization process is followed by a slow diffusion of the neutrons through the scintillator, before they are eventually captured by the gadolinium nuclei present in the scintillator. There is a statistically-distributed time lapse for a thermalized neutron to “find” such a gadolinium nucleus and be captured, which occurs on a μs scale. The most abundant isotopes ^{155}Gd (14.7%) and ^{157}Gd (15.7%) have capture cross sections for thermal neutrons of $(6.1 \pm 0.1)10^4$ and $(25 \pm 0.2)10^4$ barn, respectively. The subsequent capture γ -ray cascade, with a total energy of approximately 8 MeV, produces a delayed light pulse. Due to the statistical nature of the thermalization and diffusion process, individual neutrons entering the detector volume at the same time instance, are captured at different times, spread over several tens of μs . It is this spread in capture times that allows one to count one-by-one the individual light pulses produced in different capture

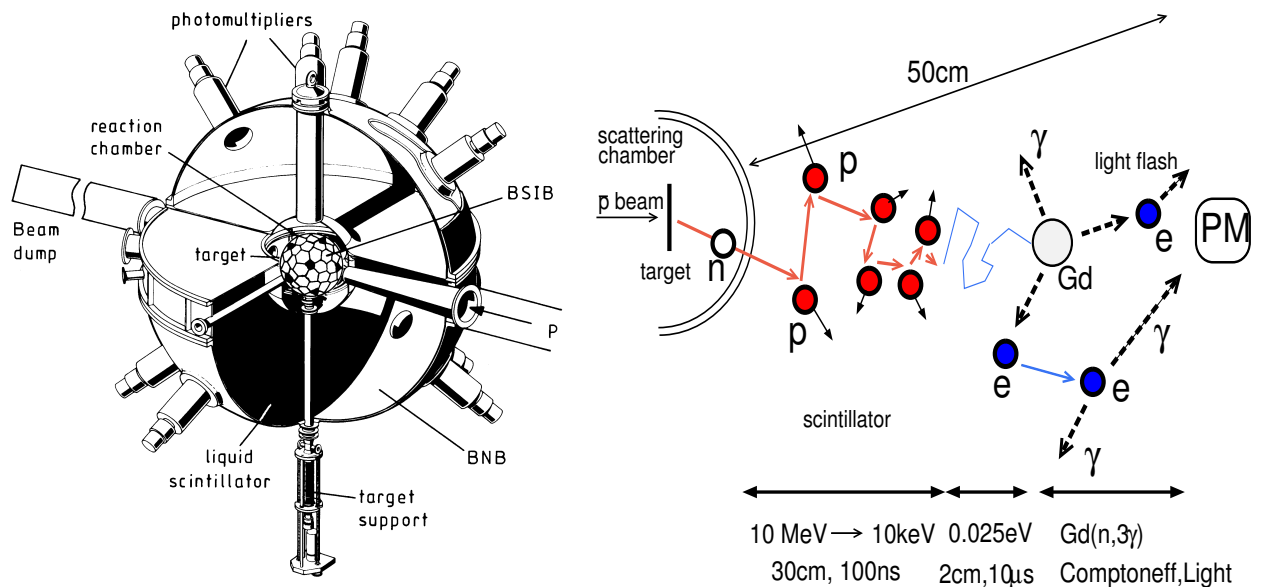


Figure 6.3: left panel: Schematical drawing of the BNB and the BSiB in the reaction chamber. right panel: Principle of neutron detection in BNB in three steps: i) slowing down/thermalization ii) storage iii) capture, counting.

events and thus, (ideally) the number of neutrons M_n that have entered the detector volume³. M_n is the essential observable of the BNB.

Summarized—in terms of time the neutron detection principle in the scintillator volume is a three step process: 1) thermalization of the neutrons 2) storage 3) capture on Gd-nuclei, counting the number of light flashes.

Efficiency of the BNB-Detector In applications of the BNB, neutron capture γ -rays are counted within a 45 μ s counting gate following each reaction event. Hence, as a neutron multiplicity counter, the BNB is a slow device, prone to event pile-up in high-intensity experiments. It is also important to note that not all neutrons are thermalized within the active volume of the detector. Some, especially high-energy neutrons, escape this volume without being captured. Such neutrons are not counted, leading to an overall capture efficiency smaller than unity.

In the NESSI experiments, the BNB counts mostly low-energy evaporation neutrons, for which the detection efficiency is typically $\varepsilon_n \simeq 82\%$. In contrast, for pre-equilibrium and INC cascade neutrons of higher energy (30-50 MeV), the detection efficiency is of the order of 20-35%.

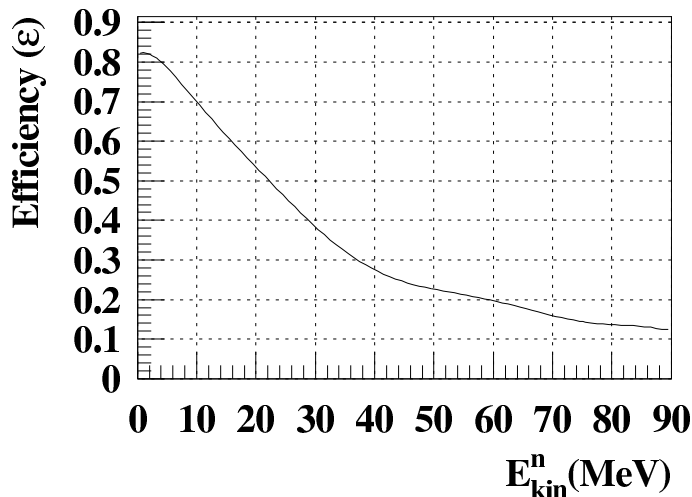


Figure 6.4: *Detection efficiency ε of the BNB as a function of neutron kinetic energy E_{kin}^n , as calculated with the DENIS code [Poi74]. A parameterization of this curve is given in ref. [Let00].*

The theoretical neutron detection efficiency ε of the BNB as a function of neutron kinetic energy E_{kin}^n is shown in Fig. 6.4. This efficiency was calculated using a Monte-Carlo simulation code [Poi74], assuming a light detection threshold of 2 MeVee (MeV electron equivalent⁴). In the simulation calculations, the latter threshold was matched to the experimental one, reproducing correctly the measured efficiency (82.6%) for 2.16 MeV fission neutrons emitted from a ²⁵²Cf-source.

In the NESSI experiments, the observed neutron multiplicities are averages over neutron energy spectra, weighted with the respective detection efficiencies. Since the information on kinetic energies of individual neutrons, E_{kin}^n is experimentally not available,

³The principle of neutron detection dates back to the investigations of Frederic Reines. In 1995 he got the Noble-Price for the recovery of neutrinos.

⁴The total reaction cross section measured using the prompt response of the BNB with this threshold corresponds to an inelasticity of at least 2 MeV.

the simulation calculations employ the neutron energy as calculated within the model. Additionally, the neutron detection efficiency is calibrated only at low neutron kinetic energies E_{kin}^n . At higher energies, the neutron detection efficiency is extrapolated based on Monte-Carlo calculations. It was checked by Y. Perier et al.[Per98] that such calculations reproduce satisfactorily the response of a similar detector for neutrons up to 70 MeV. As will be shown later in the upper panel of Fig.7.8 the bulk of neutrons is typically produced with energies lower than 10 MeV. Consequently they are detected with high efficiency.

Additional neutrons produced in the scintillator liquid

In the experiment the targets are surrounded by a shell of scintillator liquid which acts as a moderator and at the same time as a reflector for neutrons. This enables neutrons (and other reaction products) originally produced in the target to be scattered into the liquid scintillator and potentially even causing interactions with the target when reentering the target. In this section we study the contribution of additional neutrons being created by high energetic baryons and mesons leaving the target and entering the scintillator liquid of the BNB. Those ones would experimentally pretend to be created in the target or in fact give rise to an overestimation of $\langle M_n \rangle$ associated to the bare target. As an approximation the *leakage* spectra of different particles crossing the surface of the cylindrical targets towards the surrounding space have been calculated and these particles are considered as candidates for possible hadronic interactions or source of spallation reactions on C-nuclei in the scintillator liquid.

The effect could be considered as a second order influence on the experimental data which has not been considered in the previous section. We would like to show here, that these spurious events contribute only little and are justified to be neglected.

Fig. 6.5 shows the yield (solid line) corresponding to all particles produced in the target block and leakage (dashed line) energy spectra not only for neutrons (left panels) as will be discussed in Fig. 7.8, but also for protons (right panels). The spectra for 1.2 GeV proton induced reactions on 1 and 35 cm Pb-targets are confronted. While neutrons experience only a slight moderation when moving from the point of origin to the surface of the target, protons are drastically slowed down by electronic stopping. Only those protons having sufficient kinetic energy have a chance to leave the target surface and subsequently enter the scintillator liquid. The range of e.g. a 200 MeV proton in lead amounts to approximately only 5 cm and consequently the thicker the target the smaller the leakage spectrum as demonstrated by the dashed lines for 1 and 35 cm in Fig. 6.5. The distinct peak close to beam energies (dashed line) is attributed to (quasi-) elastically scattered protons having simply lost all the more of their original incident energy the thicker the target is. For the lower right panel of Fig. 6.5 the peak at approximately 700 MeV, reflecting elastically scattered protons for 1200 MeV proton impinging on the 35 cm Pb-target, is in accordance with calculated energy loss in Pb. Finally the shaded shaded area reflects the neutron- and proton leakage including the geometrical acceptance of the BNB being slightly smaller than 4π sr essentially due to the conical openings for beam in/out. The lethargy $u = \ln(E_0/E_n)$ used in Figs. 6.5 and 6.6 is the natural logarithm of the ratio of some fixed energy E_0 (e.g. the incident energy) to the kinetic energy of the neutron E_n . Therefore a small kinetic energy corresponds to a large lethargy

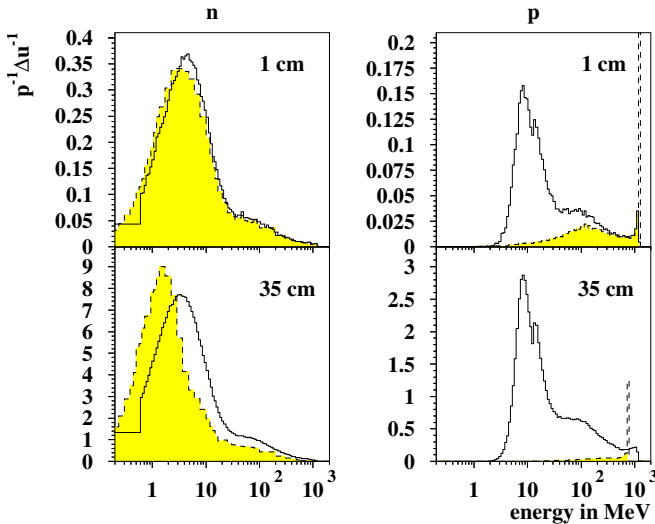


Figure 6.5: Production (solid histogram) and leakage- (dashed histogram) spectra of neutrons (left) and protons (right) for the reaction $1.2 \text{ GeV } p+\text{Pb}$. The dimension of the Pb target is $1 \text{ cm} \times 15 \text{ cm}$ and $35 \text{ cm} \times 15 \text{ cm}$ (length \times diameter), respectively. The shaded area presents those particles actually entering the BNB.

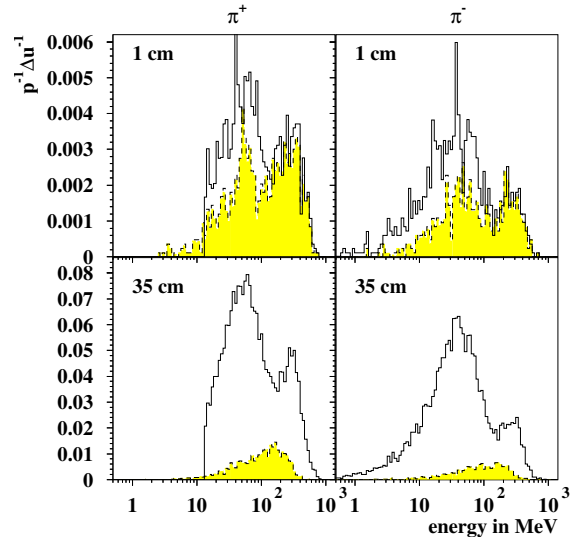


Figure 6.6: Same as Fig. 6.5 but for π^+ and π^- . Note the different absolute scales for the 1 cm and the 35 cm targets. Although the yield of pions is almost a factor of 10 higher in thick targets, the leakage finally is of the same order of magnitude. Simulated HERMES distributions are normalized per source proton and unit lethargy in Fig. 6.5 and 6.6.

and a neutron kinetic energy equivalent to beam energy $E_n = E_0$ results in $u = 0$. Note that despite the logarithmic x-axis of the lethargy presentations the integrals are a linear measure of the intensities.

Although the abundance of pions in absolute terms is much smaller than for protons or neutrons, the same phenomena are demonstrated in Fig. 6.6 for π^+ and π^- . π^0 are not being transported in the codes, instead they decay spontaneously into two γ -rays. Regarding the dashed and the solid histograms of all panels of Fig. 6.6 for both— π^+ and π^- —one observes a considerable reduction of the low energy part of the leakage spectra as compared to the production spectra. Only the high energetic pions have a chance to leave—even though slowed down—the target. Low energetic ones are absorbed. On the average also the kinetic energy of pions leaving the targets is decreasing with increasing target thickness. The effects are all the more pronounced as the target thickness increases and consequently the contribution of neutrons additionally produced in the scintillator liquid is expected to be largest for relatively thin targets—as will be shown in the following.

The relative contribution of neutrons and π^\pm entering the BNB scintillator liquid as compared to those ones which are actually leaking the 1 or 35 cm Pb target after bombardment with 1.2 GeV protons is larger than 97.5%. For protons the ratio is only 24.6 and 32.4%, respectively. The relatively small ratio for p as compared to n or π^\pm is due to the quite high probability for leading protons to leave the BNB through the 0°

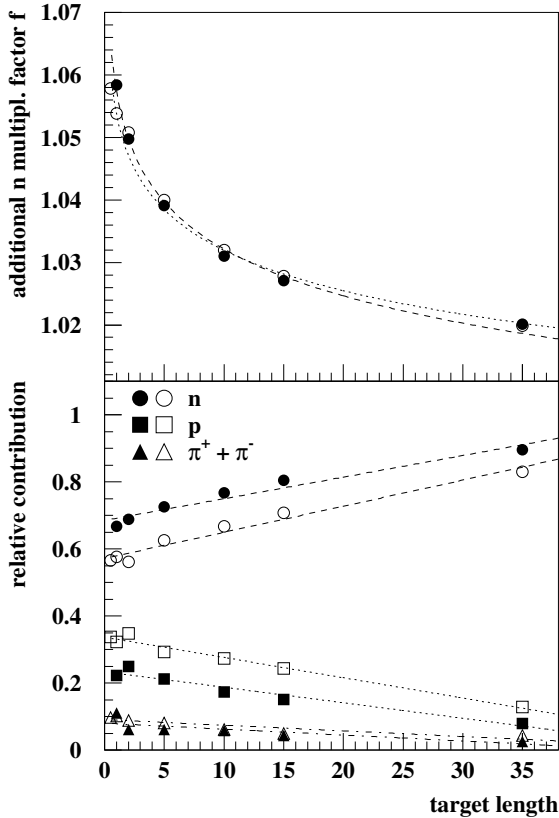


Figure 6.7: Additionally produced neutrons by reactions of n , p and π^\pm with the scintillator liquid for 1.2 GeV (open symbols) and 2.5 GeV (filled symbols) $p+Pb$ as a function of target thickness. The diameter of the Pb-target is 15cm. The lower panel shows the relative contribution of n , p and π^\pm . Lines are to guide the eye. Calculations have been performed using the HERMES code system.

beam tube even for targets of 35 cm length. Also the energy loss in the BNB stainless steel wall is slightly higher for protons as compared to pions.

The leakage spectra of n , p and π^\pm shown in Figures 6.5 and 6.6 are the basis for rating the number of neutrons additionally produced in the scintillator liquid. As described in sect. 4.3 for HERMES generally the neutron spectrum is recomposed by the HETC ($E_{\text{kin}} \geq 20$ MeV) and MORSE ($E_{\text{kin}} < 20$ MeV). Here for reactions induced by spallation products in the scintillator liquid generating additional neutrons we consider only neutrons with kinetic energy larger than 20 MeV and charged particles (p , π^\pm) with $E_{\text{kin}} \geq 1$ MeV.

As represented in the upper panel of Fig. 6.7 the effect of creating additional neutrons decreases from 6% for thin targets to less than 2% for targets of 35 cm thickness relatively independent on the incident proton energy. The calculation has been performed as a function of target thickness for 1.2 GeV and 2.5 GeV p induced reactions on Pb cylinders of 15 cm diameter. The decrease can essentially be explained by the larger absorption and slowing down processes for charged particles in thicker targets. On the lower panel the relative contribution of protons, neutrons and pions on the additional neutron production in the scintillator liquid is shown. Only those showers contribute to additional neutrons for which at least two neutrons are produced: ($n, xn\dots$) with $x \geq 2$. For all target thicknesses predominantly the neutrons entering the liquid are producing additional neutrons. While their relative contribution is increasing with target thickness, the contribution from protons and pions is substantially decreasing due to self-screening effects in thick target materials. Pions contribute only very little, because the abundance of pions created in

the cylindrical targets is low. High energy γ -rays from the π^0 -decay have not been taken into account. For the higher incident energy a larger fraction of protons leaving the BNB via the exit cone is responsible for a lower relative contribution of protons.

In summary the detector efficiency of the BNB as a function of kinetic energy is demonstrated to be well known and can therefore be taken on an event by event base into account in the calculations. In contrast all contributions giving rise to additional neutrons in the scintillator liquid are marginal and justified to be neglected in order to save computing time in the following. At most for thin targets maximal 6% of additional neutrons are created in the BNB. As will be seen in sect. 7.1.1 the discrepancy between simulation and experiment for thin targets would be even slightly enlarged if the effect of additional neutron production would be taken into account.

The 4π sr Silicon-Detector

Table 6.2: Technical data of the 4π sr Silicon ball.

individual silicon detectors	
manufacturer	Eurisys Meßtechnik ^a
type	IPH750-500 HMI C
detector-type	surface depletion layer
'backing'	ceramics
active area	763 mm ²
total thickness(=depletion zone)	500 μ m
spec. resistance	14285 Ω cm
applied voltage	\sim 100 V
Max. field strength in depletion zone	\sim 3.2 kV/cm
energy resolution (5.5 MeV α -source)	<100 keV
time resolution (5.5 MeV α -source)	<250 ps
4π sr Silicon ball BSiB	
granularity	162 detectors, self-supporting
shape	12 pentagons, 90 (ir)regular hexagons
acceptance	91% of 4π sr
radius	10cm
weight	600gr

^aEurisys Meßtechnik, F-67383 Lingolsheim, France

In addition to the neutrons, in the thin-target experiments, charged reaction products were detected. Light charged particles (LCP: H- and He-isotopes), intermediate mass- (IMF), and fission- fragments (FF) were detected and identified by the Berlin Silicon Ball (BSiB) inside the BNB. The BSiB [Enke99, Fig95] is composed of 158 independent, 500- μ m thick silicon detectors approximating a 20-cm diameter sphere and covering a solid angle of about 90% of 4π sr. Charged particles (CP: H+He+IMF+FF) were identified by

means of time of flight TOF versus energy E correlations with a mass resolution of ± 3 units for $A=20$ and ± 15 units for $A=100$. Six of the Si-ball detectors at angles between 30° and 150° have recently been replaced by ΔE - E telescopes. They consist of two fully depleted ΔE silicon detectors ($80\ \mu\text{m}$ and $1000\ \mu\text{m}$ thick) backed by a 7cm thick CsI-scintillator with photo-diode read out. These telescopes allow a fully isotopic separation up to about $A=20$ and an extension of the covered range of kinetic energy spectra above the BSiB thresholds (cf. following paragraph). For thick-target measurements BSiB is taken out and replaced by massive target blocks up to 40 cm length and 15 cm in diameter.

Efficiency of the Si-Detectors Due to absorption or specific energy loss of LCPs in the target material being evident in particular close to 90° , the overall detection efficiency of the BSiB for LCPs, calculated with Monte Carlo simulations, [Gol96] is about 79-84%, depending on the atomic number Z of the particle. This already takes into account the active area (94%) of the Si-detectors and 11 detectors missing for beam in/out, target in/out, TV-camera, some defect detectors and the 6 detectors replaced by telescopes. The lower energy threshold of the $500\ \mu\text{m}$ thick Si-detectors for all charged particles is 2.2 MeV . Protons and α -particles with energies larger than 8.2 and 32.2 MeV , respectively, are not stopped in the $500\ \mu\text{m}$ silicon detectors. Consequently the lower detection threshold represents at the same time an upper limit for detecting highly energetic p, d and t of more than 26 , 49 and 76 MeV kinetic energy, respectively. For the same reason minimum ionizing particles, π and K fall below detection threshold. For $Z \geq 2$ particles on the other hand practically no such upper energy limit exists.

6.2.3 Corrections on the data

The neutron multiplicity distributions measured with the above setup contained random and target frame related background. The magnitude of the target frame background was determined in separate measurements made without target and subtracted from the measured “raw” multiplicities. The random background was measured on-line using a second, $45\text{-}\mu\text{s}$ long counting gate pulse, started $400\ \mu\text{s}$ after the primary gate pulse. Subsequently, the experimental multiplicity distributions were corrected for this background by deconvolution techniques [Gol96b]. All experimental neutron multiplicity distributions shown in the following [Let00] have also been corrected for the detector dead time of 35 ns and for multiple scattering, but *not* for the detection efficiency. The latter correction was included in simulation calculations in comparisons to experimental data.

6.2.4 Trigger conditions

The setup for the measurement employing thick targets used only the BNB neutron detector. Massive targets up to 35 cm thick and 15 cm in diameter were used. Since essentially all the charged reaction products were stopped in the target block, only neutrons were detected (see also sect. 6.2.2 below).

For targets shorter than 7 cm , a nuclear reaction event was established based on the detection of a prompt light signal in coincidence with a valid start signal. For very thick targets (length $\geq 7\text{ cm}$), on the other hand, the reaction event was signaled, and the data

acquisition was triggered, just by a start signal from the in-beam scintillator as shown by B. Lott et al.[Lot98]. This procedure avoids bias in trigger due to the absorption of charged reaction products and γ -rays in the target material.

Since the height of the prompt signal originates from a variety of factors not exactly known (light conversion, reflection, absorption within the scintillator liquid etc.), a perfect analog is rather difficult to simulate. Therefore in the simulation the trigger condition best resembling the experiment can be accomplished by setting a trigger to the excitation energy ($E^* > 0$) at the end of the INC process of the first spallation reaction. This indicates that an inelastic reaction has occurred. Another possibility is to trigger on any particle leaving the target, except the source particles leaving the target on its front side. Both Monte-Carlo trigger conditions lead to exactly the same neutron multiplicity distributions.

The Targets

For thin targets nuclei ranging from ^{12}C up to ^{238}U have been measured with thickness of the order of some $100 \mu\text{g}/\text{cm}^2$ to g/cm^2 . The targets were mounted on a 14 cm long Al flag-pole with $0.5 \text{ mm} \times 5 \text{ mm}$ profile and positioned perpendicular to the beam axis. Thinner targets ($\leq 1 \text{ mg}/\text{cm}^2$) were generally used to measure proton-induced fission while thicker targets were employed for the measurement of neutron production and total reaction or inelastic cross sections. The target thicknesses were measured by weighing and energy loss measurements of α -particles from ThC. For thick targets three nuclides, Hg, Pb and W have been chosen which are representative of the target, structure and core materials of the ADS. For the latter measurements systematic studies of a large variety of different cylindrical geometries and incident energies as summarized in Tab. 6.3 have been studied. All pieces were made from chemically pure ($\geq 99.98\%$) material of Pb, W and Hg, the latter being encapsulated into 1 mm thick stainless steel containers.

Table 6.3: Combinations of target materials, target sizes explored at various energies.

Energy		0.4 GeV	0.8 GeV	1.2 GeV	1.8 GeV	2.5 GeV
Target	Diameter	Thickness in [cm]				
Pb	2 cm	0.5	0.2	0.2	0.2	0.2
	8 cm	1-35	1-40	35	0.5-40	2-35
	12 cm	35	1-35	35	15-39	35
	15 cm	5-35	1-35	1-35	1-35	2-35
Hg	2 cm			0.5	0.5	0.5
	15 cm	33.7	2-33.7	2-30.45	2-33.7	5-33.7
W	2 cm		0.112	0.112	0.112	0.112
	8 cm	1-34.75	0.5-34.75	5-34.75	0.5-34.49	0.5-34.75
	12 cm	34.75	34.75	5-34.75	20-34.49	2-34.75
	15 cm	10-34.75	2-34.75	1-34.75	1-34.49	1-34.75

6.2.5 Plan of anticipated research

The NESSI-program is still far from its completion with only 2 or 3 experiments dedicated to its two different aspects, respectively.

As far as the spallation neutron source-aspect is concerned we think of two different ways of extending the present investigation (apart from the more trivial choice of other materials for the extended target blocks):

The experiment with the 3 target blocks from W, Hg and Pb has shown that the maximum size (determined by the dimension of the chamber inside the Berlin neutron ball (BNB)) of the employed cylinders with 15cm in diameter and 40cm in length is still insufficient for a complete conversion of the protons kinetic energy into neutron yield. It seems that mostly neutral secondary particles extend the reaction probability beyond these dimensions, in particular for an incident energy in excess of about 1 GeV. In order to correct this deficiency we could eventually replace the neutron ball presently used by ORION, a similar but somewhat larger neutron tank (with 4.5 m^3 of liquid scintillator and a scattering chamber of 60cm in diameter and 120cm in length) from GANIL.

Another extension of the thick-target experiments inside the neutron tank, which we intend to propose to the PAC in the next year, is rather a complement than an extension to the previous experiment: We want to measure the spectral and angular distribution of all kind of fast particles which escape from the extended target block as function of its diameter and length. Of particular interest here is of course the energy spectrum of the neutrons and their origin along the targets cylindrical axis. The technique and the detectors for this purpose are readily available at HMI: 6 to 12 individual neutron TOF-detectors with NE213-cells and thin plastic detectors in front for the effective separation of different radiation (gamma, neutron, proton, pion...). The reliability of these detectors has been established in many previous experiments, more recently also with antiprotons and protons at LEAR [Pol95]. Also, the beam quality at COSY and the open geometry in the TOF-hall is very suitable for these experiments.

As to the nuclear physics aspect, here the future evolution is more difficult to estimate, because the analysis of the last July-experiment has not even started. But also for this aspect it seems evident that a TOF-experiment of the type discussed above, with very thin targets, however, would form a valuable complement.

Its predominant purpose would be the observation of the pre-equilibrium emission from the fast intra-nuclear-cascade, an essential quantity for the understanding of the spallation reaction and the following equilibration processes. It might be important for the relevant experiments to maintain the 4π sr Silicon detector ball as a filter on the impact parameter or the deposited excitation energy.

Experimental results will be shown and compared to simulations in Section 7.1.

6.3 The PISA experiment

6.3.1 Objective

The experimental program of the PISA project aims at the measurement of total and double differential cross-sections for products of spallation reactions on a wide range

of target nuclei (C - U), induced by protons of energies between 100 MeV and 2500 MeV. These cross sections are important for testing physical models of the interaction of protons with nuclei what is of crucial importance for planning and construction of the European Spallation Source ESS. The most restrictive tests of the models are provided by data from exclusive experiments. Therefore, coincidence measurements (high-energy protons with other charged particles) are performed besides the inclusive experiments. Experiments with light targets (up to Fe) will provide the data, which are very important for understanding the anomalous abundance of light elements in the cosmic rays. The mass dependence of the cross sections (for full range of targets from C to Au) should shed light on the competition of various mechanisms of interaction of protons with nuclei.

The project described in more details in ref. [Pisa99, Pisa00, Pisa01] is partly supported by the BMBF-Verbundforschung, the EU-LIFE program, the EU HINDAS project FIS5-1999-00150, and the EU TMR project ERB-FMRX-CT98-0244.

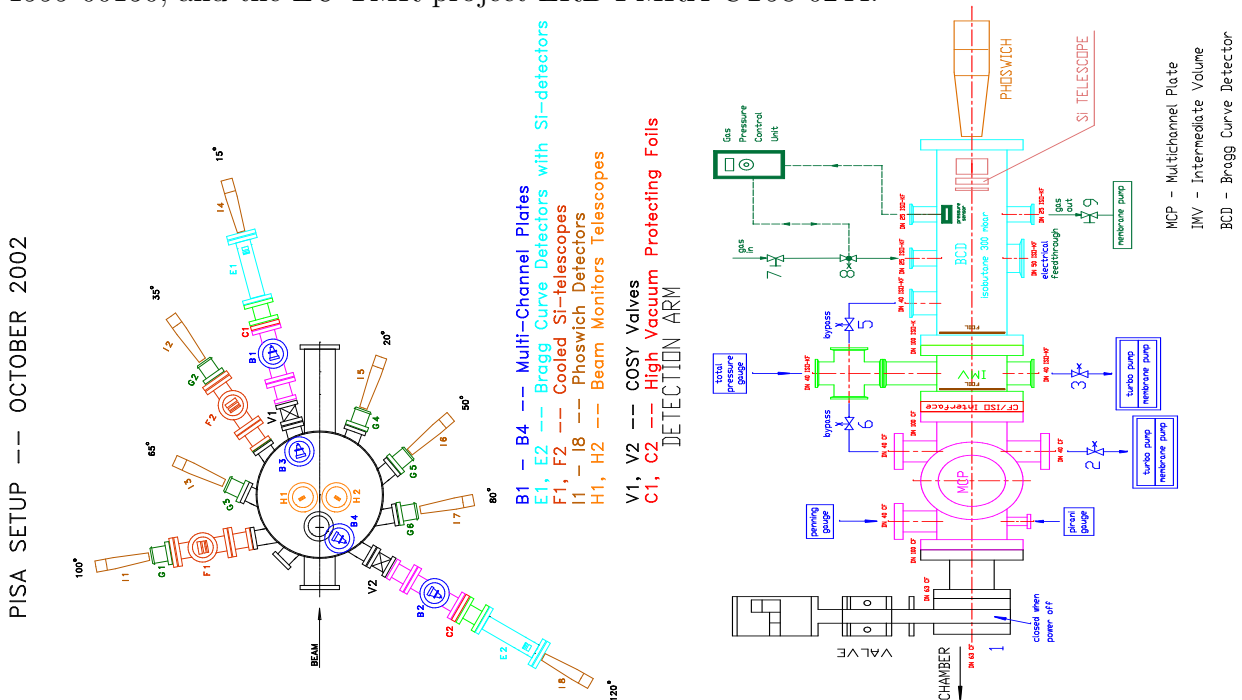


Figure 6.8: *left panel: Scattering chamber of the PISA experiment as of Oct 2002 with the 2 full detector arms mounted at 15 and 120° equipped with Bragg curve-, channelplate- and phoswich- detectors. right panel: One of the detection arms in more detail.*

6.3.2 Experimental setup

Each of the eight⁵ detection arms mounted at the scattering chamber (see Fig. 6.8) of the PISA experiment consists of two Multichannel Plates (MCP) working as “Start” and “Stop” detectors for the time of flight measurement, a Bragg Curve Detector (BCD) [Pisa99] followed by three silicon detectors of 100, 300 and 4900 μm thickness for particle

⁵currently only the most forward (15° with respect to the beam axis) and the most backward (120°) detection arms are mounted

identification using ΔE - E techniques and kinetic energy measurement of intermediate-mass spallation products, and a set of double layer scintillation detectors - fast and slow (phoswich) - in order to identify light charged evaporation and spallation products like p, d, t, He. It is shown that the TOF plus Bragg curve detectors provide identification of light heavy ions with mass up to 20 - 30 and kinetic energy starting from less than 1 MeV/amu.

The channelplate detectors

The telescope for the time of flight measurement is composed of two MCP detectors in Chevron configuration. The channel plates are manufactured by Galileo Corporation whereas the suitable housing has been designed and built by ourselves [Pisa00] (cf. Fig.6.9).

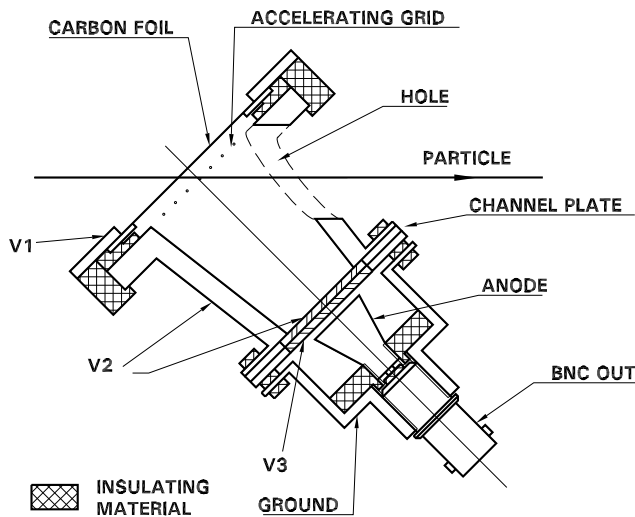


Figure 6.9: Assembly for particle detection with the multichannel plate detector. For description see text.

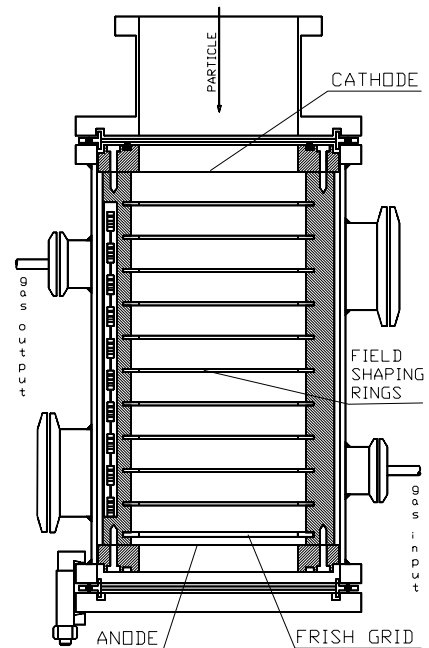


Figure 6.10: Bragg curve detector as used for spallation studies at the COSY internal proton beam; details see text.

The particles to be registered are passing the $20 \mu\text{g}/\text{cm}^2$ thick carbon foil and knock out some δ -electrons. These electrons are accelerated towards the MCP in the electric field between foil, accelerating grid and second channel plate. The particular voltages are chosen to obtain the highest multiplication factor in the channel plates (10^7) and to warrant the best signal to noise ratio. It was checked that the best performance of our MCPs is achieved for voltages of 2000 V between first and second channel plate and around 400 V between carbon foil and accelerating grid.

Timing properties of MCPs were measured at the accelerator of the Heavy Ion Laboratory in Warsaw, Poland where few, low intensity beams of various ions passed through a telescope of two such assemblies spaced by 27.4 cm. The measured resolution of the time of flight is equal to 1.1 ns. The major contribution to this value comes from the energy

spread of the beam, which is estimated to be 920 ps. The influence of the electronics is negligible (80 ps). Taking into account these values one can state that timing resolution of our telescope is equal to 580 ps.

The Bragg curve detector

After first successful attempts to use so called Bragg curve spectroscopy to identify highly ionizing particles [Sch82, Gru82] several detectors exploiting characteristic features of the Bragg curve have been built and used for various applications. The appearance of Bragg curve detectors has allowed to detect fragments with high precision over a broad range of nuclear charges with low registration thresholds [McD84, Mor84, Wes85, Kot87, Kot88, Och96]. This has also been demonstrated already in former experiments on fragment production cross sections in Carbon at GeV proton beams [And92, And98].

The design and results within the first PISA test experiment of the BCD is presented in ref. [Bud99]. The design features of the BCD are very similar to those of Ref. [Och96] and references therein. Advantages (as e.g. resistivity to radiation damage and insensitivity to minimum-ionizing particles) of BCDs compared to alternative detectors (gas-semiconductor ionization chamber, solid state detectors, CsI(Tl)-crystal scintillators,...) are outlined in ref. [Och96]. The detector as shown in Fig. 6.10 is in principle an ionization chamber with a gas volume of 22 cm in length and 5 cm in diameter. It is sealed off at the entrance by a 3 μm thick carbon-coated mylar foil supported by a wire mesh, which will be operated at ground potential and at the rear end by an anode (printed board). The mesh supporting the entrance window is electrically connected to the cathode in order to avoid undesirable charge collection near the window. The Frish grid, which defines the ionization sampling section (2 cm from the anode), is made of 20 μm gold-plated tungsten wires with 1 mm spacing. The voltage of +1800 Volt between the Frish grid and the entrance window is divided by a resistor chain, which is connected to 9 field-shaping rings in order to maintain a homogeneous electric field over the active detector volume. All internal parts are fixed to an isolating skeleton made of plexiglass. The particles enter through the cathode and leave an ionization track parallel to the electric field. For charged, nonrelativistic particles the Bethe-Bloch formula for its specific energy losses in a

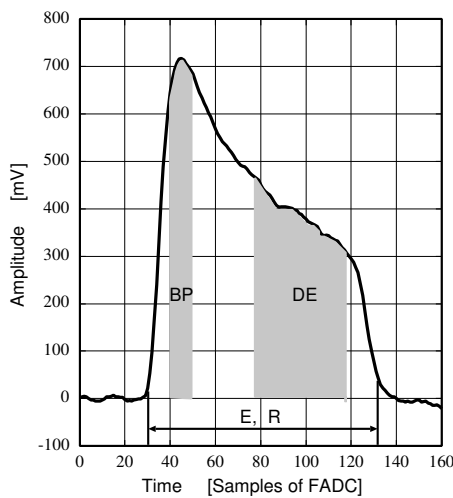


Figure 6.11: Typical output signal from BCD. The maximum of the curve gives so called Bragg peak (BP) proportional to the charge of particle. The integral over the whole length of a signal describes the kinetic energy of the particle, E . Other parameters like the range of the particle in the detector medium, R , or the partial energy losses DE can be also extracted from the shape of the curve.

given medium can be simplified to: $-dE/dx \propto cZ^2/E$, where Z, E are the atomic number and kinetic energy of the detected particle and c contains all relevant constants together with the quantities characterizing the detector medium. Since the energy loss per single collision is small, dE/dx increases slowly along the particle path. Only when the remaining energy is small dE/dx increases rapidly forming the so called Bragg Peak (BP). The electrons along the track drift through the grid and are viewed as an anode current. The output signal from the anode as function of time is proportional to the energy-loss distribution of the detected particle along its path through the detector. The atomic number of the incident detected particle is therefore related to the maximum pulse height, which corresponds to the Bragg peak and the total kinetic energy of the particle is obtained from the integration over the total output signal. The detector is filled with isobutane⁶ and operated at a pressure of about 300 mb. Practically, for a given gas pressure the voltages for anode and the Frish-grid shall be increased as long as the amplitude of the output signal is saturated and the signal length reaches the minimum. It indicates that the recombination of the electrons traveling through the detector is minimal, all of them are passing the Frish grid and are collected at the anode. The principle of Bragg curve spectroscopy is given in Fig. 6.11 where a typical output signal of a BCD is presented. The main parameters of the BCD as being used at PISA are summerized in Tab. 6.4.

Table 6.4: Main parameters of the Bragg curve detector.

Active length	200 mm
Frish grid to anode gap width	19 mm
Cathode voltage	0 V grounded
Frish grid voltage	2400 V
Anode voltage	2900 V
Number of guard rings	19
Cathode	mylar foil (3.5 μm)
Anode	mylar foil (1.5 μm)
Type of gas	Isobutane (99.9% purity)
Pressure	300 mbar

In addition to the usual charge identification by Bragg spectroscopy in the PISA experiment an isotope separation for almost all detected particles was achieved. The basic experimental information as concerns the Bragg curve detector was received from a VME-flash ADC module (CAEN Mod. V729A, 40MHz, 12bit) allowing to perform data processing of about 1000 sample Bragg curves per second. In order to test the reliability of the flash-ADC, the Bragg signals were also digitized with two standard NIM ADC modules. The output signal from the charge sensitive pre-amplifier was split into two amplifiers each with a different shaping time. While the shortest shaping time of 250 ns, which is characteristic of the electron drift time between the Frish grid and the anode, yields information on the Bragg peak of the signals, the longer shaping time of 6 μs is

⁶Since isobutane is characterized by 30% lower effective ionization potential compared to argon [Sau77] or the P10 mixture (90% of argon, 10% methane), the number of primary released electrons is increased.

related to the total drift time and corresponds to the total energy. Both amplifiers were read-out individually by standard ADCs. Data were taken with both set-ups and showed agreement within less than 1%. The principles of data acquisition and on-line analysis is subject of a forthcoming paper. If the particle was stopped in the active chamber volume, apart from the measured TOF, the following values were calculated from the pulse shape: the integral of the specific ionization over the track (total kinetic energy E of the particle), the maximum of the Bragg peak from the maximum of the specific ionization of the ion (BP proportional to Z), the duration R (corresponding to the range in the BCD gas volume) and a partial integral from the specific ionization at the beginning of the track ($\propto \Delta E/dx$). Isotope identification has been performed by using the correlations between the parameters R , E , ΔE and TOF.

The BCD is capable of measuring isotopic distributions of fragments ranging from $Z = 2$ to Si down to emission energies as low as 1 MeV/nucleon.

The phoswich detectors

While the energy and charge of the heavier spallation products ($Z \geq 3$) will be determined using Bragg curve detectors [Pisa99] combined with channel plate time-of-flight detectors [Pisa00], light spallation products ($Z = 1, 2$) will be measured by employing phoswich detectors [Pisa00] placed behind the Bragg curve detectors.

We are using the phoswich scintillation detectors of conical-hexagonal shape, produced by BICRON Corporation. The face of the detector is a 1 mm thick slow (940 ns decay time) CaF₂(Eu) scintillator - acting as an energy-loss (ΔE) detector and a 313 mm thick fast scintillator BC-412 (3.3 ns decay time) - acting as energy (E) detector. Particle identification is possible via ΔE - E technique for H- and He-isotopes. The front cross section of the phoswich detector is a hexagon of 25.2 mm diameter. In these phoswich detectors 10-stage Hamamatsu HTV 2060 photomultiplier tubes are used. Due to energy losses of particles in the "thin" slow scintillator the energy range of correctly detected light particles is 15-150 MeV/nucleon.

Preliminary experimental results will be shown in Section 7.2.

6.4 The JESSICA experiment

6.4.1 Objective

The design and construction of the world's largest and most ambitious pulsed spallation neutron system, the 5 MW average beam power ESS undoubtedly requires experimental prototyping of its major and most crucial technical components such as the heart of the machine, the neutron target station itself. JESSICA (Jülich Experimental Spallation Target Setup in Cosy Area) is a 1:1 sized ESS target/reflector/moderator mock up (as schematically shown in the right panel of Fig. 2.6 on page 18) and test facility for advanced cold moderators for high-power spallation neutron sources installed at the Jülich proton beam cooler synchrotron COSY. It aims at an optimized geometry and composition of the target/reflector material and further on neutronic performance data of ambient temperature and advanced cold moderators such as solid methane for a high-power spallation

target. With the JESSICA experiment the neutronic performance will be measured by means of neutron time of flight and scattering techniques [Nue02a, Nue02b]. Very much the same as for the previously described NESSI experiment, all results of the JESSICA experiment are important data to validate the simulation models and code systems which are used to optimize the layout of high power spallation target systems. JESSICA is an international joint collaboration of the world's leading laboratories producing and utilizing pulsed neutron beams. Settling the JESSICA experiment at Jülich is well justified by the profound expertise of the Forschungszentrum in the design of high power spallation targets [Bau81, Bau85].

6.4.2 Advanced moderators at JESSICA

Cryogenic moderators are an essential ingredient for pulsed spallation neutron sources, because they a) provide the much demanded long wavelength neutrons in sufficient quantities and b) generate short pulses in the thermal neutron energy regime by shortening the life time of the neutrons in this interval by continued slowing down to lower energies. Presently short pulses at ambient temperature moderators are generated by adding absorbing material into the moderator, which is at the expense of $\approx 40\%$ of the peak intensity. Research reactors are operated with cold hydrogen or deuterium moderators whose advantage is a time-independent high flux of cold neutrons involving low radiation damage. Deuterium has the advantage of a good scattering quality combined with low absorption. But because of the mean free path of the neutrons of ≥ 100 mm in D_2 bigger moderator volumes than with hydrogen are necessary. In H_2 collisions are frequent (mean free path ≤ 20 mm) but absorption of neutron is higher by a factor of 300. Consequently for short pulsed spallation sources like the anticipated SPTS option for ESS, H_2 and in particular D_2 are less suited since they lead to pulse broadening due to inadequate slowing down properties. Activation in hydrogen is lower than in deuterium, because tritium is formed only from the ≈ 140 ppm deuterium normally present in hydrogen. The use of hydrogen as moderator poses a further problem: the ortho-para conversion. At room temperature only one fourth of the H_2 molecules is of para-type, but with lower temperatures the equilibrium moves to higher concentrations of para- H_2 . At 25 K more than 98% of the molecules are para-hydrogen. With each conversion of an ortho- to para- molecule 1.47 meV are released (at 25 K). Below a neutron energy of 100 meV the mean neutron scattering cross section depends strongly on the ratio of ortho and para H_2 as is shown in ref. [Axm84], where scattering cross sections are given for para- H_2 and a mixture of 50% para- and ortho- H_2 . The most favorable moderator material for neutrons is considered to be methane, in the liquid form for 100 K moderators and in solid form for 20 K moderators. Early the advantages of methane as compared to hydrogen have been recognized [Car90]. The proton density (protons/ \AA^3) for H_2 and CH_4 at 20 K is 0.042 and 0.079, respectively. These numbers show that methane represents a dense source of hydrogen. Additionally, because of rotational freedom of the molecules, methane will effectively exchange energy with even low-energy neutrons. It has been postulated though, that in solid methane due to lattice bonds only a part of the molecules are available for rotational modes. One of the goals of the JESSICA experiment will be to measure the performance of possible moderator materials under terms that are similar to ESS conditions. The experimental

program of JESSICA includes studying different moderator concepts, as thermal and cold moderators. Neutron energies expected for different moderator types are summarized in Table 6.5. The Energy E and wavelength λ of the neutron are related via the de Broglie

Table 6.5: Nomenclature of neutron energies.

Moderator Type	Energy of neutrons
very cold/ultra cold	≤ 0.5 meV
cold	0.5-2 meV
thermal	2-100 meV (about 25 meV)
epi-thermal	0.1-1 eV
resonance	1-100 eV

relation $E = h^2/(2m_n\lambda^2)$, where h is the Planck constant and m_n the neutron mass. The terms “thermal” and “cold” are used to characterize a neutron’s energy. Neutrons of low energies can be obtained by slowing them down to thermal equilibrium in matter at ambient (“thermal”) or low temperature (e.g. liquid hydrogen at 20 K, “cold”).

Most effective cold moderator systems in terms of slowing down properties [Bau97] and intensity are presently based on solid methane showing in particular for energies below 0.01 eV a supremacy of a factor of two to three as compared to conventionally used liquid hydrogen as demonstrated by K. Inoue et al. [Ino74, Ino76, Ino79] and illustrated in Fig. 6.12.

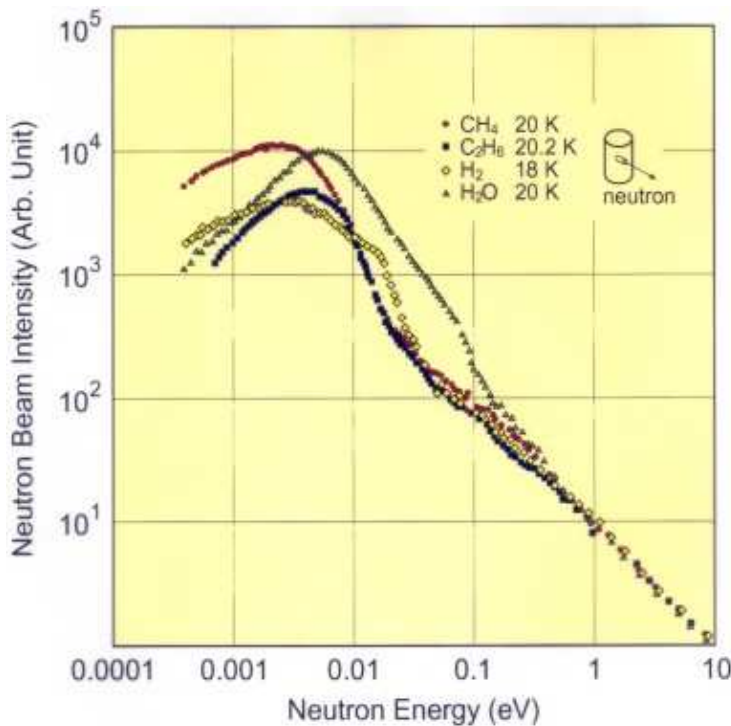


Figure 6.12: Measured neutron energy spectra (normalized in the energy region above 1 eV) for various cold moderators. The experiment was however carried out at an electron accelerator. (Fig. adopted from ref. [Ino79])

Also an ice moderator at 20 K yields higher neutron fluxes in the regime between 0.001 and 0.1 eV as compared to liquid hydrogen at similar temperature. In contrast to our proton induced spallation reactions at JESSICA the experiments carried out by

K. Inoue et al. took place at an e^- -accelerator. A 45 MeV e^- beam strikes a heavy metal target (W or Pb). There the deceleration of the e^- causes bremsstrahlung in an energy range of the resonance for (γ, n) -reactions. The generated fast neutrons were moderated in the adjoining moderators. In contrast to JESSICA no reflector was installed and a moderator geometry quite different has been used. Measurements of thermal neutron flux as a function of position in H_2O and D_2O moderators surrounding a variety of thick targets and bombarded by protons in the energy range 540 to 2000 MeV have also been performed by W.A. Coleman et al. [Col68].

Methane hydrate is regarded as an alternative to solid methane and expected to combine the advantages of ice and methane. Gas hydrates are ice-like crystalline structures of a water lattice with cavities which contain guest gases. They are bound by Van der Waals forces under low temperature and moderate pressures. The guest molecule is necessary to support the cavity. In the natural environment methane is the most common guest molecule [Slo90]. Furthermore it is being considered to use methane absorbed on porous bodies such as zeolites or porous polymer spheres. This could substantially simplify the production process and handling of the moderator pellets. Irrespective of the neutronic properties of the different moderator pellets, their mechanical properties are to be evaluated since the pellets are exposed to considerable mechanical loads during transport in the moderator system. Another task is to evaluate the behavior in the radiation field with respect to energy built-up, polymerization processes and the formation of radioactive isotopes. However technical problems of methane moderators are:

- Methane is radiolysed under irradiation. Thereby energy is stored in the radicals formed and must be removed at regular intervals. This can be achieved by temperature increase [Car87], but the procedure interrupts measuring time for the user.
- Radioactive isotopes are formed from the C-atoms of methane (or other organic substances) due to spallation. Known isotopes with half-lives larger than 1 minute are ^{11}C (20 min.), 7Be (53.4 d), 3H (12.3 a) and ^{10}Be (1.6×10^6 a).
- Neutron radiation leads to polymerization reactions in methane forming wax-like alkanes which deteriorate the moderator properties and also deposit in the moderator system. Experiments are under way to slow down the formation rate of wax-like alkanes by adding further substances (e.g. propane) [Bro97].
- The heat conductivity of solid methane is low (≤ 1 mW/cmK). Due to the high heat generation in ESS moderators (≈ 7.5 kW), solid methane cannot be used as a compact block because the heat cannot be removed fast enough [Wil88].

In order to prevent the distribution of wax-like polymers in the moderator and piping system, CH_4 is used as a solid, which is removed without melting so that system contamination is prevented. For this purpose it is proposed to use methane in form of small pellets of spherical shape. The spent methane pellets are separated from the transport fluid and either purified, reused or discharged over the stack. Depending on the kind and amount of radioactive isotopes in the methane retentive measures may have to be considered. A comprehensive compilation on the thermodynamical and mechanical properties of

solid methane moderators and radical formation or chemical reactions under irradiation is published in ref. [Bar02].

Any of the proposed moderator candidates, let it be solid methane pellets, methane hydrate or zeolites containing methane will be in liquid hydrogen for cooling, but due to the low beam intensity at COSY in particular for JESSICA a cooling flow will not be necessary. The type of moderator ultimately selected results from neutronic and technical aspects, to enable the safe and functional handling of the moderator pellets and, at the same time, satisfy the neutronic requirements.

Typical slow neutron pulse shapes are asymmetric with a sharp rising and a slow trailing edge, the latter revealing the neutron life time in the moderator. In many cases these long pulse trails spoil the full exploitation of the short proton pulses because neighboring diffraction peaks would strongly overlap. In order to cut the neutron pulse trails the neutron life time has to be shortened which can be achieved by poisoning and/or decoupling the moderator. Poisoning is most effectively done by inserting neutron absorbing sheets into the moderator, whereby the moderator is made smaller “neutronically”. In other words, neutron diffusion between adjacent parts is suppressed and the neutron life time shortened. Decoupling from the reflector is achieved by placing another slow neutron absorbing layer around the moderator in such a way, that slow neutrons scattered back from the reflector cannot reenter the moderator which again acts as a life time shortening. The peak intensity of the neutron pulses is only slightly diminished by this “tailoring” of the moderator, while the integral intensity in contrast is reduced by about an order of magnitude.

6.4.3 Experimental setup and method

The JESSICA target system is installed in an external area of the COoler SYnchrotron in Jülich as shown in Fig. 6.1 on page 64. Because of its low proton beam intensity COSY is particularly suitable for studying the neutron performance of advanced moderators, whereas radiolysis, high activation levels and background are negligible. Furthermore, only moderate shielding is necessary and the whole prototyping experiment is much easier to accomplish without any lack of scientific quality of the results. The principal arrangement resembles very much the target station of ESS. The proton beam is extracted from COSY and led through an upstream area of beam diagnostic equipment (an integrating current transformer–ICT and a wall current monitor–WCM as shown in Fig. 6.13) where for proper normalization of the data its intensity, position and spatial distribution profile is monitored simultaneously. A scintillator start detector placed right in front of the target/moderator/reflector assembly serves as a trigger for the acquisition system. The JESSICA target is located downstream just in front of a proton beam dump. The ESS-type stainless steel container is placed right in the beam and filled with approximately 35 liters of liquid Hg surrounded by a 1.5 m diameter solid Pb reflector providing space for 4 moderators and beam extraction tubes (cf. Fig. 2.6 on page 18). In contrast to the ESS, the liquid is stationary here. One moderator position will be used for the various moderator types for high intensity spallation sources. The other three positions remain idle to simulate realistic flux disturbance inside the reflector. The reflector consists of 4 tiers with 2-4cm diameter lead-rods. The gaps may be filled with polyethylene to simulate

the coolant (currently not done in the present experiment). The moderators are located in wing geometry, i.e. the neutron beam tubes do not view the target through the moderator directly in order to reduce the fast neutron background considerably. The moderator surfaces are oriented perpendicular to the neutron beam axes in order to conserve the time structure of the neutron pulse. Neutrons primarily produced by spallation reactions in the Hg-target and subsequently slowed down in the moderator are lastly extracted through beam holes of JESSICA. For both spectra- and time structure measurements an evacuated and shielded time-of-flight tube of about 5 m length is used as schematically shown in Fig. 6.13.

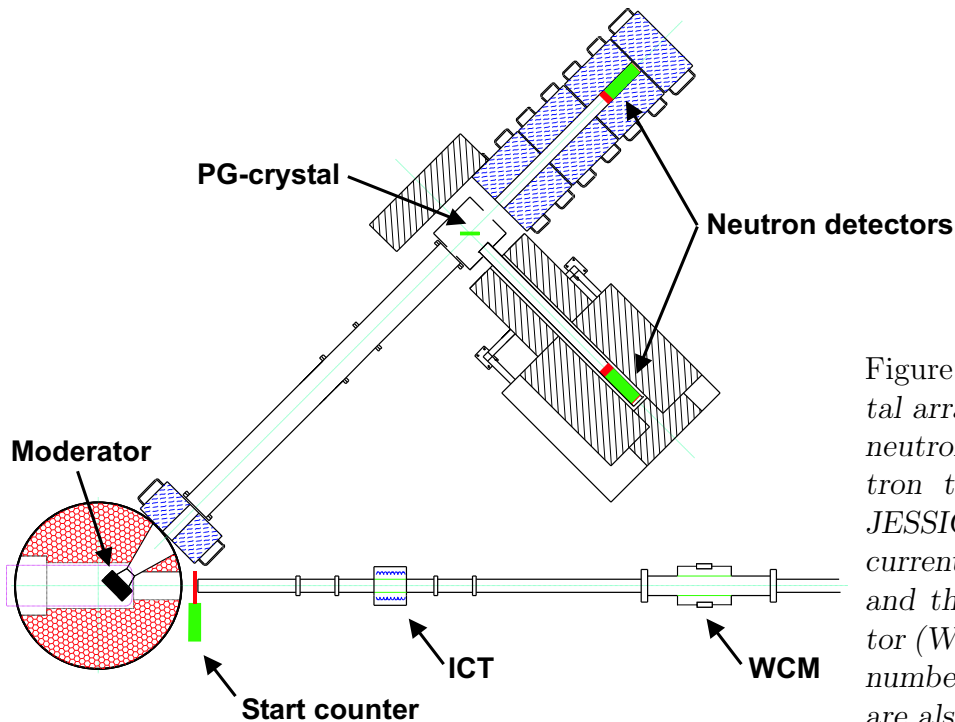


Figure 6.13: *Experimental arrangement to measure neutron spectra and neutron time distributions at JESSICA. The integrating current transformer (ICT) and the wall current monitor (WCM) for counting the number of incoming protons are also indicated.*

Thermal and cold neutron energy distributions will be measured by aligning the flight path onto the reflector beam hole axis. Either a ^3He proportional counter or a faster ^6Li -doped scintillator [Sch83, Jan92] is placed at the end of the time-of-flight tube directly viewing the moderator face (see Fig. 6.13). The latter one has a high efficiency of 0.5 at 330 meV neutron energy and more than 90% for thermal neutrons. The minimum time between two counts must not be less than 400 ns, the detector is insensitive to gamma particles. For spectral measurements it is placed 4.6 m off the moderator surface. Fig. 6.14 shows the JESSICA apparatus installed at COSY.

The determination of the time structure of the neutron pulses will be accomplished by placing an [002]-oriented pyrolytic graphite crystal into the beam path, which will according to Bragg's law

$$n\lambda = 2d_{[002]} \cos \theta, \quad n = 1, 2, 3, \dots \quad (6.1)$$

select certain well-defined neutron wavelengths, i.e. $\lambda, \lambda/2, \lambda/3, \lambda/4, \dots$, from the incident spectrum. These neutrons are diffracted off the incident direction by an angle 2θ into

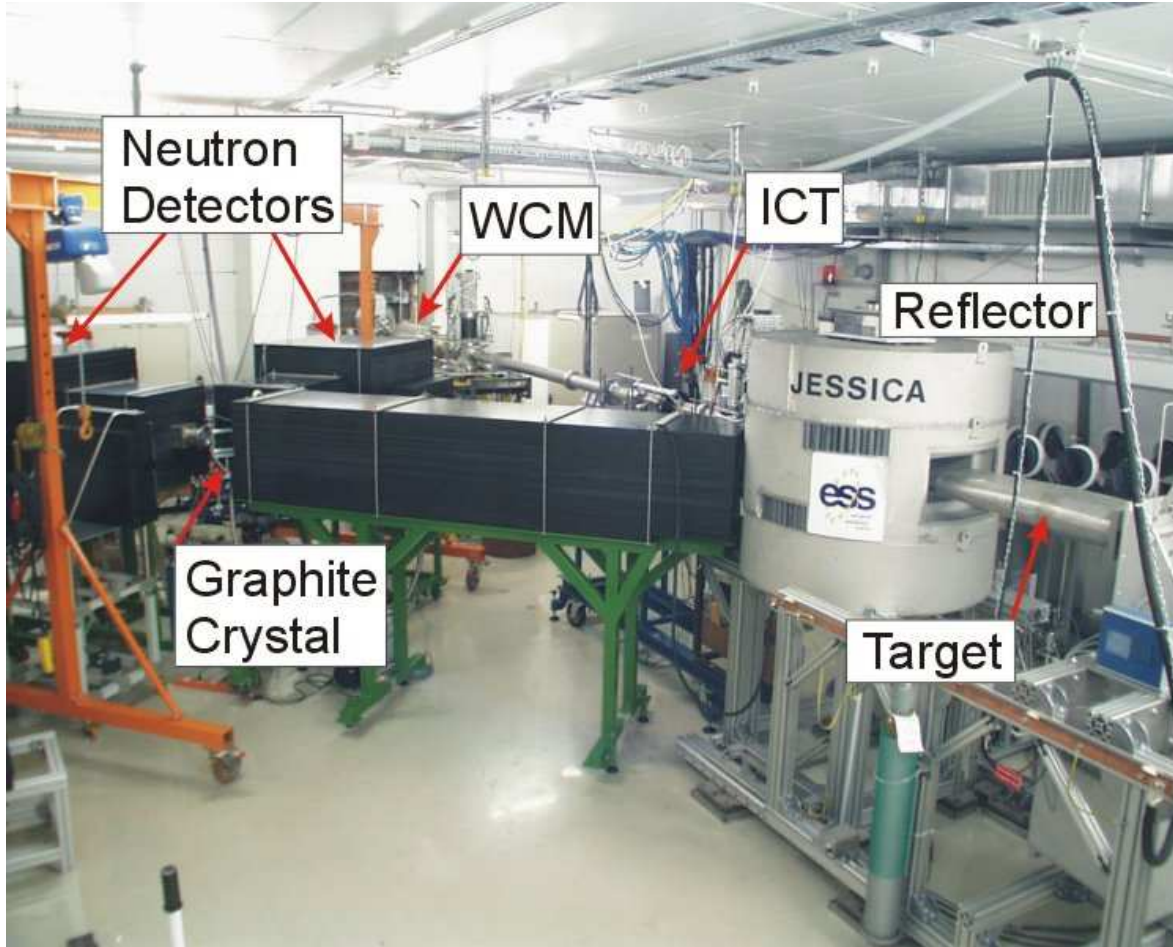


Figure 6.14: *JESSICA* apparatus at *COSY*.

the secondary time-of-flight tube, which therefore has to be positioned so as to fulfill the Bragg condition of equal incident and reflected angles θ . If selected according to their time-of arrival at the detectors, neutrons of different wavelengths are distinguished by assignment to different orders $[002_n]$ of crystal reflections. Different sets of neutron wavelengths might be selected by choosing different crystal reflection angles. It is an important advantage of the current experiment that the time structure of neutron pulses can be determined in dependence of their kinetic energy and the life times of neutrons in the moderator can be well disentangled from the time-of-flight. In order to minimize the uncertainty in the determination of these times the experimental resolution is optimized by a time-focusing arrangement of the moderator, reflecting crystal and detector face. Therefore the moderator surface, the reflecting planes of the monochromator crystal and the sensitive detector area have to be in parallel to each other as well as both the primary and the secondary flight paths have to be equal. The total flight path has to be long enough and the sensitive part of the detector small enough in order to match the time focusing quality [Car02] imposed by the parallel arrangement of the components. Intrinsic time uncertainties of less than $1 \mu\text{s}$ are well accepted relative to the calculated half width of about $25 \mu\text{s}$ of the slow neutron pulse from an ambient temperature water moderator.

Experimental results will be shown and compared to simulations in Section 7.4.

Chapter 7

Results and comparison with theory

In the following three sections (7.1, 7.2 and 7.4) the comparison between experimental results and model calculations is performed. The emphasis is on the NESSI and PISA nuclear data while for the JESSICA campaign first beam times show a promising future for a scientific programme. For the new PISA project, here only preliminary data and to some extent first results are reported. They will be complementary to the results of NESSI in the sense that energy spectra will be extended to a region so far not accessible at NESSI and isotopic resolution of light heavy fragments released after a nuclear reaction will be improved. Due to the fact that PISA is placed in the internal ring of COSY the effective intensity of the proton beam is orders of magnitude larger than for external experiments¹. This allows for employing very thin targets (low reaction probability) while enabling the measurements of fragments without any significant energy loss within the target.

7.1 Results NESSI Experiment/Theory

In the present section, predictions by the models discussed above are compared to relevant experimental observations made in NESSI experiments. The study on thick target measurements (sect. 7.1.1) considers data on reaction probabilities P_{Reac} , hadronic interaction length, average neutron multiplicities with reference either to the number of neutrons generated per reaction M_n or per incident proton M_n/p , and in particular neutron multiplicity distributions as obtained with 15-cm diameter Hg, Pb, and W targets bombarded with 0.4, 0.8, 1.2, 1.8, and 2.5 GeV protons. Due to the multitude of possible interlinkings of these models and the plurality of adjustable options and parameters within these codes here only a representative selection is executed. Thin target measurements (sect. 7.1.2) are performed in order to improve the understanding of the primary spallation process, the way nuclei are excited, the energy dissipation and the subsequent nuclear decay modes.

¹For internal experiments protons are circulating and therefore have multiple chance to interact with the target. For external beam there is only “one” chance and protons are lost in the beam dump when not interacting.

7.1.1 Thick targets

The light signal of the BNB

As described in chapter 6.2, the *prompt* light signal E_{sum} preceding the *delayed* neutron capture arises from the sum of kinetic energies of all kind of reaction products entering the BNB. In addition to the neutrons charged particles and γ quanta contribute. Since the threshold for detecting the prompt light flash is as low as 2 MeVee (electron equivalent), a nuclear reaction is characterized by the occurrence of a prompt light signal larger than this threshold, even if there are no neutrons released in the reaction at all. The complex measured correlation between the neutron multiplicity M_n and E_{sum} in the BNB is shown for 0.8, 1.2 and 2.5 GeV proton-induced reactions on Pb targets of different thicknesses in Fig. 7.1. For fixed target thickness and incident proton energy, the larger E_{sum} the smaller the measured M_n . This is due to the high energy particles generally producing more light in the scintillator than evaporative neutrons or γ -particles. The less energy these “fast” particles deposit in the target, the less effective the nuclei are heated during the intra- and inter-nuclear cascade and the less neutrons are finally evaporated. On the expense of the prompt light signal for fixed incident energy of the proton M_n increases with increasing target thickness, as also demonstrated in Fig. 7.1.

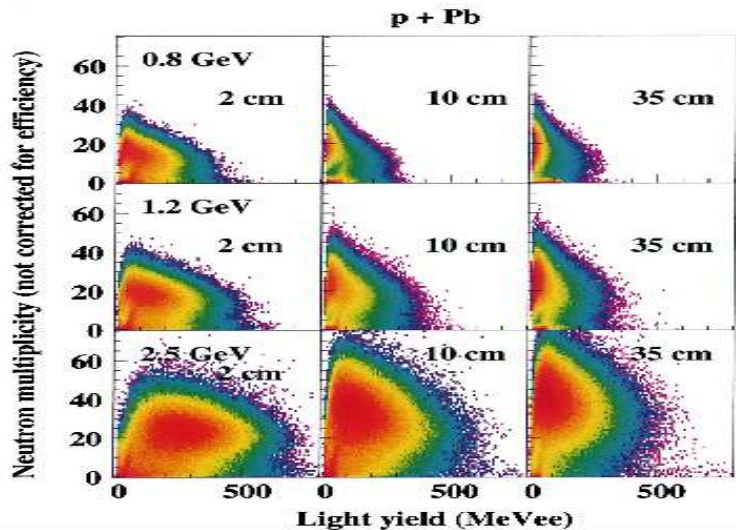


Figure 7.1: Neutron multiplicity M_n vs prompt light E_{sum} of the BNB in MeVee (electron equivalent) for proton induced reactions on 2, 10 and 35 cm thick Pb-targets of 15 cm diameter at 0.8, 1.2 and 2.5 GeV. The color-code is normalized to the same intensity for all distributions (in a.u.) in order to directly compare the yield, respectively.

Consequently for thick targets the major contribution of the prompt light signal rises from evaporative neutrons and γ -particles. Thereby low quenching factors for low energy neutrons scale the light signal down. In other words the originally available energy is converted quite efficiently into the production of neutrons in targets of several nuclear interaction lengths.

Reaction cross section and hadronic interaction length

For measurements using the 4π sr BNB detector in conjunction with thick targets with thicknesses and radii of the order of several centimeters, the key observables are the neutron multiplicity M_n (measured eventwise!) and the reaction probability P_{Reac} . P_{Reac} is deduced from the ratio of the number of triggered events (cf. sec. 6.2.4) divided by the

number of incident protons counted by detector S_1 (see Fig. 6.2, page 67). Moreover, since the incident protons were individually counted and since the BNB has a very low detection threshold (2 MeVee), the neutron multiplicity could be related to both, reaction events and to incident proton events.

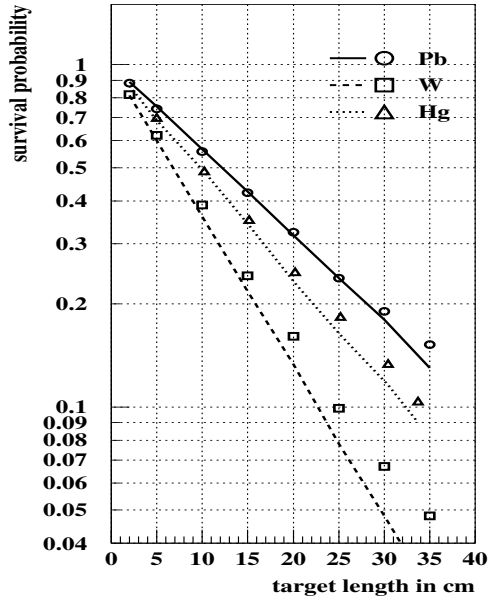


Figure 7.2: Measured (symbols, [Let00]) and calculated survival probabilities ($1 - P_{\text{Reac}}$) of the incident proton as a function of target length for 2.5 GeV $p+\text{Pb}$, Hg of 15 cm diameter and W-cylinders of 8 cm diameter. Straight lines are HERMES calculations.

Figure 7.2 illustrates the dependence of the proton survival probability ($1 - P_{\text{Reac}}$) on target thickness. The data are for 2.5 GeV incident protons and for W, Hg, and Pb target cylinders of 15-cm diameter. As seen in this figure, the experimental data are well represented by HERMES calculations. The latter follow quite accurately the exponential law $1 - P_{\text{Reac}} = \exp(-L/L_{\text{Reac}})$, where L is the target length and L_{Reac} is the interaction length found to be 10.0, 14.1, and 17.9 cm, for W, Hg, and Pb targets, respectively. These hadronic interaction lengths resulting from the Monte-Carlo calculations agree with published experimental values [Let00] of 10.84 ± 0.2 , 15.06 ± 0.3 , and 18.00 ± 0.3 cm, respectively. As a consequence of the constancy of the nucleon-nucleus cross section above some 100 MeV, the slope of the exponentials does not depend on the incident kinetic energy of the projectile. The difference in the slope for the three different materials originates mostly from their dissimilarity in density and much less from different reaction cross sections. For 35 cm length, ($1 - P_{\text{Reac}}$) approaches the 10% level in Pb and the 1% level in W, while the range due to electronic interaction is as large as 170 and 97 cm for 2.5 GeV protons in Pb and W, respectively.

P_{Reac} is used to deduce the reaction cross sections $\sigma_{\text{Reac}} = \ln(1 - P_{\text{Reac}})A/(L\rho d)$ with A, ρ, d and L being the mass, density and thickness of the target and L the Avogadro number. The experimental reaction cross sections deduced from the measured P_{Reac} , amount to $\sigma_{\text{Reac}} = 1.46 \pm 0.03$, 1.64 ± 0.05 and 1.69 ± 0.03 b for the three W, Hg and Pb targets, respectively. These values are slightly smaller than the results of the HERMES calculations of 1.62, 1.71 and 1.73 b for W, Hg and Pb, respectively.

An agreement of the same order of magnitude is found when the LCS2.70 and MCNPX codes were used instead of the HERMES code, demonstrating that the description of the

observable σ_{Reac} poses no challenge to any of these codes. The above analysis is reflected also in Tables 7.1 through 7.3 for different target thicknesses (lengths) and the incident proton energies of 1.2, 1.8 and 2.5 GeV.

Neutron multiplicities

The term “neutron multiplicity” comprises all neutrons originating from primary and succeeding secondary reactions within the target material. As a matter of fact in the thick target measurements only *neutron leakages* can be observed. The *neutron yield* is not accessible in any experiment since it reflects the neutron production at the point of origin when the neutrons are created whereas the leakage spectrum can be measured as leaking neutrons from the target surface after they have left the target material.

Mean neutron multiplicities

In Fig. 7.3 M_n/p is plotted vs. the lengths of the lead, mercury, and tungsten target cylinders, respectively, and for the two incident energies of 1.2 and 2.5 GeV, as obtained in the NESSI experiments (triangles). As expected, for every target, the mean multiplicity increases with increasing target length, albeit in a non-linear fashion. Theoretical predictions (dashed lines) with the HETC+MORSE software package are compared in this figure to experimental data. Experiment and predictions include neutrons from both, the primary and secondary reactions. The calculations also account for the fact that neutrons are slowed down in the target material. Both, fission and elastic scattering were included. All other options have been chosen according to the standard set of parameters as summarized in Tab. 4.1.

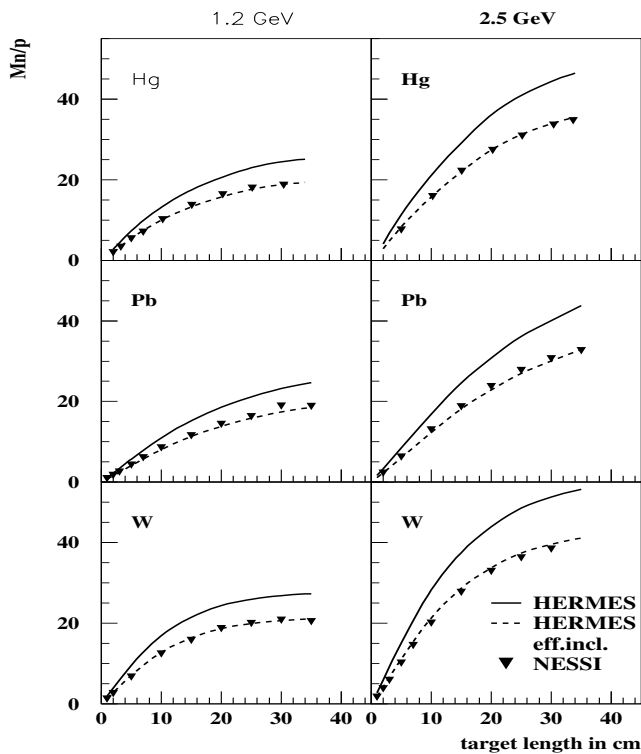


Figure 7.3: Average neutron multiplicity produced per incident proton M_n/p as a function of target thickness (diameter 15cm) for 1.2 and 2.5 GeV p+Hg, Pb and W. Solid line: HETC+MORSE, dashed line: HETC+MORSE with detector efficiency taken into account; the triangles represent the experimental data of NESSI as published in ref. [Let00]. For experimental neutron multiplicities normalized per reaction see also Tables 7.1 to 7.3.

The solid curves in Fig. 7.3 correspond to the predictions for the mean neutron (leakage) multiplicity per incident proton. In the case of the mercury target the simulation calculations also account for the 1-mm thick walls of the stainless steel capsules holding the liquid Hg.

As seen in Fig. 7.3, the model calculations agree very well with the experimental observations, over a wide range of target geometries and target materials. The observed increase in the neutron multiplicity with increasing target length is due to an increase of the reaction probability, P_{Reac} and, to a lesser extent, to an increase of secondary reactions with the target length.

A more complete and systematic comparison of the experimental and model average neutron multiplicities $\langle M_n \rangle$ and reaction probabilities P_{Reac} is presented in Tables 7.1 to 7.3 for different energies and target materials. For the sake of completeness, these tables include also the simulated mean neutron multiplicities, not corrected for the BNB neutron detection efficiency. These “true” multiplicities are denoted as $\langle M_n^c \rangle$ and shown as solid lines in Fig. 7.3. Numbers in parenthesis represent the root mean square (RMS) or standard deviation of the distributions, respectively. The agreement between calculation and experiment for the second moment of the distributions within a few percent gives additional confidence to the program packages under consideration. The statistical error of calculated mean values is typically of the order of 1%.

The comparison between theory and experiment will be separately discussed for Hg, Pb and W in the following.

Neutron multiplicity distributions

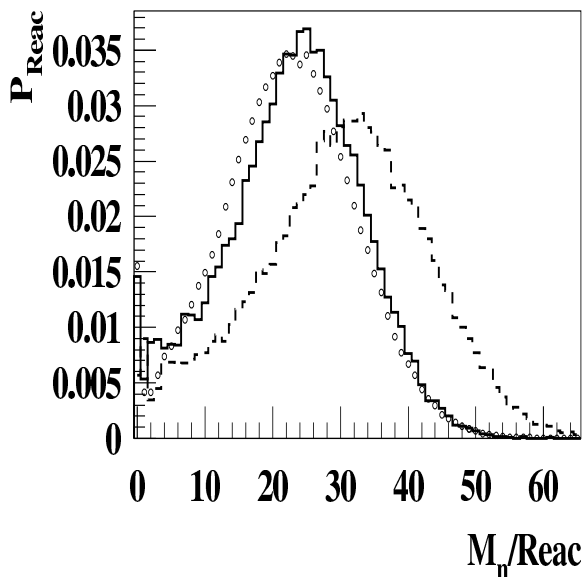


Figure 7.4: Influence of the detector efficiency ε (cf. Fig. 6.4) on the theoretical data obtained with GCCI (LCS) for a 35 cm long lead rod (diameter 15 cm) bombarded with 1.2 GeV protons. The dashed histogram represents MC-data while the solid histogram shows efficiency folded data. The open circles are the experimental data corrected for acquisition dead-time and background, but not for efficiency.

A typical, bell-shaped, experimental neutron multiplicity distribution is shown as open circles in Fig. 7.4. Here, P_{Reac} is plotted vs. the number of neutrons generated per reaction. When corrected for the finite neutron detection efficiency (cf. Fig. 6.4), the results (dashed line) of the theoretical Monte Carlo simulation calculations (solid line) are

Table 7.1: Average neutron multiplicities $\langle M_n \rangle$ and reaction probabilities P_{Reac} for a cylindrical mercury target of 15 cm diameter bombarded with protons of various energies, E_p . $\langle M_n^c \rangle$ are average neutron multiplicities before having taken detector efficiency into account. The root mean square (RMS) of the distributions is given in parenthesis. For the calculations the standard parameter set was used.

Length	HERMES			LCS2.70			MCNPX			Experiment	
	$\langle M_n \rangle$	$\langle M_n^c \rangle$	P_{Reac}	$\langle M_n \rangle$	$\langle M_n^c \rangle$	P_{Reac}	$\langle M_n \rangle$	$\langle M_n^c \rangle$	P_{Reac}	$\langle M_n \rangle$	P_{Reac}
$E_p = 1.2\text{GeV}$											
5 cm	17.2 (10.0)	23.0 (13.0)	0.313	18.0 (10.6)	24.2 (13.6)	0.310	18.1 (10.6)	24.2 (13.6)	0.315	16.9 (9.6)	0.313
15 cm	19.9 (10.3)	26.1 (13.1)	0.660	21.2 (10.9)	27.6 (13.7)	0.664	21.2 (10.9)	27.7 (13.4)	0.660	20.5 (9.6)	0.645
30 cm	21.2 (9.8)	27.5 (12.2)	0.889	22.4 (10.3)	29.0 (12.9)	0.875	22.5 (10.3)	29.1 (12.9)	0.885	21.9 (9.6)	0.847
$E_p = 1.8\text{GeV}$											
5 cm	21.9 (13.0)	29.5 (17.2)	0.315	23.4 (14.0)	31.5 (18.3)	0.311	22.0 (13.2)	29.9 (17.3)	0.313	21.7 (12.0)	0.296
15 cm	26.5 (13.8)	34.9 (17.8)	0.663	28.5 (14.8)	37.5 (18.9)	0.667	27.4 (14.1)	36.2 (18.0)	0.657	27.6 (12.9)	0.640
30 cm	29.6 (12.9)	38.6 (16.4)	0.886	31.9 (13.9)	41.4 (17.6)	0.874	30.6 (13.2)	40.0 (16.7)	0.887	30.6 (12.0)	0.851
$E_p = 2.5\text{GeV}$											
5 cm	26.1 (16.0)	35.5 (21.5)	0.314	28.5 (17.6)	38.6 (23.4)	0.310	27.1 (16.7)	36.8 (22.1)	0.310	25.1 (14.5)	0.301
15 cm	33.2 (17.6)	43.9 (22.9)	0.663	36.3 (19.1)	47.9 (24.6)	0.664	35.0 (18.2)	45.7 (23.0)	0.655	33.7 (15.9)	0.647
30 cm	38.5 (16.5)	50.3 (21.1)	0.887	41.5 (18.0)	54.2 (22.0)	0.874	40.1 (17.1)	51.6 (21.2)	0.884	38.4 (15.0)	0.866

seen to reproduce the data very well. Both, average position and shape of experimental and simulated distributions correspond well to each other. Note the specific strength of the NESSI experiment being able to provide even the probability to measure $M_n = 0$ neutrons in rather nice agreement with the simulated value. As can be seen from Fig. 7.4, the finite detection efficiency of the BNB neutron detector has a significant effect on outcome of the measurements and needs to be accounted for in comparisons of theoretical calculations with experimental data. As for example for 1.2 GeV protons on Pb the calculations show

Table 7.2: same as Tab. 7.1, but for Pb.

Length	HERMES			LCS2.70			MCNPX			Experiment	
	$\langle M_n \rangle$	$\langle M_n^c \rangle$	P_{Reac}	$\langle M_n \rangle$	$\langle M_n^c \rangle$	P_{Reac}	$\langle M_n \rangle$	$\langle M_n^c \rangle$	P_{Reac}	$\langle M_n \rangle$	P_{Reac}
$E_p = 1.2\text{GeV}$											
2 cm	14.6	20.3	0.107	15.1	21.0	0.107	15.2	21.0	0.106	14.5	0.113
	(8.5)	(11.5)		(8.5)	(11.1)		(8.7)	(11.7)		(8.6)	
15 cm	19.6	25.9	0.579	20.5	27.1	0.575	20.5	27.1	0.567	20.2	0.571
	(10.1)	(12.9)		(10.2)	(12.9)		(10.4)	(13.3)		(10.2)	
35 cm	21.4	27.9	0.867	22.2	29.0	0.863	22.1	28.8	0.859	22.2	0.848
	(9.7)	(12.2)		(9.8)	(12.3)		(10.0)	(12.6)		(9.9)	
$E_p = 1.8\text{GeV}$											
2 cm	18.0	25.3	0.109	18.9	26.5	0.107	18.7	26.3	0.107	17.7	0.113
	(10.8)	(14.9)		(10.7)	(14.2)		(11.1)	(15.3)		(10.4)	
15 cm	25.3	33.7	0.580	27.1	36.0	0.576	27.1	36.1	0.574	26.2	0.577
	(13.4)	(17.4)		(13.7)	(17.3)		(14.1)	(18.2)		(13.2)	
35 cm	29.2	38.4	0.869	31.2	40.9	0.864	31.4	41.2	0.861	30.5	0.853
	(12.8)	(16.3)		(13.0)	(16.2)		(13.4)	(17.1)		(12.7)	
$E_p = 2.5\text{GeV}$											
2 cm	21.3	30.3	0.108	22.3	31.7	0.107	22.3	31.8	0.107	19.4	0.117
	(12.9)	(18.3)		(13.0)	(17.2)		(13.6)	(19.2)		(12.3)	
15 cm	31.7	42.5	0.580	34.1	43.7	0.571	33.9	44.7	0.575	32.3	0.577
	(16.8)	(22.1)		(17.3)	(20.5)		(18.0)	(23.0)		(16.3)	
35 cm	37.7	49.7	0.865	40.5	50.5	0.860	40.4	52.2	0.861	38.4	0.848
	(16.3)	(21.0)		(16.6)	(19.0)		(17.2)	(21.3)		(15.6)	

that *independent of the target thickness* 80% of the total neutron leakage stem from the evaporation process. Especially the remaining 20% of higher kinetic INC-neutrons are detected with low efficiency.

Hg: As far as average values and Hg targets (Tab. 7.1, Fig. 7.3) is concerned, for all Monte Carlo codes considered here, one observes good agreement with the experimental results. Discrepancies between model calculations and experimental data are generally less than 5 % for both, P_{Reac} and $\langle M_n \rangle$, and a broad range of energies. The maximum discrepancy is 7.4 % in the case of the 5 cm Hg target bombarded with 2.5 GeV protons.

In Fig. 7.5 experimental neutron multiplicity distributions induced by 1.2 and 2.5-GeV protons, respectively in cylindrical mercury targets of various lengths are compared to the predictions of the codes HERMES and MCNPX.

Table 7.3: same as Tab. 7.1, but for W.

Length	HERMES			LCS 2.70			MCNPX			Experiment	
	$\langle M_n \rangle$	$\langle M_n^c \rangle$	P_{Reac}	$\langle M_n \rangle$	$\langle M_n^c \rangle$	P_{Reac}	$\langle M_n \rangle$	$\langle M_n^c \rangle$	P_{Reac}	$\langle M_n \rangle$	P_{Reac}
$E_p = 1.2\text{GeV}$											
2 cm	15.0	20.5	0.187	16.3	22.2	0.183	16.1	22.0	0.184	14.8	0.174
	(9.0)	(11.8)		(9.2)	(11.9)		(9.4)	(12.4)		(8.5)	
15 cm	20.9	26.9	0.784	22.6	29.0	0.780	22.5	28.9	0.781	21.6	0.729
	(10.2)	(12.7)		(10.6)	(13.1)		(10.6)	(13.2)		(10.2)	
35 cm	21.6	27.6	0.971	23.4	29.9	0.969	23.4	29.8	0.964	22.6	0.902
	(9.4)	(11.7)		(9.9)	(12.2)		(9.9)	(12.3)		(9.2)	
$E_p = 1.8\text{GeV}$											
2 cm	18.8	25.9	0.184	20.6	28.3	0.184	20.5	28.2	0.184	17.9	0.179
	(11.6)	(15.6)		(12.1)	(15.6)		(12.5)	(16.8)		(10.5)	
15 cm	28.5	36.9	0.786	31.5	40.5	0.780	31.5	40.7	0.786	28.9	0.747
	(13.8)	(17.4)		(14.5)	(17.8)		(14.7)	(18.5)		(12.9)	
35 cm	31.7	40.6	0.971	35.0	44.5	0.970	35.0	44.8	0.972	31.4	0.940
	(12.0)	(15.0)		(12.5)	(15.2)		(12.8)	(15.9)		(11.4)	
$E_p = 2.5\text{GeV}$											
2 cm	22.8	31.7	0.186	24.9	34.2	0.186	24.7	34.3	0.186	20.5	0.183
	(14.3)	(19.5)		(15.0)	(19.2)		(15.5)	(21.2)		(12.7)	
15 cm	36.7	47.6	0.782	40.6	48.4	0.780	40.7	52.7	0.781	36.6	0.758
	(17.9)	(22.8)		(18.7)	(21.0)		(19.4)	(24.7)		(16.5)	
35 cm	42.3	54.4	0.973	47.0	55.7	0.945	47.3	60.6	0.973	41.6	0.952
	(15.2)	(19.1)		(15.7)	(17.0)		(16.3)	(20.4)		(14.3)	

As seen from these figures, the general shapes of the experimental distributions are well represented by simulation calculations using either of the codes, although somewhat better agreement is obtained with HERMES. However, there are systematic trends in quality of the agreement between calculations and data. In particular for the thin (2- or 5-cm) targets and the higher proton energy, theoretical calculations predict slightly higher average multiplicities than experimentally observed, as can be seen from the top panels of Fig. 7.5, as well as from Fig. 7.6 corresponding to Pb targets. Discrepancies seem to become larger for even higher energies [Pie97]. The origin of these trends is presently not fully understood. The improved agreement between data and calculations for thick targets and low incident energies could conceivably be due to a cancellation of imperfections in the treatments of inter- and intra-nuclear cascades by the models.

Since high neutron multiplicities are essentially due to evaporation, overestimation of the neutron multiplicities by the models may also be caused by an overestimate of the nuclear excitation energies as will be discussed in sect. 7.1.2 or too high Coulomb barriers (cf. sect. 4.4.2) applied. The codes are also unable to reproduce the experimental data in the low-multiplicity region representing peripheral reactions. In this low M_n region both codes appear to overestimate the probabilities especially for the 2.5 GeV incident proton energy. On the one hand the experimental precision for low neutron multiplicities is limited by threshold effects and accuracies in background corrections and on the other hand the description of the nuclear density profile of the nucleus has a large influence on the distributions for low M_n .

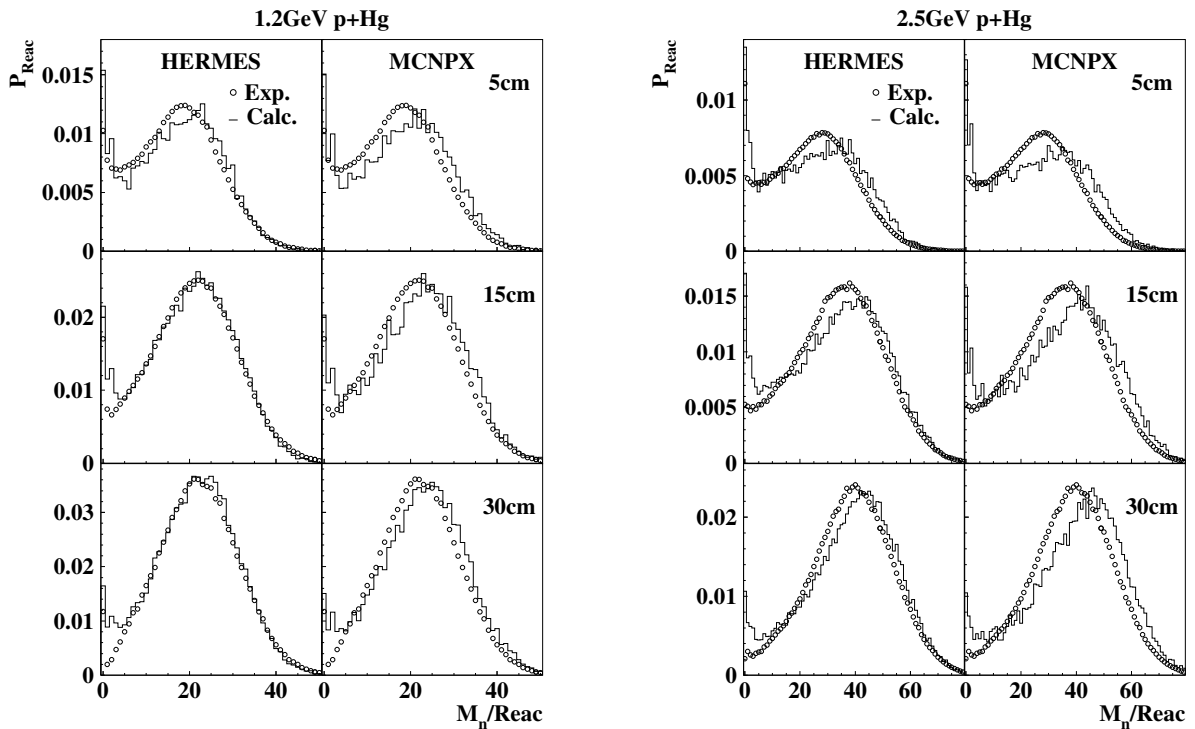


Figure 7.5: Comparison of HERMES, MCNPX and exp. data (\circ) for Hg targets of various lengths bombarded with 1.2 GeV (left) and 2.5 GeV (right) protons. Exp. data: [Let00].

Pb: Also for Pb targets the deviation of theoretical predictions with respect to experimental data decrease with increasing target thickness, while with increasing incident energy divergences increase. The maximum discrepancies are found for the 2 cm thick target bombarded with 2.5 GeV, namely 8.7 (8.3 %) for P_{Reac} and 13 (9.1 %) for $\langle M_n \rangle$ for LCS (HERMES). Note that the divergences for even higher incident proton energies (4.15 GeV) [Pie97] still increase.

W: Observations similar to those for mercury and lead were made for the tungsten target. At 1.2 GeV, agreement with experimental data is very good for the HERMES calculations, while it is still quite satisfactory for the LCS calculations (see Fig. 7.7, left panel). However, for higher incident energies, the data clearly favor HERMES over LCS calculations. At 2.5 GeV, as seen in the right panel of Fig. 7.7, deviations of the LCS

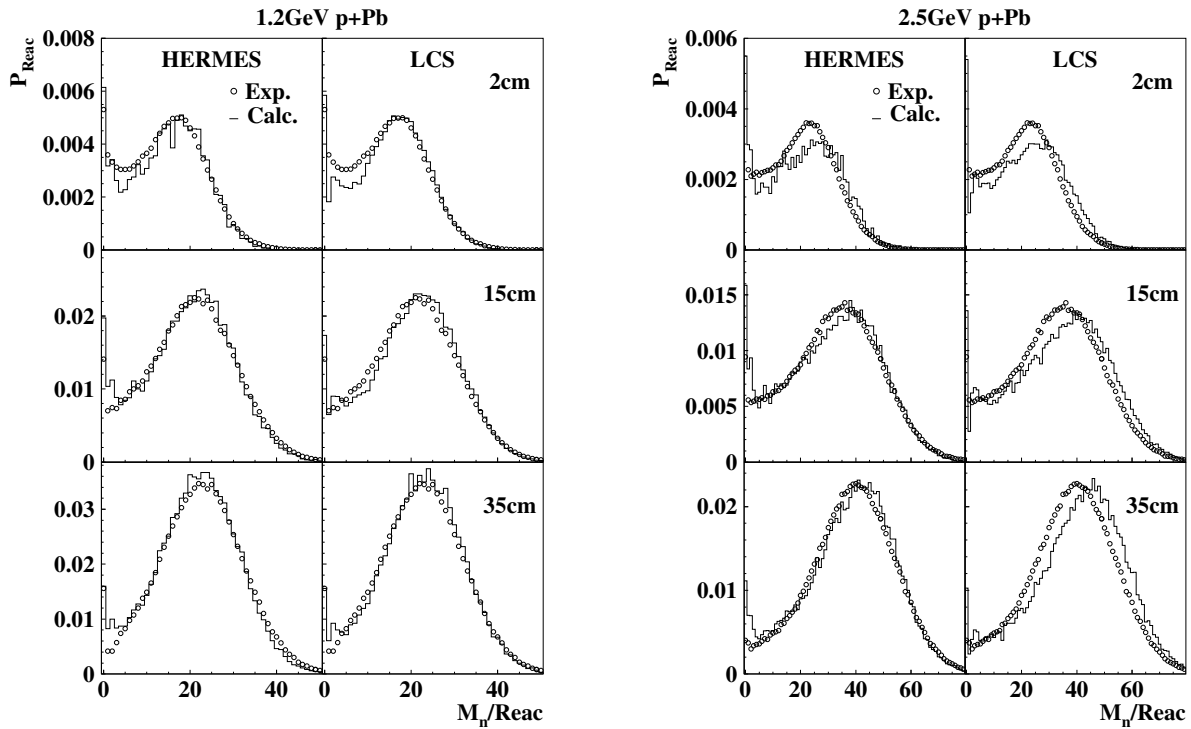


Figure 7.6: Comparison of HERMES, LCS2.70 and experimental data (\circ) for Pb targets of various lengths bombarded with 1.2 GeV (left) and 2.5 GeV (right) protons.

multiplicity distributions from the experimental data are quite substantial (17.6 % for a 2-cm long target).

In order to illustrate the differences between the HERMES and LCS predictions, the leakage- and yield spectra of neutrons from the reaction $p+W$ at 2.5 GeV are shown in the upper and lower panel of Fig. 7.8, respectively. For example, the LCS and MCNPX neutron spectra in the lower panel of Fig. 7.8 exhibit increased evaporative yields (between 1 and 5 MeV) and are slightly shifted to lower energies, as compared to HERMES calculations. This shift in neutron energy may be partly responsible for the differences in average and shape of the neutron multiplicity distributions predicted for the $p+W$ reaction by the HERMES and LCS/MCNPX simulations, in conjunction with the RAL evaporation model (cf. Tab. 7.3 and Fig. 7.7, right panel).

The INC part of the spectra is very similar for all models. The small dip at approximately 7 MeV, seen in the LCS and MCNPX spectra displayed in the bottom panel of Fig. 7.8 reflects the fixed, 7 MeV cut-off energy for neutrons in the INC (cf. sect. 7.1.1) calculations. The most probable energy of neutrons leaked from the $35\text{cm} \times 15\text{cm}$ (length \times dia.) W-target (upper panel in Fig. 7.8) is approximately 0.6 MeV. This substantial decrease in energy, compared to the spectrum of neutrons at the moment of production seen in the bottom panel of this figure, is a result of the moderation of the neutrons within the target volume. The differences in the primary evaporative energy spectra predicted by the HERMES and LCS/MCNPX packages are seen to be largely washed out in the moderation process. Consequently, differences between the predictions by models for neutron

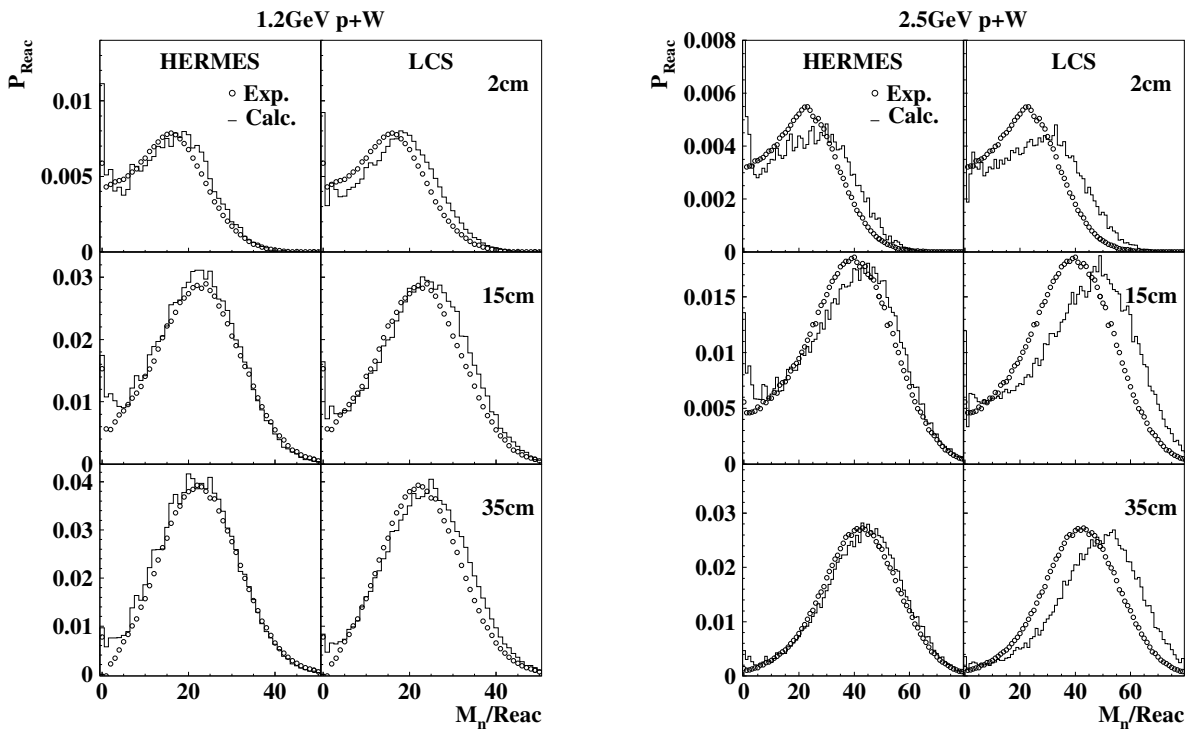


Figure 7.7: same as Fig. 7.6, but for 1.2 GeV (left) and 2.5 GeV (right) incident $p+W$.

production cross sections (most apparent for W, cf. Fig. 7.7, right panel) at high incident proton energies can probably not be traced back to differences in the treatment of the transport process. As seen in Tab. 7.3 and Fig. 7.7, for W targets and all incident energies, the HERMES calculations achieve a better agreement with averages and shapes of the experimental neutron multiplicity distributions than LCS or MCNPX calculations do.

The economy of neutron production

The various experimental results on thick target measurements can be condensed to a quantity which expresses the “economy” of neutron production, i.e. the number of neutrons produced per incident proton and per unit of beam energy. This number is displayed as a function of E_{inc} in Fig. 7.9. The presentation allows on the one hand the comparison of NESSI results with those from other methods and on the other hand, it could also be useful as a guideline to the nuclear physics aspects of neutron generation in the context of a conception of high flux neutron sources. The neutron number increases sharply with increasing E_{inc} or decreasing electronic loss of the proton in the material and culminates at 0.8 to 1 GeV when the minimum of ionization is approached. W gives a 10% higher yield than Pb for the same target size, $l=35$ cm and $\Phi=15$ cm, and it would also provide a slightly brighter neutron source. Hg, not shown, behaves similar to Pb. HERMES simulations reproduce the measured yield for Pb and W reasonably well. A calculation for a larger Pb cylinder with $l=60$ cm and $\Phi=20$ cm is also indicated in order to show the possible gain of some 20% with a larger target and because this has been the standard target in previous investigations [Ara99, Nik90]. Data from ref. [Nik90] lie close to the latter simu-

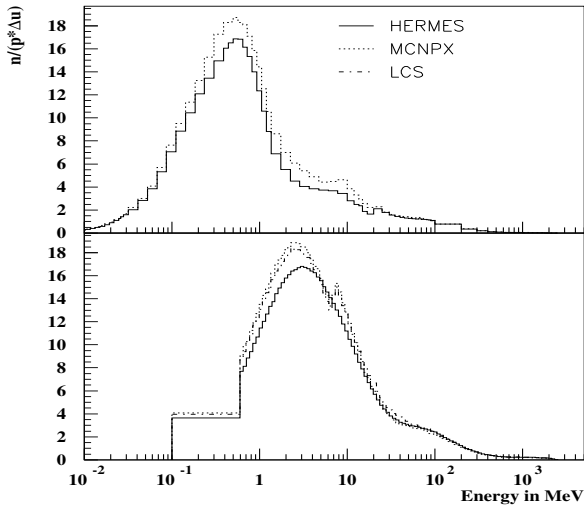


Figure 7.8: Leakage- (upper panel) and yield (lower panel) spectrum of neutrons for 2.5 GeV $p+W$ using the standard parameter set. The dimension of the W target is $35\text{cm} \times 15\text{cm}$ (length \times diameter). The simulated HERMES, MCNPX and LCS distributions are normalized per source proton and unit lethargy.

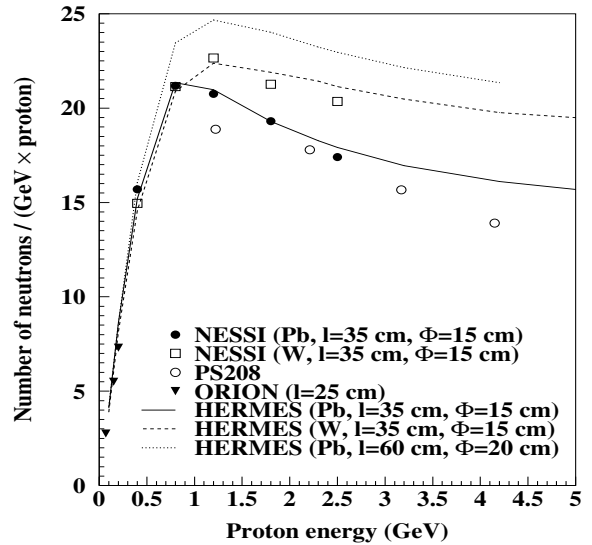


Figure 7.9: Average number of neutrons produced in Pb and W target blocks per proton and per energy unit (1 GeV) as function of incident energy. Data from NESSI, PS208 [Hil98] and ORION [Lot98] are shown. Results of simulations with the HERMES code [Fil01] for different targets are indicated by lines.

lation. Beyond the maximum near $E_{\text{inc}}=1$ GeV the yield diminishes very slowly again in the experiment and even more slowly in the simulations, a tendency which is corroborated by a recent M_n -bath experiment [Ara99] with a Pb target at $E_{\text{inc}}=12$ GeV. Since at energies well above 1 GeV pion production becomes a dominating process [Ant73] the question arises how efficient pions are for neutron production. Is a considerable fraction of the initial available energy lost via decay channels like e.g. $\pi^0 \rightarrow 2\gamma$ or $\pi^+ \rightarrow \mu^+ + \nu_\mu$? To what extent is this loss compensated for by lower electronic energy loss of charged pions prior to nuclear reactions? Pions approach their minimum ionization power at considerably lower energies (0.3 GeV) than protons (2 GeV). To study these questions the comparison of proton and anti-proton induced neutron production in thick targets is an ideal method, since in the case of \bar{p} the neutron production is mediated essentially via pions originating from \bar{p} -nucleon annihilation production on average 5 pions ($3\pi^\pm + 2\pi^0$). That is why in the following more generally hadron (π, K, \bar{p}, p, d)-induced neutron production in thick Pb targets will be compared up to 5 GeV/c.

Neutron production by π, K, \bar{p}, p, d projectiles

It might be advantageous for the operation of the accelerator and target assembly of spallation neutron sources to employ at a given beam power considerably higher beam energies than 1 GeV. But since at increasing energy meson production (mainly π 's) is increasing, an increasing part of neutron production is due to secondary-meson-induced

reactions. How efficient are these pions in producing neutrons? In order to answer this question hadron induced neutron production as a function of particle energy has been investigated. In particular neutron production for proton-, antiproton- and pion-induced reactions has been compared. In the latter reaction neutron production is predominantly induced by π^\pm and π^0 . No data exist at all for pion induced reactions which are of importance to account for the yield of secondary reactions, with the pions being produced in a primary (anti-)proton nucleus interaction.

Table 7.4: Results for thin and thick Pb and depleted U targets: the mean neutron multiplicity $\langle M_n \rangle$, the number of neutrons per incident particle $\langle N_n \rangle/p$, the most probable neutron number M_n^{max} , and the width σ , the latter two are obtained from a Gaussian fit to the distributions of M_n . These values have been multiplied with 1/0.85 in order to account for an assumed mean detection efficiency of 85%. Errors are in the order of 1 to 5%. Negative momenta p correspond to antiprotons or negative pions, L and D indicate the target length and diameter, respectively.

p $\frac{GeV}{c}$	T	L cm	D cm	protons				pions π			
				M_n^{max}	σ	$\langle M_n \rangle$	$\frac{\langle N_n \rangle}{p}$	M_n^{max}	σ	$\langle M_n \rangle$	$\frac{\langle N_n \rangle}{p}$
1.94	Pb	0.2	15	18.0	7.4	14.5	0.16	-	-	-	-
1.94	Pb	5.0	15	21.3	10.7	19.4	4.8	-	-	-	-
1.94	Pb	35	15	26.0	11.5	25.4	20.5	-	-	-	-
-1.94	Pb	35	15	-	-	52.4	35.3	-	-	-	-
2.00	Pb	35	15	26.7	13.0	26.7	22.6	35.5	16.5	32.5	20.5
3.00	Pb	35	15	42.2	16.5	41.1	34.9	48.0	20.1	46.2	34.6
4.00	Pb	35	15	53.9	20.4	51.7	44.0	57.5	22.9	55.1	38.7
-4.00	Pb	35	15	-	-	72.2	65.6	-	-	60.5	47.0
5.00	Pb	35	15	63.8	24.5	60.8	51.0	66.0	27.8	63.3	50.1
-5.00	Pb	35	15	-	-	79.5	71.2	-	-	68.6	-
1.94	U	0.3	5x5	23.3	8.8	19.9	0.53	-	-	-	-
1.94	U	40	8	38.0	19.4	38.8	35.3	-	-	-	-
4.00	U	40	8(15)	90.1	28.6	87.6	84.1	99.3	33.1	93.5	69.3
5.00	U	0.9	5x5	35.6	21.8	28.5	2.56	36.7	24.5	30.5	1.74
5.00	U	40	8(15)	112.2	30.5	106.0	101.0	115.3	36.1	107.5	72.4

For protons, antiprotons, positive and negative pions Tab. 7.4 gives the first moment $\langle M_n \rangle$ of $d\sigma/dN_{exp}$ as well as the most probable neutron number M_n^{max} as derived from a Gaussian fit to the multiplicity distribution $d\sigma/dN_{exp}$ at the position of the maximum. From the measured reaction probability P_{reac} and $\langle M_n \rangle$ we deduce the mean number of neutrons per incident proton $\langle N_n \rangle/p = \langle M_n \rangle \times P_{reac}$.

For protons we observe with increasing target thickness an increase of both the mean neutron multiplicity $\langle M_n \rangle$ as well as the most probable neutron multiplicity M_n^{max} with the relation $\langle M_n \rangle \leq M_n^{max}$. For the thickest targets of 35 cm Pb $\langle M_n \rangle$ has almost attained the value of M_n^{max} (Tab. 7.4) simply due to the fact that the intensity of low neutron multiplicity events has become very small due to secondary reactions. For 35 cm Pb as well as 40 cm U the intensity of the measured distribution which cannot be described by a Gaussian is smaller than 5% while for thin targets it amounts to 20 to 30%. For

target thicknesses larger than 35 for Pb or 40 cm for U any further increase of the neutron yield per incident proton $\langle N_n \rangle/p$ is essentially due only to further increase of the reaction probability. The observed steep increase of the number of neutrons per incident proton $\langle N_n \rangle/p$ for target thicknesses up to about 10 cm, instead, is due to the combined increase of the reaction probability P_{reac} and the mean neutron multiplicity $\langle M_n \rangle$ with target thickness. Contrary to other methods these two quantities are measured independently in the present experiment and not as a product. The observed larger neutron multiplicity for U compared to Pb can be ascribed in the case of thin targets (see Tab. 7.4) to a higher probability for energy absorption in the bigger target nucleus, to the lower neutron binding energies of U spallation products, and eventually to one or more extra neutrons from fission of the residual nucleus ($\bar{\nu}=1.92$ for spontaneous fission of ^{238}U). In a thick target of U fission can be induced by many secondary particles and become a dominating process. It multiplies the number of neutrons to the extent that the neutron yield in a 40 cm-long U-target is nearly doubled as compared to Pb: $\langle M_n^{\text{U}} \rangle / \langle M_n^{\text{Pb}} \rangle = 1.5$ and 1.7 at $E_p = 1.22$ and 4.15 GeV, respectively.

A summary of mean neutron multiplicities $\langle M_n \rangle$ for π^\pm , K^+ , p , \bar{p} and d^+ on a thick Pb-target (35 cm length, 15 cm diameter) is presented in Fig. 7.10 at incident momenta 2, 3, 4, and 5 GeV/c, respectively. These momenta are corresponding to somewhat higher kinetic energies for π 's than the respective proton energies. Since for such a thick target $P_{\text{reac}} \simeq 1$, the given values can be considered also as mean numbers of neutrons per incident particle. If $\langle M_n \rangle$ induced by p and \bar{p} is compared at the same incident energy

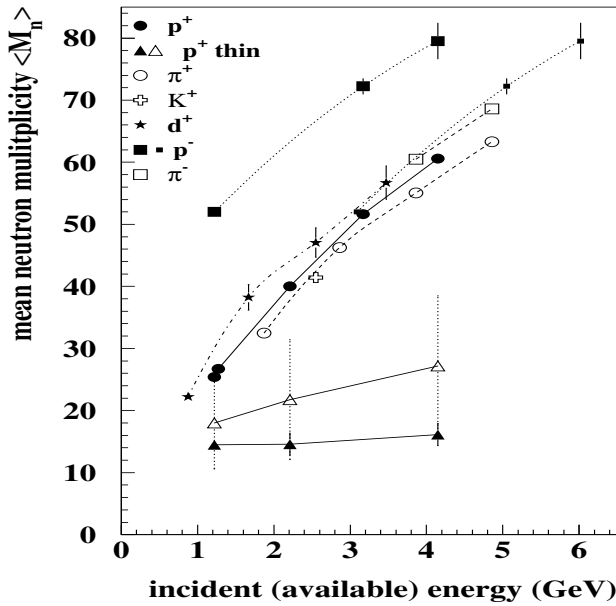


Figure 7.10: Average neutron multiplicity $\langle M_n \rangle$ for incident protons p^+ , antiprotons p^- , pions π^\pm , kaons K^+ and deuterons d^+ as a function of incident kinetic energy on 35 cm-long 15 cm-diameter Pb target. $\langle M_n \rangle$ has been corrected for a mean efficiency of $\varepsilon_n = 0.85$ (see sect. 6.2.2). For p^- the small filled squares indicate $\langle M_n \rangle$ also at the available incident energy, see text. The filled and open triangles display $\langle M_n \rangle$ and M_n^{max} for thin Pb targets. The curves are to guide the eye.

the neutron numbers in case of \bar{p} are up to a factor of two higher. If however the \bar{p} -nucleon annihilation energy of $2m_p c^2$ is taken into account the “available energy results to $E_{\text{inc}}^p + 2m_p c^2 = 1.22 + 1.88 = 3.1$ GeV. Thus, for instance, the comparison with 1.22 GeV \bar{p} should be rather made at an incident proton energy of 3.1 GeV. $\langle M_n \rangle$ is indeed very similar for p and \bar{p} -induced reactions when compared at the same available incident energy. Proton and π^\pm -induced reactions should also be compared at the same incident kinetic energy. The multiplicities are somewhat smaller for pions than for protons if compared at

the same incident energy² (see Fig. 7.10). In case of π^- one might argue that the capture of a π^- in a nucleus at the end of the INC converts the rest energy of the pion (138 MeV) to nuclear excitation [Kau80]. This would favor a comparison at an available energy of $E_{\text{inc}}^{\pi^-} + m_{\pi}c^2$. In any case we have measured $\langle M_n \rangle$ at the same momenta and consequently the best approach to the same incident kinetic energy is the comparison at $E_{\text{inc}}^p = 4.15$ GeV and $E_{\text{inc}}^{\pi^-} = 3.86$ GeV as shown in Fig. 7.10. However the neutron multiplicity distributions and the here shown corresponding average values $\langle M_n \rangle$ are relatively independent of the primary hadron species. For π^{\pm} and \bar{p} the total reaction cross section is about 13% smaller [Fas90] and 20% larger [Gol96] than for protons, resulting in correspondingly lower and higher neutron production per unit length along the trajectory of the beam particles in the target, which is a measure of the produced neutron density. Since the reaction cross section is also somewhat larger for deuterons than for protons this finding implies for the neutron yield per incident deuteron $\langle N_n \rangle/d = P_{\text{reac}} \times \langle M_n \rangle$ even larger values which qualitatively agree with the findings of Vassilkov et al. [Vas90]. However, the uncertainty for deuterons in the present experiment is considerably larger since the secondary beam of the CERN-PS contains much less deuterons than protons (2 and 8) $\times 10^{-3}$ at 5 and 3 GeV/c, respectively.

In summary $\langle M_n \rangle$ of the considered hadrons are very similar within 10% if compared at the same incident *available* energy in the energy range of 1-6 GeV [Pie97]. These findings indicate that neutron production mediated by mesons, which is increasing for proton-induced reactions with bombarding energy, is similarly efficient as that occurring without mesons being involved.

The GCCI level density and the MPM

In the case of the lead target bombarded by 1.2 GeV protons, a study of the sensitivity of the predictions to the assumed Gilbert-Cameron-Cook-Ignatyuk (GCCI) level densities (see sect. 4.4.1) and multistage pre-equilibrium model (MPM) was performed. Average multiplicities, $\langle M_n \rangle$ obtained from these studies are depicted in Tab. 7.5.

Table 7.5: $\langle M_n \rangle$ for a cylindrical lead rod of 15 cm diameter bombarded with 1.2 GeV protons. For LCS the GCCI and MPM+GCCI input parameters were used.

Length	LCS (GCCI)		LCS (MPM+GCCI)		Experiment
	$\langle M_n \rangle$	$\langle M_n^c \rangle$	$\langle M_n \rangle$	$\langle M_n^c \rangle$	$\langle M_n \rangle$
2 cm	16.0	22.1	14.9	20.8	14.5
5 cm	16.8	23.4	16.7	22.9	16.8
15 cm	21.2	28.0	19.7	26.4	20.2
35 cm	22.9	29.9	21.2	28.0	22.2

The LCS package, used in conjunction with the GCCI level density parameterization (GCCI in the Tab. 7.5) tends to overestimate mean multiplicities, compared to the experimental values. This could be a reflection of an excess of the excitation energy available

²while they are slightly larger when compared at the same momenta!

for evaporation following the INC stage of the process. Such excess may result from the neglect of pre-equilibrium emission or from an underestimate of the system temperature, related to the parameterization of the level density. Indeed, when an intermediate pre-equilibrium stage is introduced (MPM+GCCl), following INC and preceding evaporation, neutron multiplicities are reduced on average by more than one unit. This is so, because particles from the pre-equilibrium stage have on average higher kinetic energies than thermal particles (see Fig. 7.11) reducing thermal excitation energies and, hence, average multiplicities. In addition, the low-multiplicity events associated with peripheral reactions are somewhat better described, when the pre-equilibrium stage is included in the calculations (not shown here). In general, improved agreement between experimental data and theoretical predictions is achieved when the pre-equilibrium model is used together with the GCCl description.

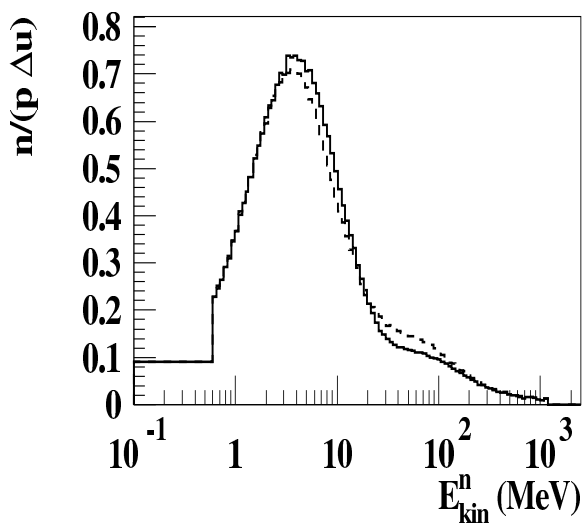


Figure 7.11: Comparison of the theoretical neutron yield spectra resulting from the bombardment of a 2 cm long Pb target with 1.2 GeV protons. The dashed line represents the calculation with LCS using the pre-equilibrium and GCCl model (MPE+GCCl), while the solid line indicates the values obtained with the standard parameter set “STAND” (cf. Tab. 4.1). Curves have been normalized per unit lethargy Δu and source proton.

In summary, all three packages - HERMES, LCS, and MCNPX, provide for a quantitative description of neutron production in cylindrical targets of various lengths, for proton energies up to 2.5 GeV. The agreement with the experimental data is generally within 10%. Only for the highest incident proton energy of 2.5 GeV and the dense tungsten target material, the predictions by the MCNPX and LCS codes deviate from the data by more than this margin (almost 18%). The model calculations show remarkable stability with respect to reasonable variations in the model parameters or assumptions. For example, varying the level density parameter B_0 within reasonable limits, or including pre-equilibrium neutron emission, may alter the neutron production only by approximately one neutron in the case of 1.2 GeV incident protons.

Coulomb barriers in thick targets

Likewise—as discussed in sect. 4.4.2—a considerable feedback on the neutron kinetic energy spectra and multiplicities is caused by the variation of the Coulomb barriers applied in the evaporation codes, because changing the emission width for charged particles effects at the same time the emission probability for neutrons, the two emissions being in

competition. Decreased barriers prefer the light charged particle emission at the expense of n production.

For thick targets the influence of modifying the Coulomb barriers on the neutron multiplicity distributions is demonstrated in Fig. 7.12 for 1.2 GeV proton induced reactions on cylindrical lead rods of 15 cm diameter and 2 or 35 cm length, respectively. The calculations are performed with the Bertini type INC implemented in MC4 [Ste98]. Optionally the Coulomb barriers could either be kept constant (dashed line) or reduced with E^* (solid line) as specified in Fig. 4.5.

The corresponding mean neutron multiplicity decreases from $\langle M_n \rangle = 16$ (27) to 15 (25) for 2 cm (35 cm) length when reducing the Coulomb barrier with E^* , because at the expense of neutrons more charged particles are released. Note also that the average multiplicities following the MC4 calculation seem to be slightly higher than the HERMES values (cf. Tab. 7.2 and Fig. 7.6, left panel) for the same reaction. This phenomenon—specifically dominant for high values of M_n —is all the more pronounced as the target gets thicker and could be related to a different propagation of the hadronic shower within MC4. As compared to the experimental neutron multiplicity distributions the RAL description coincides better with the NESSI data having averages of $\langle M_n \rangle = 14.5$ (22.2) for 2 cm (35 cm), respectively. As expected the integral reaction probabilities are not affected by the alteration of the barriers and amount (in agreement to the experiment) to 11 and 87% for 2 and 35 cm thick lead targets, respectively.

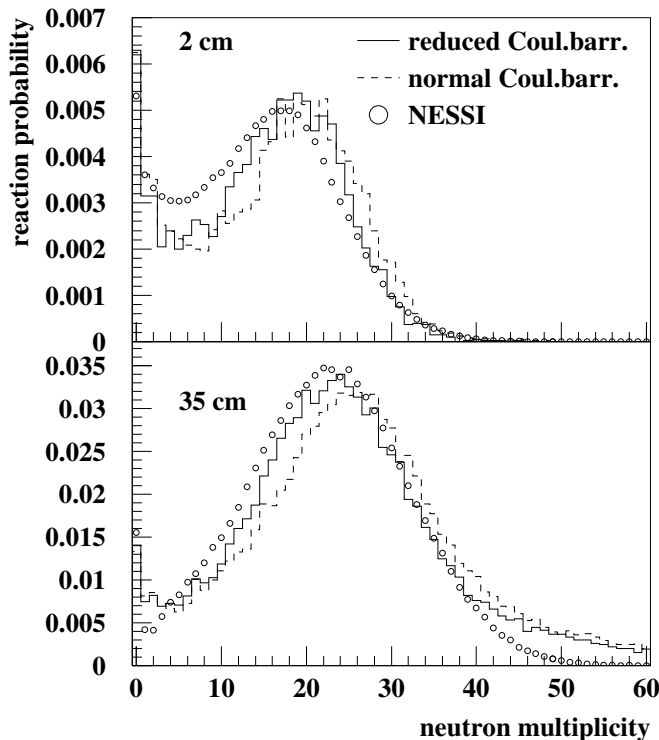


Figure 7.12: Influence of the Coulomb barrier (cf. Eq. 4.11 and 4.12) on the neutron multiplicity spectra for 1.2 GeV p on 2 cm (upper panel) and 35 cm Pb (lower panel) targets. The calculations have been performed with the Bertini type INC implemented in MC4 [Ste98].

7.1.2 Thin targets

With the simultaneous measurement of mainly evaporative-like neutrons and charged particles (CP) detailed exclusive information is obtained on an event-by event base. The multiplicity correlations are shown in Fig. 7.13 representatively for 2.5 GeV proton induced reactions on target nuclei ranging from ^{13}Al to ^{238}U . The target thicknesses between 0.1 and 1.0 g/cm^2 correspond to reaction probabilities of $1\dots 5\times 10^{-3}$. As a general tendency,

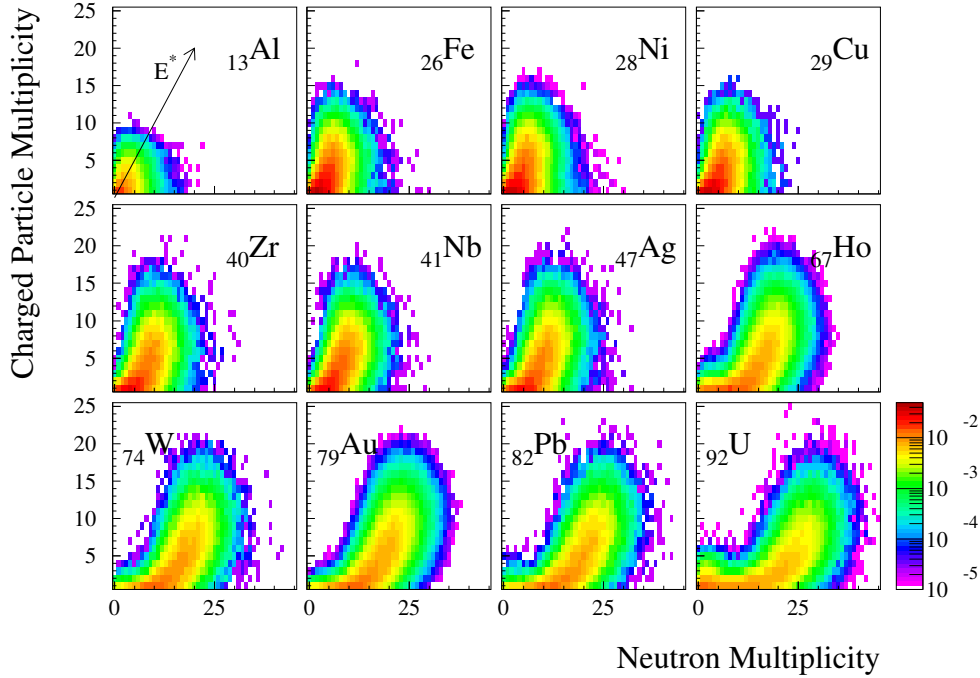


Figure 7.13: Correlation of measured LCP- vs. neutron multiplicity for 2.5 GeV proton induced reactions. The color scale indicates the relative intensity per multiplicity bin.

we note an increase of both, M_n and M_{CP} , with increasing A and Z of the target. This is mainly due to the fact that larger target nuclei incorporate more energy from the INC and have lower particle separation energies than do lighter ones. Also, at lower excitations for heavy nuclei (Au, Pb, U relative to Al, Fe,...) emission of neutrons is strongly favored over that of LCPs and at higher excitations, when comparing Au to U, we observe once more a shift of the measured distributions towards larger neutron multiplicity as a result of a further reduction of neutron separation energies. The total number of evaporative particles is strongly correlated with E^* indicated in Fig. 7.13 by the arrow for Al. The multiplicities are employed to deduce excitation energy distributions $d\sigma/dE^*$ as described in the following section. The procedure allows to analyse observables as a function of E^* .

Thermal excitation energy E^*

The reaction of energetic (up to 2.5 GeV) projectiles is exploited to deposit maximum thermal excitation (up to 1000 MeV) in massive nuclei while minimizing the contribution from collective excitation such as rotation, shape distortion and compression as discussed in section 5.3. $d\sigma/dE^*$ distributions are deduced from event-wise observation of the whole nuclear evaporation chain employing the two 4π sr detectors BNB and BSiB.

The method employed³ to determine the thermal excitation energy relies on the basic property of hot nuclei of de-excitation by evaporation of light particles (LP: neutrons + light charged particles), thereby carrying off some 10 to 20 MeV of excitation energy per particle, approximately equally divided between binding and kinetic energies. This evaporation process is almost perfectly described by the many existing statistical model codes. A prerequisite for the applicability of these models is that the source is equilibrated by the time the emission starts. In order to account for this condition we cut off at 24 MeV the relatively small (typically 15%) contribution at higher energy from the energy spectra of the detected LCPs having a different slope and verify the isotropic emission of the remaining evaporation part. The fact that the Galilean-invariant velocity distribution presented representatively for 1.2 GeV \bar{p} +Au in Fig. 7.14 follows circles centered in the origin of the velocity plane clearly demonstrates that H and He-particles are isotropically emitted from an equilibrated thermalized system, which is nearly at rest due to the small recoil from the reaction. It is also noteworthy that the most energetic $Z=1$ particles are not registered at all due to the lower energy threshold of the Si-detectors. For neutrons, however, we have only indirect information on the kinetic energy on account of the variability in detection efficiencies pointed out above.

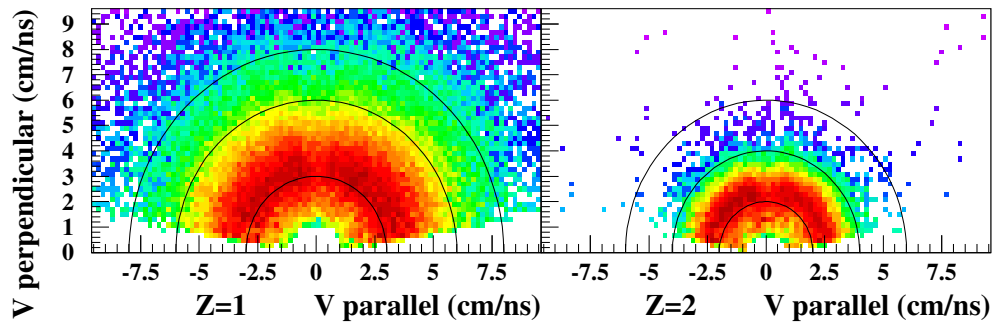


Figure 7.14: Galilean-invariant velocity plot for evaporated $Z=1$ and $Z=2$ particles for 1.2 GeV \bar{p} +Au.

In order to infer for each reaction event the induced thermal excitation E^* we use the sum of all registered light particles M_{LP} , and associate with it (after correction for efficiency) E^* . For the calculation of the relation $M_{LP}(E^*)$ we employ here a slightly extended version [Lot93] of the statistical model code GEMINI [Cha88], because this code also allows for IMF emission. Fig. 7.15 demonstrates the sensitivity of the assignment of E^* to M_{LP} , and also points out its advantage over allocating E^* from the neutron multiplicity M_n or M_{LCP} alone. The panels show, as an example, the experimental multiplicity distributions $d\sigma/dM$ for 1.2 GeV \bar{p} + Au as dotted curves for all LP (a), for neutrons only (b) and for light charged particles (LCP) only (c). Calculated multiplicity distributions $M_{LP}(E^*)$, $M_n(E^*)$ and $M_{LCP}(E^*)$ have been included for a set of fixed values $E^* = 100, 200, 300, 400, 600, 800$ and 1000 MeV. These M_{LP} distributions are very well separated from each other, showing the strong correlation between the two quantities M_{LP} and E^* . The same comparison for neutrons only is much less favorable: here the M_n

³The method can be employed for any light particle (p, \bar{p} , π , ...) induced reaction in the incident energy regime under consideration in the current work.

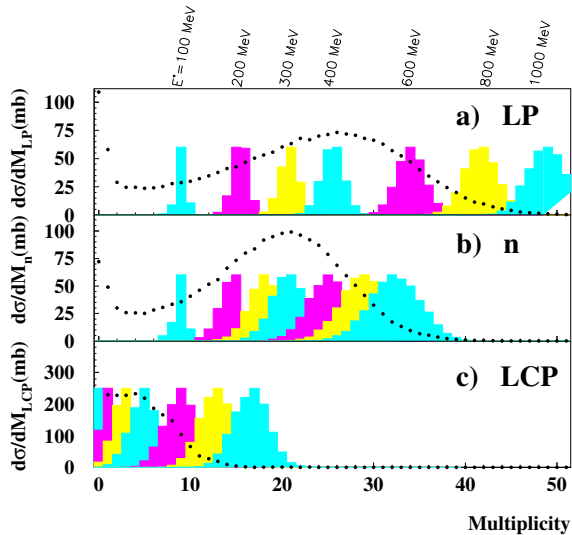


Figure 7.15: Measured multiplicity distributions (\bullet) $d\sigma/dM_{LP}$ (a), $d\sigma/dM_n$ (b) and $d\sigma/dM_{LCP}$ (c) for 1.2 GeV $\bar{p}+Au$. The colored histograms are calculated multiplicity distributions for fixed values of $E^* = 100, 200, 300, 400, 600, 800,$ and 1000 MeV (from left to right).

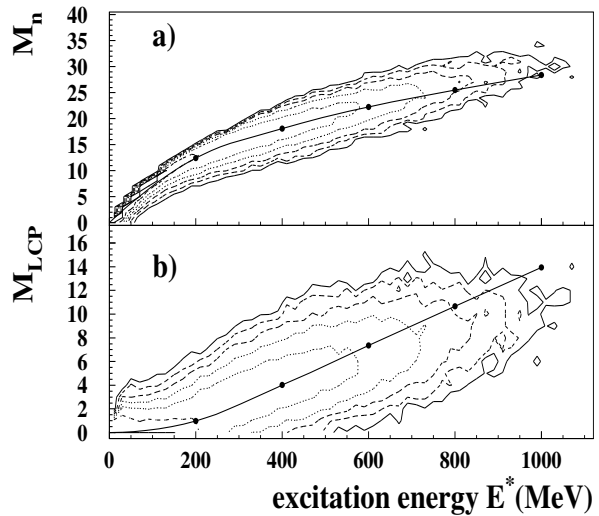


Figure 7.16: Contour diagrams of experimental event distributions following the reaction 1.2 GeV $\bar{p}+Au$ for M_n (a) and M_{LCP} (b) as a function of E^* compared with calculated average multiplicities (dots connected by a line). The intensity change between two contour lines is a factor of 3.

distributions already start overlapping at low excitation. Taking only the information of M_{LCP} is insufficient in particular for low E^* as demonstrated by the overlapping contributions in the lower panel. The FWHM of these calculated multiplicity distributions can be translated into an energy width ΔE^* defining an energy resolution $\Delta E^*/E^*$. By increasing the excitation energy from 150 to 1000 MeV for Au the thus defined energy resolution decreases from 50 to 11% if deduced from M_{LCP} , it increases from 12 to 23% for M_n , and assumes a constant value of 7% for M_{LP} . We conclude that M_{LP} is indeed a reliable observable for E^* up to 1 GeV or more but that the observation of M_n [Lot93, Jia89] and of M_{LCP} [Bow91] alone (which have been applied before for this purpose) is less sensitive to and the resolution depends strongly on the excitation energy.

It is also shown in Fig. 7.16 for 1.2 GeV $\bar{p}+Au$ that the model predictions (continuous lines) fit closely the ridge of the event distributions as a function of M_n (a) and M_{LCP} (b), showing that the sharing between n and LCP is also well accounted for on the average.

The uncertainty for E^* due to the choice of the model parameters⁴ is about $\pm 10\%$. The results from other statistical model codes, JULIAN [Ros89] or from Ref. [Fri90], are

⁴For instance, in the calculation we take into account that in the course of the fast cascade phase an original ^{238}U nucleus loses mass and charge with increasing E^* up to ^{214}At , as is suggested by the INC-calculation for $E^*=1$ GeV. For this extreme E^* the respective evaporation chain releases about 3 neutrons less but 1 CP more than it would have for an intact ^{238}U nucleus. Also, a variation of the level density parameter and the spin within reasonable limits (from $a=A/10$ to $A/8.5$ or $A/13$ and from $l=0\hbar$ to $25\hbar$) results at best in a variation of M_{LP} by 3 to 4 units at the highest excitation.

once more consistent with the ones from GEMINI within these limits. Incidentally, the results from different codes agree much better in the sum multiplicity M_{LP} than in the ratio M_{CP}/M_n . Finally, it is worth noting that a result of statistical model calculations is that, fission or break-up of the nucleus into 3 or more heavy fragments at any stage along the de-excitation chain does not alter M_{LP} or E^* by more than 10%. Therefore this method is not subject to specific splitting modes of the hot nucleus.

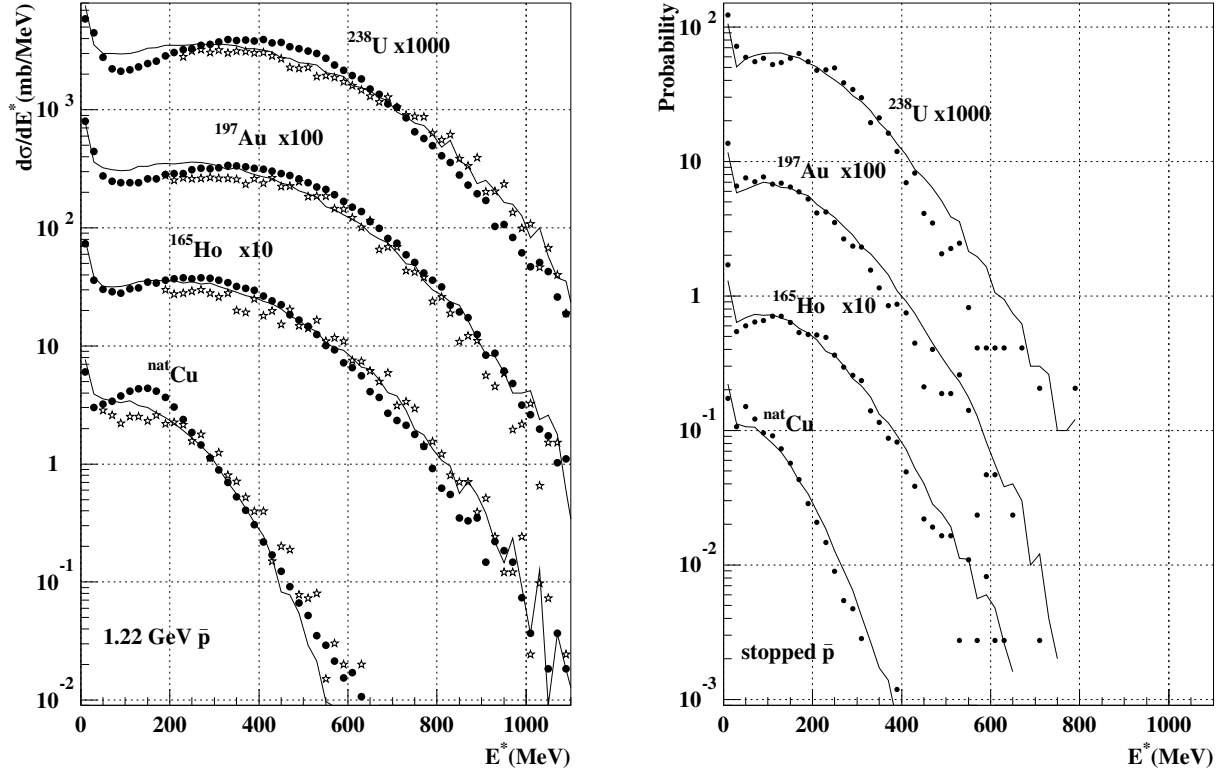


Figure 7.17: Distribution of excitation energy $d\sigma/dE^*$ deduced from M_{LP} (\bullet) or M_{LCP} (\star) compared with INC-model (histogram), for 1.22 GeV \bar{p} (left, in mb/MeV) and of probabilities for stopped $\bar{p}+U$, Au, Ho and Cu (right, normalized to 1).

Using the method described above it is possible to deduce excitation energy distributions and absolute differential cross sections $d\sigma/dE^*$ following light particle (p , \bar{p} , π , ...) induced reactions for the first time. As an example typical distributions are shown as symbols in Fig. 7.17 for 1.22 GeV \bar{p} -induced reactions (left panel) and for annihilation at rest (right panel) on various targets. Also included in Fig. 7.17 are the pertinent INC calculations (following a model described in ref. [Gol88]) as solid lines. For the heavy nuclei Ho, Au, and U we note a satisfactory agreement between experimental and model distributions both in shape and in absolute values. For Cu, however, we observe a considerable discrepancy near the maximum close to $E^*=150$ MeV. For this relatively light nucleus the experimental reconstruction of the E^* -distribution from the multiplicity M_{LP} of all light particles might be less reliable because of the difficulty in discriminating between evaporative and directly emitted neutrons and in subtracting the very few (1 or 2) additional neutrons from pion induced reactions in the scintillator liquid of BNB. This has the tendency to transfer cross section from low E^* to intermediate E^* . Since the

relative contribution of these two effects is more important for lighter target nuclei, we show in Fig. 7.17 (\star symbols) also the E^* -distribution deduced from M_{LCP} alone which seems to agree somewhat better with the INC-calculation.

All $d\sigma/dE^*$ distributions are dominated by a broad plateau which shifts to higher E^* for the heavier nuclei or increasing energy of the antiprotons. At very low E^* the intensity increases considerably, which we assign to peripheral reactions or inelastic scattering without annihilation. The cross section for these reactions (annihilation in flight) is of the order of 5 ± 3 mb for all nuclei. More important with respect to properties of hot nuclear matter are the high energy tails of the data: The 1.2 GeV- \bar{p} interaction with Uranium, for instance, leads for more than 12% of the reaction cross section to thermal energies in excess of 600 MeV, *i.e.* to temperatures larger than 5.2 MeV (with $a=A/10$). In the extreme tails of the distributions even energies as high as 1 GeV are reached, which could not be obtained with protons of still higher incident energy (2.5 GeV) as will be shown in Fig. 7.18 and had already been demonstrated in recent experiments [Pie94]. This finding verifies the expectation [Cug87] that antiprotons are more efficient in heating nuclei than protons. Table 7.6 collects for the annihilation in flight (1.2 GeV) and at rest the pa-

Table 7.6: Target dependence of $\langle E^* \rangle$, $\langle E^*/A \rangle$ and reaction cross section σ_{react} as well as geometrical cross section $\sigma_{geo}(r_0=1.38 \text{ fm})$. Numbers in parentheses show the maximum measured E^* or E^*/A corresponding to 1% of σ_{react} , assuming for $A=A_{target}-\Delta A_{INC}$ with ΔA_{INC} being the calculated mass loss in the INC stage. INC-calculations $\langle E_{INC}^* \rangle$, $\langle E_{INC}^*/A \rangle$ for 1.22 GeV- and stopped \bar{p} are also given.

${}^A_Z X$	$\langle E^* \rangle (E_{max}^*)$ (MeV)	$\langle E^*/A \rangle (E_{max}^*/A)$ (MeV/A)	σ_{react} (mb)	σ_{geo} (mb)	$\langle E_{INC}^* \rangle$ (MeV)	$\langle E_{INC}^*/A \rangle$ (MeV/A)
1.22 GeV- \bar{p}						
${}^{nat}\text{Cu}$	144±20 (516)	2.53 (11.3)	973±80	950	135	2.5
${}^{165}\text{Ho}$	269±30 (780)	1.73 (5.4)	1817±95	1800	265	1.7
${}^{197}\text{Au}$	309±30 (880)	1.65 (5.0)	1985±110	2025	295	1.6
${}^{238}\text{U}$	348±40 (940)	1.52 (4.3)	2220±130	2290	330	1.5
stopped \bar{p}						
${}^{nat}\text{Cu}$	85±18(300)	1.44(5.7)		950	87	1.52
${}^{165}\text{Ho}$	138±29(480)	0.88(3.15)		1800	145	0.93
${}^{197}\text{Au}$	142±33(505)	0.74(2.73)		2025	158	0.83
${}^{238}\text{U}$	161±42(520)	0.70(2.3)		2290	171	0.75

rameters deduced from the E^* distributions of Fig. 7.17. These parameters are the mean excitation energy $\langle E^* \rangle$, the mean excitation energy per nucleon $\langle E^*/A \rangle$, and the maximum excitation energies E_{max}^* and E_{max}^*/A , defined by the somewhat arbitrary criterion that they are associated to the upper 1% of the excitation energy distribution. The average $\langle E^* \rangle$ increases from Cu to U almost linearly with A in accordance with INC model predictions also given in Tab. 7.6. However, when converted to $\langle E^*/A \rangle$, this tendency is inverted: the lighter nucleus receives more excitation energy per nucleon or equivalently higher temperature. As to the maximum excitation energy, E_{max}^* in Tab. 7.6, we note

that for e.g. annihilation in flight and U as much as 30% of the totally available energy (3.1 GeV) is converted to intrinsic excitation⁵. Within the error bars the average excitation energies $\langle E^* \rangle$ for stopped \bar{p} given in Tab. 7.6 are in agreement with the published values [Pol94] of 187 ± 26 , 183 ± 21 and 160 ± 20 MeV for Ho, Au and U, respectively.

By integrating $d\sigma/dE^*$ we obtain the reaction cross sections σ_{react} . The values so obtained compare rather well with a geometrical cross section σ_{geo} calculated with $r_o=1.38$ fm. The radius parameter is thus slightly larger than the standard value, which indicates that annihilation can occur already in the low density periphery of the nucleus.

The very same procedure is used to deduce event wise the amount of thermal excitation energy E^* created in *proton* induced reactions. As for example Fig. 7.18 shows the E^* -distributions for p+Au and three incident energies, $E_p = 0.8, 1.2, 2.5$ GeV. All $d\sigma/E^*$ -distributions exhibit similar to the \bar{p} -induced reactions (cf. Fig. 7.17) typical Gaussian-like shapes from central collisions and a low- E^* component decreasing from low E^* towards higher E^* from peripheral collisions. The distributions extend to higher and higher excitation with increasing incident proton energy. In Fig. 7.18 the experimental values are confronted with simulations from two INC models, LAHET and INCL without any pre-equilibrium option. While the INCL model provides a good agreement at all bombarding energies, the LAHET code instead largely overestimates the cross section at high E^* for higher incident proton energy E_p .

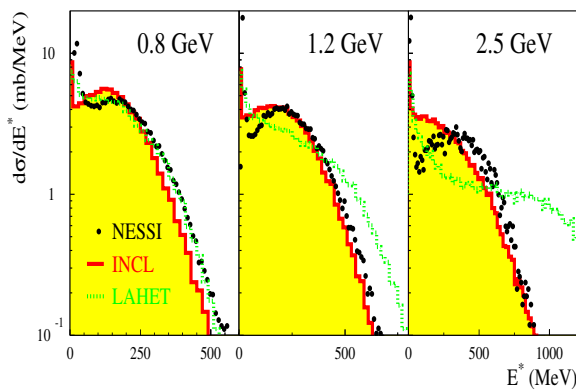


Figure 7.18: Comparison of experimental (dots) and calculated excitation energy distributions for p+Au at $E_p = 0.8, 1.2$ and 2.5 GeV. The calculations have been performed with INCL2.0 (solid histogram) and with LAHET (Bertini-like, dashed histogram). Note that the E^* scale changes from panel to panel.

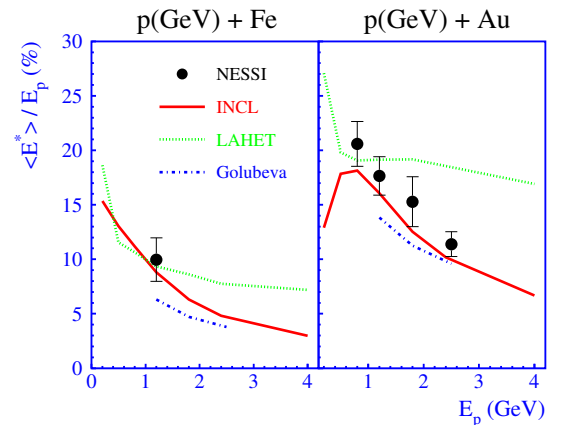


Figure 7.19: Evolution of the energy dissipation, expressed by the ratio $\langle E^* \rangle / E_p$ in the two reactions p+Fe, Au with bombarding energy E_p . Experimental data are shown as dots, results of calculations by lines.

For thermal excitation energies larger than some 10 MeV and incident proton energies up to 1.2 GeV the ISABEL code [Yar79, Yar81] coincides with the INCL2.0 predictions (not shown here). For incident proton energies larger than 1.2 GeV the validity range

⁵Nevertheless $E_{max}^*/A=4.3$ is still below the expected [Fri90] onset of non-evaporative emission of IMFs. The observed mean IMF multiplicities for all four reactions are below 1.2 up to the highest excitation energies and can be fully explained by evaporation.

of ISABEL is exceeded [Pra89] and consequently should not be applied. For the cut-off conditions determining equilibration standard parameters have been taken (Table 4.1). ISABEL and INCL2.0 calculations have been renormalized to the reaction cross section of 1688 mb (p+Au) which is widely independent on incident proton kinetic energy. The different cross sections $d\sigma/dE^*$ at low E^* caused essentially by peripheral collisions can – among other things – be explained by differences in the nuclear density description of the nuclei. Probably the 16 step approximation of the nuclear density in the ISABEL code is responsible for the enhancement of $d\sigma/dE^*$ at low E^* as compared to the other models.

In order to provide an overview of the evolution of E^* with increasing bombarding energy, Fig. 7.19 shows for p+Fe and p+Au the ratio of average excitation energy $\langle E^* \rangle$ and E_p : $\langle E^* \rangle/E_p$ as a function of E_p . This ratio qualifies the efficiency of energy dissipation. The experimental data $\langle E^* \rangle/E_p$ for Au decrease rapidly from 21% at 0.8 GeV to only 11.5% at 2.5 GeV, while $\langle E^* \rangle$ would still increase slowly from 170 to 290 MeV. The INCL2.0 prediction follows very closely this decrease, as does the calculation with the model from Golubeva et al.[Gol88]. The LAHET-simulation, however, provides good agreement with the experiment only at low E_p , while at high E_p discrepancies up to a factor of two in $\langle E^* \rangle/E_p$ are observed. Also the average values of the E^* -distributions summarized in Tab. 7.7 indicate that only a small part (approximately 1/10 to 1/5—depending on the nucleus, the incident energy, and the codes used) of the total available energy (incident kinetic energy of the proton) can be converted into thermal excitation energy. The remaining part is carried off by highly energetic nucleons and mesons during the fast INC.

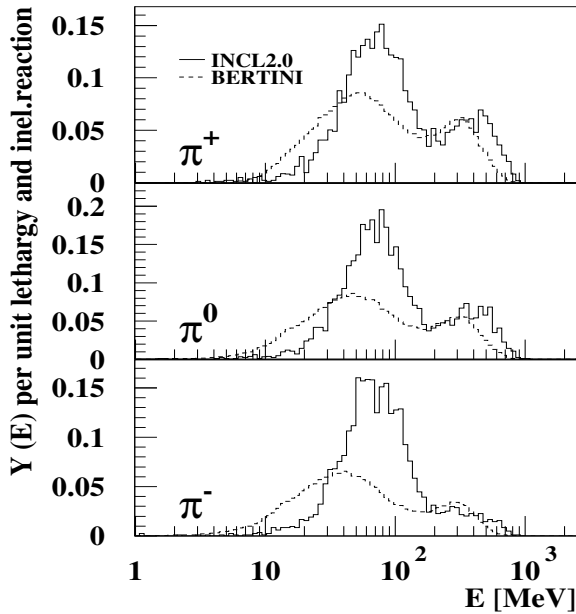


Figure 7.20: Kinetic energy spectra of π^\pm and π^0 per unit lethargy following an inelastic reaction of 1.2 GeV protons on Au for INCL2.0 and HETC (Bertini-like) codes.

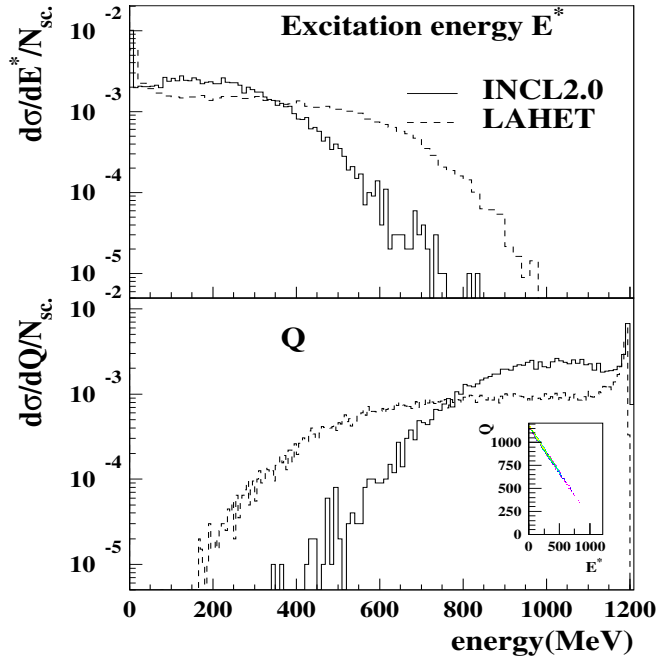


Figure 7.21: Interplay between E^* and Q (cf. Eq. 7.1) for 1.2 GeV p+Pb. The in-line graphic shows the anti-correlation of E^* and Q crossing both axis intercept close to beam energy.

The considerable deviation between LAHET/Bertini on one hand and INCL2.0/ISABEL on the other hand for higher E^* is all the more pronounced as the energy of the incident proton increases. One assertion which could explain the disagreement is the way the originally transferred energy is being exhausted or carried away by the different exit particles. While the INCL2.0 code predicts many relatively highly energetic particles during the INC, the HETC codes (LAHET or HERMES) produce not only fewer, but also less energetic particles as shown representatively in Fig. 7.20 for π^\pm and π^0 production following the reaction 1.2 GeV p+Au. All pion kinetic energy distributions shown in Fig. 7.20 are based on the same inelastic reaction cross section of 1688 mb (for the reaction p+Au). Evidently the pion spectra show a shift of the π^+ energy distributions compared to the π^- distributions due to the repelling or attractive effects of the Coulomb field of the nucleus on the emitted pions. Since the pion model implemented in HERMES and LAHET is essentially the same, the kinetic energy spectra and pion multiplicities predicted by these codes coincide perfectly.

The appraisal of the quality of pion spectra and production cross sections $\sigma_\pi^{\text{total}}$ is almost impossible due to the lack of experimental data in the energy regime beyond 1 GeV. When comparing the INCL2.0 total π^+ and π^- production cross sections (278 and 225 mb) with experimental results of Cochran et al. [Coc72] for the reaction 730 MeV p+Pb ($\sigma_{\pi^+}^{\text{total}} = 105 \text{ mb}$, $\sigma_{\pi^-}^{\text{total}} = 58 \text{ mb}$) the Bertini approach ($\sigma_{\pi^+}^{\text{total}} = 146 \text{ mb}$, $\sigma_{\pi^-}^{\text{total}} = 82 \text{ mb}$) is found to overrate only slightly the experimental values. However the measured shape of the distributions [Coc72] does not agree with the calculated one.

Conferring to Tab. 7.7 as a matter of energy balance the available thermal energy E^* right after the fast INC cascade is smallest for the INCL2.0 calculation since the energy carried off by fast cascade particles during the INC is generally larger than for Bertini based models. For the different codes, Eq. 7.1 reflects the energy conservation fulfilled on an event-by-event base when considering the particle kinetic energies E_{kin} and the rest mass of 139.6 MeV for π^\pm and 135 MeV for π^0 being abbreviated as \mathcal{Q} in the following.

$$E_p = \underbrace{\sum_{\pi^0, \pi^\pm, p, n} E_{\text{kin}} + \sum_{\pi^0, \pi^\pm} m_\pi \cdot c^2}_{\mathcal{Q}} + E^* + S + E_{\text{rec}} \quad (7.1)$$

Adding up \mathcal{Q} , the thermal excitation energy E^* , the total sum of separation energies S and the recoil energy of the residual nucleus E_{rec} the incident proton energy E_p results. Tab. 7.7 and Fig. 7.21 oppose these quantities for the INCL2.0, Bertini and ISABEL, respectively. While conserving the total incident energy in all codes, it is obvious that during the INC the originally transferred energy is re-distributed among the terms of Eq. 7.1 differently. Both on an average base (cf. Tab. 7.7) as well as on an event-by-event base (cf. Fig. 7.21) for Bertini at the expense of larger E^* (upper panel in Fig. 7.21) the sum of kinetic energies and multiplicities of emitted particles or \mathcal{Q} (lower panel in Fig. 7.21) is smaller and vice versa for the INCL2.0 approach. As far as the quantities defined in Eq. 7.1 are concerned for incident proton energies up to 1.2 GeV ISABEL results are similar to the predictions of INCL2.0. However using the default depth of the nucleon potential of $V_0 = 40$ MeV and looking carefully at the energy balance the separation energy per nucleon being 1.5 MeV/nucleon in the INCL2.0 model seems unrealistically small as compared to 7 MeV/nucleon in the Bertini approach or literature. Therefore the

Table 7.7: Average kinetic energies $\langle E_{\text{kin}} \rangle$ of pions (spectra shown in Fig. 7.20), protons and neutrons and mean multiplicities $\langle M \rangle$ of π^\pm , π^0 , p and n produced during the INC for 0.4, 1.2 and 2.5 GeV p+Au. Also values for \mathcal{Q} (cf. text and Eq. 7.1) and mean thermal excitation energies $\langle E^* \rangle$ are given.

incident proton energy		0.4 GeV		1.2 GeV		2.5 GeV	
		$\langle M \rangle$	$\langle E_{\text{kin}} \rangle$ (MeV)	$\langle M \rangle$	$\langle E_{\text{kin}} \rangle$ (MeV)	$\langle M \rangle$	$\langle E_{\text{kin}} \rangle$ (MeV)
INCL2.0	π^0	0.066	58.5	0.32	148.8	0.59	312
	π^+	0.067	57.7	0.28	158.7	0.47	325
	π^-	0.044	58.8	0.25	108.1	0.47	231
	proton	1.755	83.8	2.71	145.4	3.02	286
	neutron	3.535	39.0	4.70	76.2	4.96	146
	\mathcal{Q}	320 MeV		993 MeV		2236	
E^* (MeV)	72		192		247		
Bertini (LAHET)	π^0	0.031	42	0.24	107	0.53	182
	π^+	0.021	47	0.22	133	0.48	220
	π^-	0.014	33	0.19	86	0.50	166
	proton	1.11	119.0	2.08	179.4	3.19	241
	neutron	2.34	53.0	5.05	67.5	8.38	80
	\mathcal{Q}	267 MeV		873 MeV		1928 MeV	
E^* (MeV)	116		283		495		
ISABEL	π^0	0.014	56.8				
	π^+	0.009	73.3			not accessible	
	π^-	0.0047	51.1			due to limitations	
	proton	1.26	120.1			in the code	
	neutron	1.71	75.4				
	\mathcal{Q}	286 MeV					
E^* (MeV)	100		173				

authors recommendation should be followed and V_0 should be put to 45 MeV resulting in the correct binding energies. However this has very little influence on all observables printed in Tab. 7.7.

All multiplicities given in Tab. 7.7 refer to an inelastic reaction cross section of 1688 mb—not to the number of primary source protons. The large particle transparency ($\approx 30\%$) in Bertini-like codes (using substantially larger nuclear radii) in relation to the INCL2.0 model ($\leq 3\%$) makes this exact specification and renormalization necessary.

In addition to the different spectra and multiplicities, the Pauli blocking is treated in a different way. In Bertini, as mentioned only collisions of nucleons with momentum larger than the Fermi momentum are allowed, while in INCL2.0, the actual phase space

occupation is taken into account. This leads to a less stringent condition, therefore more cascade particles can escape and make the energy remaining in the nucleus lower.

A further crucial aspect, however, directly biasing E^* after each intra-nuclear cascade are the cut-off criteria of the codes allowing for further decay of the equilibrated excited residual nucleus by means of sequential evaporation described by the statistical model. In the INCL2.0 code the equilibration time τ is determined by reaching a constant emission rate of cascade particles during the INC process. τ depends on the size of the nucleus, the impact parameter and on the kinetic energy of the incident proton. Typically τ is of the order of 10^{-22} s or 30 fm/c. The longer this somewhat “artificially” chosen time the smaller E^* being left for the evaporation process. In the Bertini like codes the switching is performed when the most energetic scattered nucleon in the nucleus has decreased below a given cutoff energy of 7 MeV above the Fermi energy.

The question whether the different multiplicities and energies of particles are a matter of a different basic approach (following the cascade in time) or whether more sophisticated fundamental cross sections in the INCL2.0 code—enabling a dissenting production mechanism—are responsible can not yet be answered.

Neutron multiplicity M_n -distributions for thin targets

In Fig. 7.22 neutron multiplicity distributions for 1.2 GeV p+Al...U are compared with

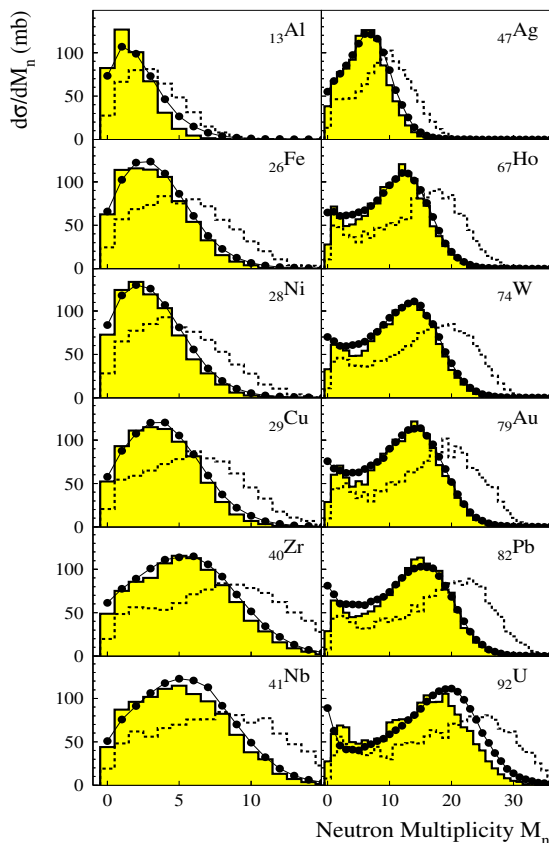


Figure 7.22: Measured (\bullet) and calculated (histogram) $d\sigma/dM_n$ for 1.2 GeV p+X.

calculations following the INCL2.0+GEMINI model. These distributions are projections onto the M_n axis of two dimensional presentations like the one given in Fig. 7.13. In order to compare the calculated with the measured distributions the calculations are shown before (dashed histogram) and after (solid, shaded histogram) folding with the neutron energy dependent detection efficiency ε of the BNB (cf. sec. 6.2.2). Note the different M_n -scales for the left and right panels. When taking ε into account, the INCL2.0+GEMINI calculations agree well with the measured distributions. For heavier targets and low M_n there exists a discrepancy between experiment and calculations. A similar discrepancy was reported previously [Pie97] and was ascribed to the sharp cut off modeling of the nuclear density distribution in INCL2.0. The neutron production cross sections are discussed in the following paragraph.

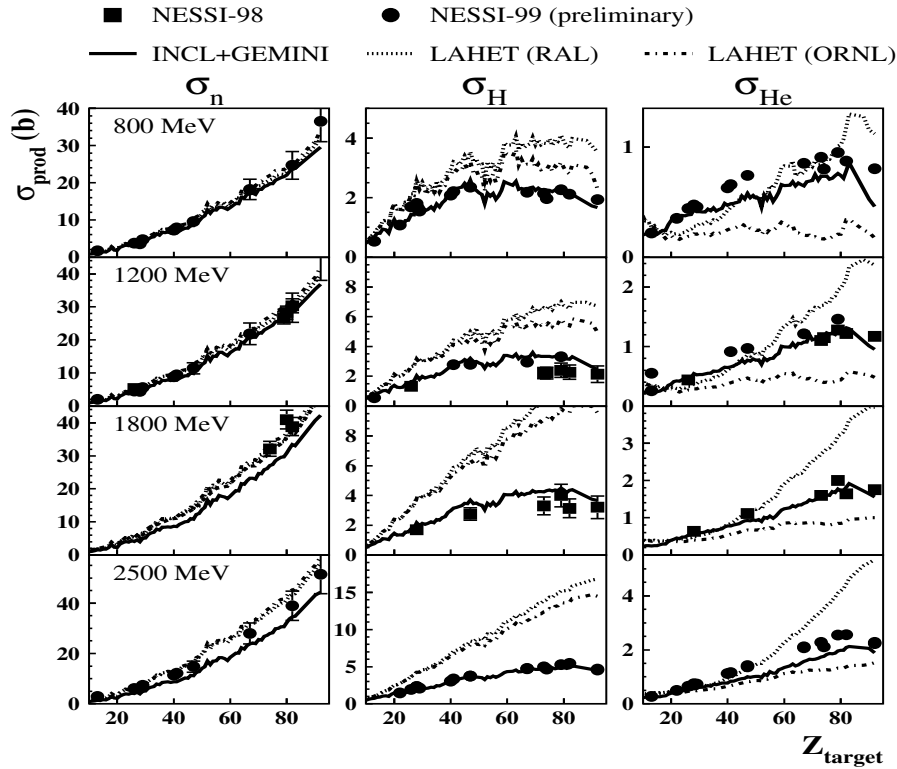
Particle production cross sections σ_n , σ_H and σ_{He} for thin targets

Figure 7.23: Experimental (symbols) and calculated neutron, H- and He production cross sections for 0.8, 1.2, 1.8 and 2.5 GeV proton induced reactions as a function of target atomic number Z_{target} . Lines are representing LAHET/ORNL, LAHET/RAL and INCL2.0+GEMINI calculations. σ_H and σ_{He} calculations consider the experimental thresholds i.e the lower cutoff energy for charged particles of 2.2 MeV and the upper ones of 26, 49 and 76 MeV for p, d and t, respectively. Note different scales of the panels.

The LP production cross sections σ_n , σ_H and σ_{He} for p-induced reactions at various incident energies are compared with model predictions in Fig. 7.23 as a function of atomic number Z_{target} of the target. For neutrons (left panel) the experimental production cross sections have been corrected for the BNB efficiency (cf. Fig. 6.4). Due to lower and upper energy thresholds of the BSiB detectors, σ_H (middle panel) corresponds to $\sigma_H = \sigma_p(2.2 - 26\text{MeV}) + \sigma_d(2.2 - 49\text{MeV}) + \sigma_t(2.2 - 76\text{MeV})$ and helium production cross sections (right panel of Fig. 7.23) to the sum $\sigma_{He} = \sigma_{^3\text{He}} + \sigma_{^4\text{He}}$ with a lower threshold of 2.2 MeV. Concerning σ_n a quite satisfactory overall agreement between the presented data and the code predictions is observed for all targets and incident energies. At higher E_{inc}^p the calculations with the Bertini-like codes tend to be slightly larger than the INCL2.0 results. HERMES results in very similar values for σ_n .

By default LAHET and HERMES HETC exert the RAL fission/evaporation code [Atc89, Atc94] which on its part reduces the Coulomb barriers with increasing E^* as discussed in sect. 4.4.2. The production cross sections for H (all targets) and He iso-

topes (for heavy targets) are generally overestimated by a factor of approximately two for Bertini based codes (HERMES, LAHET using RAL evaporation/fission model), while the INCL2.0 code coupled to the statistical evaporation model GEMINI [Cha88] gives reasonable agreement with the NESSI experimental data [Enke99, Her00] as also representatively demonstrated in Fig. 7.23 for proton induced reactions. As a consequence of the lowered barriers at high E^* (sect. 4.4.2) the He spectra also show an enlarged yield at low energies near the Coulomb barrier using LAHET(RAL) and are not in agreement with the experimental values [Enke99] as is illustrated in Fig. 7.24 for 2.5 GeV p+Au. The small bump at low energies is due to emission of α -particles from FF. In contrast

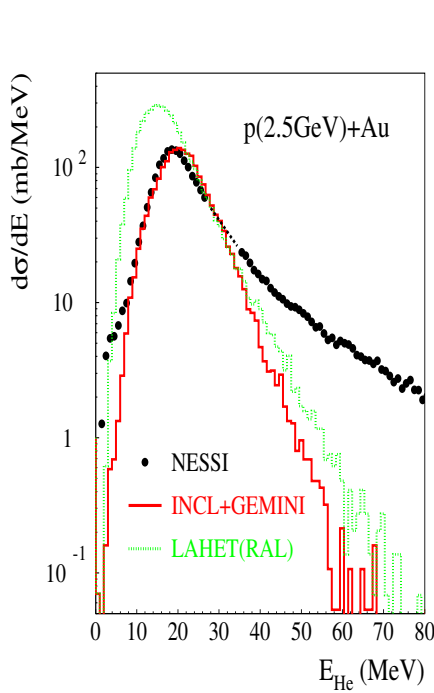


Figure 7.24: Measured (\bullet) and calculated He- energy spectra from INCL2.0+GEMINI and LAHET(RAL) for 2.5 GeV p+Au. The He-spectra are integrated over $10^\circ \leq \theta \leq 80^\circ$ and $100^\circ \leq \theta \leq 170^\circ$ and rescaled to 4π sr. (adapted from [Enke99])

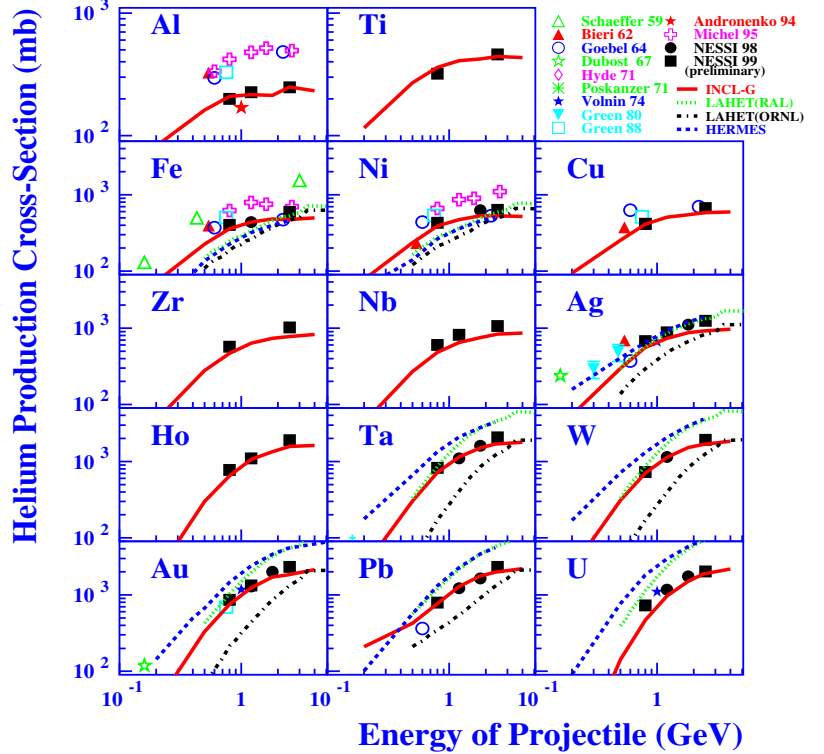


Figure 7.25: Production cross sections of He-isotopes as a function of incident proton energy. Lines are representing LAHET(ORNL), LAHET(RAL), HERMES and INCL2.0+GEMINI calculations, symbols: experimental-data from refs. indicated (cf. text). The lower cutoff energy for the He-isotopes is 2.2 MeV (also considered in the simulations).

for the LAHET code system applying the ORNL fission/evaporation formalism (dashed-dotted line in the right panel of Fig. 7.23) *not* scaling down the Coulomb barriers with E^* , the He-production cross sections reduce drastically below the experimental values, the predicted production cross sections for H isotopes (middle panel of Fig. 7.23) in contrast are still larger throughout all considered target nuclei. As a consequence of the extremely high thermal excitation energy E^* in the Bertini based codes—relative to the INCL2.0 approach—the charged particle production cross sections of $p, d, t, {}^3\text{He}$ and α are

expected to be larger, because charged particle emission is subject to Coulomb barriers and therefore preferentially emitted from high excitation energies. Smaller He- cross sections predicted with the LAHET(ORNL) fission/evaporation formalism as compared to INCL2.0+GEMINI are found to be a bit surprising, because for He-isotopes not only the Coulomb barriers of GEMINI and LAHET/ORNL are similar (cf. Fig. 4.5), but also the thermal excitation energies right after the INC used as input for GEMINI are smaller than for LAHET as shown in Fig. 7.18. This remarkable finding is interpreted [Hil01] by

1. the Coulomb barriers (at $E^*=0$) for protons being considerably smaller in LAHET than in GEMINI (cf. Fig. 4.5) and
2. an increasing fraction of ^5He being produced in addition to stable $^{3,4}\text{He}$ -isotopes in GEMINI.

A compilation of published data and NESSI results for He production cross sections is shown in Fig. 7.25 for a variety of targets as a function of incident proton energy. Previous measurements essentially exploited mass spectrometry methods [Sch59, Bie62, Goe64, Gre88, Mic95, Wal76] for gas extracted from irradiated samples and only a few measurements are based on methods with ΔE -E telescopes for isotope, mass, and energy identification [Dub67, Hyd71, Pos71, Wes78, And94, Vol75, Gre80]. As for example for p+Fe the measured helium production cross sections in the NESSI experiment (440 ± 44 mb) are about a factor of two smaller than from other experiments (792 ± 55 mb) [Mic95]. This corresponds to a discrepancy of a factor of 1.8 or about 6 standard deviations. On the other hand, the present results for Fe and Ni agree quite well with the older measurements of Goebel et al. [Goe64]. A large spread of experimental He cross sections found in literature is also evident when comparing model calculations. The cross sections as calculated with the LAHET(RAL) and HERMES code are somewhat smaller than the NESSI data in case of light targets (Fe, Ni, ...) while for heavy targets LAHET(RAL) and HERMES predict larger cross sections and LAHET(ORNL) smaller ones. The calculations with the INCL2.0+GEMINI code are in good agreement with the data throughout all nuclei and incident energies. Recent results of measured mass distributions in the reverse kinematic reaction of 800 MeV/nucleon Au+p are also well described [Tas98] by the INCL code coupled, however, to a different evaporation/fission code [Gai91, Jun98]. As pointed out above the discrepancies between the data and the HERMES and LAHET calculations are associated with the finding that these codes overestimate E^* after the prompt INC and with different handling of the Coulomb barriers in the employed evaporation codes. As a function of E_{inc}^p LCP production cross sections following spallation reactions on Au with isotopic resolution of H and He is presented in Fig. 7.26. For this purpose 6 telescopes made of successive 80 and 1000 μm thick ΔE Si diodes backed by 7 cm thick CsI crystals were installed in the BNB scattering chamber and inserted as part of the BSiB at 30° , 75° (twice), 105° (twice) and 150° . With these telescopes, clear isotopic separation was achieved and energy spectra up to 200 MeV were obtained. Again, INCL2.0 describes the experimental data quite well, except for ^3He which is known [Gre88] to be produced mostly by pre-equilibrium emission. This process however is not considered in INCL2.0. A comprehensive compilation of currently available data on H- and He- cross sections in the energy regime up to 2.5 GeV is given in the data bank quoted in sec. 7.3.

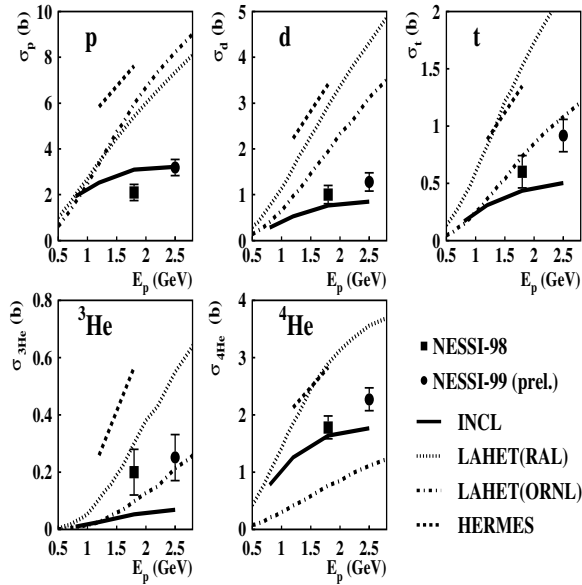


Figure 7.26: Production cross sections σ_p , σ_d , σ_t , $\sigma_{^3\text{He}}$ and $\sigma_{^4\text{He}}$ for 1.8 and 2.5 GeV p +Au measured with 6 telescopes.

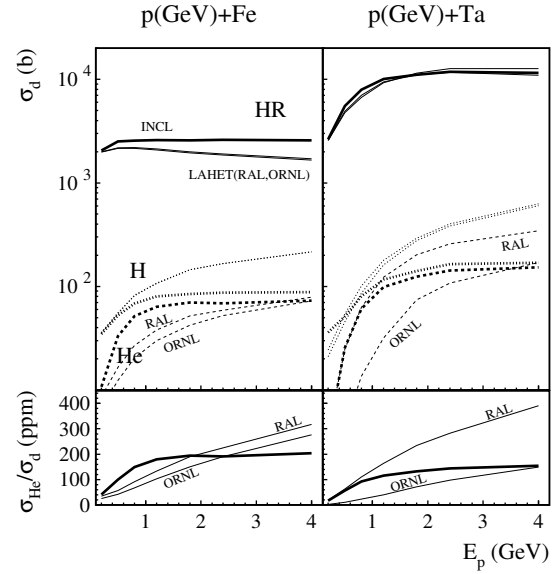


Figure 7.27: Radiation damage cross sections σ_d induced by H, He and HR as calculated by INCL2.0+GEMINI (thick lines) and LAHET(RAL,ORNL) (thin lines); He/dpa ratio $\sigma_{\text{He}}/\sigma_d$ for beam exposed 2mm windows Fe(left) and Ta (right).

Besides the He-production which might cause embrittlement a second important structural damage is due to the production of atom displacements in window materials by proton induced spallation products, in particular by recoiling heavy residues (HR). In Fig. 7.27 displacement cross sections σ_d obtained with INCL2.0+GEMINI and LAHET (RAL, ORNL) are compared [Hil01]. Both codes result in almost the same and constant σ_d . This constant σ_d above about 1 GeV implies that the proton induced damage decreases with increasing incident energy for the same amount of neutrons produced in thick targets. The ratio of He production to displacement per atom (He/dpa= $\sigma_{\text{He}}/\sigma_d$) is strongly increasing with proton energy in the case of the two versions of the LAHET code (RAL and ORNL) while it is almost constant for the INCL2.0+GEMINI code. For more details refer to [Hil01].

Composite Particle Emission

The emission of composite particles such as $^2,^3\text{H}$, $^3,^4,^6\text{He}$ and Li has long been recognized as an important decay channel in spallation reactions. The pioneering experiments of Poskanzer et al. [Pos71] have shown that the emission of these composite particles could not be accounted for by a single evaporation mechanism. Indeed, the emission is far from being isotropic in the emitter frame and the energy spectra exhibit a high-energy tail in excess of the usual evaporative component. Further experiments [Gre87] have confirmed these findings at different bombarding energies and for several target nuclei. It was also shown that the neighboring isotopes ^3He and ^4He have very different behaviors with a strong and weak component of non-evaporative particles, respectively. However in all these studies the underlying reaction mechanisms could not be investigated thoroughly due

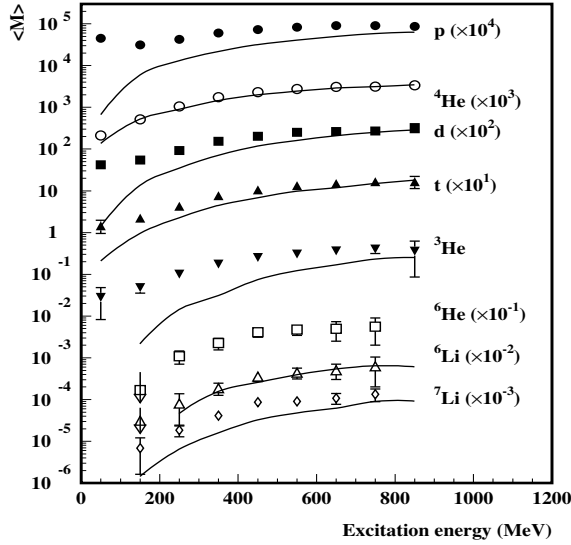


Figure 7.28: Comparison of experimental (symbols) and calculated (lines, standard INCL2.0+GEMINI) multiplicities of H, He and Li isotopes as a function of E^* for 2.5 GeV p+Au measured with 6 telescopes. No pre-equilibrium emission of composite particles is allowed in the calculation. For protons direct emission from INC is suppressed for a better comparison.

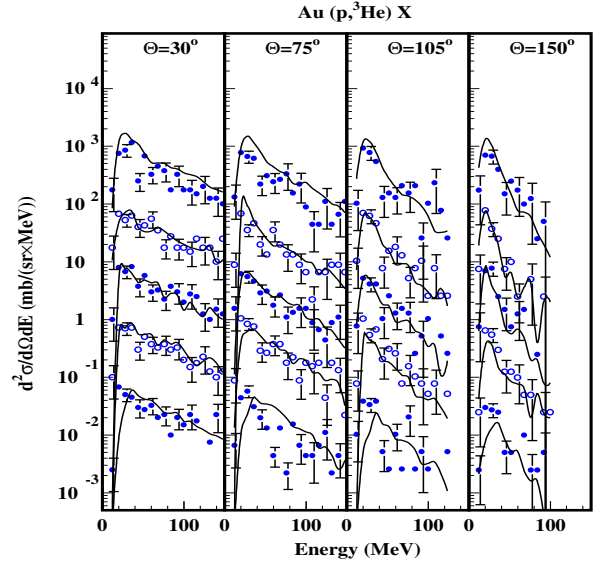


Figure 7.29: ^3He double differential cross sections at $\theta = 30^\circ, 75^\circ, 105^\circ$ and 150° and for five bins in E^* (from top to bottom: $E^* = 0 - 220, 220 - 370, 370 - 470, 470 - 570, \geq 570$ MeV). The experimental data are indicated by dots, simulations including coalescence are shown as lines. Scaling factors of 10 have been applied to the spectra except for the lowest one.

to the lack of additional experimental information. Taking advantage of the very exclusive data brought by the NESSI detector arrays a detailed study of composite particle emission was conducted on the 2.5 GeV p+Au reaction. For the first time the energy spectra could be investigated as a function of excitation energy, E^* , inferred by the method described above. The experimental multiplicities for p to Li are shown as a function of E^* in Fig. 7.28 and are compared with the result of the INCL2.0+GEMINI calculations. This simulation which is restricted to evaporation can certainly not account for the observed yield of most particle species at low E^* . The discrepancy between experiment and simulation is narrowing down, however, with increasing E^* . At high E^* some particles (e.g. ^2H , ^3H , ^4He , ^6Li) are mostly issued from a statistical emission, whereas others (^1H or ^3He) are emitted both, prior and post to the attainment of thermal equilibrium. Among all particles the two neighboring isotopes of He, ^3He and ^4He , exhibit extreme behaviors: the strongly bound ^4He is shown to be almost exclusively evaporated whatever E^* , while also independent on E^* ^3He is mostly of non-evaporative character, with at best 50% of evaporative component at high E^* . By confronting the measured multiplicities with those of the simulated evaporated ones at a given E^* , the following conclusions could be drawn:

- the multiplicity of non-evaporative particles increases with E^* .
- the relative abundance of non-evaporative particles decreases with increasing E^* .

- among all emitted charged particles, ${}^4\text{He}$ is the least “polluted” ($\leq 10\%$) by the non-evaporative component which makes ${}^4\text{He}$ the best probe of E^* and also of the thermalization time t as shown in the PhD-thesis of A. Letourneau [Let01, Let02].

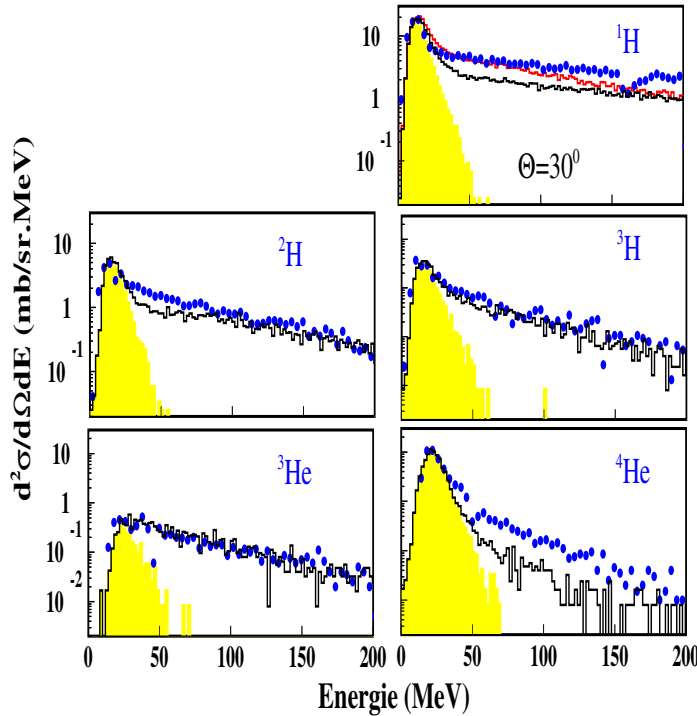


Figure 7.30: dots: the energy spectra as measured at 30° in 2.5 GeV proton induced reactions on Au; shaded area: the evaporative component; histogram: the sum of the evaporative and coalescence components for ${}^2,3\text{H}$ and ${}^3,4\text{He}$. For ${}^1\text{H}$, the upper and lower histograms represent the simulated emission (sum of evaporated (shaded) and INC components) without and with coalescence, respectively.

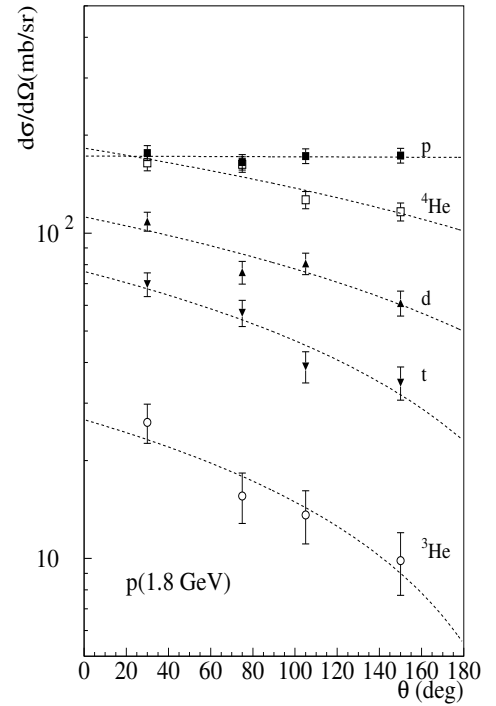


Figure 7.31: Angular distribution for p , d , t , ${}^3\text{He}$ and ${}^4\text{He}$ as measured with the telescopes for the reaction 1.8 GeV $p+\text{Au}$. The dashed curves are to guide the eye. The resulting integrated cross sections can be found in [Enke99].

The comparison done in Fig.7.28 thus reveals the strong deficiency of the INC models which do not consider pre-equilibrium emission of composite particles, although direct emission prior to evaporation is a common feature of all ejected particles. The direct emission amounts to 61, 44, 34, 68 and 11 % of the total emission for the most abundant LCP’s: p , d , t , ${}^3\text{He}$ and ${}^4\text{He}$, respectively. In the current two-step model of intra-nuclear cascade followed by evaporation, the emission of composite particles is made possible during the evaporation stage only. In the intra-nuclear cascade step only nucleons and mesons are emitted. In the PhD-work of A.Letourneau an implementation of coalescence has been made within the INCL2.0 code developed by J.Cugnon [Cug87] in order to generate composite particles prior to equilibrium [Let01, Let02]. When a nucleon -either a proton or a neutron- is about to leave the nucleus an inspection of all other nucleons is

made in phase space in order to check whether one or more nucleons are able to coalesce with the leaving nucleon.

Energy spectra of composite particles are thus generated for ${}^2\text{H}$, ${}^3\text{H}$, ${}^3\text{He}$ and ${}^4\text{He}$. In Fig. 7.29 it is shown for ${}^3\text{He}$ that not only the integrated cross section can be reproduced but also the double differential ones (at 4 emission angles) for several E^* bins. While a similar good agreement is found also for d and t, the coalescence concept in its present form seems to fail for the strongly bound ${}^4\text{He}$ as can be seen in Fig. 7.30. Also the somewhat better description of composite particles is done at the expense of free proton production which becomes slightly underestimated when coalescence is introduced as is demonstrated in the upper right panel of Fig. 7.30.

In Fig. 7.31 the angular distribution of H and He isotopes emitted from the reaction 1.8 GeV p+Au is shown as measured with the telescopes. The lower energy cuts were somewhat higher as the ones described above for the BSiB detectors, since the particles had to punch through the first 80 μm ΔE detector before reaching the second silicon detector: 2.8, 3.6, 4.1, 9.7, 10.8 MeV for p, d, t, ${}^3\text{He}$ and ${}^4\text{He}$, respectively. For all particles except for protons a slight forward backward anisotropy is observed. For protons the pre-equilibrium component is cut off by the upper energy threshold. Furthermore, a part of the forward/backward asymmetry of about 25% for α -particles is due to the momentum transfer of the recoiling Au-nucleus. The integrated production cross section for tritium is found to be 600 ± 140 mb for 1.8 GeV p+Au which is of particular relevance⁶ for ESS.

Particular attention has also been put on ${}^{3,4}\text{He}$ and ${}^{7,9,10}\text{Be}$ emitted following the reaction 2.5 GeV p+Au. The telescopes allowed for a mass resolution of $\Delta A \leq 0.2$ amu for $E/A > 3.5$ MeV/A and $\Delta A \leq 0.4$ amu for $E/A < 3.5$ MeV/A [her02]. Kinetic energy

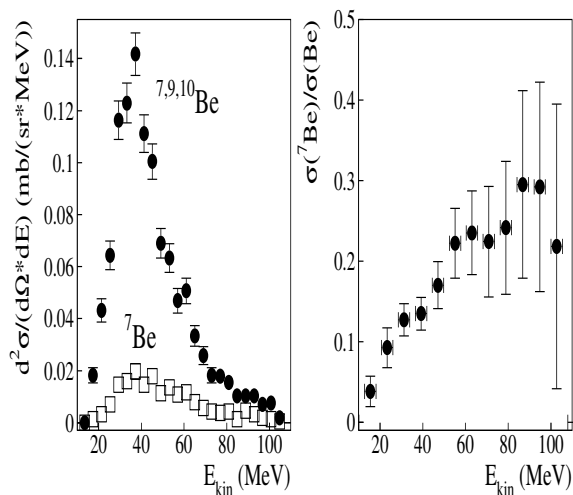


Figure 7.32: Kinetic energy spectrum of ${}^{7,9,10}\text{Be}$ isotopes detected at 30° in respect to the proton beam (left panel) and relative contribution of ${}^7\text{Be}/\Sigma{}^{7,9,10}\text{Be}$ (right panel) for 2.5 GeV proton induced reaction on Au.

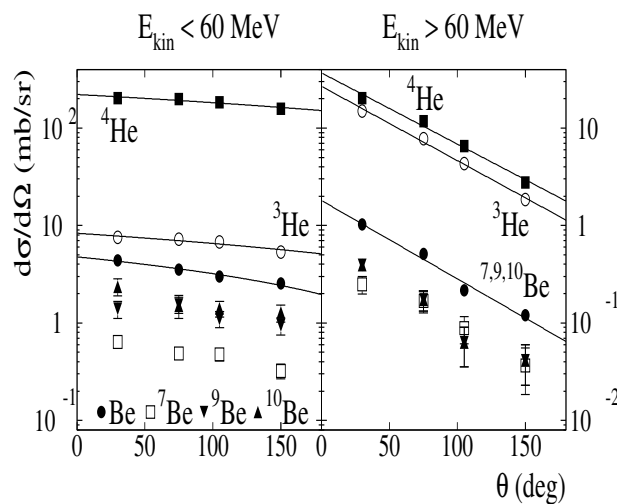


Figure 7.33: Angular distribution of ${}^{3,4}\text{He}$ and ${}^{7,9,10}\text{Be}$ emitted in the reaction 2.5 GeV p+Au. The yield with $E \leq 60$ MeV (left panel) and $E > 60$ MeV (right panel) is dominated by evaporation and pre-equilibrium, respectively.

⁶In respect to spallation reactions a Au-target behaves very similar to the Hg-target favoured for ESS.

spectra detected at 30° in respect to the proton beam are shown in Fig. 7.32 for the sum of all Be isotopes (\bullet) and for ${}^7\text{Be}$ separately (open squares). The ${}^7\text{Be}$ contribution in the low-energy range, which is dominated by statistical evaporation, is small as compared to ${}^9,{}^{10}\text{Be}$ (see right panel of Fig. 7.32), while for higher kinetic energies the yield arising from pre-equilibrium emission turns out to be identical for all three Be-isotopes. This result is also shown in Fig. 7.33, which exhibits the angular distribution of He and Be for kinetic energies below (left panel) and above (right panel) 60 MeV. The strong declines of the angular distributions for the higher energetic particles (right panel) are almost identical for all He and Be isotopes. Also the differential cross section for particles with equal Z , but different A do not vary substantially. However—as expected—lower kinetic particles show an almost isotropic angular distribution, and the slopes are similar for the various isotopes (left panel). The absolute differential cross sections, however, differ considerably, since they are governed by the binding energies of the composite particles. The ratio of the overall yield for Be and He amounts to 0.02, corresponding to a total production cross section of 8 mb, 20 mb and 20 mb for ${}^7\text{Be}$, ${}^9\text{Be}$ and ${}^{10}\text{Be}$, respectively.

Fission

The experimental challenge is to measure fission probabilities of hot nuclei at low spin up to highest E^* including also nuclei with higher fission barriers. For this purpose D. Hilscher et al. [Hil95, Pie94] proposed to study fission induced by high energetic light particles. As discussed in sec. 5.3 light ion-induced particles provide an ideal tool for the investigation of fission and other decay channels almost free of inducing collective excitations in the target nucleus. In this paragraph the experimental fission probability as a function of excitation energy, $P_f(E^*)$ is discussed. Angular correlations between α -particles and fission fragments (FFs) and the measurement of pre- and post scission α -multiplicities allow insights into the fission dynamics. $P_f(E^*)$ has also been calculated using statistical models taking dissipative effects into account [Gol96b, Gol99d, Jah99, Lot01]. Both - the experimental angular correlations as well as the simulations - determine an upper limit of the pre-saddle delay time of $\tau_f \leq 0.5 \times 10^{-21}$ s.

Integrated fission cross sections have been measured for a large variety of projectiles on Thorium and Uranium. M.H. Simbel et al. studied proton-induced fission on Th and U in the energy range 0.1–30 GeV [Sim89]. These data exhibit an almost constant cross section up to 1 GeV and a decline beyond. This decline is interpreted by M.H. Simbel by the onset of multifragmentation [Gro86]. Also for d -, α - [Lau84] and heavy ion-induced [Beg92] fission of U and Th the fission cross section decreases with incident energy of the projectiles, respectively. This tendency is corroborated by Ar+Th measurements [Sch94], which show complementary an increase of (heavy residual) HR cross sections with increasing incident energy. X. Ledoux [Led95] measured the relative fission probability of 475 MeV- p and 2 GeV- ${}^3\text{He}$ -induced reactions on U as a function of evaporated neutrons.

Fig. 7.34 shows for 1.8 GeV p on Au and U the capability of the experimental set up to measure not only evaporative light particles (as discussed in the previous section), but also IMFs and FFs as characterized by the two bumps peaked at masses around $A = 10$ for IMFs and around $A = 100 \approx A_{\text{target}}/2$ for FFs. The substantially higher fission probability of the U as compared to Au is demonstrated. The angle-integrated,

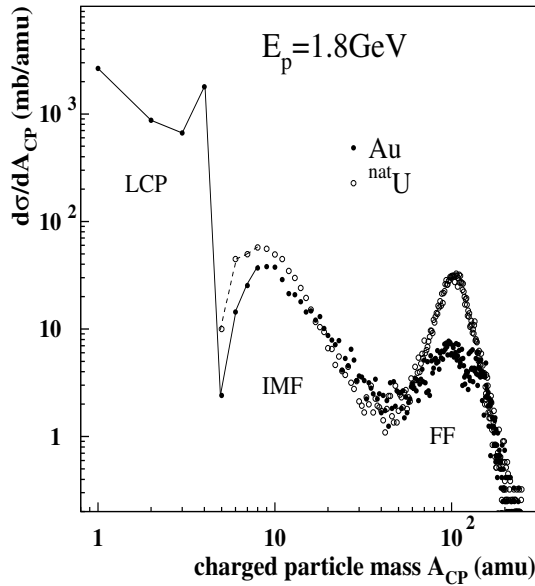


Figure 7.34: Mass distribution of LCP, IMF and FF for 1.8 GeV p on Au and U, not corrected for detection efficiency for $A > 4$. For proton cross sections the threshold $2.2 \leq E_p \leq 26$ MeV applies.

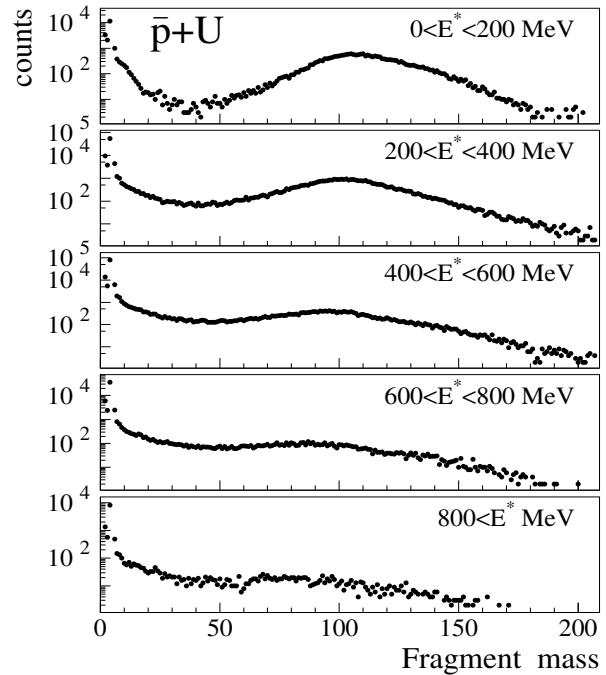


Figure 7.35: Mass distribution of fragments emitted in the reaction 1.2 GeV $\bar{p} + U$. The evolution with E^* is demonstrated.

total (E^* -integrated) fission cross sections amount to 185 ± 81 and 940 ± 200 mb for the Au and U targets, respectively. Clearly these cross sections increase with target fissility, as expected for conventional fission. For 3 GeV protons, associated with an E^* range comparable to that for 1.2 GeV \bar{p} , the latter cross sections were found as 103 ± 21 mb [Hud76] or 100 mb [Klo89] for Au and 1210 ± 180 mb [Hud76] or 1321 ± 100 mb [Rem70] for U. These cross sections are compatible with those of the present work within the error bars, although they appear slightly lower for Au and greater for U. Due to their low range and high probability to be stopped within the target material, heavy evaporation residues (HR) are not found in Fig. 7.34. The detection of HR even though with low efficiency of about 6% at $E^* = 200$ MeV and 35% at highest E^* for the same reactions was subject of a recent publications by B. Lott, F. Goldenbaum and U. Jahnke et al. [Lot01, Jah99].

Fig. 7.35 presents as an example for the reaction 1.22 GeV $\bar{p} + U$ the measured mass distribution for different cuts in E^* . Due to the relatively short path length for the time of flight of 10 cm, the mass resolution (RMS) of fragments being identified by energy versus time of flight correlations is about 3 mass units for fragment mass $A = 20$ and about 10 mass units for $A = 100$. For E^* below 200 MeV the FF dominate in the mass region around $A = 110$ and are well separated from the IMFs and LCPs. Also in Fig. 7.35 the expected mass peak for HR, fragments with mass around $A = 200$, are not visible, because HR are as already mentioned too slow to escape from the 2 mg/cm^2 U-target. At larger excitation energies the different decay modes become more and more superimposed and the question is whether any new decay mechanisms might be identified. For highest $E^* > 800$ MeV, heavy fragments up to $A = 150$ are observed. The associated mass of the detected light particles (n,p, α) including the IMFs is about 60 and thus the mass region

around 150 in the lower panel of Fig. 7.35 corresponds most likely to those heavy residues which got enough energy (mainly from recoil of light particles during the decay chain) to be detected, whereas the lower mass region corresponds predominantly to FF as will be shown below. In order to make the identification less ambiguous for binary fission, events with at least two detected heavy fragments were selected in the further data analysis.

Fig. 7.36 shows (as \bullet) the sum of the masses of the two heaviest fragments $A_1 + A_2$ detected as a function of E^* . A condition $A_1 \geq A_2 > 20$ has been applied. The measured sum of $A_1 + A_2$ agrees well with theoretical predictions (dotted line in Fig. 7.36) performed with the INC [Gol88] coupled to the evaporation code GEMINI [Cha88, Cha95]. For GEMINI a constant level density of $a = A/10$ has been chosen and no corrections for dynamical effects have been considered. Also shown in Fig. 7.36 is the total mass of detected particles $A_1 + A_2 + n + p + \alpha + \text{IMFs}$ (solid line) which agrees very well with the calculated mass following INC+GEMINI predictions (not plotted here). The contribution from IMFs is demonstrated by the dashed line in Fig. 7.36 which does not include IMFs in the total detected mass. Since the average IMF multiplicity $\langle M_{IMF} \rangle$ is around one at high E^* as will be shown, the mean mass carried off by an IMF is about 10 mass units.

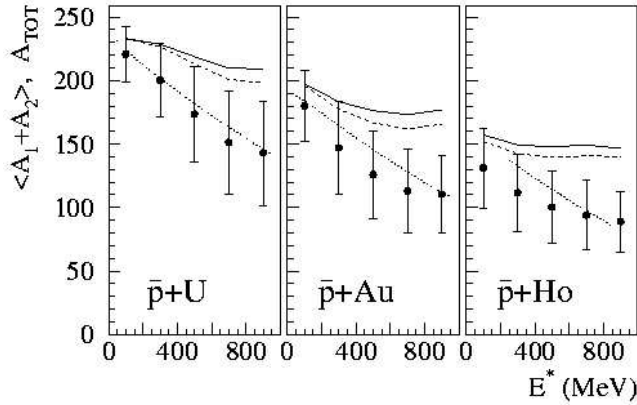


Figure 7.36: Measured FF mass $A_1 + A_2$ (\bullet) as a function of E^* for $\bar{p}+U, Au$ and Ho . The error bars correspond to the RMS of the distribution; dotted line: INC+GEMINI simulation for $A_1 + A_2$; solid (dashed) line corresponds to the total detected mass (not) including IMFs.

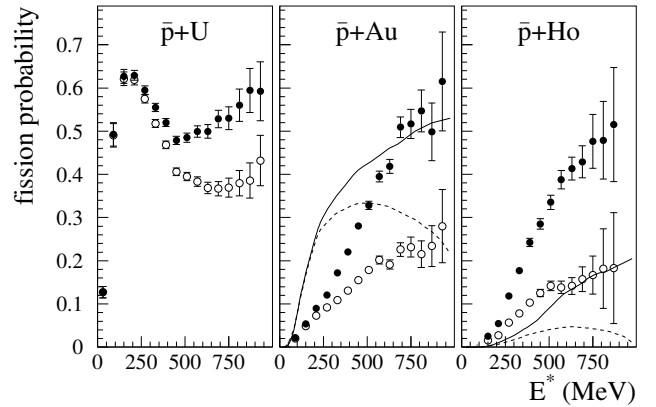


Figure 7.37: Fission probability for 1.22 GeV \bar{p} -induced reactions on U, Au and Ho as a function of E^* . \bullet : $A_1 \geq A_2 > 20$, \circ : $A_1 \geq A_2 > 40$; the solid (dashed) lines are the result of INC+GEMINI calculations for FF selected with cuts $A_1 \geq A_2 > 20$ and $A_1 \geq A_2 > 40$, respectively.

Fig. 7.37 shows the fission probability $P_f(E^*)$ for 1.22 GeV \bar{p} -induced reactions on U, Au and Ho as a function of E^* . A slow and continuous increase of $P_f(E^*)$ with E^* is observed for Au and Ho as well as a broad maximum near 150 MeV for U. In case of U, the high P_f (65%) at low E^* is related to the low fission barrier while the decrease at higher E^* might be a consequence of the onset of competing processes [Gol96b] and the depletion of the target nucleus in the INC step (cf. Fig. 7.36). For $E^* \geq 800$ MeV the fission process approaches 50% of the reaction cross section for U, Au and Ho-like nuclei. For events with a selection $A_1 \geq A_2 > 20$ the integrated P_f for U, Au and Ho are $P_f = 49 \pm 5, 16 \pm 3$ and $14 \pm 3\%$, respectively. When applying a condition $A_1 \geq A_2 > 40$

on the FFs, P_f drops down to $P_f = 44 \pm 5, 9 \pm 3$ and $6 \pm 2\%$, respectively. The latter values are in good agreement with previously published results on the same data [Sch97] however obtained with a different data analysis method. In particular at high E^* and with the condition $A_1 \geq A_2 > 40$ (\circ in Fig. 7.37) P_f is much smaller than in case the mass cut is selected at 20 mass units (\bullet). This is mainly related to the mass of the fissioning nucleus drastically decreasing with E^* by LCP and IMF emission as indicated in Fig. 7.36. Additionally it is expected, that as a consequence of an onset of all asymmetric mass splits at high E^* , the FF-mass distribution is much broader than at low E^* . For Au and Ho the INC+GEMINI predictions for P_f also shown in Fig. 7.37 differ significantly from the experimental data. It should however be noted that at about $E^* = 500$ MeV the compound nucleus lifetime becomes as short as 10^{-22} s, i.e. as short as the equilibration time and that therefore the applicability of the evaporation/fission model GEMINI in the high energy regime may become questionable. Also the calculations were performed with a simple set of parameters, as the level density parameter taken to be $a = A/10$, no difference between the level density at the equilibrium deformation and at the saddle point and no corrections for dynamical effects taken into account. When extending the condition of two FF in the binary fission process being larger than 20(40) mass units it is of particular interest to study the probability that *three* fragments are larger than 20(40). For the highest E^* and reactions on U, Au or Ho about 10-15% (1-3%) of the fission events contain three fragments with masses larger than 20(40), respectively. The probability for a mass split into three fragments heavier than 20 or 40 mass units is about 5-8% or less than $2-8 \times 10^{-3}$, respectively. There is no transition towards multifragmentation observed, as will be discussed in the following section.

A frequently raised question is the time scale of the fission process [Hil92, Gol96b]. The NESSI data allow to draw at least a qualitative picture. The total kinetic energy of the FF, TKE, is very close to the Coulomb repulsion energy calculated for two sticking spherical fragments [Vio85]. Fig. 7.38 displays the relative velocity of the two heaviest FF normalized to the Coulomb velocity v_{Coul} that would be expected for the measured fragments of mass A_1 and A_2 as calculated with the prescription given in ref. [Hin87]. The non-measured charge of the FF was assumed to be equal to the charges of the stable nuclei of mass A_1, A_2 . The pattern of the velocity plots shown in Fig. 7.38 is very similar at low, medium and high E^* . The conclusion, that the fission process is slow can be obtained from the angular correlations of light particles in respect to the fission axis. Fig. 7.39 displays the invariant cross section of alpha particle velocities in respect to the fission axis. The important point is that the velocities are mainly on a circle centered at $v_{\parallel}=0$ indicating that the alphas are essentially emitted prior to acceleration of the FF in their mutual Coulomb field. If the α -particles were evaporated from the accelerated FFs, circles around the centers of the respective fragment velocities (centers of the histograms) with somewhat smaller radii resulting from lower Coulomb repulsion would be expected. The message from this plot is that most of the evaporation precedes scission, or that the fission process is slow and the FFs are relatively cold at scission. Such a conclusion had been drawn previously and light particles were found to be mostly evaporated before scission [Hil92] however at lower E^* ; here, it is important that fission retains this singularity up to much higher E^* .

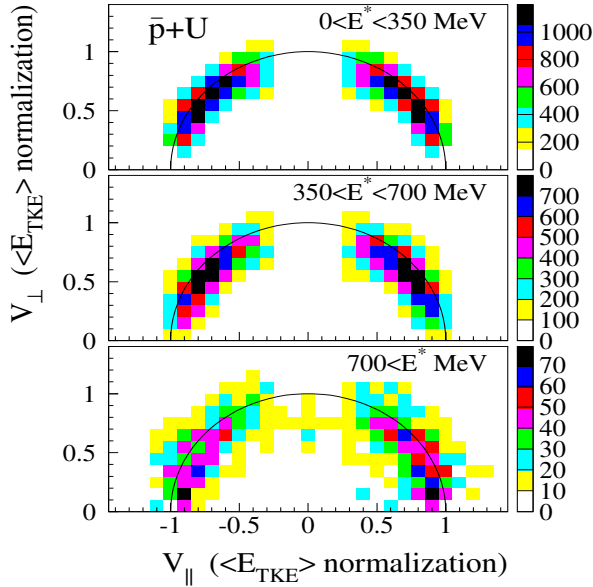


Figure 7.38: *Invariant cross section (in relative units) of the two heaviest FF's ($A_1 \geq A_2 > 20$) relative velocity plotted in respect to the beam axis for 1.22 GeV $\bar{p}+U$ and three bins of E^* . Rings of radius 1 represent expected Coulomb velocities. The “hole” in the data around $\theta = 90^\circ$ is due to the target shadow effect.*

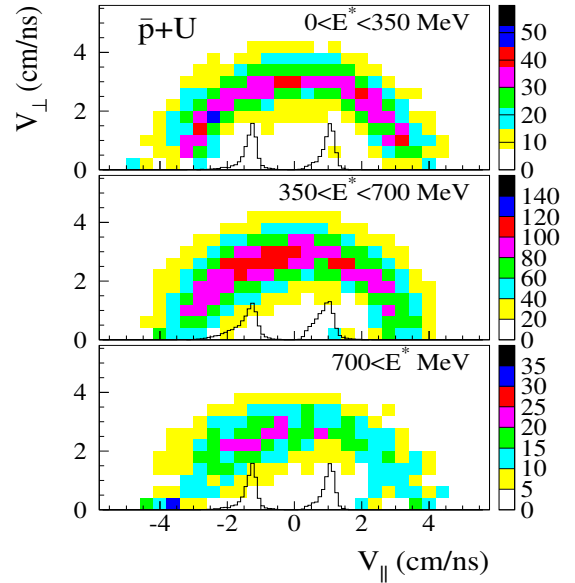


Figure 7.39: *Invariant cross section of alpha particle velocities in respect to the fission axis in the lab-system for 1.22 GeV $\bar{p}+U$ and three bins of E^* . The included histograms correspond to the velocity distributions of the fission fragments A_1, A_2 at positive and negative v_{\parallel} , respectively and $A_1 \geq A_2 > 20$.*

Because of the large extension in E^* of the present experiment, $P_f(E^*)$ becomes very sensitive as compared to previous investigations [Mor95b], to the issue of the transient time τ for fission (as introduced in sec. 4.5.1). An increased τ allows for a longer presaddle evaporation and consequently for a stronger reduction of E^* and therefore smaller $P_f(E^*)$. Calculations introducing such a delay in the range of $\tau = 0.1$ to 2×10^{-21} s however demonstrate that any delay in excess of about 0.5×10^{-21} s would considerably worsen the agreement with the data shown in Fig. 7.37.

Summarized, the observations presented in Figs. 7.36, 7.38 and 7.39 are consistent with the expectations of a binary and slow fission, which is present up to extreme excitations.

Vaporization and Multifragmentation

Besides the evaporation and fission, the event group with IMFs as the heaviest detected fragments deserves particular attention in the context of multifragmentation (MF). The question is whether these events stem from true MF, i.e., the complete fragmentation solely into IMFs and light particles, or are only the remnants from events where heavier masses have eluded detection. Such processes can be reliably identified only using highly efficient detector arrays like NESSI or the one which is reported by the INDRA collaboration [Bac96, Riv96, Bor96]. The INDRA collaboration observed the onset of vaporization in the Ar+Ni reaction at an available energy of 12 MeV/nucleon for the excitation of the

composite system with an overall probability of 5×10^{-6} . In the following the observations made for 1.2 GeV \bar{p} induced reactions on Cu (1.1 mg/cm²) and Ag (1.5 mg/cm²) targets are discussed as a function of E^* . It has been demonstrated in sec. 7.1.2 page 106 ff., Tab. 7.6 and refs. [Hil95c, Gol96, Jah96, Lot97, Sch97, Pie99, Jah99] that the maximum thermal excitation energy in heavy nuclei (Ho-U) is about 4-5 MeV/nucleon. The conclusion drawn for such energies was that, essentially, the nucleus either survives as a self bound entity (evaporation residue), or undergoes fission. However for lighter nuclei such as Cu, excitation energies larger than the total binding energy of the system are expected and thus vaporization might be reached [Bon95, Fri90b, Gro90].

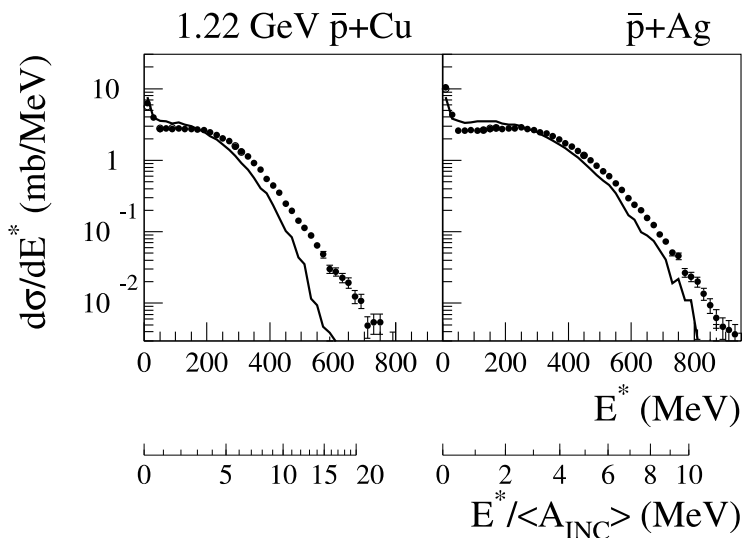


Figure 7.40: Reconstructed experimental excitation energy distributions $d\sigma/dE^*$ (\bullet) for \bar{p} (1.2 GeV)+Cu (left panel) and Ag (right panel). Lines correspond to INC-calculations [Ilj94, Gol88]. The bottom scale shows E^* divided by the average mass of the hot nucleus $A_{\text{hot}} = \langle A_{\text{INC}} \rangle$ at equilibrium, where $\langle A_{\text{INC}} \rangle$ is taken from INC-model simulation.

The reconstructed experimental excitation energy distributions $d\sigma/dE^*$ for Cu and Ag following \bar{p} -induced reactions are shown in Fig. 7.40 as solid dots. The experimental results are in good agreement with the predictions on INC-model calculations. Both distributions extend beyond the total binding energy (≈ 8 MeV/nucleon) and, hence, processes such as MF and vaporization are energetically possible in both reactions.

For both systems studied, a continuous decrease of the heaviest detected fragment is observed with increasing E^* . The “canonical” $A = 4$ limit is reached only for the $\bar{p} + \text{Cu}$ system, at E^* of about 350 MeV or 7.5 MeV/nucleon, taking into account the loss of mass in the INC stage of the process. For the $\bar{p} + \text{Ag}$ reaction, however, the heaviest detected fragment is always larger than about 15 mass units. For the $\bar{p} + \text{Cu}$ reaction about 300 good candidates for vaporization events were detected—corresponding to a cross section of about 3 ± 1 mb or 0.3% of the total reaction cross section. The angular distribution of evaporated-like LCPs of this event class is almost isotropic, similar to the distribution of particles from other decay modes—indicating the vaporization of a thermalized source. The total probability for vaporization in the current experiment is found to be a factor of 10 larger than the value reported at similar E^* by the INDRA-collaboration [Bac96, Bor96, Riv96]. This discrepancy might be associated with the faster heating mediated by \bar{p} - compared to heavy-ion reactions.

The ratio of vaporization cross section relative to the reaction cross section is presented for the $\bar{p} + \text{Cu}$ system in Fig. 7.41 as a function of E^* . Even for highest E^* (600 MeV or

15 MeV/nucleon) this ratio does not exceed 15%. The dashed line illustrates the same observable predicted by the GEMINI code. As already mentioned note that GEMINI predictions should be taken with some care because the fact that the emission times are large compared to the energy relaxation times (as is implicitly assumed in sequential-evaporation models) might *not* be fulfilled at E^* larger than about 4-5 MeV/nucleon. However, the excitation energy threshold for statistical decay depends mainly on the mass excess balance and Coulomb repulsion energy, so obviously GEMINI is at least able to estimate correctly the observed threshold energy for the $\bar{p} + \text{Cu}$ reaction. For the $\bar{p} + \text{Ag}$

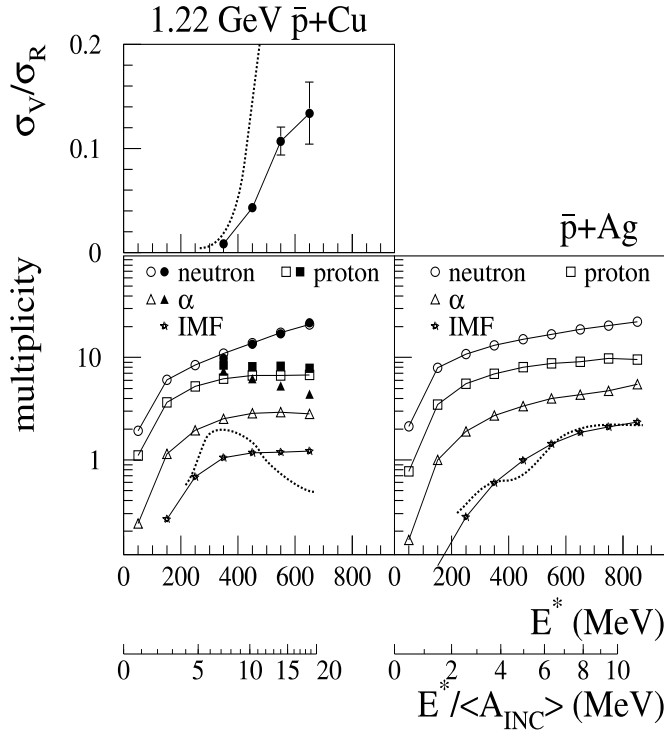


Figure 7.41: *Top panel:* ratio of vaporization cross section, σ_v , to the reaction cross section σ_R , for 1.2 GeV $\bar{p} + \text{Cu}$. The dashed line presents the INC+GEMINI simulation. *Bottom panels:* Mean multiplicities of n, LCPs ($Z=1,2$) and IMFs as a function of E^* for Cu (left panel) and Ag (right panel). The open (filled) symbols are for all (vaporization) events. The dashed lines illustrate the mean IMF multiplicity for INC+GEMINI calculations.

reaction the INC+GEMINI calculations predict the onset of vaporization at excitation energies about 9-10 MeV/nucleon, close to the maximum excitation energies observed in this reaction. This finding corroborates the observed absence of vaporization events among the collected data for the $\bar{p} + \text{Ag}$ system.

For both reactions $\bar{p} + \text{Cu}$, Ag the lower panels of Fig. 7.41 present the mean multiplicities of n, LCPs ($Z = 1, 2$) and IMFs ($4 \leq A_{\text{IMF}} \leq 25$) as functions of E^* . The open and solid symbols in the figure represent all events and vaporization events, respectively. Near

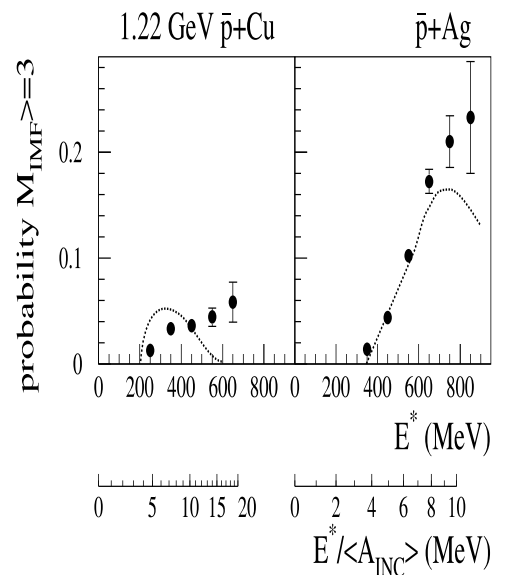


Figure 7.42: *Probability of events with detected (not corrected for efficiency) 3 or more IMFs as a function of E^* for $\bar{p} + \text{Cu}$ (left panel) and $\bar{p} + \text{Ag}$ (right panel) reactions. Dashed lines illustrate the prediction by the INC model coupled with the statistical model calculations GEMINI and filtered with the experimental detection efficiency.*

the vaporization threshold the ratio $M_{Z=2}/M_{Z=1}$ is approximately one and is considerably larger than for other decay modes at the same E^* . Beyond the vaporization threshold $M_{Z=2}$ is decreasing with E^* , while M_n is increasing. This finding was also observed by the INDRA collaboration for the Ar+Ni system at 12 MeV/nucleon [Bac96, Bor96, Riv96]. Close to the vaporization threshold the INC+GEMINI code also predicts $M_{Z=2}/M_{Z=1} \approx 1$.

IMF production in the 1.2 GeV $\bar{p} + \text{Cu, Ag}$ reactions are illustrated in Figs. 7.41 and 7.42. The average IMF multiplicity $\langle M_{\text{IMF}} \rangle$ saturates with increasing E^* around $\langle M_{\text{IMF}} \rangle \approx 1$ and $\langle M_{\text{IMF}} \rangle \approx 2$ for the $\bar{p} + \text{Cu}$ and $\bar{p} + \text{Ag}$ systems, respectively. No sudden onset of MF can be observed in the data and the trends in Fig. 7.41 do not indicate MF as a conceptually distinct process. Instead the observed multi-fragment events may reflect statistical fluctuations in the decay modes. This conclusion is justified all the more when looking at the good agreement of multi-fragment events of the sequential-emission model GEMINI with the experimental data. When defining MF as a process ending with 3 or more IMFs in the exit channel, one can obtain quantitative characteristics for the so-defined phenomenon. The relative abundances of events with 3 or more IMFs (not corrected for the IMF detection efficiency of $\varepsilon_{\text{IMF}} \approx 70\text{-}75\%$) is shown in Fig. 7.42 as a function of E^* . A saturation of the probability at about 5% is observed for the $\bar{p} + \text{Cu}$ system, while for the $\bar{p} + \text{Ag}$ system a monotonic increase up to 20% at highest E^* is deduced. In agreement with the predictions in ref. [Bon95], for both systems studied the threshold excitation for such MF is around $E^* \approx 4$ MeV/nucleon. This agreement, however, does not provide sufficient arguments for a conclusion that the IMF production proceeds in the studied systems according to the general scenario regarded in ref. [Bon95]. Rather, it is an indication that no exotic scenarios are needed in this case to explain the experimental results. For ion-induced reactions the phenomenon of MF [Kim89, Tro89, Kwi95, Lip94, Bow91] and the extraction of the time scales [Fox93, Fox94] have intensively been studied in the past. For \bar{p} -induced reactions, MF has been measured for the first time. The cross section for the MF process as defined is estimated at 20 ± 5 mb and 30 ± 7 mb for the \bar{p} -induced reactions on Cu and Ag targets, respectively. The latter value for the $\bar{p} + \text{Ag}$ system is very close to the 35 mb reported [Ren96] for $M_{\text{IMF}} \geq 3$ events in the $^3\text{He} + \text{Ag}$ reaction at 3.6 and 4.8 GeV. In any case the mean IMF multiplicities of the analysis in this work and the values quoted by K. Kwiatkowski et al. [Kwi95] for 4.8 GeV $^3\text{He} + ^{\text{nat}}\text{Ag}$ - and ^{197}Au -reactions are substantially smaller than the published data of V. Lips et al. [Lip94] for relativistic α -particle induced reactions. The discrepancies may be based on the larger angular momenta involved in ion-induced reaction mechanisms.

7.1.3 Conclusion NESSI

The NESSI experiment has been consulted to validate models with regard to reaction cross sections or reaction probabilities, neutron production cross sections and multiplicity distributions following proton induced reactions on thin and thick Hg, Pb and W targets in a broad range of incident energies. In the current contribution we outlined the influence of important parameters optionally chosen in the models, faced different approaches and confronted the model calculations with the experimental NESSI data.

Due to the large variety of options, parameters, and—to some extent—liberties in the various models it is almost impossible to judge the quality of the codes in respect to all

observables. Both the HERMES code system and the LCS or MCNPX packages master generally the prevision of *neutron* production in thick (and thin!) targets for a wide spectrum of incident energies and geometrical shapes of the target. The predictive power of reaction probabilities and neutron multiplicities or neutron multiplicity distributions is almost perfect for the HERMES code for all target materials under consideration (Hg, Pb, W), but shows—especially for LCS and MCNPX—some weaknesses in the high incident energy domain (2.5 GeV) for dense targets like tungsten. HERMES coincides with the NESSI experiment within $\pm 4\%$ for average neutron multiplicities and therefore fulfills the grade of accuracy requested to design a target-station for spallation neutron sources. Generally LCS and MCNPX overrate the neutron production by 4-8% as compared to HERMES calculations or the experiment. In LCS a part of these discrepancies can be eliminated by considering pre-equilibrium processes using the multistage exciton model. Currently HERMES appears to be best suited for predicting the neutron production in thick targets. The reaction cross sections predicted by all codes generally slightly exceed the experimental values. For Pb a minor deviation of 2% is observed while the discrepancy for W is at most 11%. Experimentally the observed neutron multiplicities were found to depend essentially on the incident available energy only while the variation with incident particle species for p, d, \bar{p}, K and π is within 10%.

In particular the H- and He- up to intermediate mass fragment production cross sections are of great importance for estimations of damages of target- and structure- materials of the planned spallation source since the lifetime of window and target materials is directly associated to those cross sections. Exactly these H- and He- measurements show—as compared to neutron production cross sections—large discrepancies not only between experiments and theory, but already among different models. Partly, the discrepancies within the models are understood: On the one hand the energy originally transferred to the nucleus during the intra nuclear cascade is differently re-distributed in various exit channels and on the other hand strongly different Coulomb barriers lead to differing production cross sections of charged particles. An acceptable overall agreement between NESSI data and model calculations is found for n, H- and He production cross sections only for the INCL2.0+GEMINI code. Presumably in the Bertini INC model too high thermal excitation energies are involved and the RAL fission/evaporation model is found to underestimate the Coulomb barriers. Even though in respect of such discrepancies the emission of charged particles is drastically affected, please note, that the abundance of neutron production is accurately described by all codes under consideration. The deficiencies are identified in the present contribution and shall be amended in future releases of high energy transport codes.

The studies have shown energetic (anti-)protons to be a promising tool to create high thermal excitation with minimum stimulation of collective motion. As for example excitation energy spectra for 1.2 GeV \bar{p} +Cu, Ho, Au and U extend with appreciable cross section (1% of σ_{reac}) up to 500 MeV for Cu and as far as about 1000 MeV for U.

The persistence of fission with its inherent slow time scale up to the highest E^* may be taken as the most obvious indication that the nucleus has survived this excitation as a self-bound and dense system. The total fission time till scission is long and pre-saddle delay has been shown to be shorter than 5×10^{-21} s. Multifragmentation (as defined by the simple requirement $M_{IMF} \geq 3$) of light nuclei ($A \leq 100$) sets in around excitation energies

of 4 MeV/nucleon and increases to a probability of about 5% (20%) at 10 MeV/nucleon for Cu and Ag targets bombarded with 1.2 GeV \bar{p} , respectively. Regarding the IMF production rates at highest E^* identified, the average IMF multiplicity in the $\bar{p} + \text{Cu}$ and $\bar{p} + \text{Ag}$ reactions attain values of 1 and 2, respectively. As a function of E^* , one observes for the $\bar{p} + \text{Cu}$ system the onset of vaporization at about 7.5 MeV/nucleon, with a total vaporization cross section not exceeding 3 mb. MF and vaporization are essentially thermally driven.

The complete implementation of a modern INC approach in MC4 is waiting for the latest release of the Liege (INCL4.2) code which is supposed to describe the excitation energy distributions and, as a consequence, the charged particle production cross sections superior than the Bertini based INC codes. This has already been indicated in the present contribution using the INCL2.0 version. It has also been demonstrated, that especially for large incident proton energies discrepancies between the codes in pion production are obvious, most likely due to different absorption cross sections of Δ -resonances. Therefore additional experimental data is required; in particular detailed pion spectra of GeV induced spallation reactions are in dire need of.

The excellent proton beam of COSY and the help of the COSY team is appreciated. This research was partly supported by the EU-TMR Program (Contract No.: FMRX-CT98-0244), the German Helmholtz-Strategy Fonds and the French program GEDEON.

7.2 Results PISA Experiment/Theory

The experiments at the internal beam of COSY allow to perform the investigation of the reactions induced by protons on thin targets (of the order of $50\text{-}200\mu\text{g}/\text{cm}^2$) thus they enable to get the cross sections without uncertainties (e.g. absorption and energy loss) involved by propagation of reaction products in the material of the target. The multiple circulation of the beam in the COSY ring is used to compensate for the small reaction rate of beam-protons with the thin target and to allow for measurement with optimal counting rates (of the order of $1000\text{-}2000\text{ s}^{-1}$) for a total intensity of about 10^{10} protons in the ring. The constant reaction rate is achieved by a negative back coupling between the counting rate and degree of overlapping of the proton beam with the surface of the target via controlled shifting of the beam in respect to the axis of the COSY beam line. Thus such an internal beam experiment offers a unique possibility to measure efficiently and precisely the cross sections on the thin targets.

Table 7.8: Energy measured for light ejectiles using Si-detectors (100 and 300 μm).

Ejectile	He	Li	Be	B	C
E_{min} / MeV	12	25	40	50	65
E_{max} / MeV	30	60	90	125	155

A first test measurement at COSY of one week allocated beam time at 1.9 GeV incident proton energy and Au target took place in August 2001 [Pisa01] with the aim to test all experimental equipment.

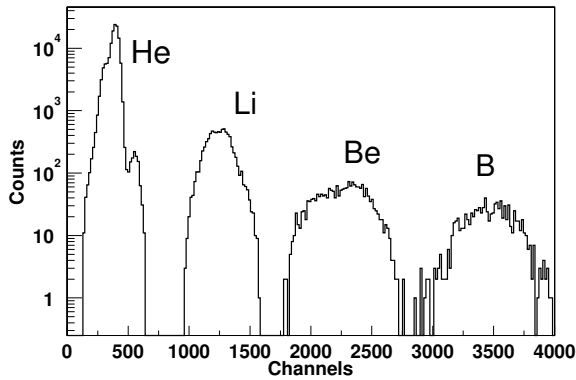


Figure 7.43: Histogram of coincidence events for light heavy-ions with $Z=2-5$ registered by Si-telescope – obtained by projection of two-dimensional spectrum $\Delta E(\text{Si1})-E(\text{Si2})$ onto the $\Delta E(\text{Si1})$ axis.

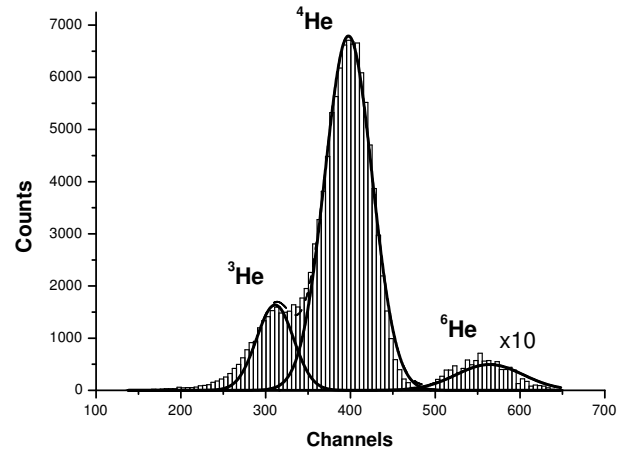


Figure 7.44: Same as in Fig. 7.43 but for He-ions. Solid lines show the Gaussian peaks fitted to the histogram. Note the linear scale now.

Unfortunately the experiment has been strongly hampered by the unexpected breakdown of a foil in the Bragg curve detector. Consequently only a part of the detecting system was tested. Here we present results obtained for two silicon detectors (100 and 300 μm) working as a telescope. The light ejectiles ($Z < 7$) were clearly visible in the coincidence spectra in the energy range given in Tab. 7.8.

As illustrated in Fig. 7.43 excellent Z identification has been achieved whereas only moderate A identification has been possible. Fig. 7.44 shows in a linear scale the spectra of He isotopes and demonstrates that due to the instability of ${}^5\text{He}$ a nice separation of ${}^6\text{He}$ from other isotopes is evident. The same is true for ${}^7\text{Be}$, since ${}^8\text{Be}$ is not stable. This enabled also to estimate the typical width of peaks in the spectra and thus allows to continue separation of other isotopes by fitting of Gaussian curves with fixed width parameter. Although Figs. 7.43 and 7.44 demonstrate that separation of particles originating from ejectiles differing in the mass number by 1 unit is, in principle, possible even with silicon telescope alone, strong overlapping of Gaussian peaks calls for some improvement of the detecting system. The mass number identification can be significantly improved by increasing the energy resolution of silicon detector telescope and/or by adding independent information from time-of-flight (TOF) detectors. Cooling the silicon detectors to $\sim -10^\circ\text{C}$ has shown to improve their energy resolution to values better than about 0.4%. This has shown to enable good mass resolution of “light heavy” ions (up to $A \sim 16$) by silicon telescope alone and allow to measure spectra of these ions in energy range of $\approx 3.5 \text{ MeV/amu}$ to 50 MeV/amu . The ions with larger mass number and energy range mentioned above will be stopped in the gas of the Bragg-curve detector or in the first Si-detector of the telescope and therefore cannot be identified by Si-telescope itself.

Previous tests of the Bragg curve detectors and phoswiches showed that they allow to achieve a good energy resolution for the lowest and the highest energies of light ejectiles, respectively. Tests of a prototype BCD have been performed for a variety of beam particles ranging from ${}^6\text{Li}$ to ${}^{16}\text{O}$ and energies available at INFN LNS Catania in Italy.

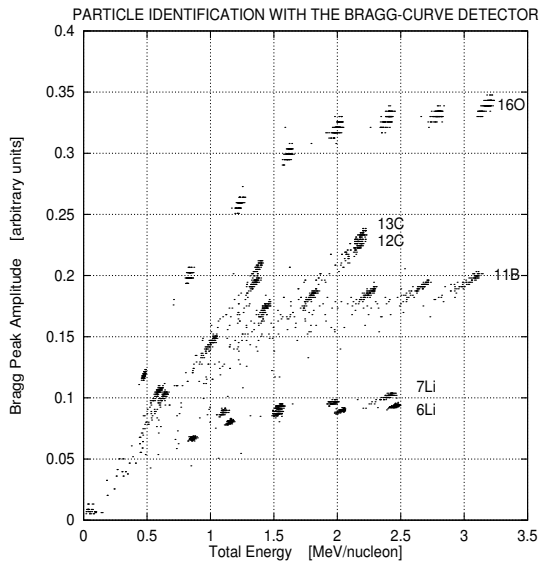


Figure 7.45: Identification of ions with a prototype Bragg Curve Detector.

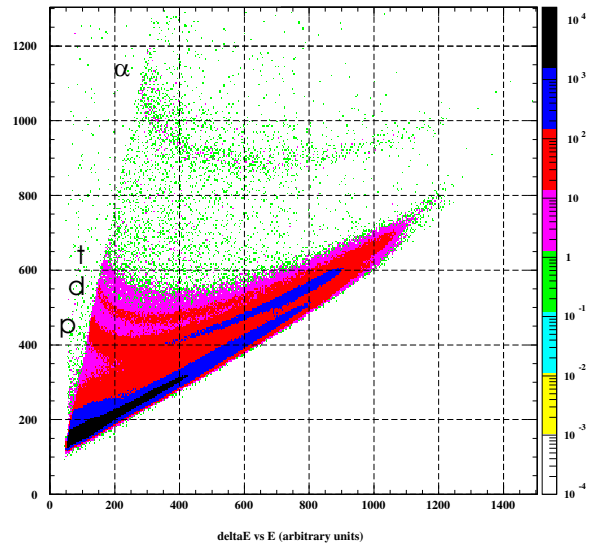


Figure 7.46: The "slow" (ΔE) versus "fast" (E) components spectrum from a phoswich detector.

The accelerated ions specified above have been elastically scattered on a gold target and registered by the BCD. Fig. 7.45 confirms very good charge and energy resolution of the BCD. Isotopic identification for light ions is possible - note the very clearly separated spots of events for ${}^7\text{Li}$ and ${}^6\text{Li}$.

In a test experiment the registration of the light particles was performed using the 1.4 GeV/c proton beam at COSY. The phoswich detector was placed at the distance of 70 cm and at the angle of 60 degrees with respect to thick carbon target. The anode signals from the photomultiplier were split into two branches, fast and slow. Separate discriminators produced "slow" (long) and "fast" (shorter) gate signals. The analog signals were digitized in separate charge-to-digital converters LeCroy 4300B using "fast" and "slow" gate signals. The duration of "fast" gate is 150 ns and the "slow" one 800 ns. The ΔE - E spectrum is shown in Fig. 7.46. The lines of p, d, t and α 's as well as the punching through particles are visible. It is planned also to use phoswich detectors with degraders for registration of higher energy light particles but with poorer energy resolution.

In the recently (Oct. 2002) performed experiment 1.9 GeV p+Ni(Au) we observed in the Bragg-curve detectors unambiguously identified charge of fragments from helium up to silicon, i.e. $2 \leq Z \leq 14$, and only small statistics of heaviest fragments prevented us to find the upper limit of the charge of emitted fragments. Figure 7.47 illustrates this showing the identification spectrum (Bragg curve peak BP versus energy E deposited in the gas volume) for the reaction 1.9 GeV p+Ni at the fragment emission angles of 15° (left panel) and 120° (right panel) in respect to the proton beam, respectively.

The measured range of kinetic energies is limited by the lower and upper registration thresholds. The first one is connected with the energy losses of the emerging fragments in the target material and the BCD window foils to be penetrated. In Fig. 7.47 the merging of the loci formed by the IMFs at the lowest energy (less than about 1 MeV/nucleon) corresponds to particles with insufficient energies to form their Bragg peak in the counter.

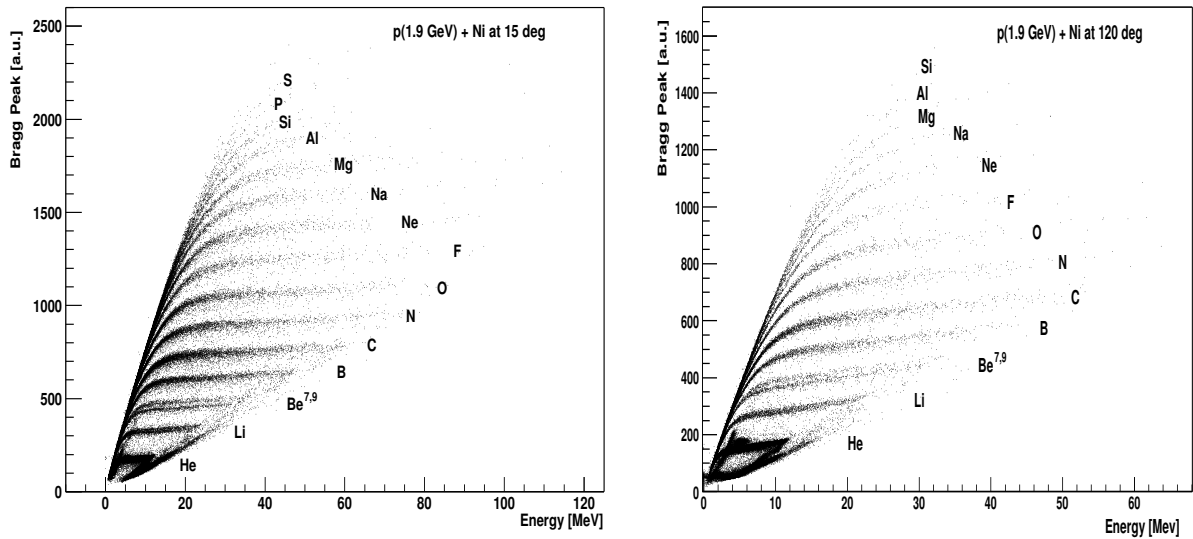


Figure 7.47: left panel: identification spectrum of emitted fragments in forward direction (15°) from 1.9 GeV $p+Ni$ collisions. The maximum of the Bragg peak is plotted versus energy deposited in the detector. The helium ions are not well visible in this representation but Li, Be, C up to Si lines can be distinguished, and there are also visible points in the area where Al and Si ions are expected. right panel: same as left panel, but for fragments detected in backward direction (120°).

The upper registration threshold is due to the finite active depth of the BCD which mainly depends on the used gas and its pressure. The measurable energy range depends also on the registered isotope and it is different for the forward and backward angles as Fig. 7.47 illustrates. Note that for forward angles the kinetic energy of particles emitted is larger than for particles emitted in backward direction. Generally the Coulomb threshold in the energy spectra of fragments produced in $p+Ni$ and $p+Au$ collisions is expected at $E_{kin} \approx 2 - 3$ MeV/nucleon which is well above the registration threshold of the BCD. Consequently, with the BCD the maximum of the kinetic energy spectra due to the Coulomb barrier could be clearly identified. The rather good separation of elements for $2 \leq Z \leq 16$ is demonstrated in Fig. 7.48.

The mass identification of the emitted fragments can be obtained in our experiment by two methods. First method consists in measuring the time-of-flight between two multi-channel plates placed in front of the Bragg-curve detectors. After selecting an element of given Z in the Bragg-curve identification spectrum shown in Fig. 7.47, an isotope separation or mass identification of the emitted fragments is possible due to different time-of-flight for different isotopes. As demonstrated in Fig. 7.49 our preliminary data analysis indicates that combination of the energy measured in the Bragg-curve detector with the TOF enables to distinguish isotopes at least for elements up to $^{13,14}N$. Note that due to the lack of 8Be , for $^{7,9}Be$ ions an isotopic separation was possible even in Fig. 7.47.

The second method of isotope identification consists in using Si-detector telescopes cooled down to -10 degrees C. Actually the telescope at 35° in respect to the proton beam consisted of four Si-detectors: 50, 100, 400 and 300 μm and 20, 50, 100 and 400 μm for the one mounted at 100° . Excellent mass identification of all simultaneously measured

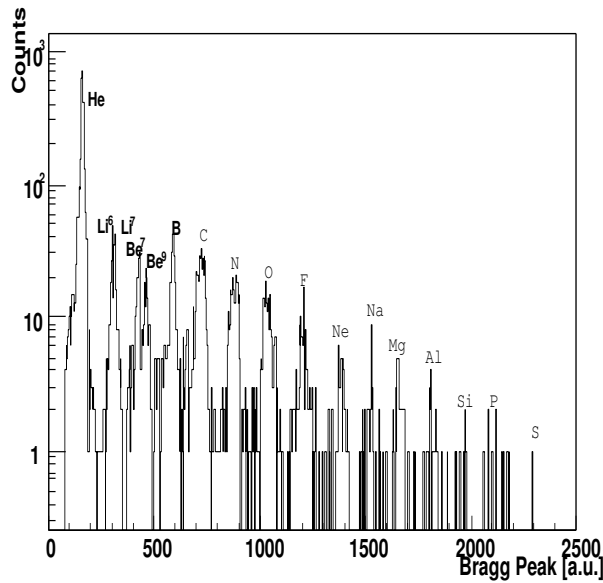


Figure 7.48: Separation of elements by projection of Fig. 7.47 (1.9 GeV $p+Ni$, 15°) onto the axis representing the Bragg peak. For the projection a cut for the kinetic energies of the particles has been performed at $1.3 \leq E_{\text{kin}} \leq 3$ MeV/N.

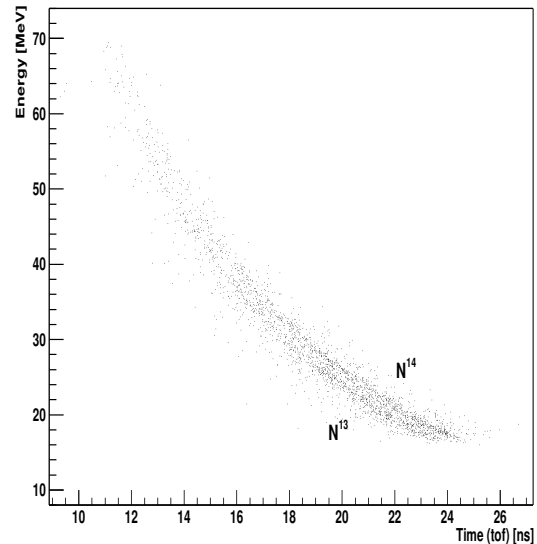


Figure 7.49: Mass identification spectrum of ejectiles emitted from $p+Ni$ collisions at 1.9 GeV proton energy. The energy deposited by $^{13,14}N$ ions in the BCD is plotted versus time-of-flight of these ions between two multi-channel plates.

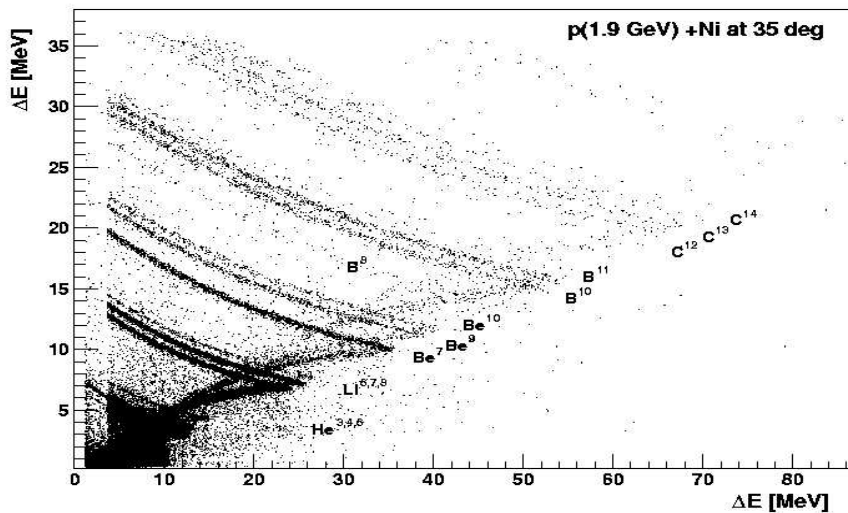


Figure 7.50: Mass identification spectrum of ejectiles emitted from $p+Ni$ collisions at 1.9 GeV at 35° in respect to the proton beam. Energy loss of the ejectiles in the first silicon detector ($50\mu\text{m}$ thick) is plotted versus energy loss in the second silicon detector ($100\mu\text{m}$) of the cooled Si telescope. The helium, (^4He and ^6He), lithium (^6Li , ^7Li , ^8Li), beryllium (^7Be , ^9Be , ^{10}Be), boron (^{10}B , ^{11}B), and carbon (^{11}C , ^{12}C , ^{13}C) ions are well separated. There are also visible individual points in this part of the figure where N ions are expected.

fragments from helium to carbon was obtained as shown in Fig. 7.50 for ejectiles emitted from p+Ni collisions at 1.9 GeV and 35° in respect to the proton beam. The solid angle of silicon telescopes has to be small in comparison to Bragg-curve detector in order to achieve good resolution. Note that the yield ratios of $^{7,9,10}\text{Be}$ and $^{8,10,11}\text{B}$ given in Fig. 7.50 reproduce the ones published in ref. [And98].

In summary, the recent test experiment has shown that we are able to measure using the proposed technique the products of proton–nucleus collisions with Z-identification up to at least $Z=14$ and isotope identification to masses up to 12-13. Note that a detailed energy calibration has been performed for the energy of the spectra in Figs. 7.47 and 7.50. As can be clearly seen in the scatter plots (Fig. 7.47), there is a turning in the particle loci which correspond to ions that stop just at the anode of the BCD. One can then determine the particle's energy from the range-energy relation in the isobutane gas at given pressure. Providing an extra reference, the relations between different Z and its energies, thus deduced, are consistent. Currently the analysis for double differential cross sections obtained for fragment production at laboratory angles 15° and 120° is in progress. The next beam time for PISA is requested for the early summer of 2003. It is desired that thinner films for the entrance windows are available to reduce the energy loss.

7.3 Data Library of H- and He in p-induced reactions

At the beginning of 2001 the creation of a data base [Pisa01] for hydrogen and helium production cross sections in a wide energy range (up to several GeV) on thin targets has been initiated in the framework of the HINDAS project (**H**igh and **I**ntermediate energy **N**uclear **D**ata for **A**ccelerator-driven **S**ystems). The motivation was essentially driven by the lack of cross sections for production of the lightest isotopes.

The data base is a compilation of experimental cross sections for proton-induced isotope production at energies from a few MeV to 10 GeV. There are also some data for energies up to 30 GeV. Presently, for proton-induced reactions, this compilation contains about 15,000 data points, for 38 targets of 50 elements. All data are derived from available literature and private communications. Each record of the data base contains the following information: atomic mass and atomic number of the target, incident energy of the projectile [MeV], type (A, Z) of ejectile, total production cross section [mb], error of the production cross section [mb], angle, references, comments. The whole database was originally written in "Microsoft Excel format". Actually this database is also available for users through the internet: <http://www.nuph.us.edu.pl/~pisa/baza/sign.html>. The user has a variety of options in order to select the data he is interested in. Also downloading the selected data in ASCII format is possible. The library is continuously in progress and frequently updated.

7.4 Results JESSICA Experiment/Theory

In the framework of JESSICA measurements with ambient water (300 K), H_2O -ice (20, 70 K) and polyethylene moderators have been performed. The proton beam intensity

amounts to $4 - 40 \times 10^8$ protons per pulse with a repetition rate of $1/30$ Hz, a pulse length of about 500 ns and an energy of 1.33 GeV. As mentioned in sec. 6.4.3, the measurement of the number of incident protons per pulse is indispensable to determine and compare the experimental and simulated neutron to proton ratios on an absolute scale.

As an example the left panel of Fig. 7.51 represents as a solid histogram the measured neutron flux density Φ of a decoupled H_2O -moderator mounted in the geometry as illustrated in Fig. 2.6, page 18. The according background spectrum of the same moderator, but Cd-detached has been subtracted bin-wise after normalization to the number of incident protons. As far as the position of the maximum and the shape of the distributions is concerned, the thermal spectra measured (solid histogram in Fig. 7.51) can be well reproduced by Monte-Carlo simulations (open symbols) using the MCNPX2.1.5 [Hug97] code system. The maxima of the curves are normalized to 1. The distinct hump at $t \approx 800 \mu s$ arising when the spectrum for Cd-shielded moderator is subtracted is a consequence of the neutron absorption cross sections of Cd. For advanced cold moderators first neutron scattering kernels for ice at 20 and 70 K were developed in collaboration with the Institut für Kernenergetik in Stuttgart [Ber02]. With these data, simulations using MCNPX [Hug97] are on the way.

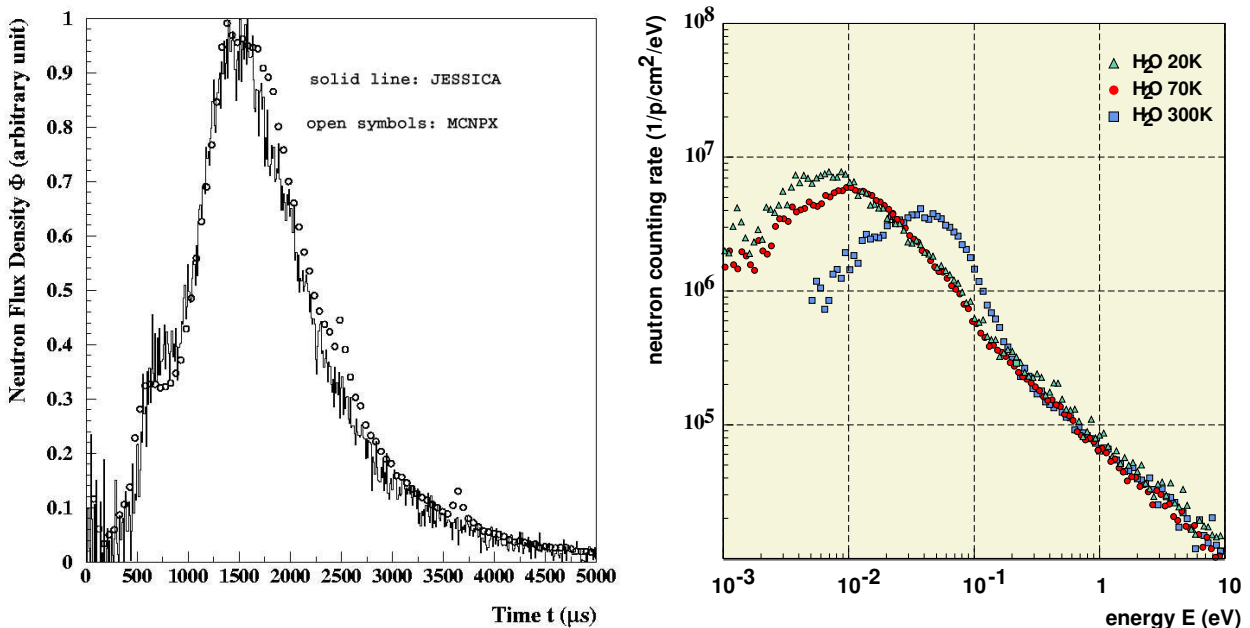


Figure 7.51: *left panel: Comparison between experimental (histogram) and simulated (open dots) neutron flux density of a H_2O -moderator at ambient temperature. For the calculations MCNPX2.1.5 [Hug97] has been used. right panel: measured neutron energy spectra for moderators of 20 and 70 K H_2O -ice and water at room temperature (300 K).*

In addition to energy spectra for the ambient H_2O -moderator also the neutron energy spectra⁷ for an ice moderator at 20 and 70 K are shown in the right panel of Fig. 7.51. The

⁷The energy is calculated via time of flight measurement as shown in the left panel of Fig. 7.51 and is neglecting the relatively short moderation times of a few 10 μs .

spectra are normalized to the number of incident protons as measured by the ICT and the active detector surface. Data are corrected for background and detector efficiency. It is worthwhile to mention, that the presented data are normalized on an absolute scale in contrast to older experiments which just scale the curves to the $1/E$ slope in the eV-region [Ino74, Ino79]. In contrast to the behaviour in the slowing down regime ($E \geq 0.2$ eV) where all three moderators show similar slopes, considerable differences are observed at lower energies. H_2O at 300 K is superior in the energy domain between $3 \times 10^{-2} \leq E \leq 0.2$ eV compared to ice moderators. Low energetic neutrons are significantly more abundant for the cold ice moderators. As expected for cold moderators the peak position is shifted towards lower neutron energies. The peak positions for 20, 70 and 300 K moderators are found at about 6 – 7, 10 and 30 meV, respectively. As far as the position of the maxima for cold H_2O -moderators at 20 K and the overall shape of the energy distributions is concerned an agreement to the data published by K. Inoue et al. [Ino74, Ino76, Ino79] (cf. Fig. 6.12, page 84) is obvious. Unfortunately those curves cannot be compared on an absolute scale.

Currently a comparison between simulations and experimental data can be performed only for ambient temperature water moderators due to the lack of neutron scattering kernels for cold moderator materials. In particular these neutron scattering kernels currently under development are intended to be confronted with data measured at JESSICA.

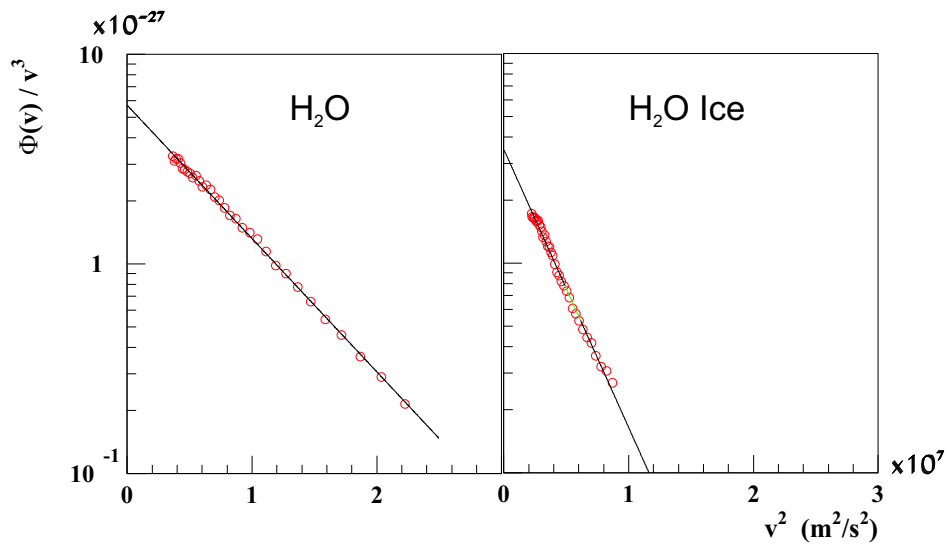


Figure 7.52: Regression lines for an ambient water (left panel) and a cold ice moderator (right panel) at liquid Nitrogen temperatures (70 K). From these fits the moderator temperatures can be derived.

In order to determine the temperature of an ambient water and a cold ice moderator, the time-of-flight spectra as shown in Fig. 7.51 following essentially a Maxwellian distribution, have been transformed to velocity spectra. Using the equation $\ln(\Phi(v)/v^3) = \text{const.} + (m/2 * k * T)v^2$ with velocity v , mass m , temperature T and Boltzmann constant k a linear regression has been performed in the range from 1.1 to 2.65 ms (cf. histograms in

Fig. 7.51) with a correlation coefficient larger than 0.999 for both moderators. For the ambient temperature water moderator (left panel of Fig. 7.52) the experimental data results to a temperature of 307 K—slightly higher than room temperature of about 300 K. The moderator temperature derived for the ice moderator is 147 K (right panel of Fig. 7.52) instead of 70 K of liquid Nitrogen. A careful interpretation might be that on the one hand the neutrons are not fully equilibrated in the cold moderator, on the other hand because in ice neutrons might not effectively couple to rotational or vibrational modes.

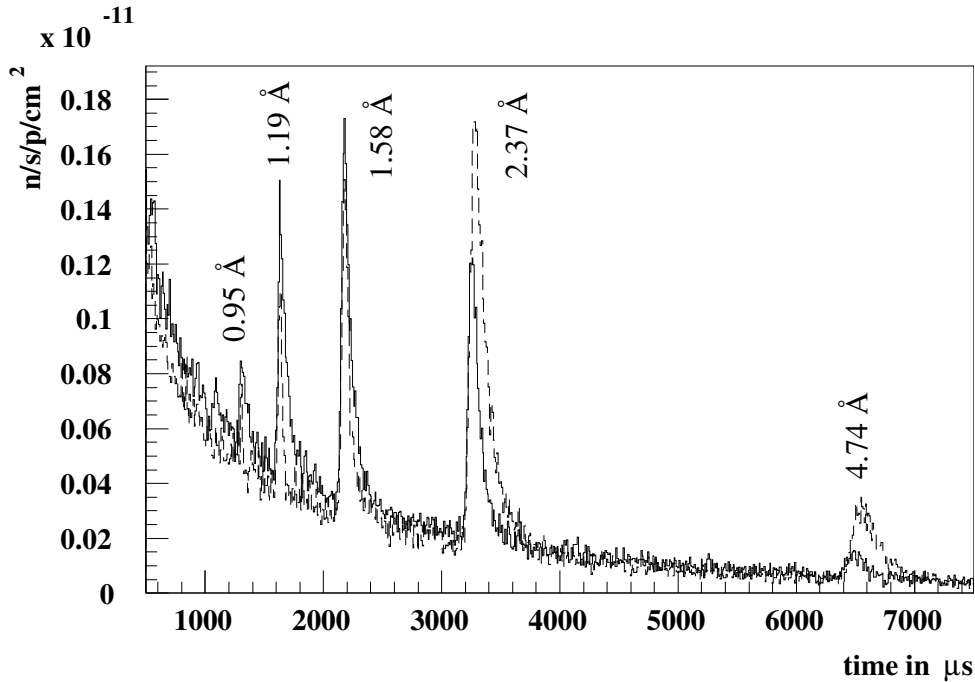


Figure 7.53: Comparison of scattered neutrons from an ambient water (solid line) and an 20 K cold ice moderator (dotted line). Different selected wavelengths are indicated.

Table 7.9: Pulse widths and decay times as a function of wavelength (1.19Å, 1.58Å and 2.37Å) for ambient temperature water (300 K) and ice moderators at 20K. (see Fig.7.53)

	1.19Å	1.58Å	2.37Å
300 K			
pulse width FWHM [μs]	60	90	100
decay constant [μs^{-1}]	0.016	0.014	0.015
20 K			
pulse width FWHM [μs]	30	50	90
decay constant [μs^{-1}]	0.057	0.039	0.019

In order to study the neutron flux densities as a function of wavelength, the neutrons were scattered according to equation 6.1 on a pyrolytic graphite crystal as described in Section 6.4 and detected by a second neutron detector. Time structures of neutron

pulses for five specific wavelengths (energies) are visible in Fig. 7.53: 0.95, 1.19, 1.57, 2.37 and 4.74 Å corresponding to 91.2, 58.10, 33.4, 14.6 and 3.66 meV, respectively. When comparing the ambient water (solid line in Fig. 7.53) and the 20 K ice moderator (dotted line) it can be seen that relative to the ambient water moderator the peak intensity for the ice moderator increases at longer wavelengths or smaller energies.

In particular for longer wavelengths cold moderators are therefore clearly superior to H_2O -moderators at room temperature as illustrated in Fig. 7.53. For these wavelength dependent time-of-flight measurements the pulse widths and the decay times of the pulses are listed in Tab. 7.9. As compared to ambient temperature water moderators, cold ice moderators exhibit 50%, 44% and 10% smaller pulse widths for wavelengths of 1.19Å, 1.58Å and 2.37Å, respectively. Furthermore the decay constant is higher—resulting in a faster decay of the pulse. These effects allow for a better time resolution in real neutron spallation sources.

In the future further measurements at low temperature for coupled and decoupled, shielded and poisoned moderators of various geometrical shapes and different properties are anticipated with special attention on methane-hydrate at 20 K and liquid hydrogen. Very preliminary data for methane-hydrate moderator experiments at JESSICA exist and are currently analysed. The data on methane hydrate already indicate for the very first time the benefit to combine ice and methane in terms of maximum neutron intensity over a broad range of energies. With the set of data gathered at JESSICA newly developed scattering kernels for neutron transport codes will be checked and optimized.

Chapter 8

Conclusion

The studies performed within this contribution aimed at obtaining fundamental information on GeV proton induced spallation reactions. Experimental investigations on such reactions have been carried out at various laboratories (CERN, COSY, GSI, SATURNE) with different, but complementary experimental methods. The results added to the knowledge and understanding of nuclear fragmentation in an energy range, which is also very important with regard to –amongst others– assessing radiobiological effects in nuclear medicine, resolving the origin and the anomalous abundances of the light nuclei produced in cosmic rays and provide and supplement cross sections to the data required for accelerator-driven transmutation research and spallation neutron sources.

Actually this work has thematically been motivated by the conception and the feasibility study of the high-intense European spallation neutron source ESS discussed as one of the large-scale scientific projects. Its design and reliable modeling requires the evaluation of several nuclear physics parameters having considerable impact on the design parameters of the source. How does a spallation target design affect the neutron yield?

It has been shown that spallation reactions induced on heavy nuclei allow the conversion of an incident GeV proton into several tens of evaporated neutrons. The objective in designing a spallation target is to increase the leakage of low-energy neutrons and to decrease the leakage of high energy neutrons from the target. Low energy neutrons that leak from the target are potentially useful, because suitable materials (moderators) can reduce their kinetic energy (by factors of 10 to 10^{10}) to produce pulsed neutron beams useful for research in materials science and nuclear physics. Three primary variables can affect the number of low-energy neutrons produced by a target:

- the energy of incident protons
- the target material
- the target geometry

More importantly, these factors also influence the energy and spatial distribution of neutrons leaking from the target. The lower the energy of neutrons leaking from the target, the more readily hydrogen and other moderating materials can moderate neutrons to energies suitable for neutron scattering experiments.

Why are neutrons needed? Due to their unique properties (charge neutrality and deep penetration, magnetic moment, energy-momentum correlation, large scattering cross section for light elements as hydrogen and oxygen, sensitivity to neighbouring elements, strongly isotope-dependent scattering length, ...) neutrons play an extremely important scientific role as has been addressed in the motivation of this work. While pioneering experiments originally derived from solid state physics, later significant contributions in materials- and life sciences emerged as corroborated by the donation of the Nobel price to Shull and Brockhouse in 1994. Nowadays experiments with neutrons span questions in particle physics and even in history of art. They could also be utilized for the transmutation of long-lived nuclear waste or for the feeding of sub-critical nuclear reactors.

Not only for a basic understanding of the spallation process as such, but also for a reliable modeling of the target stations of any accelerator driven system or spallation neutron source detailed theoretical models are indispensable for the calculation of the neutron production, radiation damage of materials and cause of radioactivity (tritium, ^7Be , heavy residues) in the target medium.

Therefore the main aim of the current contribution was to check, revise and improve the predictive power of nuclear reaction models for spallation source relevant data and the identification of deficiencies of existing intra-nuclear cascade and evaporation codes. The results of these findings have than been exploited to improve these codes. A multitude of nuclear model calculations has been performed and compared to latest benchmark experiments. In summary the three experiments NESSI, PISA and JESSICA carried out at the Cooler Synchrotron COSY in Jülich and performed in the framework of this work yielded conceptually new data on details of the physics of the spallation process.

The objective of the NESSI (NEutron Scintillator Silicon Detector)-collaboration was to investigate experimentally the neutron production in thick heavy-material target blocks, the radiation damage created by proton induced reactions in structural-, window-, and target-materials and to confront the experimental data with the results of computer codes as a function of the incident proton energy. Neutron production and multiplicity distributions have been measured for 0.4-2.5 GeV proton induced reactions in cylindrical targets of W, Hg, and Pb of different thicknesses (0.1-35 cm) and diameters (8-15 cm). In order to demonstrate the inherent capabilities of the high efficiency 4π sr neutron detector array employed, the methods to obtain the experimental observables (total reaction cross section, neutron multiplicity distribution, summed kinetic energy,...) have been described.

As concerns the fundamental physics aspect, in addition to the neutrons charged particle double differential cross sections as measured by the silicon ball BSiB, the 6 ΔE - ΔE -E telescopes of NESSI and the experiment PISA have been analysed. The whole, neutral and charged, de-excitation cascade of the excited reaction complex as well as heavier reaction products, i.e. intermediate mass and fission fragments and heavy residues have been registered eventwise. These studies allowed the investigation of evaporation and fission as well as more exotic decay channels as multifragmentation and vaporization. The two latter decay modes can be accounted for without evoking any substantial lowering in the nuclear density, brought about by an expansion due to thermal pressure or by dynamical effects in the intra-nuclear cascade. It has been found that in the energy range of 1-6 GeV π^\pm, p, \bar{p}, K and d -induced reactions result in very similar mean neutron multiplicities, i.e. the thermal excitation energy brought into a nucleus does not depend on

the incident particle species, but essentially on the total energy available in the entrance channel. A very good general agreement between experimental and calculated neutron multiplicities is found both for thin targets (one single nuclear reaction) and for thick targets (where also secondary reactions take part). If one decouples however the entire transport of the whole particle ensemble within thick targets and regards the primary reaction and specific decay channels (protons, neutrons, π ,...) separately, then serious inconsistencies not only between experiment and simulation, but also among the codes themselves arise. As for example measured production cross sections of H and He are drastically overestimated by the codes LAHET, HERMES, and FLUKA while the Intra-Nuclear-Cascade code INCL2.0 coupled with the evaporation code GEMINI reproduces the experimental data. Investigation of the energy spectra of light composite particles (isotopically separated) has shown experimentally that their emission is fed from both the INC and pre-equilibrium phase of the reaction as well as from the equilibrated evaporation, while the model generally does not allow for the composite particle emission from the INC phase. It could be demonstrated that the implementation of a simple coalescence model in the INC code can provide a reasonable description of the multiplicities of high-energy composite particles such as ${}^2\text{H}$, ${}^3\text{H}$ and ${}^3\text{He}$. However, this is done at the expense of ${}^1\text{H}$ which then fails to reproduce the experimental energy spectra.

The PISA (Proton Induced Spallation) experiment performed at the internal beam of the COSY storage ring in Jülich aims at precise measurement of double differential cross sections in a broad range of energies and angles for spallation reaction induced by protons of energies of 200-2500 MeV in various targets. PISA is complementary to the NESSI experiment since very clean and distinct spallation product identification (with atomic charge Z of the ejectiles up to $Z \sim 14$, $\Delta Z/Z \leq 0.025$) and an energy of detected particles as low as 0.5 MeV/nucleon could be achieved using Bragg curve spectroscopy. The data analysis on absolute cross sections, the evaluation of energy spectra and the comparison to known reference data of the first experiment is ongoing.

With the help of both experiments a variety of the identified model deficiencies have been eliminated by now. In general, in contrast to neutron production cross sections, charged particle cross sections show much more variations in literature both from the experimental point of view as well as from the computational one. The present work illustrates the importance of experimentally addressing all decay channels at play to enable a comprehensive understanding of the properties of highly excited nuclei to emerge. Although the presented experiments NESSI and PISA created a set of benchmark data allowing to face theoretical approaches with severe constraints, in order to fully understand quantitatively the complex spallation process, the reaction mechanism itself and the deexcitation of hot nuclear matter even more complete detection systems are mandatory for simultaneously registering in 4π solid angle all hadrons, mesons, fragments and heavy residuals in terms of multiplicities, kinetic energies, angular distributions and emission times. Eventually the competition between simultaneous and sequential emission of fragments, the production mechanism of intermediate-mass fragments and its relation to possible liquid-gas phase transition as well as the question of expansion of the excited nucleus during the emission of particles could then be addressed. A very first realistic step for approaching a more comprehensive collection of *all* ejectiles in pN reactions is the extension of our experimental PISA set up for the detection of mesons (π^\pm , π^0 , K^\pm , ...).

JESSICA—being a 1:1 “prototype” experiment for ESS, as concerns the nuclear performance of the target-moderator-reflector assembly, provided many new data on advanced cold moderators. Measurements with H₂O moderators at 300 K, 70 K and 20 K were performed. Also neutron time of flight measurements of coupled and decoupled H₂O moderators have been investigated and compared to MCNPX Monte-Carlo calculations. Effective moderator temperatures were extracted from analysing the neutron time of flight spectra. The time structure of neutron pulses was deduced for different neutron wavelengths by scattering the neutrons using a pyrolytic graphite crystal. For the very first time data on methane-hydrate moderators showed the advantage to combine ice and methane in terms of maximum neutron intensity over a broad range of energies. Using the set of data gathered at JESSICA enabled the development of new and improvement of existing scattering kernels for optimized neutron transport codes being of large interest in the international community.

Bibliography

- [Aba01] A. Abanades et al., *Experimental Verification of Neutron Phenomenology in Lead and of Transmutation by Adiabatic Resonance Crossing in Accelerator Driven Systems: A Summary of the TARC Project at CERN*. **Nucl.Instr.Meth.** **A463**, 586 (2001).
- [Aba02] A. Abanades et al., *Results from the TARC experiment: spallation neutron phenomenology in lead and neutron-driven nuclear transmutation by adiabatic resonance crossing*. **Nucl.Instr.Meth.** **A478(3)**, 577 (2002).
- [Abr71] R.J. Abrams et al., *Absorption cross sections of K^\pm on carbon and copper in the region 1.0–3.3 GeV/c*. **Phys.Rev.** **D4**, 3235 (1971).
- [Ack02] K. Ackerstaff et al., *A hadron-nucleus collision event generator for simulations at intermediate energies*. **NIM A** **491**, 492-506 (2002).
- [Adr93] O. Adriani et al., *Results from the L3 experiment at LEP*. **Phys.Rep.** **236**, 1 (1993).
- [Agn57] L.E. Agnew et al., *Experiments on antiprotons: Cross sections of complex nuclei*. **Phys.Rev.** **108**, No. 6, 1545 (1957).
- [Ahm93] S. Ahmad et al., *Antiproton-nucleus interactions at 5 to 9 GeV/c*. **Nucl.Phys.** **A558**, 393 (1993).
- [Aic85] J. Aichelin and G. Bertsch, *Numerical simulation of medium energy heavy ion reactions*. **Phys.Rev.** **C31**, 1730 (1985).
- [Aic91] J. Aichelin, **Phys.Rep.** **202**, 233 (1991).
- [Aih81] H. Aihara et al., *Absorption cross sections for antiprotons on carbon, aluminium and copper at 485 and 597 MeV/c*. **Nucl.Phys.** **A360**, 291 (1981).
- [AIP94] **AIP conference proc.** **346**, *Int.conf.on accelerator driven transmutation technologies and applications.*, Las Vegas NV, ISBN 1-56396-505-4, LA-UR-95-1792 (1994).
- [Ale90] J.M. Alexander et al., *Inverse reactions and the statistical evaporation model: Ingoing-wave boundary-condition and optical models*. **Phys.Rev.** **C42**, 1092 (1990).

- [Als65] F.S. Alsmiller, *A general category of solvable nucleon-meson cascade equations. Report ORNL-3746*, (1965).
- [Ami92] W.B. Amian et al., **Nucl.Sci.Eng.** **B112**, 78 (1992).
- [And92] L.N. Andronenko et al., **Nucl.Inst.Meth** **A312**, 467 (1992).
- [And94] L.N. Andronenko et al., **Nucl.Phys.Inst.Gatchina**, NP-38-1980 (1994).
- [And95] S. Andriamonje et al., **Phys.Lett.** **B348**, 697 (1995).
- [And98] L.N. Andronenko et al., **Nucl.Phys.Inst.Gatchina**, Preprint 2217, NP-3-1998, (1998).
- [Ant73] M. Antinucci et al., **Lett.Nuovo Cimento** **6**, 121 (1973).
- [App95] B. Appleton, **Proc. ICANS-XIII** Report PSI 95-02, 814 (1995).
- [Ara99] M. Arai et al., **Jour. Neutron Research Vol.8**, 71 (1999).
- [Arm84] T.W. Armstrong et al., **NIM** **222**, 540 (1984).
- [Atc89] F. Atchison, **Juel-Conf-34**, Kernforschungsanlage Juelich GmbH (1980).
- [Atc94] F. Atchison et al., *Aspects of calculational needs for spallation facilities. A Treatment of fission for HETC.*, **OECD Documents 1994**, Proc. of a specialists' meeting, pp. 349, May 30–Jun 1, ISSY-CES Molineaux, France (1994).
- [Axm84] A. Axmann und K. Gobrecht, *Die Wahl des kalten Moderators für die kalte Neutronenquelle des BER-II* **HMI-B 479**, (1984).
- [Bac96] Ch.O. Bacri et al., **Phys.Lett.** **B353**, 27 (1996).
- [Bar66] G.A. Bartholomew and P.R. Tunnicliffe, *The AECL study for an intense neutron generator. Report AECL-2600* (1966).
- [Bar78] G.A. Bartholomew et al., *Accelerator Breeder Concept. Atomic Energy of Canada Limited report AECL-6363*, (1978).
- [Bar73] V.S. Barashenkov et al., *Inelastic interactions of high energy nucleons with heavy nuclei.* **Nucl.Phys.** **A222**, 204 (1974).
- [Bar81] J. Barish et al., **ORNL/TM-7882**, Oak Ridge National Laboratory (1981).
- [Bar02] H. Barnert-Wiemer, *Conceptual design of a cold methane moderator system for the european spallation source ESS. Report Jül-3967*, ISSN 0944-2952, (2002).
- [Bau81] G.S. Bauer et al., *Realisierungsstudie zur Spallations-Neutronenquelle. Report Jül-Spez-113 and KfK 3175*, KFA Jülich and KfZ Karlsruhe (1981).
- [Bau85] G.S. Bauer et al., *The SNQ Target and Moderator System for an optimized Neutron Economy.* **IAEA-CN-46/79**, 267 (1985).

- [Bau86] W. Bauer et al., **Nucl.Phys. A452**, 699 (1986).
- [Bau92] W. Bauer et al., *Bubble and ring formation in nuclear fragmentation*. **Phys.Rev.Lett. 69**, 1888 (1992).
- [Bau96b] G. Baur et al., *Production of antihydrogen*. **Phys.Lett. B368**, 251 (1996).
- [Bau96] G.S. Bauer, *The european spallation source study, ESS, 2nd Int. Conf. on Accelerator driven Transmutation Technologies*, pp. 159, Kalmar, Sweden, June 3-7 (1996); <http://www.psi.ch/>.
- [Bau97] G.S. Bauer, *Pulsed Neutron Source -Moderator Engineering. Int. Workshop on Cold Moderators for Pulsed Neutron Sources*, Argonne, Illinois (USA), Sept.28-Oct.2 (1997).
- [Bea94] L. Beaulieu et al., *Excitation energies in statistical emission of light charged particles in heavy-ion reactions*. **TASCC-P94-24**, Preprint Chalk River Laboratories Canada, submitted to Phys.Lett.B. (1994).
- [Beg92] M. Begemann-Blaich et al., *Fission from Fe and Nb reactions with heavy targets at 50–100 MeV/nucleon*. **Phys.Rev. C45**, 677 (1992).
- [Bel73] J. Bell et al., *The ORNL Isotope Generation and Depletion Code*. **Report ORNL 118680** (1973).
- [Ben67] B.G. Bennett et al., *Legendre, Tschebyscheff and half-range Legendre polynomial solutions of the gamma ray transport equation in infinite homogeneous and two media geometry*. **USAEC report HASL-185** (1967).
- [Ben93] F. Benrachi et al., *Light particle emission in the reaction $^{144}\text{Sm} (^{32}\text{S}, \text{fission})$ at $E_{\text{lab}} = 838 \text{ MeV}$* . **Phys.Rev. C48**, 2340 (1993).
- [Ben94] G. Bendiscioli und D. Kharzeev, *Antinucleon-nucleon and antinucleon-nucleus interaction. A review of experimental data*. **Rivista Del Nuovo Cimento, Vol. 17**, No. 6, (1994).
- [Ben01] J. Benlliure et al., **Nucl. Phys A683**, 513 (2001).
- [Ber63] H.W. Bertini et al., **Phys. Rev. 134**, 1801 (1963).
- [Ber69] H.W. Bertini et al., **Phys. Rev. 188**, 1711 (1969).
- [Ber70] H.W. Bertini et al., **Phys. Rev. C1**, 423 (1970).
- [Ber72] H.W. Bertini et al., **Phys. Rev. 6**, 631 (1972).
- [Ber81] O. Bersillon, Report CEA-N-2227,NEANDC(France)220”L”, INDC(E) 49/L (1981).

- [Ber02] W. Bernnat et al., *Scattering kernels for cryogenic media 6th meeting of the int. collaboration on Advanced Cold Moderators (ACoM)*, Jülich, Germany, 11-13.Sep. (2002).
- [Bes79] H.J. Besch et al., *An experimental study of the antineutron-light nucleus annihilation at 1.44 GeV/c*. **Zeitschrift für Physik A292**, 197 (1979).
- [Ber96] O. Bersillon et al., *TIERCE: A code system for particles and radiation transport in thick targets.*, 2nd **Int. Conf. on Accelerator driven Transmutation Technologies**, pp. 520, Kalmar, Sweden, June 3-7 (1996).
- [Bie62] R.H. Bieri, W. Rutsch **Helvetica Physica Acta** **35**, 553 (1962).
- [Bie81] J.P. Biersack et al., **NIM** **174**, 257 (1980) and *Calculation of projected ranges - analytical solutions and a simple algorithm*. **NIM** **182/183**, 199 (1981).
- [Bla75] M. Blann, **Annu. Rev. Nucl. Sci** **25**, 123 (1975).
- [Bla94] M. Blann et al., *Evaluation of LLNL-ALICE code contribution.*, **OECD Documents** **1994**, Proc. of a specialists' meeting, pp. 23, May 30-Jun 1, ISSY-CES Moulinaux, France (1994).
- [Blo78] J. Blocki et al., *One-body dissipation and the super-viscosity of nuclei*. **Ann. Phys. (N.Y.)** **113**, 330 (1978).
- [Boh39] N. Bohr und J.A. Wheeler, *The mechanism of nuclear fission*. **Phys.Rev.** **56**, 426 (1939).
- [Boh75] A. Bohr et al., *Nuclear Structure*, Benjamin, New York (1975).
- [Boh85] W. Bohne et al., *The influence of plasma effects on the timing properties of surface-barrier detectors for heavy ions*. **NIM** **A240**, 145 (1985).
- [Boh92] W. Bohne et al., *The 4 π -Si-detector ball*. **HMI B507** Annual Report, 79 (1992), and W. Bohne et al., *Development of a 4 π -Si-detector ball*. **HMI B497** Annual Report, 92 (1991).
- [Bon86] J. Bondorf et al., *Statistical multifragmentation of nuclei. Decay of the fragments* **Nucl.Phys.** **A448**, 753 (1986); *Application of the model to finite nuclei disassembly*. **A444**,460 (1985); *Formation of the model*. **A443**, 321 (1985).
- [Bon95] J. Bondorf et al., **Phys.Rep.** **257**, 133 (1995)
- [Bor96] B. Borderie et al., **Phys.Lett.** **B388**, 224 (1996).
- [Bot87] A.S. Botvina et al., *Statistical simulation of the break-up of highly excited nuclei*. **Nucl.Phys.** **A475**, 663 (1987), cf also **Nucl.Phys.** **A448**, 753 (1986); **Nucl.Phys.** **A444**,460 (1985); **Nucl.Phys.** **A443**, 321 (1985).
- [Bot95] A.S. Botvina, D.H.E. Gross, *Sequential or simultaneous multifragmentation of nuclei*. **Phys.Lett.** **B344**, 6 (1995).

- [Bow91] D.R. Bowman et al., *Multifragment disintegration of the $^{129}\text{Xe}+^{197}\text{Au}$ system at $E/A=50$ MeV*. **Phys.Rev.Lett.** **67**, 1527 (1991).
- [Bow92] C.D. Bowman et al., **NIM A320**, 336 (1992).
- [Bow93] D.R. Bowman et al., *Sources and emission time scales in $E/A = 50$ MeV $^{129}\text{Xe}+^{nat}\text{Cu}$ reactions*. **Phys.Rev.Lett.** **70**, 3534 (1993).
- [Bre81] D.J.Brenner et al., **Proc. 4th Symp. on Neutron Dosimetry**, EUR-7448, Muenich-Neuherberg (1981).
- [Bre93] S. Bresson, *Etude de la réaction $^{208}\text{Pb}+^{197}\text{Au}$ à 29 MeV/u à l'aide de la multiplicité de neutrons associée*. Thèse, Université de Caen, (1993) und:
S. Bresson et al., *Fission of spin aligned projectile-like nuclei in the interaction of 29 MeV/nucleon ^{208}Pb with ^{197}Au* . **Phys.Lett.** **B294**, 33 (1992).
- [Bri97] J.F. Briesmeister, **LA-12625-M** (1997).
- [Bro94] BROND-2, A.I.Blokhin et al., *Current Status of Russian Evaluated Neutron Data Libraries*, **Proc. International Conference on Nuclear Data for Science and Technology**, Gatlinburg, Tennessee, USA, May 9-13, 1994, Vol. 2, p.695 (1994).
- [Bro97] T.A. Broome, *The ISIS Cold Moderators*, **Int. Workshop on Cold Moderators for Pulsed Neutron Sources**, ANL, Argonne (USA) 28.9-2.10.1997 (1997).
- [Bow96b] C. Bowman et al., **2nd Int. Conf. on Accelerator driven Transmutation Technologies**, pp. 11 and pp. 253, Kalmar, Sweden, June 3-7 (1996).
- [Bro96] J.C. Browne et al., **2nd Int. Conf. on Accelerator driven Transmutation Technologies**, pp. 101, Kalmar, Sweden, June 3-7 (1996); <http://public.lanl.gov/apt/>.
- [Bud99] A. Budzanowski et al, **IKP/COSY Annual Report 1999**, p.176
- [But91] R. Butsch et al., *Time scales for fusion-fission and quasifission from giant dipole resonance decay*. **Phys.Rev.** **C44**, No. 4, 1515 (1991).
- [Cah83] M. Cahay et al., *Low-energy antiproton annihilation in nuclei*. **Nucl.Phys.** **A393**, 237 (1983).
- [Car64] B.G. Carlson, *Numerical formulation and solution of neutron transport problems*. **Report LA-2996** (1964).
- [Car68] B.G. Carlson et al., *Transport theory, the method of discrete ordinates*. **Gordon and Breach** (1968).
- [Car93] F. Carminati et al., **Report CERN/AT/93-47(ET)**, (1993).
- [Car75] L.L. Carter et al., *Particle Transport simulation with the Monte-Carlo method*. **Tech. Inf Center, TID-2607** (1975).

- [Car79] Carroll et al., *Absorption cross sections of π^\pm , K^\pm , p and \bar{p} on nuclei between 60 and 280 GeV/c.* **Phys.Lett.** **80B**, 319 (1979).
- [Car78] J.M. Carpenter et al., *IPNS - A national Facility for Condensed Matter Research.* **Report ANL-78-88** (1978).
- [Car87] J.M. Carpenter, **Nature** **330**, 358 (1979).
- [Car90] J.M. Carpenter et al., **Proc. of the 11th meeting of the ICANS**, Tsukuba, Japan (1990).
- [Car02] J.M. Carpenter et al., *Time focusing of pulsed-source crystal analyzer spectrometers. Part I: general analysis, Part II: practical expressions.* **NIM A** **483**, pp.774 and pp.784 (2002).
- [Cec79] R.A. Cecil et al., *Improved predictions of neutron detection efficiencies for hydrocarbon scintillators from 1 MeV to about 300 MeV.* **NIM** **161**, 439 (1979).
- [Cen91] CENDL-2, Chinese Nuclear Data Center, *Communication of Nuclear Data Progress, No. 6*, **INDC(CPR)-025/L** (1991).
- [Cen92] CENDL-2, Chinese Nuclear Data Center, *Communication of Nuclear Data Progress, No. 6, Supplement*, **INDC(CPR)-028/L** (1992).
- [Cha88] R.J. Charity et al., *Systematics of complex fragment emission in niobium-induced reactions.* **Nucl.Phys.** **A483**, 371 (1988).
- [Cha91] N.C. Chao et al., **Nucl.Part.Phys.** **17**, 1851 (1991).
- [Cha95] R.J. Charity et al., *Limitations to presaddle neutron emission from fission-fragment charge distributions.* **Phys.Rev.** **C51**, 217 (1995).
- [Che96] S.L. Chen et al., *Emission of intermediate mass fragments during fission.* **Indiana reprint INC-40814-105**, (1995).
- [Chi96] S. Chiba et al., **Rev.Rev.** **C54**, 285 (1996).
- [Cho94] Ph. Chomaz et al., *Brownian one-body dynamics in nuclei.* **Phys.Rev.Lett.** **73**, No. 26, 3512 (1994).
- [Clo82] M.R. Clover, R.M. DeVries, N.J. DiGiacomo, and Y. Yariv, *Low energy antiproton-nucleus interactions.* **Phys.Rev.** **C26**, 2138 (1982).
- [Clo88] P. Cloth et al., HERMES, **Report Juel 2203**, ISSN 0366-0885, (1988).
- [Coc72] D.R.F. Cochran et al., **Phys. Rev.** **D6**, 3085 (1972).
- [Coh74] S. Cohen et al., *Equilibrium configurations of rotating charged or gravity liquid masses with surface tension.* **Ann. Phys. (N.Y.)** **82**, 557 (1974).

- [Col68] W.A. Coleman et al., *Thermal-neutron flux generation by high-energy protons*. **Nuclear Science and Engineering** **34**, 104 (1968).
- [Col89] N. Colonna et al., *Incomplete fusion and complex-fragment emission: A continuum of isotropic sources*. **Phys.Rev.** **62**, No 16, 1833 (1989).
- [Col92] N. Colonna et al., *Dynamics and statistics in multifragment production*. **Phys.Lett.** **B283**, 180 (1992).
- [Con01] **Intermediate Report on the Feasibility Study of CONCERT**, Saclay, March 1, 2001, draft available on a web page: <http://web.concert.free.fr/Publications/DraftReport.htm>.
- [Coo63] B.C. Cook, *Least structure solution of photonuclear yield functions*. **NIM** **24**, 256 (1963).
- [Cor56] B. Cork et al., *Antineutron produced from \bar{p} : in charge exchange collisions*. **Phys.Rev.** **104**, 1193 (1956).
- [Cre91] E. Crema et al., *Hot composite systems with $A > 200$ and $T > 6$ MeV*. **Phys.Lett.** **B258**, 266 (1991).
- [Cug81] J. Cugnon, T. Mizutani, and J. Vandermeulen, *Equilibration in relativistic nuclear collisions*. **Nucl.Phys.** **A352**, 505 (1981).
- [Cug84] J. Cugnon and J. Vandermeulen, *Antiproton nucleus interaction*. **Phys.Lett.** **B146**, 16 (1984).
- [Cug87] J.Cugnon, **Nucl. Phys.** **A462** 751 (1987).
- [Cug87a] J. Cugnon, P. Jasselette, and J. Vandermeulen, *Nucleus excitation and deexcitation following \bar{p} -annihilation at rest*. **Nucl.Phys.** **A470**, 558 (1987).
- [Cug89] J. Cugnon and J. Vandermeulen, *Antiproton nucleus interaction*. **AAnn.Phys.Fr.** **14**, 49 (1989), **Nucl.Phys.** **A500**, 701 (1989).
- [Cug89a] J. Cugnon, *Nuclear physics with antiprotons*. **Nucl.Phys.** **B8** (Proc. Suppl.), 255 (1989).
- [Cug92] J. Cugnon, *Antideuteron annihilation on nuclei*. **Nucl.Phys.** **A542**, 559 (1992).
- [Cug93] J. Cugnon, *Nuclear multifragmentation. Antiprotons versus protons and heavy ions*. Invited talk to NAN93-Second Biennial Workshop on Nucleon-Antinucleon Physics. **Yad.Fez.****57**, 1705 (1994).
- [Cug97a] J. Cugnon et al., **Nucl. Phys.** **A620**, 475 (1997).
- [Cug97b] J. Cugnon et al., **Phys.Rev.** **C56**, 2431 (1997).
- [Cug00] Joseph Cugnon, priv.communication.

- [Dak73] M. Dakowski et al., *Reconstruction of particle multiplicity distributions using the method of statistical regularization*. **NIM** **113**, 195 (1973).
- [Dav76] K.T.R. Davies et al., *Effect of viscosity on the dynamics of fission*. **Phys.Rev.** **C14**, 1977 (1976).
- [Den73] S.P. Denisov et al., *Absorption cross sections for pions, kaons, protons and antiprotons on complex nuclei in the 6 to 60 GeV/c momentum range*. **Nucl.Phys.** **B61**, 62 (1973).
- [Die98] J. Dietrich, **FZJ-IKP, COSY internal note** (1998).
- [Dol82] Th.J. Dolon, *Fusion research*. **Pergamon Press**, New York. (1982).
- [Dor65] D.E. Dorfan et al., *Observation of antideuterons*. **Phys.Rev.Lett.** **14**, 1003 (1965).
- [Dos58] I. Dostrovsky et al., **Phys. Rev.** **111**, 1659 (1958).
- [Dre62] L.Dresner, *EVAP- A FORTRAN program for calculating the evaporation of various particles from excited compound nuclei* **ORNL/TM-196**, Oak Ridge National Laboratory, (1962).
- [Dub67] H. Dubost et al., **J. Phys.** **28**, 257 (1967).
- [Dui82] P. Duinker, *Review of e^+e^- physics at PETRA*. **Rev.Mod.Phys.** **54**, 325 (1982).
- [Ead93] J. Eades, *How long do antiprotons last*. **Europhys.News** **24**, 172 (1993).
- [Egi87] T. von Egidy, *Interaction and annihilation of antiprotons and nuclei*. **Nature** **328**, No 6133, 773-778 (1987).
- [Egi95] T. von Egidy et al., *Nuclear Physics with Antiprotons*. **Z. Naturforsch.** **50a**, 1077 (1995).
- [Egi00] T. von Egidy et al., *Neutrons produced by 1.22 GeV antiproton interactions with nuclei*. **Eur. Phys. J.** **A8**, 197 (2000).
- [Eme69] D. Emendörfer, K.H. Höcker, *Theorie der Kernreaktoren.*, Teil II, BI-Hochschultaschenbücher 412/412a, (1969).
- [Emm75] M.B. Emmett, **ORNL-4972** (1975).
- [End79] ENDF-5 format, Revised by R. Kinsey, *ENDF-102, Data Formats and Procedures for the Evaluated Nuclear Data File, ENDF*, **BNL-NCS 50496, 2nd Edition (ENDF/B-V)** (1979).
- [End01] ENDF-6 format, (Ed.) V. McLane, *ENDF-102, Data Formats and Procedures for the Evaluated Nuclear Data File, ENDF-6*, **BNL-NCS 44945-01/04-Rev** (2001). available from <http://www.nndc.bnl.gov/nndcscr/documents/endl/endl102/>

- [ENEAO1] *A European roadmap for developing accelerator driven systems (ADS) for nuclear waste incineration.*, **ENEA report**, ISBN 88-8286-008-6 (2001).
- [Eng01] ESS-SAC/ENSA Workshop on *Scientific Trends in Condensed Matter Research and Instrumentation Opportunities at ESS*, Engelberg/Switzerland, 3.5.2001, **ESS/SAC Report/1/01**, report available on web page: http://www.ess-europe.de/documentation/ESS_SAC_ENSA_2001.pdf (2001).
- [Enke99] M. Enke et al., *Evolution of a spallation reaction: experiment and Monte-Carlo simulation.* **Nucl. Phys. A657**, 317 (1999).
- [Enq01] T. Enqvist et al., **Nucl. Phys. A686**, 481 (2001).
- [Ens72] J.E. Enstrom et al., *$\bar{N}N$ and $\bar{N}D$ interactions — A compilation.* Berkeley **LBL-58**, (1972).
- [ess96b] *Outline design of the european spallation neutron source.* Workshop on Long Pulse Spallation Sources, Hahn-Meitner-Institut Berlin vom 24.–27. Juni 1996, **ESS 95-30-M**, (1996).
- [ess96-II] **The European Spallation Source Study ESS, vol II, The Scientific Case**, ISBN 090 237 6500 and 090 237 6608, (1997); <http://www.risoe.dk/ESS>
- [ess96-III] The European Spallation Source Study ESS, vol III, The ESS Technical Study, **report ESS-96-53-M**, ISBN 090 237 6659, (1997); <http://www.fz-juelich.de/ESS/> and http://www.ess-europe.de/ess_js/about.html
- [ess02-I] **The ESS Project, Vol. I, European Source of Science.**, ISBN 3-89336-301-7, (2002).
- [ess02-II] **The ESS Project, Vol. II, New Science and Technology for the 21st Century.**, ISBN 3-89336-302-5, (2002).
- [ess02-III] **The ESS Project, Vol. III, Technical Report**, ISBN 3-89336-303-3, (2002).
- [ess02-IV] **The ESS Project, Vol. IV, Instruments and user support**, ISBN 3-89336-301-1, (2002).
- [Fab94] D. Fabris et al., *Alpha particle emission as a probe of the level density in highly excited $A \sim 200$ nuclei.* **Phys.Rev. C50**, No 3, 1261 (1994).
- [Fas90] A. Fasso et al., Landolt Börnstein, **New Series 1/11**, 71 (1990) and references therein.
- [Fas00] A. Fasso et al., *.Fluka: Status and Prospects for hadronic applications.*, **Proceedings of the Monte Carlo 2000 Conference**, Advanced Monte Carlo for radiation physics, particle transport simulation and applications, Lisbon, Portugal, Springer ISBN 3-540-41795-8, pp. 955, A.Kling et al.(Eds.), 23-26 October (2000).

- [Fat87] M. Fatyga et al., *Source properties of intermediate-mass fragments emitted in the reaction $^{14}\text{N} + ^{232}\text{Th}$ at $E/A=35$ MeV.* **Phys.Rev.** **58**, 2527 (1987).
- [Fer96] A. Ferrari and P.R. Sala, *The physics of high energy reactions.* Proceedings of the int. workshop on nuclear reaction data and nuclear reactor physics, Design and safety, Int. Centre for theoretical physics, Miramare-Trieste, Italy, Apr.15th - May 17th 1996 (1996).
- [Fox93] D. Fox et al., *Extraction of the multifragmentation time scale in intermediate energy heavy-ion reactions.* **Phys.Rev.** **C47**, No 2, 421 (1993).
- [Fox94] D. Fox et al., *Time scale for multifragmentation in intermediate energy heavy-ion reactions.* **Phys.Rev.** **C50**, No 5, 2424 (1994).
- [Fie92] D.E. Fields et al., *Neck emission of intermediate mass fragments in the fission of hot heavy nuclei.* **Phys.Rev.Lett.** **69**, 3713 (1992).
- [Fig95] P. Figuera et al., *Maximum excitation energy in fusion-evaporation reactions from light particle multiplicity measurements in $^{32}\text{S} + ^{58}\text{Ni}$ at 25 MeV/A.* **Z.Phys.** **A352**, 315 (1995).
- [Fil96] D. Filges et al., *The Status of Nuclear and Neutronic Model Calculations,* **2nd Int. Conf. on Accelerator driven Transmutation Technologies**, pp. 490, Kalmar, Sweden, June 3-7 (1996).
- [Fil97] D.Filges et al., **Proc.Int. Workshop on nuclear methods for transmutation of nuclear waste**, Dubna, World Scientific, 117 (1997).
- [Fil99] D. Filges et al., *ESS Target Development Experiments with up to 2.5 GeV incident Protons.* **Topical Meeting on Nuclear Applications of Accelerator Technology (AccApp99)**, Long Beach, California, Nov. 14th–18th (1999).
- [Fil00] D. Filges, F. Goldenbaum and Y.Yariv (editors): **Proceedings of the Fifth Workshop On Simulating Accelerator Radiation Environments.** (SARE-5), Models and Codes for Spallation Neutron Sources, ISSN 1433-559X, ESS 112-01-T, OECD-Headquarters, Paris, France, July 17-18, 2000, (edit. 2001).
- [Fil00b] D. Filges et al., *Spallation Reactions and Energy Deposition in Heavy Target Materials: Comparison of Measurements and MC-Calculations.* **ICANS-XV**, 15th Meeting of the Int. Collaboration on Advanced Neutron Sources, Tsukuba, Japan, Nov. 6-9,(2000).
- [Fil00c] D. Filges et al., *The HERMES Monte Carlo Program System: a versatile tool for spallation physics and detector applications.*, **Proceedings of the Monte Carlo 2000 Conference**, Advanced Monte Carlo for radiation physics, particle transport simulation and applications, Lisbon, Portugal, Springer ISBN 3-540-41795-8, pp. 937, A.Kling et al.(Eds.), 23-26 October (2000).

- [Fil01] D. Filges, F. Goldenbaum et al., *Spallation Neutron Production and the Current Intra-Nuclear Cascade and Transport Codes*. **Eur.Phys.Jour.** **A11**, I4, 467 (2001).
- [Fil01b] D. Filges, F. Goldenbaum et al., *Spallation Neutron Production and the Current Intra-Nuclear Cascade and Transport Codes*. **ESS-Report 118-08-T**, Aug.2001, 29 pages, ISSN 1433-559X (2001).
- [Fil01c] D. Filges et al., *Neutronic performance of moderators of the ESS mercury target-moderator-reflector system*. **ESS int.Report**, ESS-SAC-MOD-No.3 (2001).
- [Fil01d] D.Filges et al., proc. of the ANS Topical meeting on AccAPP/Acc driven transmutation technologies and applications '01, Nuclear Applications in the New Millennium, ISBN 0-89448-666-7 (2001) and D.Filges et al., *Nuclear simulation and radiation physics investigation of the target station of the European Spallation Neutron Source* **Nuclear Technology Vol. 132**, ANS Reprint (2000).
- [Fra65] J.S. Fraser et al., *Nuclear production in thick targets bombarded by high energy protons*. **Phys. in Canada vol. 21**, 17 (1965).
- [Fri83] W.A. Friedman et al., *Yields of medium mass nuclear fragments: Statistical emission*. **Phys.Rev. C28**, No 2, 950 (1983).
- [Fri90] W.A. Friedman, *Determining average E^** . **Phys.Lett. 242B**, 309 (1990).
- [Fri90b] W.A. Friedman, *Rapid massive cluster formation*. **Phys.Rev. C42**, 667 (1990).
- [Fro93] P. Fröbrich et al., *What are sensitive probes for nuclear friction in heavy-ion induced fission*. **Nucl.Phys. A563**, 326 (1993).
- [Fro93b] P. Fröbrich et al., *Langevin fluctuation-dissipation dynamics of hot nuclei: pre-scission neutron multiplicities and fission probabilities*. **Nucl.Phys. A556**, 281 (1993).
- [Gab96] T.A. Gabriel and S.G. Mashnik, *Semiempirical Systematics for different Hadron-Nucleus Interaction Cross Sections*. **JINR Preprint E4-96-43**, Dubna (1996).
- [Gai91] J.J. Gaimard and K.H. Schmidt, **Nucl.Phys. A531**, 709 (1991).
- [Gal94] J. Galin, U. Jahnke, *Hot nuclei as viewed through 4π neutron multiplicity filters*. **Nucl.Part.Phys. 20**, 1105-1142 (1994).
- [Gal01] J. Galin, *Spallation reactions studied with 4π -detector arrays*. **Pramana-journal of physics Vol. 57, No.1**, Indian academy of science, 67-73 (2001).
- [Gar99] I.S.K. Gardner et al., *Revised design for the ESS Linac*. **ESS-99-94-A** (1999).
- [Gav80] A. Gavron, *Statistical model calculation in heavy ion reactions*. **Phys.Rev. C21**, 230 (1980).
- [Gav87] A. Gavron et al., *Neutron emission in the fissioning ^{158}Er composite system*. **Phys.Rev. C35**, 579 (1987).

- [gea93] GEANT-*Description and simulation tool*. **CERN Program Library long writeup W5013**, (1993).
- [Gil65] A. Gilbert et al., **Can. J. Phys.** **43**, 1446 (1965).
- [Gil83] J.S. Gilmore et al., *Fertile-to-fissile conversion and fission measurement for thorium bombarded by 800 MeV protons* **Report LA-UR-83-3628** (1983).
- [Glo96] M. Gloris et al., *Proton-induced nuclide production in heavy target elements at medium energies.*, **2nd Int. Conf. on Accelerator driven Transmutation Technologies**, pp. 549, Kalmar, Sweden, June 3-7 (1996).
- [Glo01] M. Gloris et al., *Proton-induced production of residual radionuclides in lead at intermediate energies.* **NIM A463**, 593 (2001).
- [Goe64] K. Goebel et al., **Report CERN 64-12** (1964).
- [Gol80] A. Goldstein, *Classical mechanics*. **Addison-Wesley, Reading**, (1980).
- [Gol88] Ye.S. Golubeva, A.S. Iljinov, et al., *Inelastic interactions of intermediate-energy antinucleons with nuclei.* **Nucl.Phys. A483**, 539 (1988).
- [Gol94] E.S. Golubeva et al., *Correlations between multiplicities of pions and protons produced in inelastic interactions of intermediate-energy particles with nuclei.* **Physics of Atomic Nuclei**, vol. **57**, No 11, 2007 (1994).
- [Gol95] F. Goldenbaum: *Schwere Hadronen. XXVII. Arbeitstreffen Kernphysik in Schleching/Obb.*, 27.2–7.3.1995.
- [Gol96] F. Goldenbaum et al., *Heating of nuclei with energetic antiprotons.* **Phys.Rev.Lett.** **77**, Nr.6, 1230 (1996) und **HMI B540** Annual Report, 68 (1995).
- [Gol96b] F. Goldenbaum, **PhD thesis Berlin**, (1996).
- [Gol98] F. Goldenbaum et al., *Excitation energy dependent fission lifetime evolution for the $24\text{ A.MeV }^{238}\text{U} + ^{28}\text{Si}$ system measured by the blocking technique.* **Proceedings of the XXXVI International winter meeting on nuclear physics** edited by I. Iori, Bormio (Italy), January 26th–31th (1998).
- [Gol98b] F. Goldenbaum et al., *Production and decay of highly excited hot nuclei following antiproton annihilation at rest and in flight.* **4th INDRA workshop**, GANIL, France, May 25-28 1998.
- [Gol99] F. Goldenbaum et al., *Fission Time Evolution with Excitation Energy from a Crystal Blocking Experiment* **Phys.Rev.Lett.** **82**, Issue 25, 5012 (1999).

- [Gol99b] F. Goldenbaum for the NESSI-Collaboration: *Validation of Spallation Physics Experiments up to 2.5 Incident Proton Energy—Neutron and Charged Particle Production on Spallation Materials*. **Third International Workshop on Spallation Materials Technology**, LA-UR-00-3892, Santa Fe, New Mexico, April 29–May 4 (1999).
- [Gol99c] F. Goldenbaum et al., *Fission lifetimes as a function of E^* applying the blocking technique*. **XIIth Colloque GANIL**, Seignosse le Penon, France, May 17th–21st (1999).
- [Gol99d] F. Goldenbaum et al., *Decay modes induced by light particles (with special emphasis on antiprotons)*. **International Workshop XXVII on Gross Properties of Nuclei and Nuclear Excitations**, Waldemar-Petersen-Haus, Hirschegg, Kleinwalsertal, Austria, January 17-23, 1999, GSI Darmstadt, 1999, ISSN 0720-8715, pp. 104-115.
- [Gol99e] F. Goldenbaum for the NESSI-collaboration: *Validation of Hadron-Nucleus Transport Models in the GeV Range for thick W, Hg and Pb Targets*. Contributions to the 6th **ESS General Meeting**, Volume M1: Plenary Sessions, ISSN 1433-559X, ESS99-99-M-1 Nov. 99, Ancona, Italy, Sep. 20–23th (1999).
- [Gol99f] F. Goldenbaum et al., *Neutron and Charged Particle Production for GeV Proton-Nucleus Spallation Reactions* Nuclear Physics Spring Meeting Freiburg (Germany), 22.–26.3.1999, **Verhandl. DPG (VI) 34**, 127 (1999).
- [Gol00] F. Goldenbaum et al., *Validation of MC-Calculations of Spallation Reactions in Thin and Thick Targets in the GeV Range.*, **Proceedings of the Monte Carlo 2000 Conference**, Advanced Monte Carlo for radiation physics, particle transport simulation and applications, Lisbon, Portugal, Springer ISBN 3-540-41795-8, pp. 1003-1008, A.Kling et al.(Eds.), 23-26 October (2000).
- [Gol00b] F. Goldenbaum et al., *Models and Codes for Spallation Neutron Sources. Validation of Hadron-Nucleus Transport Models in the GeV Range*. **Proceedings of the Fifth Workshop On Simulating Accelerator Radiation Environments**. (SARE-5/SATIF-5 Meeting), Models and Codes for Spallation Neutron Sources, ISSN 1433-559X, ESS 112-01-T, OECD/NEA Headquarters, Paris, France, July 17-18, 2000, (edit. 2001).
- [Gol00c] F. Goldenbaum, *The European Spallation Source ESS: A next generation neutron source for Europe*. **XXXI. Arbeitstreffen Kernphysik** in Schleching/Obb., 8.3–16.3.2000.
- [Gol01] F. Goldenbaum, *Spallation Neutron Production and Validation of Transport Codes*. **Proceedings of the International Conference on Nuclear Data for Science and Technology ND2001**, Tsukuba, Japan, Nuclear Data Center, JAERI, Tokai-mura, Naka-gun, Ibaraki-ken, 319-1195, Japan, Oct. 7-12, 2001.

- [Gol02] F. Goldenbaum and D. Filges: *The ESS future project: Research with neutrons*, **MESON2002**, 7th International Workshop on Meson Production, Properties and Interaction of Mesons, Cracow, Poland, 24-28 May 2002, World Scientific, edit.: L Jarczyk, A. Magiera, C. Guaraldo, H. Machner, pp. 269-280, ISBN 981-238-160-0 (2002).
- [Got79] P.A. Gottschalk et al., *Shell-correction approach to nuclear state densities*. **Nucl.Phys. A278**, 16 (1977).
- [Gra80] P. Grangé and H.A. Weidenmüller, *Fission probability and the nuclear friction constant*. **Phys.Lett. 96B**, 26 (1980).
- [Gra83] P. Grangé et al., *Induced nuclear fission viewed as a diffusion process: Transients*. **Phys.Rev. C27**, 2063 (1983).
- [Gra84] P. Grangé et al., *Effects of transients on particle emission prior to fission in a transport description of the fission process*. **Nucl.Phys.A428**, 37c (1984).
- [Gra86] P. Grangé et al., *Effect of nuclear dissipation on neutron emission prior to fission*. **Phys.Rev. C34**, 209 (1986).
- [Gre80] R.E.L. Green et al., **Phys. Rev. C22**, 1594 (1980).
- [Gre87] R.E.L. Green et al., **Phys. Rev. C35**, 1341 (1987).
- [Gre88] S.L. Green et al., **J.Nucl.Matter 155-157**, 1350 (1988).
- [Gro75] D.H.E. Gross, *Theory of nuclear friction*. **Nucl.Phys. A240**, 472 (1975).
- [Gro86] D.H.E. Gross et al., *Decay of very hot nuclei*. **Phys.Rev.Lett. 56**, 1544 (1986).
- [Gro90] D.H.E. Gross, *Statistical decay of very hot nuclei—the production of large clusters*. **Rep.Prog.Phys. 53**, 605 (1990).
- [Gru82] C.R. Gruhn et al., **Nucl. Instr. Meth. 196**, 33 (1982). D. Guerreau et al., *Formation and decay of hot nuclei*. **Proc. of the 20th Mikolajki Summer School on Nuclear Physics**, Adam Higer, Bristol, 159 (1989).
- [Hah39] O. Hahn und F. Straßmann, **Naturwiss. 27**, 11 und 89 (1939).
- [Hau52] W. Hauser und H. Feshbach, *The inelastic scattering of neutrons*. **Phys.Rev. 87**, 366 (1952).
- [Her00] C.M. Herbach et al., **Proceedings of the Fifth Workshop On Simulating Accelerator Radiation Environments**. (SARE-5/SATIF-5 Meeting), Models and Codes for Spallation Neutron Sources, ISSN 1433-559X, ESS 112-01-T, OECD/NEA Headquarters, Paris, France, July 17-18, 2000, (edit. 2001).

- [Her01] C.M. Herbach et al., *Light Particle Production in Spallation Reactions Induced by Protons of 0.8 to 2.5 GeV Incident Kinetic Energy*.
Proceedings of the International Conference on Nuclear Data for Science and Technology ND2001, Tsukuba, Japan, Nuclear Data Center, JAERI, Tokaimura, Naka-gun, Ibaraki-ken, 319-1195, Japan, Oct. 7-12, 2001.
- [her02] C.M.Herbach for the NESSI Coll., **IKP/COSY Annual Report 2002**, to be publ. (2002).
- [Her03] C.M. Herbach et al.,: *A combination of two 4π detectors for neutrons and charged particles. II The Berlin Silicon Ball BSiB for light- and heavy ion detection*.
submitted to NIM, (2003).
- [Hil79] D. Hilscher et al., *Neutron emission in the reaction $^{165}\text{Ho}+^{56}\text{Fe}$ at $E_{\text{lab}}=8.5$ MeV/u*. **Phys.Rev. C20**, 576 (1979).
- [Hil81] D. Hilscher et al., *Neutron emission in heavy ion collisions at energies below 15 MeV/u*. **Proceedings of the 3rd Adriatic Europhysics Conference on Dynamics of Heavy-Ion Collisions**, Hvar, Yugoslavia, North Holland Publishing Company, 225 (1981).
- [Hil87] D. Hilscher et al., *Energy and linear-momentum dissipation in the fusion reaction of $^{165}\text{Ho}+^{20}\text{Ne}$ at 30 MeV/nucleon*. **Phys.Rev. C36**, 208 (1987).
- [Hil89] D. Hilscher et al., *Observation of cold scission of highly excited fissioning nuclei*. **Phys.Rev.Lett. 62**, 1099 (1989).
- [Hil91] D. Hilscher, *Wie langsam ist die Kernspaltung?* **Phys.Bl. 47**, Nr. 12, 1073 (1991).
- [Hil92] D. Hilscher und H. Rossner, *Dynamics of nuclear fission* **Ann.Phys.Fr. 17**, 471 (1992).
- [Hil92b] D. Hilscher, *Dynamics of hot nuclei*. **Proceedings of the international Conf. on New Nuclear Physics with advanced techniques**, Ierapetra, Greece, World Scientific 1992, edi.: F.A. Beck et al., 113 (1992).
- [Hil93] D. Hilscher et al., *Decay of hot nuclei at low spins produced by antiproton-annihilation in heavy nuclei*. **Proposal CERN/SPLC 93-8**, SPLC/P274 (1993).
- [Hil95] D. Hilscher, **Proc. of the XV EPS Nuclear Physics Divisional Conference**, St.Petersburg (Russia), World Scientific 1995, 165 (1995).
- [Hil95b] D. Hilscher et al., *Measurement of neutron multiplicity distributions for 1.22 GeV proton induced spallation reactions in 0.2–35 cm thick Pb targets*. **HMI B540 Annual Report**, 72 (1995).
- [Hil95c] D. Hilscher et al., *First Results on the Decay of Hot Nuclei at Low Spin (PS208)*. **Proceedings of the Third Biennial Conference on Low-Energy Antiproton Physics**, Bled, Slovenia, 12.–17.9.1994, edited by G. Kernel et al. (World Scientific 1995, ISBN 981-02-2236-X), 381 (1995).

- [Hil95d] D. Hilscher et al., *Antiprotonic heating of nuclei*. **CERN-Courier**, Physics Monitor, Jan./Feb. 1995, 18 (1995).
- [Hil96] D. Hilscher, *Calculation of the efficiency of the Si-Ball for fission fragments*. **Internal Report HMI**, (1996).
- [Hil96b] D. Hilscher et al., *Neutron Multiplicity Distributions for GeV Proton induced Spallation Reactions on thin and thick Targets of Pb and U*. **Proceedings of the International Workshop on Nuclear Methods for Transmutation of Nuclear Waste: Problems, Perspectives, Cooperative Research**, May 29 - 31, 1996, Dubna, Russia, editors M.Kh. Khankhasayev, H.S. Plendl, Z.B. Kurmanov, (World Scientific 1997, ISBN 981-02-3011-7), p. 176-190 (1996).
- [Hil98] D. Hilscher et al., *Neutron production by hadron-induced spallation reactions in thin and thick Pb and U targets from 1 to 5 GeV*. **NIM A414**, 100 (1998).
- [Hil97] D. Hilscher et al., **Proc.Int. Workshop on nuclear methods for transmutation of nuclear waste**, Dubna, World Scientific, 176 (1997).
- [Hil00] priv. communication with D.Hilscher.
- [Hil01] D. Hilscher et al., *Helium production for 0.8-2.5 GeV proton induced spallation reaction, Damage induced in metallic window materials*. **J. of Nucl.Materials** **296**, 83-89, (2001) proceedings of the Int. Materials Workshop-4, Schruns, Austria, Oct. 8-13 2000.
- [Hin86] D.J. Hinde et al., *Neutron multiplicities in heavy-ion induced fission*. **Nucl.Phys. A452**, 550 (1986).
- [Hin87] D.J. Hinde et al., *Mass-Split Dependence of the Pre- and Post-Scission Neutron Multiplicities for Fission of ^{251}Es* . **Nucl.Phys. A472**, 318 (1987) and **J.Phys.Soc.Jpn. 56**, 2357 (1987).
- [Hin89] D.J. Hinde et al., *Systematics of fission time scales*. **Phys.Rev. C39**, 2268 (1989).
- [Hin92] D.J. Hinde et al., *Neutron emission as a probe of fusion-fission and quasifission dynamics*. **Phys.Rev. 45**, 1229 (1992).
- [Hof92] P. Hofmann, *Antiprotoninduzierte Spaltung von ^{232}Th und ^{209}Bi* . **Dissertation**, TU München (1992).
- [Hof83] H. Hofman und J.R. Nix, *Fission dynamics simplified*. **Phys.Lett. 122B**, 117 (1983).
- [Hsi97] W.C. Hsi et al., **Phys.Rev.Lett. 79**, 817 (1997).
- [Hud69] J. Hudis und S. Katcoff, *High-energy-proton fission cross sections of U, Bi, Au and Ag measured with mica track detectors*. **Phys.Rev. 180**, 180 (1969).

- [Hud76] J. Hudis and S. Katcoff, **Phys.Rev. C13**, 1961 (1976).
- [Hug97] H.G.Hughes et al., MCNPX–The LAHET/MCNP Code Merger, X-Division Research Note XTM-RN(U)97-012, **LA-UR-97-4891**, Los Alamos National Laboratory (1997); <http://www-xdiv.lanl.gov/XTM/hughes/LA-UR-97-4891/cover.html>.
- [Hug00] H.G. Hughes et al., *Status of the MCNPX Transport Code.*, **Proceedings of the Monte Carlo 2000 Conference**, Advanced Monte Carlo for radiation physics, particle transport simulation and applications, Lisbon, Portugal, Springer ISBN 3-540-41795-8, pp. 961, A.Kling et al.(Eds.), 23-26 October (2000).
- [Hyd71] E.K. Hyde et al., **Phys.Rev. C4**, 1759 (1971).
- [IAEA97] **IAEA-TECDOC-985**, Accelerator driven systems: Energy generation and transmutation of nuclear waste, status report of the IAEA (1997).
- [icru93] ICRU Report 57, *Conversion coefficients for use in radiological protection against external radiation. Int.Commission on radiation units and measurements*, 7910 Woodmont Avenue Bethesda, Maryland 20814 USA (1998).
- [Ign75] A.V. Ignatyuk et al., *Fission of pre-actinide nuclei. Excitation functions for the (α, f)-reaction.* **Yad. Fiz. 21**, 1185 (1975), **Sov.J. of Nucl.Phys.21**, 612 (1975).
- [Ilj78] A.S. Iljinov et al., *An Analysis of nuclear fissility for intermediate-energy proton induced reactions.* **Z.f.Phys. A287**, 37 (1978).
- [Ilj82] A.S. Iljinov et al., *Nuclear absorption of stopped antiprotons.* **Nucl.Phys. A382**, 378 (1982).
- [Ilj94] A.S. Iljinov et al., *Intermediate energy nuclear physics.* **CRC Press**, (1994).
- [Ilj92] A.S. Iljinov et al., *Phenomenological statistical analysis of level densities, decay widths and lifetimes of excited nuclei.* **Nucl.Phys. A543**, 517 (1992).
- [Ill01] **ILL Yellow Book**, www.ill.fr
- [Ing84] G. Ingold, *Neutronenemission in Schwerionenreaktionen als Mass für die Anregungsenergie und den Übertrag von linearem Impuls — Experimente mit einem 4π -Szintillatortank.* **Dissertation** am Fachbereich Physik der Freien Universität Berlin, (1984).
- [Ino74] K. Inoue et al., *Slow neutron Spectra in cold moderators* **Journal of Nuclear Science and Technology**, 11(5), 228 (1974).
- [Ino76] K. Inoue and N. Otomo, *Pulsed cold Neutron Source* **Journal of Nuclear Science and Technology**, 13, 389 (1976).
- [Ino79] K. Inoue et al., **Atomic Energy Society Japan**, 21, 865 (1979).
- [Ish97] K. Ishibashi et al., **Journal of Nuclear Science and Technology**, 34, 529 (1997).

- [Isi99] **Ann. Rep.1998-99**, <http://www.isis.rl.ac.uk> (1999).
- [Jah83] U. Jahnke et al. *Lecture Notes in Physics*. **Springer Verlag, Berlin**, 178 (1983).
- [Jah86] U. Jahnke et al. *Violence of heavy-ion reactions from neutron multiplicity: (11 to 20)A-MeV $^{20}\text{Ne}+^{238}\text{U}$* . **Phys.Rev.Lett.** **57**,No 2, 190 (1986).
- [Jah86b] U. Jahnke et al. *Neutron multiplicity and high excitation energies. Experiments with a 4π -neutron multiplicity meter*. **Journal de Physique C4**, N° 8, 317 (1986).
- [Jah95] U. Jahnke et al., *Neutron generation with GeV-ion-beams: A pilot experiment with 1.2 GeV \bar{p} on kg-lead-targets*. **International Nuclear Physics Conference**, 21-26 August, 1995, Beijing, China.
- [Jah95b] U. Jahnke et al., *Production and Decay of Hot Nuclei by Antiproton Annihilation at Rest and in Flight*. **Third International Conference on Nucleon-Antinucleon Physics**, Moscow, Russia, 11.-16.9.1995.
- [Jah96] U. Jahnke et al., *Production and Decay of Hot Nuclei by Antiproton Annihilation at Rest and in Flight*. **Proceedings of the Fourth Biennial Conference on Low-Energy Antiproton Physics**, Moscow, GUS, September 11-16, 1995, Physics of Atomic Nuclei, Vol. 59, No.9, 1567 and **Yadernaya Fizika Vol. 59**, No.9, 1625 (1996).
- [Jah99] U. Jahnke et al., *Prevalence of Fission and Evaporation in the Decay of Heavy Nuclei Excited up to 1000 MeV with Energetic Antiprotons*. **Phys. Rev. Lett.** **83**, 4959 (1999).
- [Jah01] U. Jahnke et al., *Experimental Investigation of Neutron Generation in Thick Target Blocks of Pb, Hg and W with 0.4 to 2.5 GeV Proton Beams*. **Proceedings of the International Conference on Nuclear Data for Science and Technology ND2001**, Tsukuba, Japan, Nuclear Data Center, JAERI, Tokai-mura, Naka-gun, Ibaraki-ken, 319-1195, Japan, Oct. 7-12, 2001.
- [Jah03] U. Jahnke et al.,: *A combination of two 4π detectors for neutrons and charged particles. I The Berlin Neutron Ball BNB – a neutron multiplicity meter and a reaction detector*. **submitted to NIM**, xxx (2003).
- [Jan92] E. Jansen et al. **Physica B180**, 917 (1992).
- [Jas95] J. Jastrzebski et al. *Nuclear structure and nuclear excitations from antiproton-nucleus interaction*. **Acta Physica Polonica B26**, 527 (1995).
- [Jef94] JEFF-2.2, C.Nordborg and M.Salvatores, *Status of the JEF Evaluated Data Library*, **Proceedings of International Conference on Nuclear Data for Science and Technology**, Gatlinburg, Tennessee, USA, May 9-13, 1994, Vol. 2, p.680 (1994).

- [Jef02] JEF-3.0, R.Jacqmin et al., *Status of the JEFF-3 Project*, **Proc. International Conference on Nuclear Data for Science and Technology**, Oct. 7-12, 2001, Vol. 1, p.54 (2002).
- [Jen95] JENDL-3.2, T.Nakagawa et al., *Japanese Evaluated Nuclear Data Library Version 3 Revision-2: JENDL-3.2* **J. Nucl. Sci. Technol.** **32**, 1259 (1995).
- [Jen02] JENDL-3.3, K. Shibata et al., *Japanese Evaluated Nuclear Data Library Version 3 Revision-3: JENDL-3.3*, **J. Nucl. Sci. Technol.** **39**, 1125 (2002).
- [Jia89] D.X. Jiang et al., *Saturation of the thermal energy deposited in Au and Th nuclei by Ar projectiles between 27 and 77 MeV/u*. **Nucl.Phys.** **A503**, 560 (1989).
- [Joa63] G.D. Joanon et al., *A B3 code for the calculation of fast neutron spectra and associated multigroup constants*. **Report GA-4265** (1963).
- [Jun98] A.R. Junghans et al., **Nucl.Phys.** **A629**, 635 (1998).
- [Kah54] H.Kahn, *Application of Monte-Carlo*. **RM-1237-AEC** (1954).
- [Kah84] H. A. Kahn und A. Kahn, *Fission and spallation induced by 7-GeV protons on U, Bi, Pb, Au, W, Ho and Ag*. **Phys.Rev.** **C29**, 2199 (1984).
- [Kau74] S.B. Kaufmann et al., *A calibration procedure for the response of silicon surface-barrier detectors to heavy ions*. **NIM** **115**, 47 (1974).
- [Kau80] S.B. Kaufmann et al., **Phys.Rev.** **C22**, 167 (1980).
- [Kel87] J.G. Keller et al., *Distribution of the reaction strength in $^{32}\text{S}+^{182}\text{W}$ collisions*. **Phys.Rev.** **C36**, 1364 (1987).
- [Kim89] Y.D. Kim et al., *Multifragment emission observed for the reaction $^{36}\text{Ar} + ^{238}\text{U}$ at $E/A=35$ MeV*. **Phys.Rev.** **63**, No 5, 494 (1989).
- [Klo89] G. Klotz-Engmann et al., **Nucl.Phys.** **A499**, 392 (1989).
- [Kon92] A.Yu.Konobeyev et al., **Data library for radiation damage**, Carl Hanser Verlag, München 1992, Kerntechnik 57, No. 3 (1992).
- [Kon99] A.Yu.Konobeyev et al., **Fission product yields in nuclear reactions induced by intermediate energy particles**, Carl Hanser Verlag, München 1999, Kerntechnik 64, No. 4 (1999).
- [Kor01] Yu.A.Korovin et al., *Evaluated nuclear data files for accelerator driven systems and other intermediate and high energy applications*. **NIM** **A463**, 544 (2001).
- [Kot87] R. Kotte et al., **Nucl.Instr.Meth.** **A257**, 244 (1987).
- [Kot88] A.A. Kotov et al., **Exp. Technik der Phys.** **36**, 6, 513 (1988).

- [Kra40] H.A. Kramers, *Brownian motion in a field of force and the diffusions model of chemical reactions*. **Physica** **7**, 284 (1940).
- [Kuz92] V.F. Kuzichev et al., **Report ITEP 92-46**, Moscow (1992).
- [Kwi95] K. Kwiatkowski et al., *Multifragmentation in the 4.8-GeV $^3\text{He}+^{nat}\text{Ag}$, ^{197}Au reactions*. **Phys.Rev.Lett.** **74**, 3756 (1995).
- [Kwi86] K. Kwiatkowski et al., *Intermediate-mass-fragment production in the reaction of 200 MeV ^3He with Ag*. **Phy.Lett.** **B171**, No1, 41 (1986).
- [Lan66] M.B. Lang et al., *The angular momentum-dependence of the nuclear level density*. **Nucl.Phys.** **77**, 345 (1966).
- [Lan91] M. Lujan, *Spallation Physics*. **Newsletter LANSCE**, number 12, (1991).
- [Lau84] F. Saint-Laurent et al., *Momentum transfer in light-ion-induced fission reactions*. **Nucl.Phys.** **A222**, 307 (1984).
- [Lau95] F. Saint-Laurent et al., *Study of the nuclear multifragmentation: recent results obtained with the INDRA detector in the intermediate energy domain*. **Nucl.Phys.** **A583**, 481 (1995).
- [Led95] X. Ledoux, *Formation et déexcitation des noyaux chauds*. **Thèse**, Université de Caen, (1995).
- [Led98] X. Ledoux et al., **Phys.Rev.** **C57**, 2375 (1998).
- [Led99] X.Ledoux et al., **Phys. Rev. Lett.** **82**, 4412 (1999).
- [Ler01] S. Leray et al., *Spallation neutron production by 0.8, 1.2 and 1.6 GeV protons on various targets*. **DAPNIA/SPhN-01-44** 12/2001 (submitted to Phys.Rev.C, (2001).
- [Les91] J.P. Lestone et al., *Fission time scales from pre-scission charged particle multiplicities*. **Phys.Rev.Lett.** **67**, 1078 (1991).
- [Les93] J.P. Lestone et al., *Pre-scission charged-particle multiplicities following the reactions $^{164,167,170}\text{Er}+^{28}\text{Si}$* . **Nucl.Phys.** **A559**, 277 (1993).
- [Les93b] J.P. Lestone et al., *Determination of the time evolution of fission from particle emission*. **Phys.Rev.Lett.** **70**, 2245 (1993).
- [Let00] A.Letourneau et al., *Neutron Production in Bombardments of thin and thick W, Hg, Pb targets by 0.4, 0.8, 1.2, 1.8 and 2.5 GeV Protons*. **NIM** **B170**, 299 (2000).
- [Let01] A.Letourneau et al., PhD-Thesis to be published.
- [Let02] A. Letourneau et al., *Composite-particle emission in the reaction $p+\text{Au}$ at 2.5 GeV*. **Nucl.Phys.** **A712**, Issue 1-2, 133-166 (2002).

- [Lip94] V. Lips et al., *Multifragmentation induced by relativistic α -projectiles*. **Phys.Rev.Lett.** **72**, 1604 (1994).
- [Lot93] B. Lott et al., *Inclusive excitation-energy distributions of hot nuclei from 44 MeV/n Ar- and 32 MeV/n Kr-induced reactions*. **Z.Phys.** **A346**, 201 (1993).
- [Lot96] B. Lott et al., *Heating nuclei with high-energy antiprotons*. **Proceedings of Fourth Biennial Conference on Low-Energy Antiproton Physics**, Dinkelsbühl, August 27-31 1996.
- [Lot97] B. Lott et al., *Heating nuclei with high-energy antiprotons*. **Nucl.Phys.B** **56a** (Proc. Suppl.), 114 (1997).
- [Lot98] B. Lott et al., *Neutron multiplicity distributions for 200 MeV proton-, deuteron- and ^4He -induced spallation reactions on thick Pb targets*. **NIM** **A414**, 117 (1998).
- [Lot99] B. Lott et al., *Formation and Decay of Nuclei Heated with High-Energy Antiprotons*. **Nucl.Phys.** **A654**, 803c-806c (1999).
- [Lot01] B. Lott, F. Goldenbaum et al., *Thermal excitation and decay of nuclei following antiproton-nucleus interactions at 1.22 GeV*. **Phys.Rev.C****63**, 034616 (2001).
- [Lub94] P. Lubiński et al., *Neutron halo in heavy nuclei from antiproton absorption*. **Phys.Rev.Lett.** **73**, 3199 (1994).
- [Mac94] R.E. MacFarlane et al., *The NJOY nuclear data processing system, version91'* **LA-12740-M**, Los Alamos National Laboratory (1994).
- [Mai97a] R. Maier et al., *Cooler Synchrotron COSY* **Nuclear Physics** **A626**, 395c-403c (1997).
- [Mai97b] R. Maier, *Cooler Synchrotron COSY - performance and perspectives* **Physics Research** **A390**, 1-8 (1997).
- [Mar97] E.Martinez, **Ph.D. Thesis**, University of Caen (1997).
- [Mat68] E.S. Matusevich und V.I. Regushevskii, *Cross sections for fission of Bi, U, Np and Pu by 1-9 GeV protons*. **Sov.J.Nucl.Phys.** **7**, 708 (1968).
- [McD84] R.J. McDonald et al., **Nucl. Instr. Meth.** **219**, 508 (1984).
- [McG86] P.L. McGaughey, M.R. Clover and N.J. DiGiacomo, *Antiproton annihilations in nuclei may not produce high nuclear temperatures*. **Phys.Lett.** **B166**, 264 (1986).
- [Mei39] L. Meitner und R.O. Frisch, *Disintegration of uranium by neutrons: A new type of nuclear reaction*. **Nature** **143**, 239 (1939).
- [Mei99] S.Meigo et al., **NIM.A****431**, 521 (1999).
- [Mic95] R.Michel et al., **NIM** **B103**, 183 (1995).

- [Mok98] N.V. Mokhov et al., *Mars Code development*. Proc. of the fourth workshop on simulating accelerator radiation environments, pp.87-99, SARE-4, Sep. 14-16, Knoxville, Tennessee, edit. T.A. Gabriel (1998). **Phys.Rev.** **179**, 1176 (1969).
- [Mok00] N.V. Mokhov et al., *MARS Code Status.*, **Proceedings of the Monte Carlo 2000 Conference**, Advanced Monte Carlo for radiation physics, particle transport simulation and applications, Lisbon, Portugal, Springer ISBN 3-540-41795-8, pp. 943, A.Kling et al.(Eds.), 23-26 October (2000).
- [Mor69] L. G. Moretto et al., *Electron- and Bremsstrahlung-induced fission of heavy and medium-heavy nuclei*. **Phys.Rev.** **179**, 1176 (1969).
- [Mor75] L. G. Moretto, *Statistical emission of large fragments: A general theoretical approach*. **Nucl.Phys.** **A247**, 211 (1975).
- [Mor92] L. G. Moretto et al., *New Rayleigh-Taylor-like surface instability and nuclear multifragmentation*. **Phys.Rev.Lett.** **69**, 1884 (1992).
- [Mor84] A. Moroni et al., **Nucl.Instr.Meth.** **225**, 57 (1984).
- [Mor93] L. G. Moretto et al., *Experimental signature for statistical multifragmentation*. **Phys.Rev.** **71**, No 24, 3935 (1993).
- [Mor93b] L. G. Moretto und G. Wozniak, *Multifragmentation in heavy-ion processes*. **Annu.Rev.Nucl.Part.Sci.** **43**, 379 (1993).
- [Mor95] L. G. Moretto et al., *Are multifragment emission probabilities reducible to an elementary binary emission probability*. **Phys.Rev.** **74**, 1530 (1995).
- [Mor95b] L. G. Moretto et al., *Scaling laws, shell effects, and transient times in fission probabilities*. **Phys.Rev.Lett.** **75**, No 23, 4186 (1995).
- [Mor96] M. Morjean, Private Kommunikation (1996).
- [Mor98] M. Morjean et al., *Fission lifetime measured by the blocking technique as a function of excitation energy in the 24 A.MeV $^{238}\text{U} + ^{28}\text{Si}$ reaction*. **Nucl.Phys.** **A630**, 200c (1998).
- [Mor98b] M. Morjean et al., *Investigation of fission time distributions by the blocking technique in single crystals*. **Proceedings of the 4th International Conference on Dynamical Aspects of Nuclear Fission (DANF'98)** held in Casta-Papiernicka, Slovakia, on Oct. 19-23, 1998.
- [Mou78] J.B. Moulton et al., *A new method for calibrating the pulse-height defect in solid state detectors*. **NIM** **157**, 325-331 (1978).
- [Mus02] G. Musulmanbekov and A.Al-Haidary, *Fragmentation of nuclei at intermediate and high energies in modified cascade model*. **arXiv:nucl-th/0206054 v5**, 7th July (2002).

- [Mye67] W.D. Myers and W.J. Swiatecki, *Anomalies in nuclear masses*. **Ark.Fys.** **36**, 343 (1967).
- [Nag99] S.Nagamiya, JAERI-KEK Joint Project on high Intensity Proton Accelerator, **9th Int. Conf. on radiation shielding**, Oct. 17-22nd, Tsukuba, Int. Congress Center, Japan (1999).
- [Nat90] J.B. Natowitz et al., *The determination of fission time scales from excitation function data*. **Phys.Lett.** **B247**, 242 (1990).
- [Nei80] H.O. Neidel et al., *Improved determination of plasma delays of fission fragment and alpha-particle pulses in surface barrier detectors*. **NIM** **178**, 137 (1980).
- [Nel85] W.R.Nelson et al., SLAC-Report 265 (1985).
- [New90] J.O. Newton, *Nuclear fission induced by heavy ions* Fiz. Elem. Chastits At. Yadra **21**, 821 (1990) [engl.Übers.: **Sov. J. Part. Nucl.** **21**, 349 (1990)].
- [Nif99] H.Nifenecker et al., Hybrid Nuclear Reactors, Institut des Sciences Nucleaire des Grenoble, ISN 99.04 (1999).
- [Nii95] K. Niita et al., **Phys.Rev.** **C52**, 2620 (1995).
- [Nii01] K. Niita et al., *High energy particle transport code NMTC/JAM* **JAERI Data/Code 2001-007**, (2001).
- [Nik90] V.A.Nikolaev et al., **Int.collaboration of advanced neutron sources**, **Proc. ICANS-XI**, KEK, Tsukuba, Japan, Oct.22-26, 612 (1990).
- [Nix69] J.R. Nix, *Further studies in the liquid-drop theory of nuclear fission*. **Nucl.Phys.** **130**, 241 (1969).
- [Nor70] L.C. Northcliffe und R.F. Schilling, *Nuclear data tables*. **A7**, N3-4, (1970).
- [Nue02a] K. Nünighoff et al.: *Investigation of the Neutronic Performance of Cold Moderators with JESSICA* **Nucl.Phys.News Vol. 12, No. 4** (2002).
- [Nue02b] K. Nünighoff et al., *Cold moderator and neutron experiments on JESSICA COSY-Prop.*, No.105 (2002).
- [Och96] H. Ochiishi et al., **Nucl.Meth&Inst.** **A369**, 269 (1996).
- [Orm89] J. Ormand et al., *Nuclear level density parameter in hot nuclei*. **Phys.Rev.** **C40**, 1510 (1989).
- [Pab97] Pablo Lizana-Allende, *Unterkritische Systeme in der Nukleartechnik, Energieproduktion, Transmutation und Spaltstofferzeugung*. **Report Jül-3387**, Dissertation FZJ-ISR, ISSN 0944-2952 (1997).
- [Pab99] M. Pabst et al., *Progress on intense proton beam dynamics and halo formation*. **EPAC98** (1999).

- [Par67] J.B. Parker et al., *Monte carlo studies of scintillator efficiencies and scatter corrections for $(n,2n)$ cross section measurements*. **NIM 60**, 7-23 (1968).
- [Pas62] C.Passow, *Phenomenologische Theorie zur Berechnung einer Kaskade aus schweren Teilchen in Materie*. **Report DESY AR.85** (1962).
- [Pau92] G. Pausch et al., *Particle identification in solid-state detectors by exploiting pulse shape information*. **NIM A322**, 43 (1992).
- [Paw94] PAW94, edi. by R. Burn et al., *PAW users guide*, **Program Library Q121**, (1994).
- [Pea88] G.F. Peaslee et al., *Sources of light-charged-particle emission in the reaction $480^{57}\text{Fe} + \text{nat}\text{Ag}$* . **Phys.Rev. C38**, 1730 (1988).
- [Per98] Y.Perier et al., **NIM A413**, 312 (1998).
- [Pet94] R.J. Peterson et al., *Pion-induced fission and fragmentation*. **Jahresbericht Boulder**, 40 (1994).
- [Phy94] *Particles and fields*. **Phys.Rev. D50**, part I, Review of particle properties, 1173 (1994).
- [Pie94] L. Pienkowski et al., *Hot nuclei in reactions induced by 475 MeV , $2\text{ GeV}^1\text{H}$ and $2\text{ GeV}^3\text{He}$* . **Phys.Lett. B336**, 147 (1994).
- [Pie95] L. Pienkowski et al., *Comparison of neutron multiplicities measured with TOF and 4π -detectors*. **HMI B540** Annual Report, 70 (1995).
- [Pie96] L. Pienkowski, Private Kommunikation (1996).
- [Pie97] L. Pienkowski et al., *Neutron multiplicity distributions for 1.94 to $5\text{ GeV}/c$ proton-, antiproton-, pion-, kaon- and deuteron-induced spallation reactions on thin and thick targets*. **Phys. Rev. C56**, 1909 (1997).
- [Pie99] L. Pienkowski et al., *Decay of Hot Nuclei Formed with Energetic Antiprotons (PS208)*. **Nucl.Phys. A655**, 269c-274c (1999).
- [Pie00] L. Pienkowski et al., *Vaporization and Multifragmentation in the Reaction $1.2\text{ GeV } \bar{p} + \text{Cu}$ and Ag* . **Phys.Lett. B472**, 15 (2000).
- [Pisa99] The PISA Coll., **IKP/COSY Annual Report 1999**, Jül-3744, ISSN0944-2952, p.175ff (1999).
- [Pisa00] The PISA Coll., **IKP/COSY Annual Report 2000**, Jül-3852, ISSN0944-2952, p.172ff (2000).
- [Pisa01] The PISA Coll., **IKP/COSY Annual Report 2001**, Jül-3978, ISSN0944-2952, p.210ff (2001).

- [Poc95] J. Pochodzalla et al., *Probing the nuclear liquid-gas phase transition*. **Phys.Rev.Lett.** **75**, 1040 (1995).
- [Poi74] J. Poitou und C. Signarbieux, *A Monte-carlo-simulation of the capture and detection of neutrons with large liquid scintillators*. **NIM** **114**, 113 (1974).
- [Pol94] D. Polster, *Nichtgleichgewichtsprozesse in Kernreaktionen*. **Dissertation** an der Freien Universität Berlin (1994).
- [Pol95] D. Polster et al., *Light particle emission induced by stopped antiprotons in nuclei: Energy dissipation and neutron-to-proton ratio*. **Phys.Rev.** **C51**, No 3, 1167 (1995).
- [Pos71] A.M. Poskanzer et al., **Phys. Rev.** **C3** 882 (1971).
- [Pra88b] R. E. Prael et al., **Los Alamos NM 87545** (1988).
- [Pra88b] R.E.Prael et al., **Report LA-UR-88-3238**, Los Alamos National Laboratory (1988).
- [Pra89] R.E.Prael et al., **Report LA-UR-89-3014**, (1989).
- [Pra97] R.E.Prael et al., **Report LA-UR-97-1744 and LA-UR-97-1745**, Los Alamos National Laboratory (1997).
- [Pug76] A. Pugh, *Polyhedra: A visual approach*. **Univ. of California Press** (1976).
- [Pro01] A. Prokofiev, *Compilation and systematics of proton induced fission cross section data*. **NIM** **A463**, 557 (2001).
- [Raf80] J. Rafelski, *\bar{p} -annihilation on heavy nuclei*. **Phys.Lett.** **91b**, 281 (1980).
- [Ray88] J. Raynal, *Coupled channel calculations*. **Workshop on applied nuclear theory and nuclear model calculations for nuclear technology applications**, Trieste, 15-19 Feb 1988, 506 (1988).
- [Ree70] H. Reeves, W.A. Fowler, F. Hoyle **Nature** **226**, 727 (1970).
- [Ree94] H. Reeves, **Rev.Mod.Phys.** **66**, 193 (1994).
- [Rej01] F. Rejmund et al., **Nucl. Phys.** **A683**, 540 (2001).
- [Rev99] J.P. Revol et al., *The TARC experiment (PS211): neutron-driven nuclear transmutation by adiabatic resonance crossing.*, **Report CERN 99-11**, (1999).
- [Rem70] G. Remy et al., *Cross sections for binary and ternary fission induced by high energy protons in uranium and lead*. **Nucl.Phys.** **A163**, 583 (1970).
- [Ren96] E.Renshaw Foxford, **Phys.Rev.** **C54**, 749 (1996).
- [Ris89] H. Risken, *The Fokker-Planck equation*. **Springer-Verlag Berlin**, (1989).
- [Riv96] M.F. Rivet et al., **Phys.Lett.** **B388**, 219 (1996).

- [Rob79] T.J. Roberts et al., *Neutron-nucleus inelastic cross sections from 160 to 375 GeV/c*. **Nucl.Phys. B159**, 56 (1979).
- [Ros89] H. Rossner et al., *Analysis of pre- and post-scission neutrons emitted in the reaction $^{169}\text{Tm} (^{39}\text{Ar},f)$ at $E_{\text{lab}} = 205 \text{ MeV}$* . **Phys.Rev. C40**, 2629 (1989).
- [Rub93] C. Rubbia et al., *An energy amplifier for cleaner and inexhaustible nuclear energy production driven by a particle beam accelerator*. **Report CERN/AT/93-47(ET)**, (1993).
- [Rub94] C. Rubbia et al., *Status report on the energy amplifier*. **CERN**, (1994).
- [Rub95] C. Rubbia et al., *Conceptual design of a fast neutron operated high power energy amplifier*. **Report CERN/AT/95-44(ET)**, (1995).
- [Rub96b] C. Rubbia, *Status of the energy amplifier concept, 2nd Int. Conf. on Accelerator driven Transmutation Technologies*, pp. 35, Kalmar, Sweden, June 3-7 (1996).
- [Rub96] Th. Rubehn et al., *Scaling laws and transient times in ^3He induced nuclear fission*. **LBNL-38865, UC-413 Preprint**, subm. to Phys.Rev. C, (1996).
- [Rub97] C. Rubbia et al., *CERN-group conceptual design of a fast neutron operated high power energy amplifier.*, **IAEA-TECDOC-985**, pp. 187, Accelerator driven systems: Energy generation and transmutation of nuclear waste, status report of the IAEA (1997).
- [Rub01] V.A. Rubchenya et al., *Neutron and fragment yields in proton-induced fission of ^{238}U at intermediate energies*. **NIM A463**, 653 (2001).
- [Rus80] G.J. Russell et al., *Spallation target moderator-reflector studies at the weapons neutron research facility*. **Report LA-UR-80-1360** (1980) and *Some results of applied spallation physics research at Los Alamos*. **Report LA-UR-84-778** (1984).
- [San93] A.J. Santiago et al., **Nucl.Part.Phys. 19**, 349 (1993).
- [Sau77] F. Sauli, *Principles of Operation of Multiwire Proportional and Drift Chambers*, **CERN 77-09**, (1977).
- [Sch59] O.A.Schaeffer, A.Zähringer, **Phys.Rev. 113**, 674 (1959).
- [Sch82] Ch. Schiessl et al., **Nucl. Instr. Meth. 192**, 291 (1982).
- [Sch83] J. Schelten et al., **NIM 205**, 319 (1983).
- [Sch94] E. Schwinn et al., *Evolution of fission and competing decay mechanism in ^{40}Ar -induced reactions on Au, Th at 27–77 MeV/u of incident energy*. **Nucl.Phys. 568**, 169 (1994).
- [Sch95] S. Schmid, *Antiprotoninduzierte Kernspaltung*. **Diplomarbeit**, TU München (1995).

- [Sch96] W. Schmid, *Neutronen in Koinzidenz zur antiprotoninduzierten Spaltung von ^{238}U* . **Dissertation**, TU München (1996).
- [Sch97] S. Schmid et al., *Probability of fission induced by 1.2 GeV antiprotons*. **Zeitschrift für Physik A359**, Issue 1, 27 (1997).
- [Ser47] R. Serber, **Phys. Rev.** **72**, 1114 (1947).
- [Shu97] Yu.N.Shubin et al., **Proc.Int. Workshop on nuclear methods for transmutation of nuclear waste**, Dubna, World Scientific, 135 (1997).
- [Sie86] A.J. Sierk, *Macroscopic model of rotating nuclei*. **Phys.Rev.** **C33**, 2039 (1986).
- [Sik71] T. Sikkeland, *Fission excitation functions in interactions of ^{11}B , ^{12}C , ^{14}N , and ^{19}F with various targets*. **Phys.Rev.** **C3**, 329 (1971).
- [Sil90] R. Silverberg, C.H. Tsao, **Phys.Rep.** **191**, 351 (1990).
- [Sim89] M.H. Simbel, *Phenomenological analysis of fission induced by high-energy protons*. **Z. Phys.** **A333**, 177 (1989).
- [Slo90] E.D. Sloan, *Clathrate Hydrates of Natural Gases* Marcel Bekker Inc., New York (1990).
- [sns02] Spallation Neutron Source SNS, **Status Report**, Oak Ridge National Laboratory, USA; <http://www.ornl.gov/sns/>.
- [Sob94] N.M. Sobolevsky et al., *Intermediate energy nucl. data: Models and codes; Shield—a Monte-Carlo hadron transport code.*, **OECD Documents 1994**, Proc. of a specialists' meeting, pp. 237, ISSY-CES Moulinaux, France (1994).
- [Sta93] S. Stamer et al., **Phys.Rev.** **C47**, 1647 (1993).
- [Ste91] J. Steinberger, *First results at the LEP e^+e^- collider*. **Phys.Rep.** **203**, 345 (1991).
- [Ste98] G.Sterzenbach et al., **2nd Int. Topical meeting on nuclear Application of Accelerator Technology**, AccApp98', ISBN 0-89448-633-0, Sep. 20–23, Gettlingburg (1998).
- [Sto97] H. Stockhorst et al., *The Cooler Synchrotron COSY facility*. **Particle Accelerator Conference 1997**, Vancouver (1997).
- [Sto85] R.G. Stokstad, *The use of statistical models in heavy-ion reaction studies*. Treatise on Heavy Ion Science, ed. D.A. Bromley, New York, **Plenum Press vol. 3**, 81 (1985).
- [Sto86] H. Stöcker and W. Greiner, *High energy heavy ion collisions-Probing the equation of state of highly excited hadronic matter*. **Phys.Rep.** **137**, 277 (1986).
- [Str78] J.A. Strong, *Calibration of a large multi-element neutron counter in the energy range 8.5–430 MeV*. **NIM** **156**, 411 (1978).

- [Swi80] W.J. Swiatecki, **Prog.Part.Nucl.Phys.** 4, 383 (1980).
- [Tak97] H. Takada et al., *Reaction rate distribution measurement and analysis for 0.895 and 1.21 GeV proton bombardement on thick tungsten target. 3rd workshop on simulating accelerator radiation environments*, May 9th, KEK, Tsukuba, Japan (1997).
- [Tak00] H. Takada et al., *Present status of nucleon-meson transport code NMTC/JAERI., Proceedings of the Monte Carlo 2000 Conference*, Advanced Monte Carlo for radiation physics, particle transport simulation and applications, Lisbon, Portugal, Springer ISBN 3-540-41795-8, pp. 949, A.Kling et al.(Eds.), 23-26 October (2000).
- [Tas98] L. Tassan-Got et al., cont. paper to **ANS Int. Conf. on the Physics of Nuclear Science and Technology**, Long Island, NY, USA, Oct.5-8 (1998).
- [Tav92] O.A.P. Tavares und M.L. Terranova, *Analysis of ^{209}Bi and ^{238}U photofission cross section in the quasi-deuteron region of photonuclear absorption.* **Z.Phys. A343**, 407 (1992) und **Nuovo Cimento A105**, Nr. 5, (1992)
- [The92] D. Theis, *Inelastic hadron-nucleus collisions for general porpose detector simulations at intermediate energies.* **Dissertation**, Universität Bonn (1992).
- [Tit00] Y.E.Titarenko et al., **Proceedings of the Fifth Workshop On Simulating Accelerator Radiation Environments.** (SARE-5), Models and Codes for Spallation Neutron Sources, ISSN 1433-559X, ESS 112-01-T, OECD-Headquarters, Paris, France, July 17-18, 2000, (edit. 2001).
- [Tok81] J. Töke et al., *Surface-layer corrections to the level density formula for a diffuse Fermi gas.* **Nucl.Phys. A372**, 141 (1981).
- [Tok95] J. Töke et al., *Intermediate-mass fragment decay of the neck zone formed in peripheral collisions at $E_{\text{lab}}/A=28$ MeV.* **Phys.Rev.Lett.** 75, 2920 (1995).
- [Tro89] R. Trockel et al., *Onset of multifragment emission in heavy-ion collisions.* **Phys.Rev. C39**, No 2, 729 (1989).
- [Tso95] K. Tso et al., *Evidence for the reducibility of multifragment emission to an elementary binary emission in Xe-induced reactions.* **LBL-36858, UC-413 Preprint**, Submitted to Phys.Lett. B, (1995).
- [Van73] R. Vandenbosch und R.J. Huizenga, *Nuclear fission.* **New York**, (1973).
- [Vas90] R.G. Vassilkov et al., *Neutron emission from an extended lead target under the action of light ions in the GeV region.* **Proc. ICANS-XI**, Tsukuba, 340 (1990).
- [Ven96] F. Venneri et al., *The Los Alamos accelerator-driven transmutation of nuclear waste (ATW) concept development of the ATW target/blanket system., 2nd Int. Conf. on Accelerator driven Transmutation Technologies*, pp. 758, Kalmar, Sweden, June 3-7 (1996).

- [Vio85] V.E.Viola et al., *Systematics of fission fragment total kinetic energy release*. **Phys.Rev. C31**, 1550 (1985).
- [Vol75] E.M. Volin et al., preprint LNPI No. 101, Leningrad 1974, **Phys.Lett. B55**, 409 (1975).
- [Wal76] J.R.Walton et al., **J. Geophys.Res. 81**, 5689 (1976).
- [Wat52] B.E. Watt, *Energy spectrum of neutrons from thermal fission of ^{238}U* . **Phys.Rev. 87**, 1037 (1952).
- [Weg74] G. Wegmann, *Static viscosity of nuclear matter*. **Phys.Lett. 50b**, 327 (1974).
- [Wei80] H.A. Weidenmüller, *Progress in particle and nuclear physics.*, Pergamon Press, Oxford vol. vol.3, 49 (1980).
- [Wei87] H.A. Weidenmüller, *Transient times in nuclear fission*. **Nucl.Phys. A471**, 1c (1987).
- [Wei40] V.F. Weisskopf et al., **Phys. Rev. 57**, 472 (1940).
- [Wes78] G.D. Westfall et al., **Phys. Rev. C17**, 1368 (1978).
- [Wes85] G.D. Westfall et al., **Nucl.Instr.Meth. A238**, 347 (1985).
- [Wil80] W.W. Wilke et al., *Table of reaction parameters for heavy ion reactions*. **Atomic Data and Nuclear Data Tables 25**, 389 (1980), and Nuclear Structure Research Laboratory, **Report UR-NSRL-221**, 242 (1980).
- [Wil88] K.D. Williamson et al., *A combined H_2/CH_4 Cold Moderator for a short pulsed Neutron Source*. **Proc. of the 10th Meeting of the Int. Collaboration on Advanced Neutron Sources (ICANS)**, Los Alamos (USA), 3-7.10.1988, (1988).
- [Wla00] W. Wlazlo et al., submitted to **Phys. Rev. Lett.** (2000).
- [Wu84] San Lan Wu, *e^+e^- physics at PETRA—The first five years*. **Phys.Rep. 107**, 59 (1984).
- [Yar79] Y. Yariv et al., **Phys. Rev. C 20**, 2227 (1979).
- [Yar81] Y. Yariv et al., **Phys. Rev. C 24**, 448 (1981).
- [You92] P.G. Young et al., *Comprehensive nuclear model calculations: Introduction to the theory and use of the GNASH code*. Proc. ICTP Workshop on comp. and anal. of nuclear data relevant to nuclear en. and safety, 10 Feb-13 Mar, 1992, Trieste, Italy, **LA-12343-MS**, Los Alamos National Laboratory, (1992).
- [Zie94] P. Ziem et al., *The PS208 experiment control*. **HMI B526** Annual Report, 143 (1994).
- [Zie96] Ziem et al., *An OS9-UNIX data acquisition system with ECL readout*. **IEEE Trans. on Nuclear Science, vol. 43**, 128 (1996).

Danksagung

Die hier vorliegende Habilitationsarbeit wurde im Institut für Kernphysik der Forschungszentrum Jülich GmbH unter Leitung von Prof. Dr. D. Filges angefertigt. Durch ihn ist nicht nur mein Ansinnen einer Habilitation an der Bergischen Universität geboren, sondern sein hohes Interesse und seine starke fachliche Unterstützung haben mich ermutigt, dieses Ziel weiter zu verfolgen.

Besonderer Dank gilt meinen Kollegen der Arbeitsgruppe Strahlungstransport um Herrn Prof. Dr. D. Filges für ihre fachliche und auch sehr persönliche Unterstützung, sowie ihre Anregungen und ihr stets offenes Ohr. Deren ständige Diskussionsbereitschaft war im hohen Maße nützlich. Insbesondere in Fragen auf dem Gebiet der Hochenergie-Teilchentransportmodelle und Codes hätte ich auf die weitreichenden Kenntnisse von Günter nicht verzichten wollen. Er hat meine Bewunderung nicht zuletzt durch seinen unerschöpflichen Enthusiasmus neue Ideen und Programmpakete zu implementieren geerntet.

Die Realisierung der vorgestellten Experimente ist sicherlich nur dem Engagement und guten Zusammenwirken aller jeweiligen Kollaborationsmitglieder zu verdanken. Dabei gebührt meinen französischen und Berliner Freunden und Kollaborationspartnern des ehemaligen PS208 Experiments (CERN) aus dem später die "NESSI-Aktivitäten" am Cooler Synchrotron in Jülich gewachsen sind mein besonderer Dank.

Mein Dank gilt Kay und Christoph sowie allen Kollegen der JESSICA crew, die sicherlich durch ihr zielstrebiges Vorgehen wichtige Beiträge auf dem Gebiet der Target/Moderator/Reflektor-Auslegung beigetragen haben. Als eine besondere Ehre habe ich die Entscheidung der PISA-Kollaboration empfunden, mich zum Sprecher der deutsch-polnisch-südafrikanischen Arbeitsgruppe zu nominieren. Der Kontakt insbesondere zu meinen polnischen Kollegen war mir stets wissenschaftlich und sozial eine große Bereicherung.

Prof. Dr. J. Cugnon von der Universität Liege danke ich für die ausgesprochen gute Zusammenarbeit im Rahmen des HINDAS-Projektes und die Überlassung seines einzigartigen Codes, der half, zahlreiche Verständnisprobleme zu lösen.

Für ihre Hilfsbereitschaft danke ich all denen im Institut und in meinem persönlichen Umfeld, die auf ihre Weise zum Zustandekommen dieser Arbeit beigetragen haben. Die Interpretation experimenteller Resultate insbesondere bzgl. der Observable "Anregungsenergie" war stets durch die ausführliche aufschlußreiche Kommunikation mit Hartwik begleitet. Der Aufbau der komplexen Experimente wäre ohne den fachmännischen Einsatz und die ingenieurmässig ausgefeilten Ideen von Norbert Paul nicht realisierbar gewesen.

An erster Stelle gilt jedoch mein grösster Dank meiner Familie, insbesondere meiner lieben Frau, ohne deren langwährendes Verständnis diese Arbeit undenkbar gewesen wäre.

Author: Frank Goldenbaum currently working as a physicist at the Institute of Nuclear Physics, Forschungszentrum Jülich GmbH has been active in the field of nuclear reaction mechanisms such as spallation physics, multifragmentation, fission and vaporization since 1993. He accomplished his PhD at the Hahn-Meitner-Institute Berlin in 1996 on the formation and subsequent decay of highly excited hot nuclear matter using the annihilation of antiprotons provided by the LEAR accelerator (CERN, Geneva). This book was accepted as postdoctoral lecture qualification at the University of Wuppertal in 2003.

A recent renaissance of interest for energetic proton induced production of neutrons originates largely from the inception of projects for target stations of intense spallation neutron sources (ESS, SNS in the US and J-PARC in Japan), accelerator-driven nuclear reactors, nuclear waste transmutation, and also from the application for radioactive beams. The objective of this book is not only to summarize and identify the essential high- and intermediate energy nuclear data, required in the framework of such applications, but also to gain insights into the complex reaction mechanisms itself. In this work the issue has quite successfully been addressed experimentally at the Cooler Synchrotron COSY in Jülich by varying relevant parameters — providing an exhaustive matrix of benchmark data. However, the challenge was to increase the predictive power of transport codes employed for applications in particle physics. To scrutinize several of such codes, reaction cross sections, hadronic interaction lengths, neutron multiplicity and energy distributions, and the development of hadronic showers are here investigated. The performance and flexibility of state-of-the-art of Monte-Carlo particle interaction models and transport codes is demonstrated.